UC Berkeley
UC Berkeley Electronic Theses and Dissertations

Title

Seismic Performance and Modeling of Reinforced Concrete and Post-Tensioned Precast Concrete Shear Walls

Permalink

https://escholarship.org/uc/item/7231r2g9

Author

Tanyeri, Ahmet Can

Publication Date

2014

Peer reviewed|Thesis/dissertation

Seismic Performance and Modeling of Reinforced Concrete and Post-Tensioned Precast Concrete Shear Walls

by

Ahmet Can Tanyeri

A dissertation submitted in partial satisfaction of the

requirements for the degree of

Doctor of Philosophy

in

Engineering - Civil and Environmental Engineering

in the

Graduate Division

of the

University of California, Berkeley

Committee in charge:

Professor Jack P. Moehle, Chair

Professor Stephen A. Mahin

Professor David R. Brillinger

Fall 2014

Seismic Performance and Modeling of Reinforced Concrete and Post-Tensioned Precast Concrete Shear Walls

ABSTRACT

Seismic Performance and Modeling of Reinforced Concrete and Post-Tensioned Precast Concrete Shear Walls

by

Ahmet Can Tanyeri

Doctor of Philosophy in Engineering - Civil and Environmental Engineering

University of California, Berkeley

Professor Jack P. Moehle, Chair

Past earthquakes have shown examples of unsatisfactory performance of buildings using reinforced concrete structural walls as the primary lateral-force-resisting system. In the 1994 Northridge earthquake, examples can be found where walls possessed too much overstrength, leading to unintended failure of collectors and floor systems, including precast and post-tensioned construction. In the 2010 Maule Chile earthquake, many structural wall buildings sustained severe damage. Although Chilean design standards result in different reinforcement detailing than is common in U.S. walls, the failure patterns raise concerns about how well conventionally reinforced structural walls in U.S. buildings will perform during the next earthquake. Alternative wall design philosophies that offer more predictable response, with better damage control, should be investigated.

After the M_w 8.8 Chile earthquake, the 15-story Alto Rio building in Concepción sustained failures near the base, overturned, and came to rest on its side. The collapse of the Alto Rio building was significant because it was designed using the Chilean Building Code NCh433.Of96, which requires the use of ACI 318-95 for design of reinforced concrete structural elements intended to resist design seismic forces. The failure of the Alto Rio building is significant for many reasons. It is the first modern shear wall building of its type to collapse by overturning during an earthquake. The building is studied using forensic data and structural models of the framing system subjected to earthquake shaking. The study identifies the likely failure mechanism and suggests areas for which design and detailing practices could be improved. The capabilities and shortcomings of the analyses to identify details of the failure mechanism are themselves important outcomes of the study.

A second study explores the behavior of structural wall buildings using unbonded post-tensioned structural walls. Such walls offer the opportunity to better control yielding mechanisms and promote self-centering behavior. The study focuses on the measured responses of a full-scale, four-story building model tested on the E-Defense shaking table in Japan. The seismic force-resisting system of the test building comprised two post-tensioned (PT) precast frames in one direction and two unbonded PT precast walls in the other direction. The building was designed using the latest code requirements and design recommendations available both in Japan and the U.S., including the ACI ITG-5.2-09. The test building was subjected to several earthquake ground motions, ranging from serviceability level to near collapse. Analytical studies were carried out to test the capability of the structural models to replicate behaviors important to

structural engineers, and to assess whether available analysis tools are sufficient to model dynamic behavior that results when a full-scale building is subjected to realistic earthquake ground shaking. Measured response data from such an outstanding test provides an opportunity to fully understand the response characteristics of PT walls and assess the ability of nonlinear analytical models to reproduce important global and local responses, including three-dimensional system interactions, both prior to and after loss of significant lateral strength. Moreover, this study to assess behavior and system interaction of PT walls leads to improvements of the current design ideas and performance expectations.

The present study examines both the collapse of the Alto Rio building in Chile and the shaking table tests of the unbonded post-tensioned wall building in Japan. The collapse study suggests areas of improvement in current design and detailing practice. The shaking table study suggests an alternative approach to design of shear walls in buildings. Both studies demonstrate the use of modern structural analysis tools to interpret building responses to earthquake shaking. Taken together, the studies provide added confidence in earthquake simulation capabilities and demonstrate alternatives for designing earthquake-resistant buildings that use structural walls.

To my dear parents, Nermin and Haluk Fahri Tanyeri,

and my sister Bike Naz Tanyeri.

ACKNOWLEDGMENTS

Most importantly, I greatly appreciate the unconditional support and mentorship of Professor Jack P. Moehle. I learned a lot from him professionally and even more personally. I can never pay him back for these four years.

I would like to thank particularly Professors John W. Wallace, James M. Kelly, Stephen A. Mahin and David R. Brillinger for serving as members in my qualifying exam and dissertation committees and for providing me with guiding comments related to my research work.

Lead participation of T. Nagae, T. Matsumori, H. Shiohara, T. Kabeyasawa, S. Kono, K. Tahara, and M. Nishiyama from Japan and J. Wallace, W. Ghannoum, and R. Sause from the U.S is gratefully acknowledged.

I would also like to thank my fellow Davis Hall colleagues and more importantly academic family. Thanks to Marco Broccardo, Sunny J. Mistry, Panagiotis Galanis, Gian Giacomo Palombo, Gerd Brandstetter, Tea Visnjic, Mayssa Dabaghi, Simon Kwong, Mohamed Moustafa, Grigoris Antonellis, James Goulet, Hamed Hamedifar, and Tonguc Deger.

I am also grateful for my friends I met in Berkeley and I-House. They made Bay Area an unforgettable place. Thanks to Tom Nunziata, D.J. Gustashaw, Alexander Petuskey, Daniel Wilcoxon, Alexander Stack, Ersen Akici, Samantha Baime, Emily Vaughan, Clara Nagy, Vicky Kaasa, Amy Nemirovsky, Cecile Basnage, Roel Dobbe, Thomas Feldt, Alper Taner, Ola Berg Swensson, and Giovanni Labatte.

I would like to express my deepest gratitude to my friends in Turkey, Sabrican Bozkurt, Kemal Cihan Simsek, Bahar Ozdemir, Yigit Isbiliroglu, Emre Cift, Koray Saydar, Arda Akgun, Bora Demirel, Tuna Demirel, and Ezgi Arslantay for their continuous support all these years.

I would like to extend my special thanks to my good friend Nevzat Tekin for his kind support throughout my studies and for our legendary Vegas trip in 2013. That spring break was unforgettable and re-motivated me to complete my dissertation.

Special thanks to Calvin Harris and Swedish House Mafia, for providing the soundtrack of my entire time here at Berkeley.

Son olarak ve en onemlisi, canim annem Nermin, babam Haluk Fahri Tanyeri, ve de kardesim Bike Naz Tanyeri'ye tesekkur etmek istiyorum. Her seyi sizlere borcluyum. Anneannecim Asiye Yuksel huzur icinde uyu.

TABLE OF CONTENTS

LIST OF FIGURES

LIST OF TABLES

Chapter 1. Introduction

1.1 Motivation

Reinforced concrete structural shear walls are a very common and effective choice of lateral-load-resisting system to resist wind and earthquake loading. Structural walls provide the required lateral stiffness and strength for performance-based design of mid- and high-rise buildings under strong ground motions. Reinforced concrete shear walls are also popular due to the relatively small amount of floor area they occupy and the confidence of engineering community to the satisfactory performance of a well detailed structural wall.

Despite the popularity and general success of structural walls as earthquake-resisting elements, past earthquakes have shown examples of unsatisfactory performance of buildings using reinforced concrete structural walls as the primary lateral force-resisting system. In the 1994 Northridge earthquake, many older reinforced concrete buildings experienced severe damage, and some collapsed due to brittle failure modes. Some examples can be found where walls possessed too much overstrength, leading to unintended failure of collectors and floor systems, including precast and post-tensioned construction. Similarly, in the 2010 Maule (Chile) and 2011 Christchurch (New Zealand) earthquake, many modern structural wall buildings sustained severe damage, and some even collapsed. Although Chilean and New Zealand design standards result in different reinforcement detailing than is common in U.S. walls, the failure patterns raise concerns about how well conventionally reinforced structural walls in U.S. buildings will perform during the next earthquake. There is a need to investigate the seismic performance of the current design practice in the U.S. and the ability of current engineering models to simulate the seismic behavior of reinforced concrete shear walls.

After the Mw 8.8, 27 February 2010 Maule Chile earthquake, at least 50 multi-story reinforced concrete buildings were severely damaged and four collapsed partially or totally. Among these, the 15-story Alto Rio building in Concepción sustained failures near the base, overturned, and came to rest on its side. The collapse of the Alto Rio building was significant because it was designed using the Chilean Building Code NCh433.Of96, which requires the use of ACI 318-95 for design of reinforced concrete structural elements intended to resist design seismic forces. It is the first modern shear wall building of its type to collapse by overturning during an earthquake. The failures and analysis results suggest areas for which design and detailing practices could be improved in the current engineering practices using ACI 318.

Observations of unsatisfactory performance of the Alto Rio building and other similar buildings in Chile and Christchurch are very important for advancing engineering practice. Engineering studies of such buildings can help engineers understand those aspects that may have led to the collapse, and may lead to improvements in engineering practices.

Observations of unsatisfactory performance of convention reinforced concrete construction can also serve as a impetus for developing new structural framing systems that are less prone to critical damage. One system that has received attention in the past decade incorporates unbonded post-tensioned structural walls. Such walls can be designed to have a predictable inelastic fuse

with required strength and energy dissipation characteristics, and with self-centering response to result in a building that returns to its original up-right position following an earthquake.

In December 2010, the National Research Institute for Earth Science and Disaster Prevention (NIED) in Japan conducted a three-dimensional earthquake simulation test on a full-scale, four-story building using the E-Defense shaking table. Design, instrumentation, preliminary analytical studies, and testing of the building were a collaboration among researchers from Japan and the U.S. (lead researchers in the U.S. were J. Moehle, W. Ghannoum, R. Sause, and J. Wallace). The seismic force-resisting system of the test building comprised two PT frames in one direction and two unbonded PT precast walls in the other direction. The building was designed using the latest code requirements and design recommendations available both in Japan and the U.S., including the ACI ITG-5.2-09. The test building was subjected to several earthquake ground motions, ranging from serviceability level to near collapse.

Three-dimensional earthquake simulation testing of full-scale specimens is rare. Data from this test give a unique opportunity to understand the behavior of the unbonded PT walls and their interaction with other structural elements during an earthquake. Analytical studies were carried out as part of the overall research program. The studies, which are reported here, aim to develop practical structural engineering models, to conduct analytical simulations to test the capability of the structural models to replicate behaviors important to structural engineers, and to assess whether available analysis tools are sufficient to model dynamic behavior that results when a full-scale building is subjected to realistic earthquake ground shaking.

The present study examines both the collapse of the Alto Rio building in Chile and the shaking table tests of the unbonded post-tensioned wall building in Japan. The collapse study suggests areas of improvement in current design and detailing practice. The shaking table study suggests an alternative approach to design of shear walls in buildings. Both studies demonstrate the use of modern structural analysis tools to interpret building responses to earthquake shaking. Taken together, the studies provide added confidence in earthquake simulation capabilities and demonstrate alternatives for designing earthquake-resistant buildings that use structural walls.

1.2   Scope of the Study

The first part of the study examines the collapse of the Alto Rio building during the 2010 Chile earthquake. The study aims to identify various hypotheses to explain the collapse, and uses structural analysis to test the validity of those different hypotheses. The study emphasizes practical approaches to assessing the collapse of a complex conventional reinforced concrete building subjected to earthquake shaking. The results of analyses and failures identify details of the failure mechanism and suggest areas for which design and detailing practices could be improved. The capabilities and shortcomings of the analyses to identify details of the failure mechanism are themselves important outcomes of the study.

The second part of this study examines the response of the unbonded, post-tensioned building model tested on the E-Defense shaking table. The study develops practical structural engineering models to conduct analytical simulations to test the capability of the structural models to replicate behaviors important to structural engineers, and to assess whether available

analysis tools are sufficient to model dynamic behavior that results when a full-scale PT shear wall building is subjected to realistic earthquake ground shaking. Measured response data from such an outstanding test provides an opportunity to fully understand the response characteristics of PT walls and assess the ability of nonlinear analytical models to capture important global and local responses, including three-dimensional system interactions, both prior to and after loss of significant lateral strength. Moreover, this study to assess behavior and system interaction of PT walls leads to improvements of the current design ideas and performance expectations.

1.3   Manuscript Organization

This dissertation is organized in five chapters, with specific content identified below.

Chapter 2 reviews previous studies of structural walls, including experimental studies on reinforced concrete shear walls, numerical simulation and modeling of reinforced concrete shear walls, and the research on post-tensioned precast concrete shear walls.

Chapter 3 assesses the collapse of the Alto Rio building in the 2010 Chile earthquake. Several analyses of the building are presented to investigate the possible reasons for the collapse. The results of analyses and failures identify details of the failure mechanism and suggest areas for which design and detailing practices could be improved.

Chapter 4 assesses the performance of the unbonded, post-tensioned building model tested on E-Defense. Extensive test data from the tests are presented. The chapter also develops practical structural engineering models and conducts analytical simulations to test the capability of the structural models to replicate behaviors important to structural engineers and assess the ability of nonlinear analytical models to capture important global and local response.

Chapter 5 presents a summary of research findings and conclusions as well as a list of topics for future research.

Chapter 2.   Previous Studies

This chapter presents a brief review of the state of the art in seismic design and performance of reinforced and post-tensioned precast concrete shear walls. Section 2.1 presents a review of the previous experimental work on slender reinforced concrete walls, providing the code compatibility of test specimens and observed damage. In Section 2.2, the previous research on the numerical simulation and modeling techniques of reinforced concrete shear walls is presented. Finally, Section 2.3 presents the experimental and numerical research done on post-tensioned precast concrete and rocking shear walls.

2.1   Experimental Studies on Reinforced Concrete Shear Walls

Numerous laboratory-based studies of reinforced concrete structural walls have been reported in the literature. This section reviews a representative sample of those studies.

Oesterle et al. (1976 and 1979) at Portland Cement Association Construction Technology Laboratories conducted a comprehensive experimental research program of sixteen approximately 1/3 scale reinforced concrete structural walls for earthquake resistant structures. The objective of the experimental program was to introduce design recommendations for walls with enhanced energy dissipation achieved through nonlinear response of the constituent concrete and steel materials.

The test variable considered for the experiments were i) shape (rectangular, barbell, flanged), ii) amount of the flexural reinforcement, iii) amount of horizontal web reinforcement, iv) amount of boundary element transverse reinforcement, v) axial load level (zero or constant axial load ranging from 0.06 to $0.13 A_g f_c'$), vi) loading protocol (monotonically and cyclically), and vii) concrete compressive strength (5600 to 7800 psi, or 38 to 54 MPa).

The wall specimens were designed according to the 1971 ACI building code. The design yield strength of the steel was 60 ksi (414 MPa) and the design concrete compressive strength was 6.0 ksi (41 MPa). The aspect ratio of wall specimens was 2.4. Figure 2.1 shows the cross-sections of the specimens tested. All of the wall specimens were 4 in (102 mm) thick, 75 in (190cm) long and 15 ft (4.60 cm) tall. The specimens with the barbell shape had 12 in (305 mm) square boundary elements. The specimens with the flanges had 4 in (102mm) thick and 36 in (910 mm) long flanges. The wall specimens had longitudinal boundary reinforcement ratios of 1.1 to 4.4%, and vertical web reinforcement ratios of 0.25 to 0.31%. The horizontal web reinforcement ratios of the walls tested were 0.31 to 1.38%. Figure 2.2 shows the test setup.

The results of the Oesterle et al. (1976 and 1979) concluded that the shear stress level of the structural wall had a dramatic impact on the overall behavior and crack pattern (Figure 2.3). In walls with low shear stress demands, where maximum shear stresses are less than $3.0\sqrt{f_c'}$, the damage was consisted of crushing of concrete core and buckling of the longitudinal reinforcement. Figure 2.3.a indicates this flexure-dominated failure mode. For walls with high

shear stress demands, where maximum shear stresses are more than $7.0\sqrt{f_c'}$, the damage consisted of crushing of wall web under shear. Figure 2.3.b shows the shear-dominated damage state. Because shear-dominated response limits the wall ductility dramatically, it is concluded that the level of nominal shear stress had an adverse effect in the wall ductility.
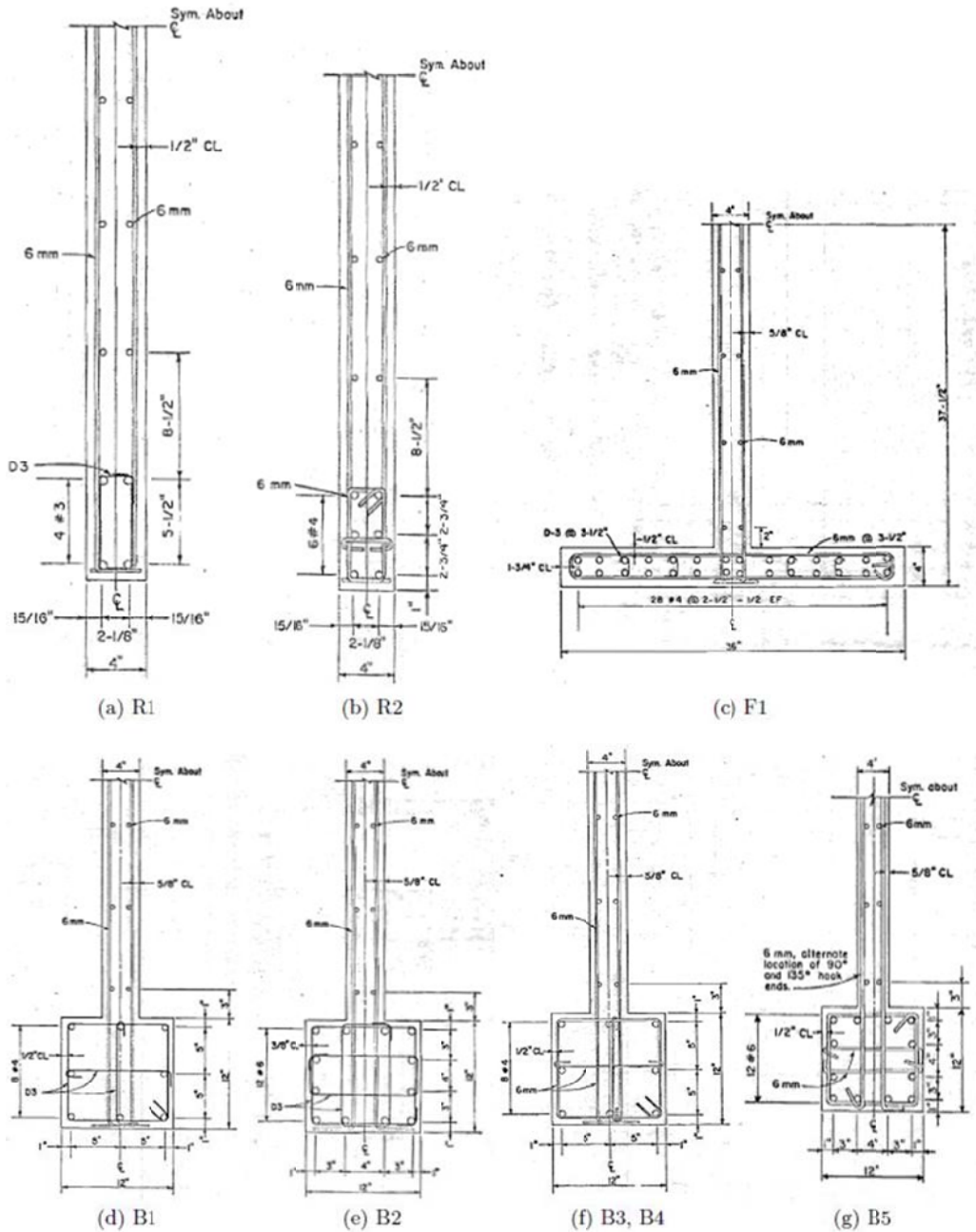
Figure 2.1 - Wall specimen cross-sections of Oesterle et al. (1976 and 1979)

Oesterle et al. (1976 and 1979) also concluded that the 1971 ACI Building Code requirements did not substantially improve wall strength or ductility. Improved confinement in the boundary elements enhanced the inelastic response. Shear distortions coupled with the

5

flexural rotations contributes significantly to the total lateral deformations. The study also showed that loading protocol had an influence on the strength and deformation capacity of walls, causing the cyclically loaded specimens to have less strength and deformation capacity than similar walls loaded monotonically.
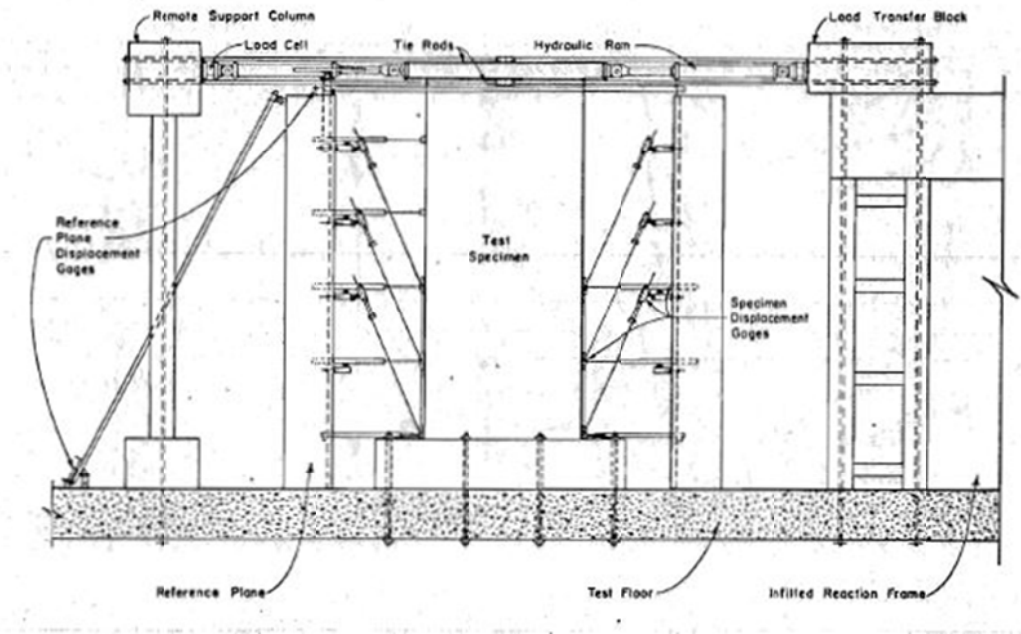
Figure 2.2 - Test setup of Oesterle et al. (1976 and 1979)
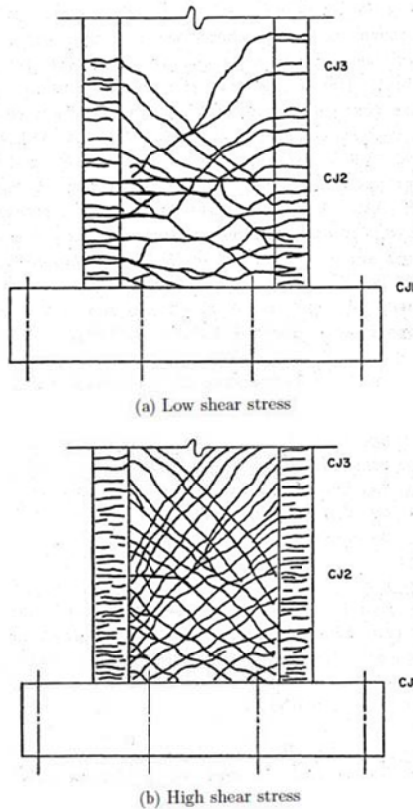
Figure 2.3 - Crack map of Oesterle et al. (1976 and 1979)

Thomsen and Wallace (1995 and 2004) conducted an experimental research program of four one-quarter scale slender cantilever reinforced concrete shear walls at the Structural Laboratory at Clarkson University. Two of these walls had a rectangular shape and other two had a T-shaped cross-section. Specimen walls were 4 in (102 mm) thick, 4 ft (1.2 m) long and 12 ft (3.7m) tall. The flange of the T-shaped walls had the same size with the web portion of the wall, which was 4ft (1.2m) length and 4 in (102mm) thickness. Figure 2.4 and Figure 2.5 shows the cross-sections of the rectangular and T-shaped specimens, respectively.

The experimental program was to verify the Wallace and Moehle (1993) displacement-based design approach, which determines the region of special confinement according to a linear strain distribution. Between rectangular walls RW1 and RW2, the size of the boundary element was kept the same but the detailing and spacing of the crossties were changed. For the T-walls, TW1 had the same boundary element details with the rectangular walls, but TW2 had a longer boundary region according to the Wallace and Moehle (1993) displacement based design approach. The concrete compressive strength ranged from 4200 to 8500 psi (29 to 58 MPa), and the reinforcing steel yield strength was around 63 to 65 ksi (435 to 450 MPa). All specimens were subjected to a constant axial load of approximately $0.1A_g f_c'$. All specimens were subjected to cyclic deformations up to 2.5% drift ratio with 0.5% increments.

7
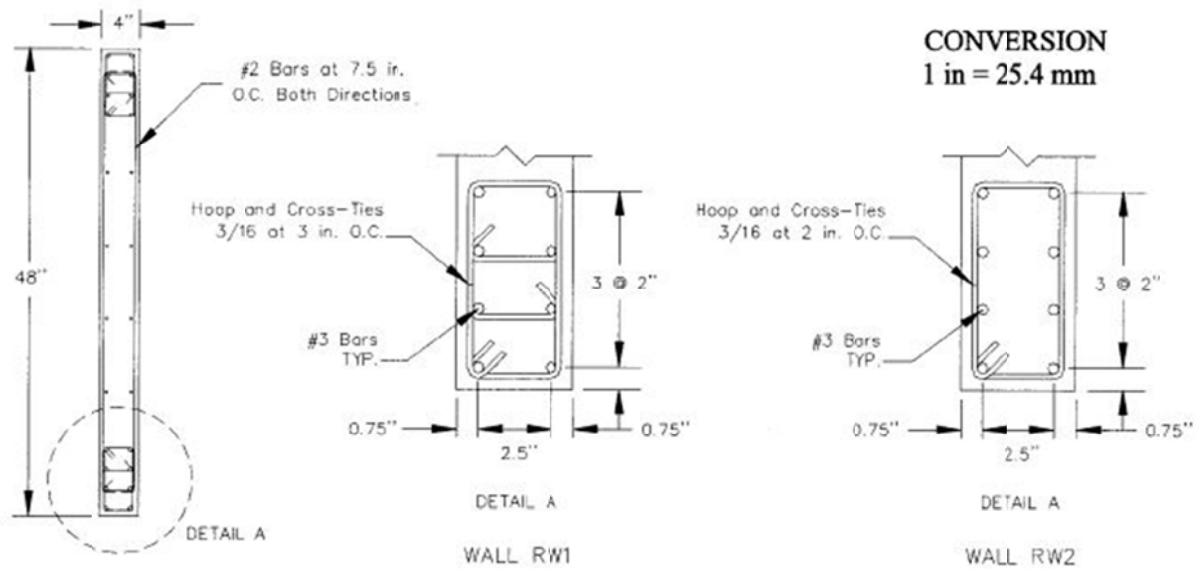
Figure 2.4 - Rectangular specimens of Thomsen and Wallace (1995 and 2004)

For the walls RW1 and RW2, yielding of longitudinal reinforcement, splitting and crushing of concrete were observed at around the same drift demands. More closely detailed RW2, delayed the buckling of longitudinal reinforcement. On the other hand, there was a dramatic difference in the behaviors of TW1 and TW2. Poorly detailed TW1 failed at a drift ratio of 1.25% due to the buckling of longitudinal bars. However, the same failure mode was observed at 2.5% drift ratio for the TW2. Figure 2.6 shows the damaged states of the walls.
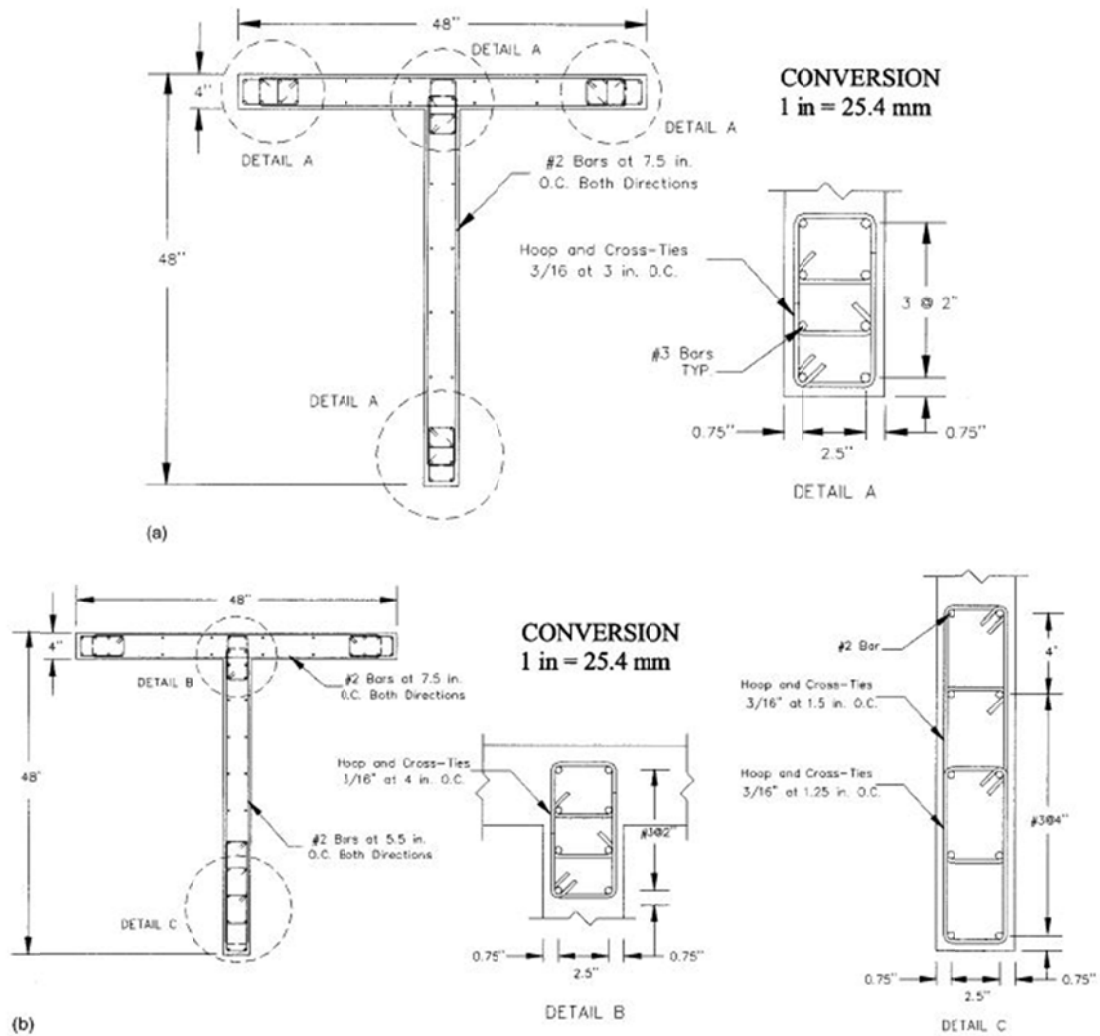
Figure 2.5 - Flanged specimens of Thomsen and Wallace (1995 and 2004)

Thomsen and Wallace (1995 and 2004) concluded that the smaller detailing of transverse reinforcement can delay the buckling of longitudinal reinforcement. This study also proved that the assumption of linear strain distribution on structural walls is acceptable for design purposes and the proposed displacement-based design approach was a robust way for detailing of boundary elements of structural walls. Figure 2.6 shows pictures of the damaged state of the specimens.

9

(a) RW1 (prior to fail-ure)

(b) RW2

(c) TW1

(d) TW2
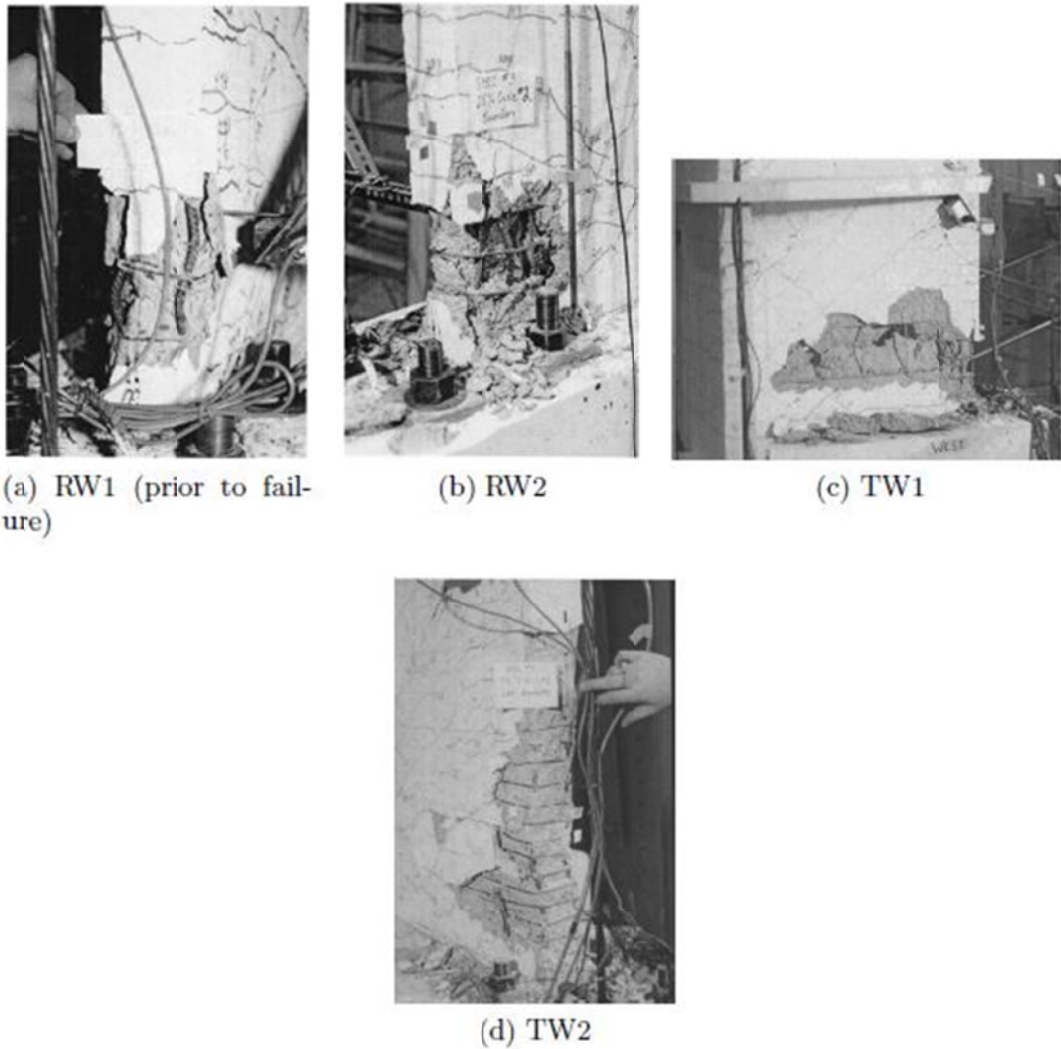
Figure 2.6 - Damaged specimens of Thomsen and Wallace (1995 and 2004)

Pilakoutas and Elnashai (1995) tested six 1/2.5 scale rectangular reinforced concrete structural walls. The wall specimens had an aspect ratio of 2.0. The main variable between wall specimens was the change in the amount of shear reinforcements. All of the six walls were 60 mm (2.4 in) thick, 0.6 m (24 in) long, and 1.2 m (48 in) tall. The longitudinal reinforcement ratio was 3% at the boundary regions, vertical and horizontal reinforcement ratios at the web ranged from 0.3 to 0.48%. The amount of transverse reinforcement at the boundary region did not meet the ACI 318-11 requirements; however, the web reinforcement was adequate for the same code. The concrete compressive strength ranged from 4600 to 6700 psi (32 to 46 MPa), and the reinforcing steel yield strength was around 58 to 80 ksi (400 to 550 MPa). No axial load was applied. All specimens were subjected to cyclic deformations. Figure 2.7 shows the reinforcement details of the specimens.

10

Specimen SW4 and SW6 failed with concrete crushing at the boundary region at around drift ratios of 2.0% and 1.8%, respectively. SW7 failed due to fracture of the longitudinal reinforcement at a drift ratio of 1.8%, while SW5 failed due to diagonal shear failure at a drift ratio of 0.8%. The only difference between these specimens was the higher shear reinforcement ratio of SW7. Lateral drift ratio of approximately 2.0% was reached by SW8 and SW9, without substantial loss of lateral load capacity. It was concluded that the excessive amounts of horizontal web reinforcement more than the amount required would not dramatically affect the strength and deformation capacity of walls. Figure 2.8 shows pictures of the damaged state of the specimens.
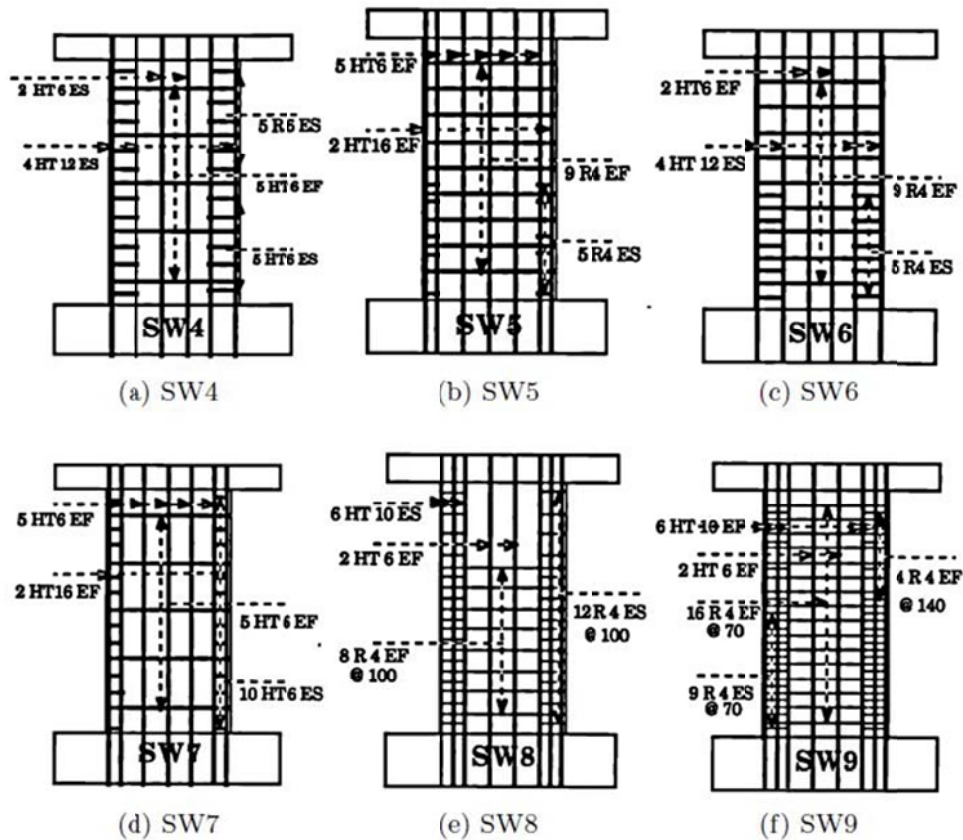
Figure 2.7 - Reinforcement details of Pilakoutas and Elnashai (1995)
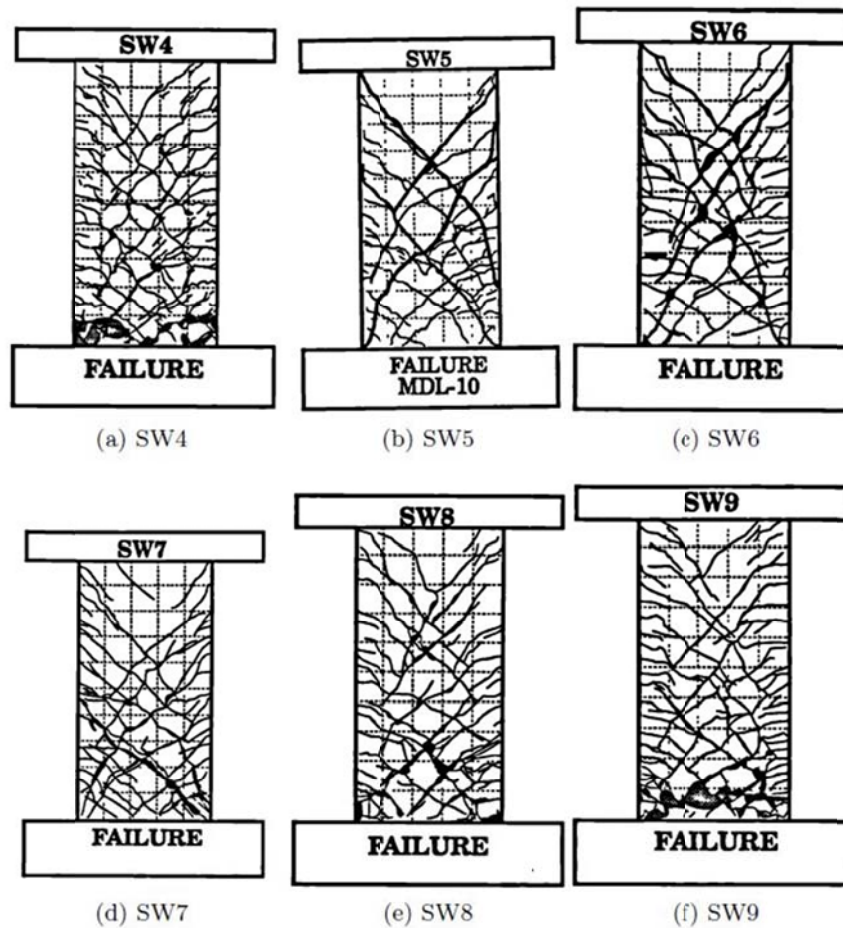
Figure 2.8 - Damaged specimens of Pilakoutas and Elnashai (1995)

Dazio et al. (2009) at ETH Zurich conducted a comprehensive experimental research program of six approximately 1/2 scale reinforced concrete structural walls. The objective of the experimental program was to understand the effects of the ductility and amount of vertical reinforcement on deformation capacity and failure mode of reinforced concrete shear walls. All specimens had a thickness of 5.9 in (150 mm), 79 in (2.0 m long, and 15 ft (4.5 m) tall, with an aspect ratio of 2.25. The concrete compressive strength ranged from 5500 to 6700 psi (38 to 46 MPa), and the reinforcing steel yield strength was around 72 to 94 ksi (500 to 650 MPa).). All specimens were subjected to a constant axial load of approximately 0.05 to $0.13 A_g f_c'$. All specimens were subjected to cyclic deformations up to 2.5% drift ratio with 0.5% increments. Figure 2.9 shows the reinforcement details of the specimens.

Two of the specimens failed due to crushing of concrete, other four of walls failed due to fracture of the longitudinal reinforcement. This study concluded that the wall deformation capacity is directly related to the amount of longitudinal reinforcement, and ductility of the reinforcing steel. Figure 2.10 shows pictures of the damaged state of the specimens. It is noteworthy that the tested specimens are designed for the regions of moderate seismicity in Central Europe, and they did not meet the ACI 318-11 Building Code requirements.

12
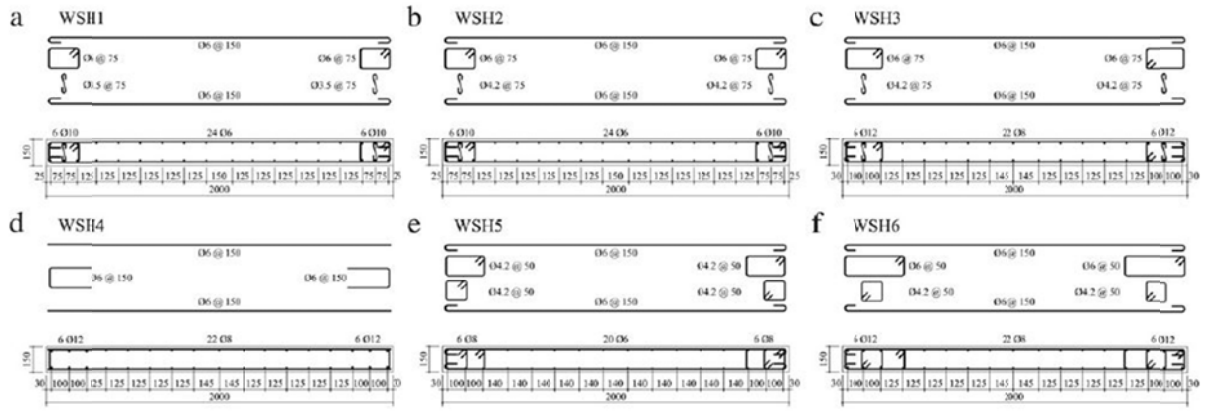
Figure 2.9 - Reinforcement details of Dazio et al. (2009)
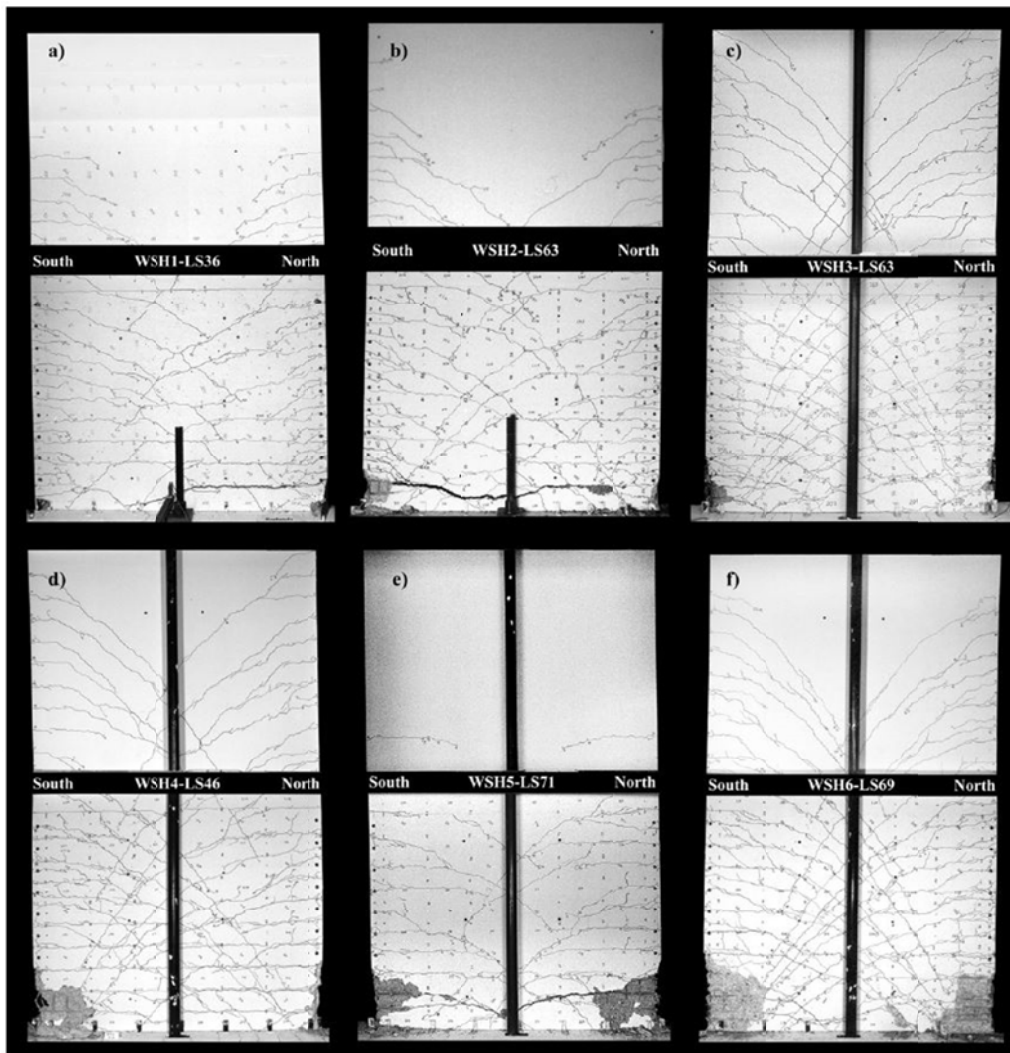
Figure 2.10 - Damaged specimens of Dazio et al. (2009)

2.2 Research on Numerical Simulation and Modeling of Reinforced Concrete Shear Walls

Several numerical modeling techniques have been studied for simulating the response of reinforced concrete shear walls. The most common and the simplest approach is the lumped plasticity using beam-column elements. In this model, the element is located at the centroid of the wall with rigid links on beam girders. The beam-column element consists of two nonlinear rotational springs at the critical section of the wall that the inelastic actions are expected to happen and an elastic flexural element that represents the rest of the wall. Figure 2.11shows a representation of the beam-column elements.

The moment-rotation relationship assigned to the rotational springs of beam-column elements can be selected in two ways. The commonly used way in engineering practice is the use of basic backbone curves for the flexural response of the walls from ASCE 41 Supplement 1 (2007). These backbone curves are established from the gathered experimental data on structural walls. The backbone curves vary according to the nominal flexural capacity, reinforcement ratio, shear and axial demands on the walls. The rotational spring is usually located at the center of the plastic hinge region which is defined by the one-half of the wall length (l_w). This is a very simple way to model the behavior of structural walls. The rotation capacities defined by the ASCE41 document are conservative and may not represent the behavior of different configuration of shear walls. The second way is to calculate a moment-rotation relationship of the wall using a section-analysis software. This approach is more reliable for walls with peculiar details and strongly relies on the assumption of the linear distribution of the strains in wall cross-sections. However, a big pitfall of these models is that the moment-rotation spring cannot capture the interaction of the flexural response with axial and shear forces. Therefore, in a wall with significant axial or shear force variation, this model will misrepresent the behavior. This simple beam-column model is the most computationally efficient tool for analyses of slender structural walls.

Some modifications to standard beam-column model has been proposed for improved representation such as use of multiple springs by Takayanagi and Schnobrich (1976), varying inelastic zones by Keshavarzian and Schnobrich (1984), and different behavior for inelastic shear by Aristizabal (1983). One big pitfall of the beam-column models is the lack of representation of the bar slip effects. The study done by Lehman and Moehle (2000) that the bar slip plays a significant role in the total displacement of columns tested. Therefore, ignoring this effect can cause misleading results for the neutral axis depth of such wall cross-sections. Similar modeling problems occur for rocking walls due to the different kinematic translation due to the neutral axis shift shown in Figure 2.12 and Kabeyasawa et al. (1983).

A more complicated (and arguably more advanced) solution for modeling of reinforced concrete shear walls is the use of distributed plasticity elements or lumped plasticity elements with fiber cross-sections. These models use fiber cross-sections to define the moment-curvature response and a predefined plastic hinge length to calculate the moment-rotation response. The fibers are used to discretize the cross-section into concrete and steel fibers for which uniaxial stress-strain curves are defined from material coupon tests or constitutive models. From the axial and flexural loads acting on the section, strains of the individual fibers are calculated assuming a linear strain distribution. Calculated strains are transformed into fiber stresses from the assigned

14

constitutive material models, and used to compute the forces in that section from the fiber stresses and discretized fiber areas. Force equilibrium of the element is checked and computation is done again for the next iteration step. Fiber cross-sections are commonly used in engineering practice and thus in commercial software such as ETABS and Perfrom 3D (CSI) and research oriented software such as OpenSees (Mazzoni et al. 2006). On the contrary of the lumped plasticity model with rotational springs, fiber cross-section models can simulate the effect of the axial force variation to the flexural response. However, similar to the lumped plasticity model with rotational springs, fiber cross-section models cannot simulation the interaction of shear forces to the flexural response of structural walls. Moreover, the assumption of linear strain distribution employed fiber cross-section model may cause inaccurate results for some wall configurations and rocking shear walls. This model is computationally efficient, robust, and widely used in engineering practice. Figure 2.13 shows a representation of the distributed plasticity element with fiber cross-sections.
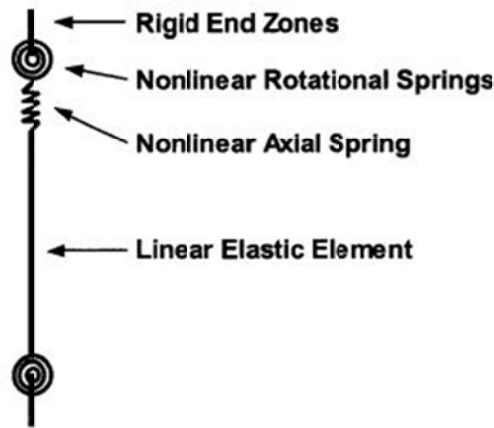
Figure 2.11 - Simple representation of the beam-column element (Orakcal (2004))

(a)Beam-colum element   (b) Observed behavior
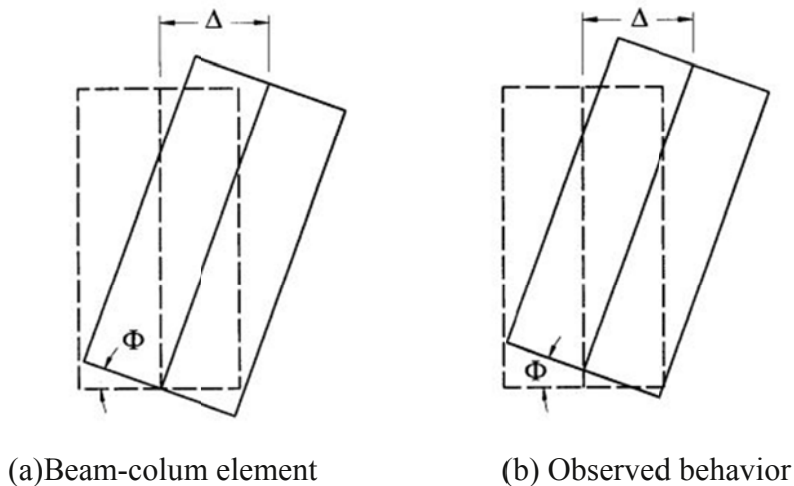
Figure 2.12 - Wall rocking and shift of neutral axis (Orakcal (2004))

15

Fiber Cross-Section
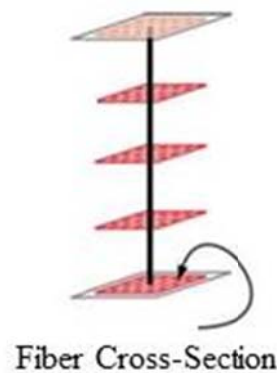
Figure 2.13 - Simple representation of the beam-column element with fiber cross section

Kabeyasawa et al. (1983) proposed a new macroscopic Three- Vertical-Line-Element-Model (TVLEM) to analyze a seven story reinforced concrete frame wall building test in Tsubaka, Japan. They observed that the experimentally observed behavior could not be simulated by a beam-column element. The wall was represented as three vertical line elements with infinitely rigid beams at the top and bottom of the element (Figure 2.14). Two outer truss elements were representing the boundary elements. The central element was a series of vertical, horizontal and rotational springs.
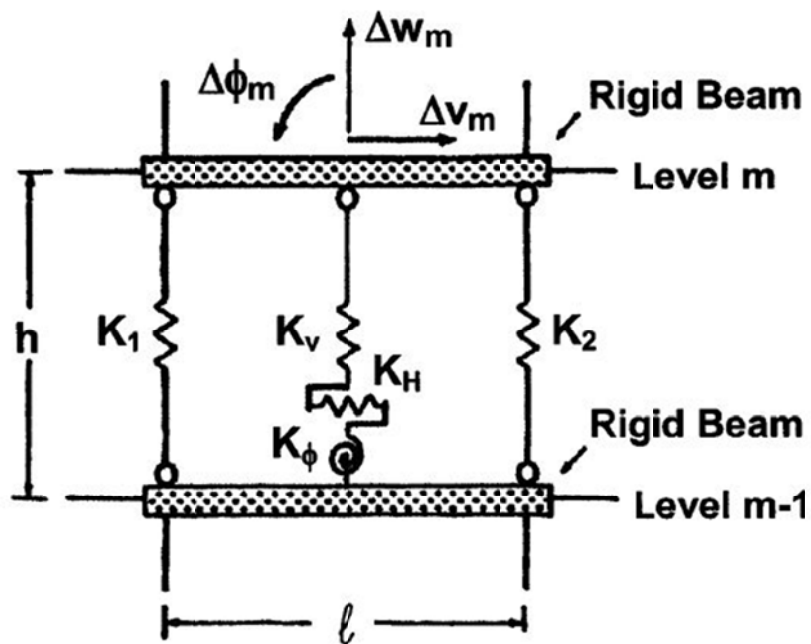
Figure 2.14 - Three-Vertical-Line-Element-Model (TVLEM) (Kabeyasawa et al., 1983)

The axial force-deformation relationship of the three vertical springs (K_1, K_2, and K_v) was defined by the axial-stiffness-hysteresis model (ASHM), shown in Figure 2.15. Similarly the

16

force-deformation hysteretic rules for the horizontal and rotational springs were defined by the origin-oriented-hysteresis model (OOHM), Figure 2.16. The stiffness of the rotational spring was defined by the wall area except the boundary elements. The model was capable of simulating the stiffness degradation but it was uncoupled from the axial and flexural forces. The model simulated the neutral axis position and the global responses compared with the experimental responses. Moreover, model was able to provide the interaction of the wall with connected frame elements. However, the application of this model is very subjective and limited.
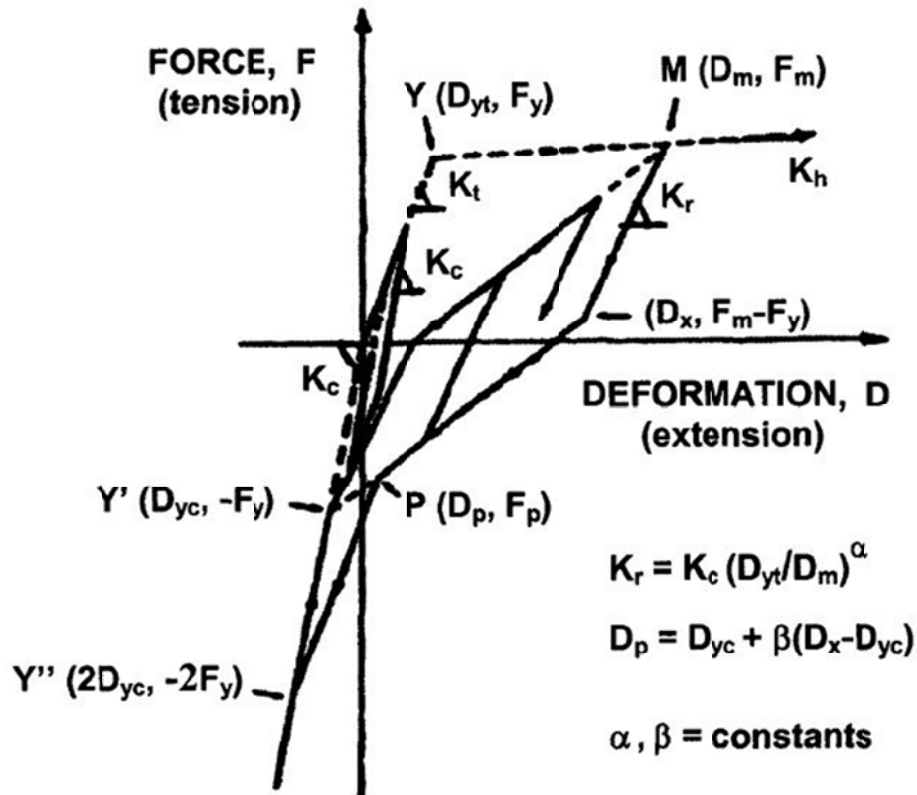
Figure 2.15 - Axial-Stiffness-Hysteresis Model (ASHM) (Kabeyasawa et al., 1983)

Vulcano and Bertero (1986) proposed a modification to the TVLEM by introducing the two-axial-element-in-series model (AESM) instead of the axial-stiffness-hysteresis model (ASHM). AESM was consisted of two elements in series (Figure 2.17). Element 1 was a one-component model representing the axial stiffness of the boundary column where the bond between longitudinal reinforcement and concrete is intact. Element 2 is a two-component model representing the steel (S) and cracked concrete (C) at rest of the boundary columns where the bond is not intact. The AESM aims to simulate the hysteretic behavior of steel and concrete and their interaction. The Element 1 had a linear elastic behavior assigned. For Element 2, the steel component had a bilinear behavior with strain hardening and the concrete component had a linear elastic behavior under compression with no tensile strength. The force-deformation relationship of AESM is shown in Figure 2.18. Similar to the TVELM proposed by Kabeyasawa et al. (1983), the origin-oriented-hysteresis-model (OOHM) was used for the horizontal and rotational springs.

17

Figure 2.16 - Origin-Oriented-Hysteresis-Model (OOHM) (Kabeyasawa et al., 1983)

Figure 2.17 - Axial-Element-in-Series-Model (AESM) (Vulcano and Bertero 1986)
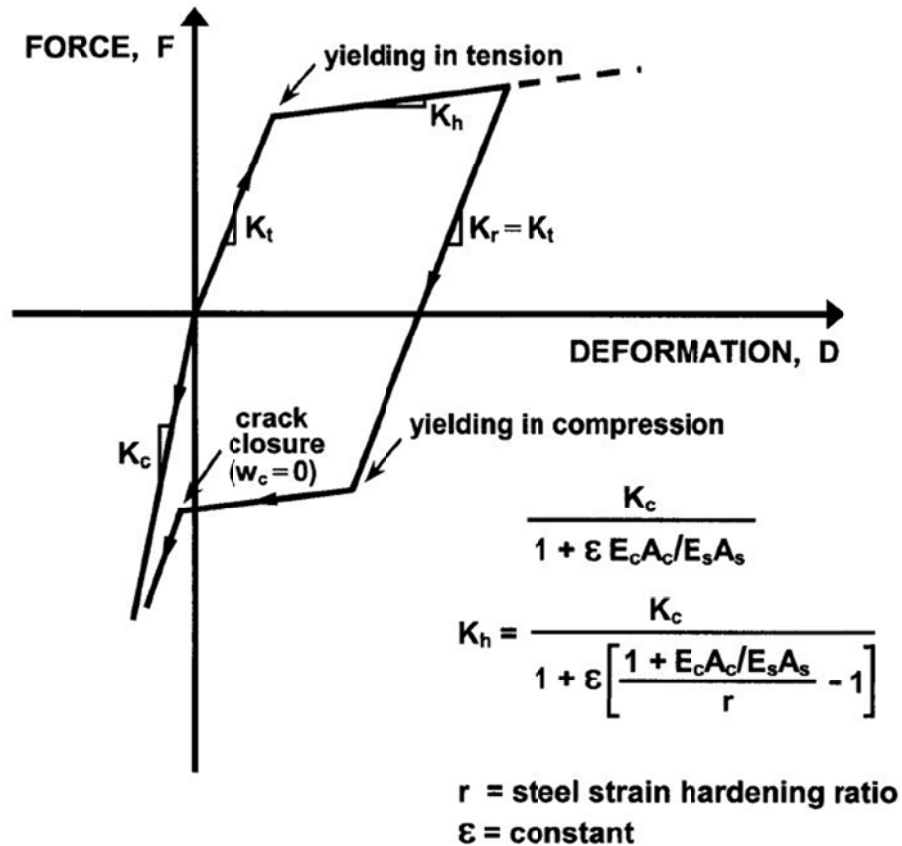
Figure 2.18 - Force-deformation relationship for AESM (Vulcano and Bertero 1986)

The modified TVLEM simulated the global response of the experimental results very well for the cases with no major shear deformation observed. The authors concluded that the AESM is a robust way to simulate the flexural behavior, and the OOHM was not able to simulate the inelastic shear deformations. Similar to the TVLEM, modified version lack the displacement compatibility between the rotational spring and the boundary springs. Moreover, the modeling parameters are very subjective and may not be practical for practical applications.

Vulcano, Bertero, and Colotti (1988) proposed a further modified version of TVLEM, called Multiple-Vertical-Line Element Model (MVLEM). This modified model had a capability to simulate the progressive yielding of reinforcement and used more complex constitutive material models. Similar to the TVLEM, MVLEM used the multi-uniaxial-element-in-parallel model with two infinitely rigid beams. MVLEM employs two outer truss elements represented the boundary elements (K_1 and K_2). Differently from TVLEM, in MVLEM there are two or more interior truss elements (K_3 and K_n) represented the axial and flexural behavior of the rest of the wall, as shown in Figure 2.19. The nonlinear shear response of the wall is represented through a horizontal spring (K_h) with OOHM hysteresis rules. The rotational spring at the bottom of the element of TVLEM is moved up by ch, where h was the height of the element and c was a variable based on the expected curvature distribution of the wall with values of 0 to 1 (for single curvature).
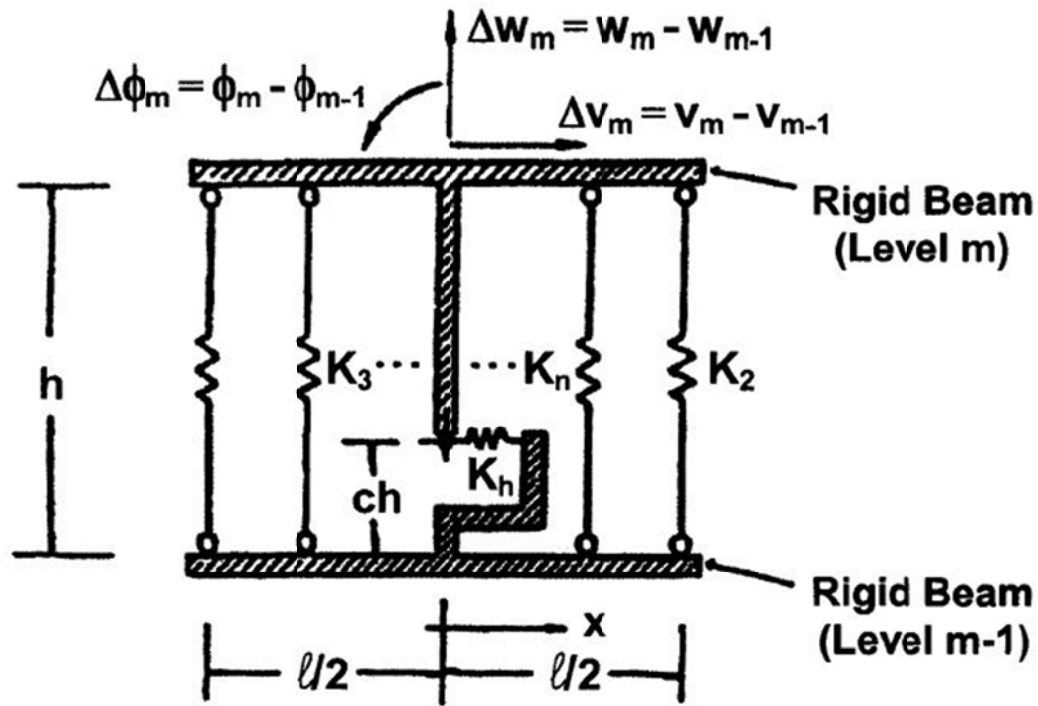
Figure 2.19 - Multiple-Vertical-Line-Element-Model (MVLEM) (Vulcano et al, 1988)

Vulcano, Bertero, and Colotti (1988) also proposed a modified version of AESM to be assigned to the vertical truss elements (Figure 2.20). Similar to the original AESM, this model consisted of two elements in series. The modification is the change in the Element 1 with two parallel springs to represent the uncracked concrete (C) and the steel reinforcement (S). The Element 2 was not in this model. The parameter λ was defined for the length of cracked section to establish the tension stiffening. Authors used the constitutive model developed by Menegotto and Pinto (1973) for the reinforcing steel (Figure 2.21). For the axial springs representing the uncracked concrete the constitutive model proposed by Colotti and Vulcano (1987). Similarly for the axial springs representing the cracked concrete the stress-strain relationship, that accounts the contact stresses in cracks, model proposed by Bolong et al. (1980). Comparison of the experimental results with the MVLEM with $n=4$, showed very good agreement in prediction of the overall behavior, such as the relationship between base shear and roof drift ratio. Moreover, varying the value of the parameter c, authors were able to obtain greater precision. Even though MVLEM was a reliable model for simulation of reinforced concrete shear walls, it still did not address the interaction of shear and flexural responses.

Fischinger et al. (1990) proposed a modified-MVLEM, the vertical and horizontal spring hysteresis relationships are substituted with simplified force-deformation relationships. Figure 2.23 and Figure 2.24 show the proposed force-deformation relationships for the modified-MVLEM for the vertical springs and horizontal springs, respectively. The response of this model was highly dependent on the force-deformation parameters, which were hard to define and used for building the hysteresis curves. Later, Fajfar and Fischinger (1990) proposed suitable values for parameter c to clarify the modeling process of the modified-MVLEM.

20
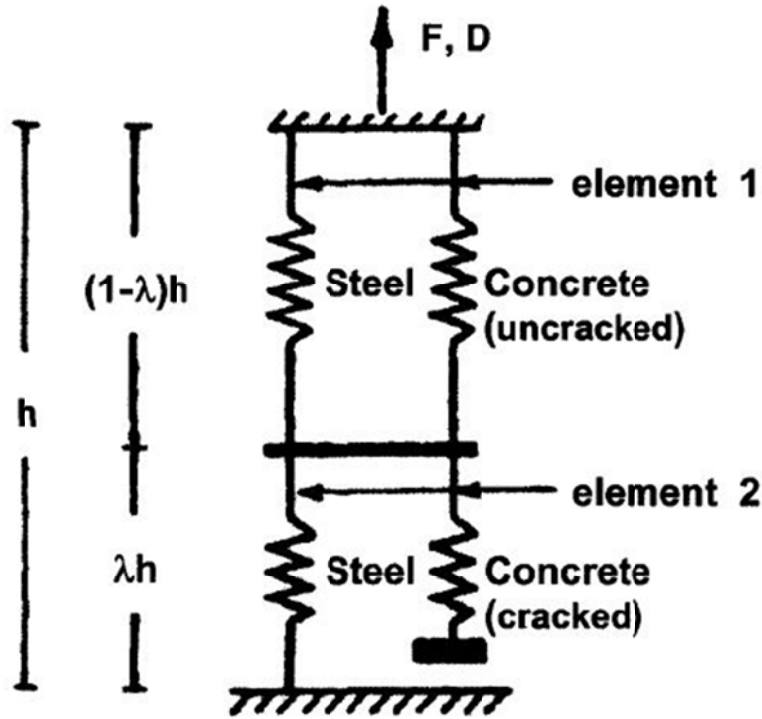
Figure 2.20 - Modified AESM (Axial-Element-in-Series-Model) (Vulcano et. al, 1988)

Figure 2.21 - Menegetto and Pinto (1973) constitutive steel model
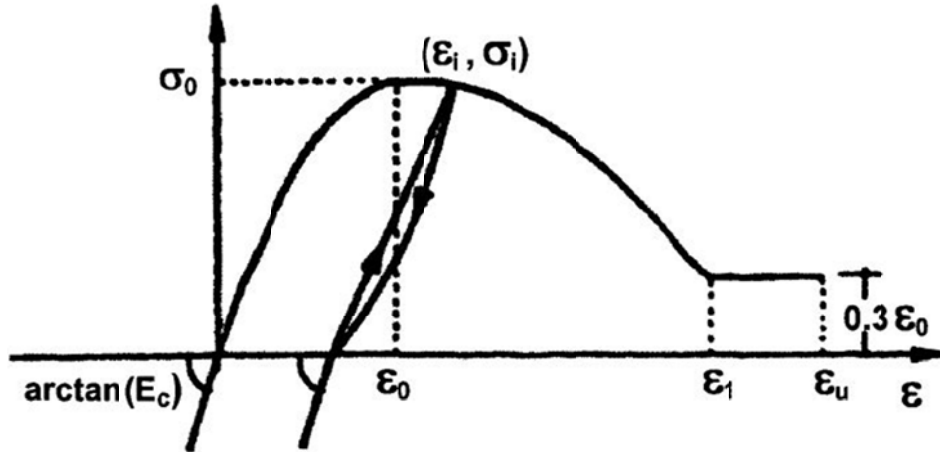
(a) Concrete constitutive model (Colotti and Vulcano, 1987)
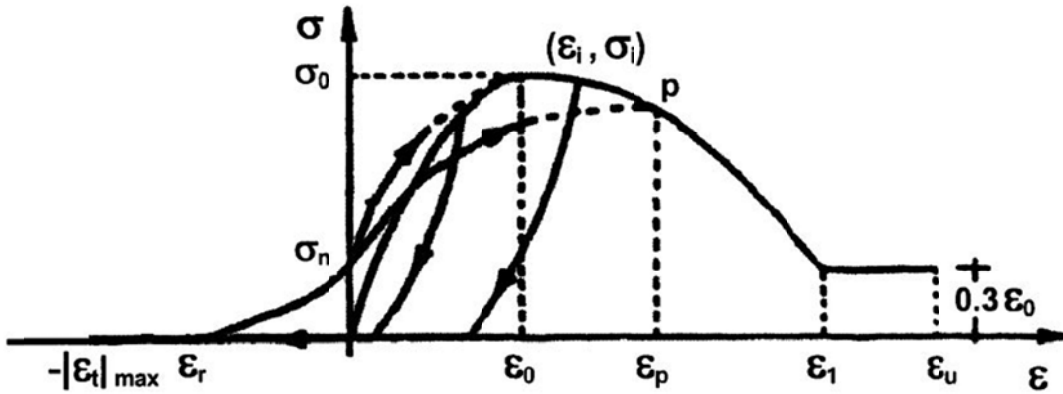
(b) Cracked concrete constitutive codel (Bolong et al., 1980)

Figure 2.22 - Concrete hysteresis relationships used in MVLEM

Another study by Kabeyasawa (1997) proposed a modified Three-Vertical-Line-Element (TVLEM). The authors introduced a two-dimensional nonlinear panel element instead of the vertical, horizontal and rotational springs in the middle of the element, as shown in Figure 2.25. The comparisons with experimental results showed that the modified TVLEM can confidently simulate coupled walls. However, this model was unstable for the walls with extensive nonlinear shear deformations and high axial loads.

Orakcal and Wallace (2006) proposed an improved Multiple-Verical-Line-Element Model (MVLEM) by employing simple one-dimensional constitutive models to define the concrete and reinforcing steel and an elastic shear force-deformation model to simulate the shear behavior of the wall. After conducting calibration studies to investigate the effectiveness of the model in predicting inelastic wall response, Orakcal and Wallace (2006) show that the assumptions of the plane sections remain plane, elastic shear material and ignoring the shear flexure interaction are valid to accurately simulating nonlinear behaviors of reinforced concrete structural walls.

22
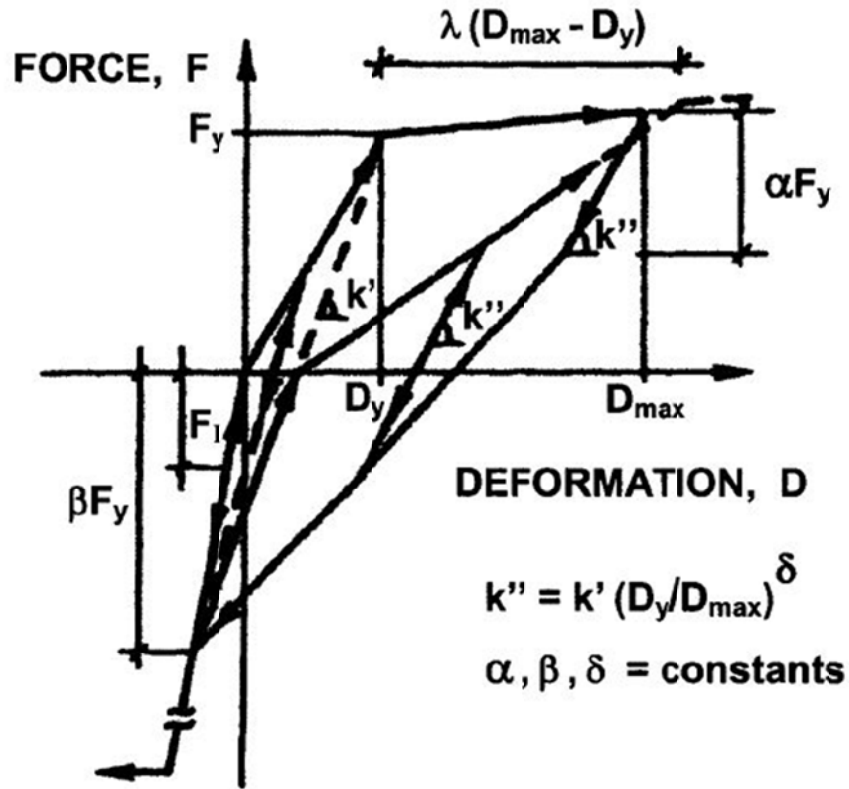
Figure 2.23 - Force-deformation relationship for vertical springs of Fischinger et al., (1990)
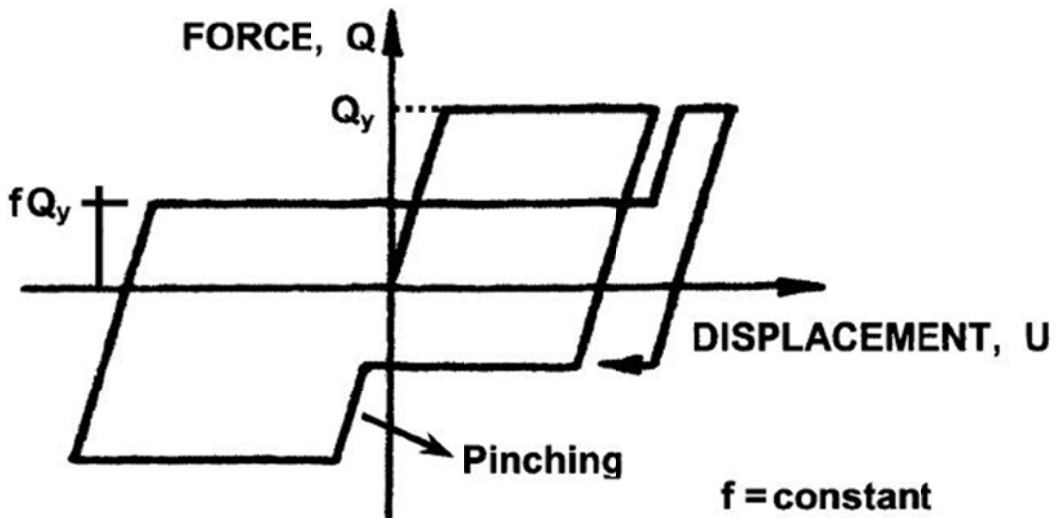
Figure 2.24 - Force-deformation relationship for horizontal springs of Fischinger et al., (1990)
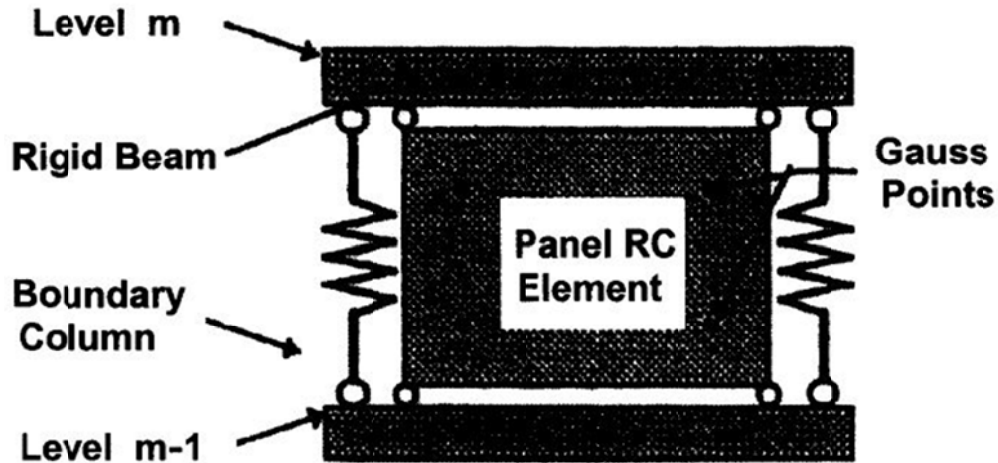
Figure 2.25 - Modified TVLEM (Kabeyasawa et al., 1997)

Some researchers proposed models to incorporate the shear-flexure interaction due to the experimental results showing it cannot be ignored. Petrangeli et al. (1999) and Jiang and Kurama (2010) introduced models using the microplane model to define biaxial concrete constitutive models. Bentz (2000) also uses a similar approach using the Modified Compression Field Theory (Vecchio and Collins, 1986) to model biaxial concrete models. However, these modeling techniques are computationally demanding and might be too complicated for engineering practice.

Panagiotou et al. (2009) proposed a two-dimensional truss model to simulate a T-shaped wall (nonplanar). This model idealizes the entire flange lumping the concrete and steel components into a single nonlinear vertical truss element. Figure 2.26 shows the elevation view of the 2-D nonlinear strut and tie model. Authors chose to use relatively simple hysteresis curves for constitutive material models, as shown in Figure 2.27. The biggest advantage of this model was that it was able to account for the shear-flexure interaction observed in the experimental studies. Simulating three-dimensional walls wih this model requires constraints on the out-of-plane degrees of freedom and it is not able to capture the out-of-plane flexural rigidity and wrapping effect of the wall segments. The comparison of this model with dynamic experiments showed that the response is very to the selection of material properties.

Barbosa (2011) proposed a three-dimensional model for simulation of reinforced concrete walls. This model accommodated beam column elements with fiber cross-sections representing the boundary regions of walls and nonlinear truss elements for concrete and steel in vertical and horizontal direction. Out-of-plane flexural stiffness is modeled using linear elastic beams. However, this model did not account for the shear-flexure interaction and biaxial behavior of concrete in diagonal direction.

Later, Lu and Panagiotou (2014) proposed a three-dimensional beam-truss model for nonplanar reinforced concrete walls. Authors used nonlinear beam-column elements with fiber cross-sections to represent the steel and concrete in the vertical direction and nonlinear truss elements to represent the steel in the horizontal direction and concrete in both horizontal and diagonal directions. Linear elastic beam elements located parallel with the horizontal truss

24

elements are used to simulate the out-of-plane flexural rigidity of the walls. Figure 2.28 shows a representation of the 3D beam-truss model of Lu and Panagiotou (2014). This model simulates the shear-flexure interaction by accounting for the stress and strains in the horizontal and vertical axes and using biaxial concrete behavior in diagonal direction for shear. In the study, the model is used to model T-shaped, C-shaped and I-shaped reinforced concrete shear wall experiments. Simulated overall force-deformation and local strain responses showed very good agreement with the experiment.
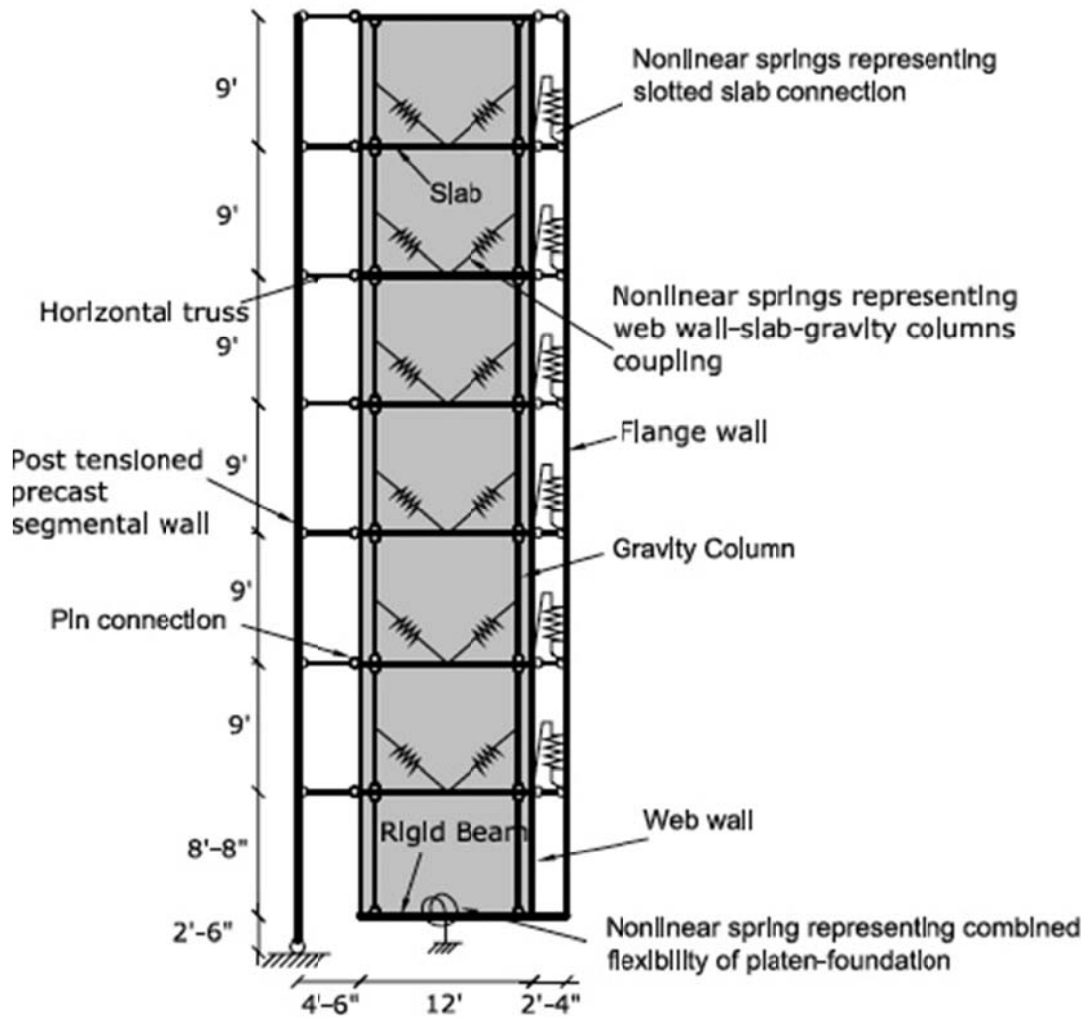
Figure 2.26 - 2-D nonlinear strut and tie model (Panagiotou et al., 2009)

Some researchers developed and employed three dimensional nonlinear cyclic finite element models that use plasticity models and smeared crack models (Sittipunt and Wood 1993; I; El-Tawil et al. 2002; Palermo and Vecchio 2007; Hassan and El-Tawil 2003; Balkaya and Kalkan 2004; Kotronis et. al. 2009). The complexity, modeling and computational effort needed for nonlinear three-dimensional finite elements made them stay in research purposes only unless for very special projects.

a) Reinforcing steel

b) Concrete

c) Spring representing
wall-slab-columns coupling

d) Spring representing
slotted slab

e) Bilinear center
origin rule

f) Bilinear Inelastic rule for combined
foundation-table platen flexibility
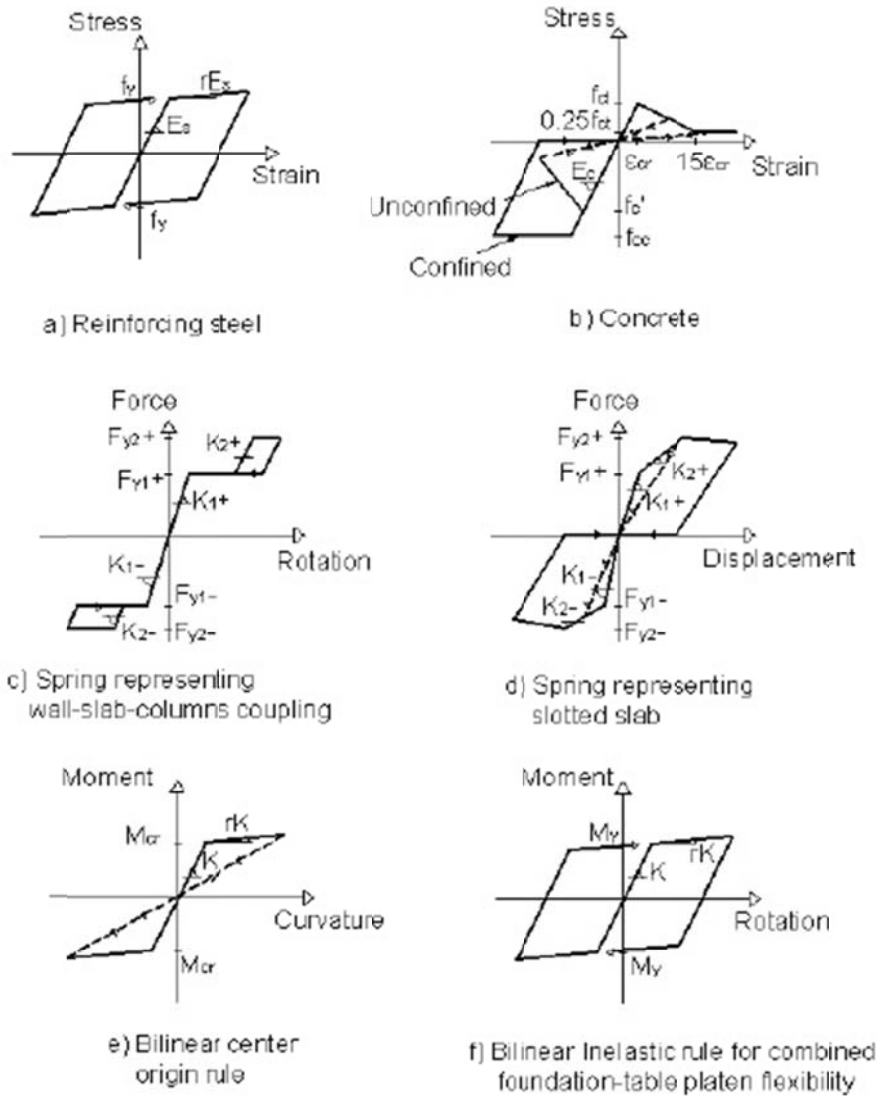
Figure 2.27 - Hysteresis rules (Panagiotou et al., 2009)
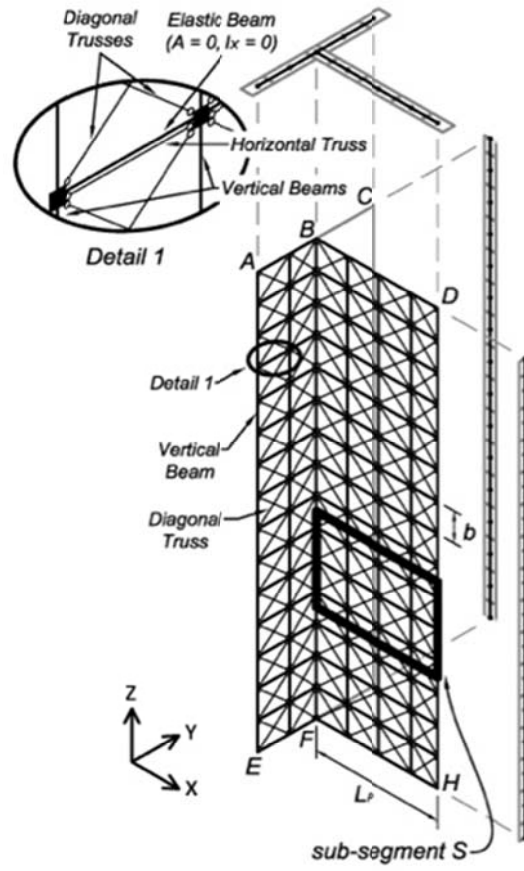
Figure 2.28 - 3-D cyclic beam-truss model (Lu and Panagiotou, 2014)

2.3   Research on Post-Tensioned Precast Concrete Shear Walls

The first examples of rocking in structural design can be traced back to South Rangitikei Rail Bridge in New Zealand, and a chimney at Christchurch International Airport (Skinner et al. 1993). Priestley and Tao (1993) was the first to propose the idea of rocking beam-column connections for special moment frames, using unbonded prestressing tendons designed to provide the restoring force. This innovative concept was tested by Stanton et al. (1997).

Priestley et al. (1999) designed, built and tested a five-story precast building under simulated seismic loading at the University of California at San Diego in The PREcast Seismic Structural Systems (PRESSS) research program (Figure 2.29). The five-story precast concrete test building was 60% scale, which was 90 feet tall. The test building had four different structural frame systems in one principal direction, and a jointed precast wall system was the lateral load resisting system in the orthogonal direction. The walls were built with 19ft wall (2.5 stories) four panels. These two walls were connected through four unbonded post-tensioning tendons vertically and by 20 U-shaped flexural plates (UFP connectors) located between two walls.

The test results were satisfactory, with minimal damage in the wall direction. At the design level earthquake loading, the wall had a roof drift ratio of 1.8% (8 in). At the MCE level loading, the roof drift ratio reached to 2.5% (11 in). Some minor flexural cracking as well as minor crushing of cover concrete was observed at the base of the wall. The residual drift after the MCE level loading was very limited and measured as 0.06%. In a following study researchers at Iowa State University validated the proposed design guidelines for precast hybrid frames and joint wall systems (Celik and Sritharan, 2004; Thomas and Sritharan, 2004). The subsequent research efforts led to the codification of design guidelines and publication of the ACI ITG 5.1: *Acceptance Criteria for Special Unbonded Post-Tensioned Precast Structural Walls Based on Validation Testing* and ACI ITG 5.2: *Special Unbonded Post-Tensioned Precast Structural Walls*.

Mander and Cheng (1997) proposed the damage avoidance design (DAD), which was a new seismic design and construction methodology. DAD used damage-free rocking connections. DAD proposed to terminate the column longitudinal reinforcement at the foundation beam-column interface. This allows the column to freely rock, and prevents the damage in the reinforcing steel and concrete. The specially reinforced rocking toe regions ensure that the structure behaves in a bilinear elastic manner without any damage. An energy based method to assess the equivalent viscous damping in rocking structures and a complete force-deformation model for rocking columns was developed by Mander and Cheng (1997). The force-deformation behavior is validated with results of a quasi-static test of a nearly full-size precast concrete rocking column bridge structure.
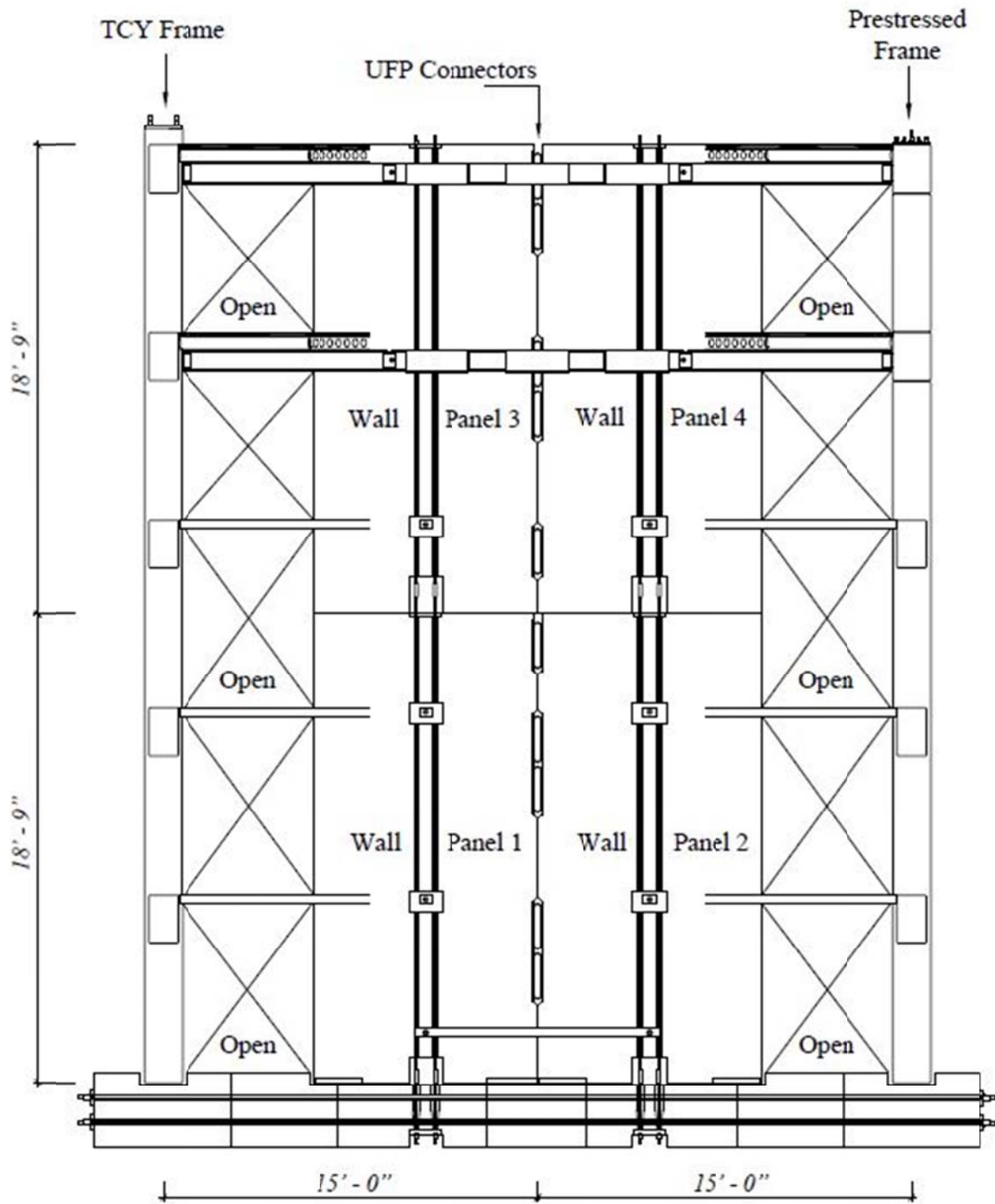
Figure 2.29 - Elevation view of the specimen at PRESSS (Priestley et al. (1999))

Kurama et al. (1999) described the behavior of the unbonded post-tensioned precast concrete walls under lateral load and proposes a seismic design approach for them. The study proposes four states of the lateral force displacement response of precast walls (Figure 2.30 and Figure 2.31). The first state defined is the "Decompression State", where the gap opening is

initiated between the base of the wall and the foundation. The next point is the "Softening State", which represents the beginning of the lateral stiffness degradation of the wall. This softening is caused by the gap opening of the wall base and the nonlinear behavior of the concrete in compression. The third state is called the "Yielding State", where the unbonded post-tensioning tendon reaches the limit of proportionality. The final stage of the response is called "Failure State", which marks the point where the wall fails in flexure due to the crushing of concrete. In a following study, Kurama et al. (2002) evaluated the seismic behavior of a set of unbonded post-tensioned precast concrete walls under design and MCE level excitations using nonlinear models. Significant seismic response characteristics of the walls are discussed with the evaluation of the design methodology.
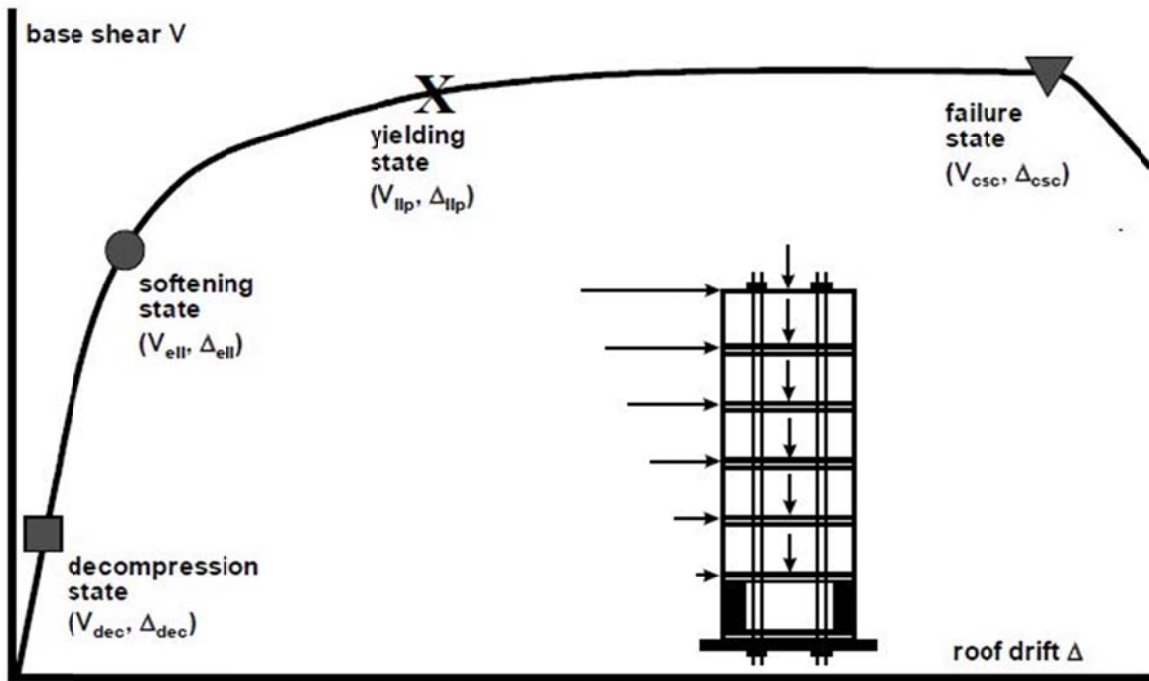
Figure 2.30 - Unbonded post-tensioned precast concrete shear wall base shear-roof drift ratio relationship (Kurama et al. 1999)
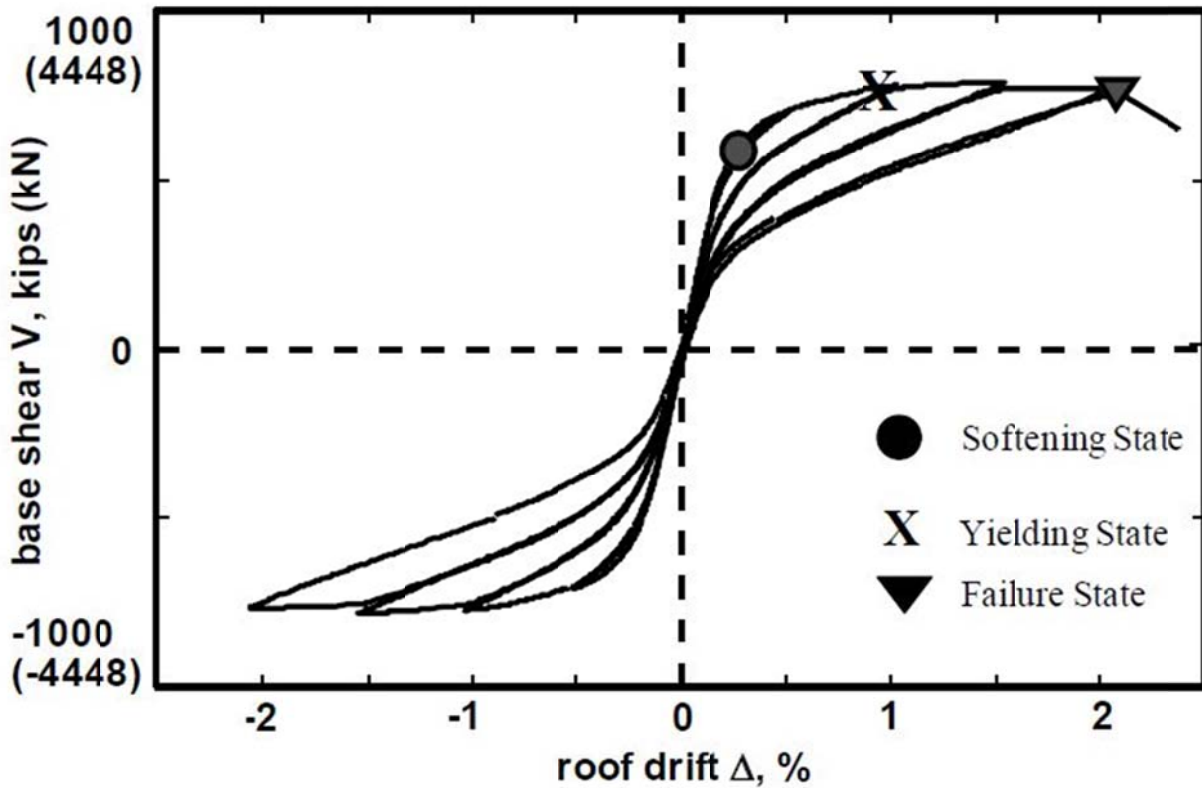
Figure 2.31 - Base shear-roof drift ratio response of unbonded post-tensioned precast concrete shear walls (Kurama et al. 1999)

Holden et al. (2003) tested two geometrically identical half-scale precast concrete cantilever wall units under quasi-static reversed cyclic lateral loading (Figure 2.32). One unit was a code-compliant conventional cast-in-place reinforced concrete shear wall. The other unit was a precast concrete shear wall utilizing post-tensioned unbonded carbon fiber tendons and steel fiber reinforced concrete. The latter unit used hysteretic energy dissipation devices in the form of low yield strength longitudinal reinforcement as a fuse connection between the wall panel and the foundation beam. The conventional reinforced concrete wall performed very well in terms of ductility capacity and energy dissipation. The specimen reached 2.5% drift ratio before significant degradation occurred. The precast post-tensioned unit achieved a drift ratio of 3% with no visible damage to the wall panel. The paper presented the results and performance comparisons between these two systems.

Restrepo and Rahman (2007) tested three half-scale precast concrete wall units, representing a 4-story building, using a quasi-static reversed cyclic loading (Figure 2.33). All three walls had similar reinforcement details, prestressing strand arrangement, and loading patterns. Gravity loads were not accounted for in the first specimen, Unit 1. Units 2 and 3 were designed with a standard reinforcing bar with a reduced diameter over a specific length for energy-dissipation, called "dog-bones". Gravity load effects were simulated in Unit 3 by means of external post-tensioning. All of the walls were designed with conventional rectangular transverse reinforcement and longitudinal bars to perform satisfactorily up to 2.5% drift. All

31

specimens performed as expected, having only cosmetic damages at the toes of the walls. All three tests were pushed up to 2.5% drifts. At these drift levels, in which the prestressing strands stayed in the elastic region, there were no residual drifts. The energy dissipation bars worked effectively, resulting in equivalent viscous damping ratios up to 14%.
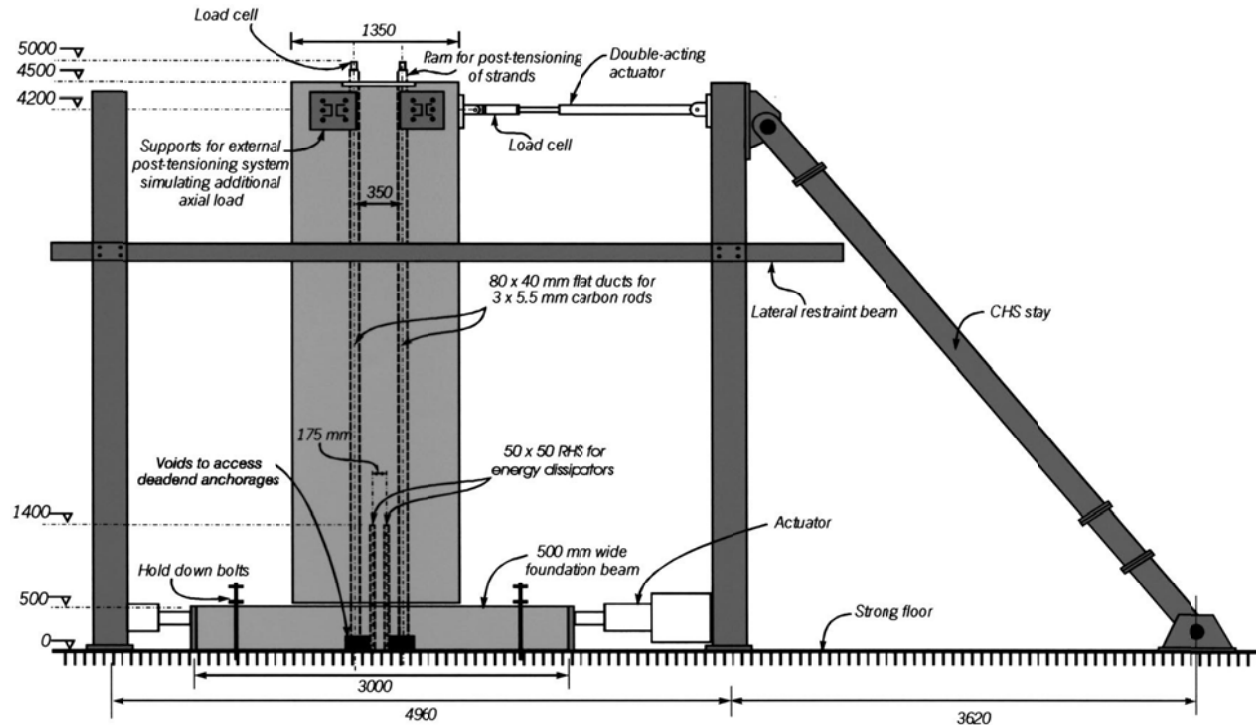
Figure 2.32 - Test setup of Holden et al. (2003)

Perez et al. (2007) introduced a design-oriented analytical model using simple formulas to calculate the nonlinear lateral load behavior of unbonded post-tensioned (UPT) precast concrete walls, and benchmarks this model with the available experimental results. Study also compared the results with the UPT wall model based on fiber elements by Kurama et al. (1999). Each model is formulated to simulate several critical limit states in the lateral load behavior of UPT walls. For the three test specimens considered, the analytical and experimental results showed generally good agreement under monotonic and cyclical loading. Figure 2.34 and Figure 2.35 show the comparisons for one of the specimens. The proposed model proved to be sufficiently accurate for seismic design of UPT walls, and the fiber model by Kurama et al. (1999) was found to be accurate for estimating the UPT wall response under earthquake loading.

This system has been implemented in a 39-story building in California (Priestley 1996) and in bridges (Priestley et al. 1999). The self-centering framing system tested by the PRESSS program involved relatively complex beam-column connection details. Subsequent research has been conducted to develop alternative systems/details (Englekirk 2002) and to extend the concept to steel structures (Pampanin et al. 2006]) and timber structures (Pampanin 2005). The concept of rocking systems on different material types has also been studied; such as steel systems (Constantin et al. 2001; Ricles et al. 2001) and masonry infilled reinforced concrete frames (Toranzo et al. 2001)
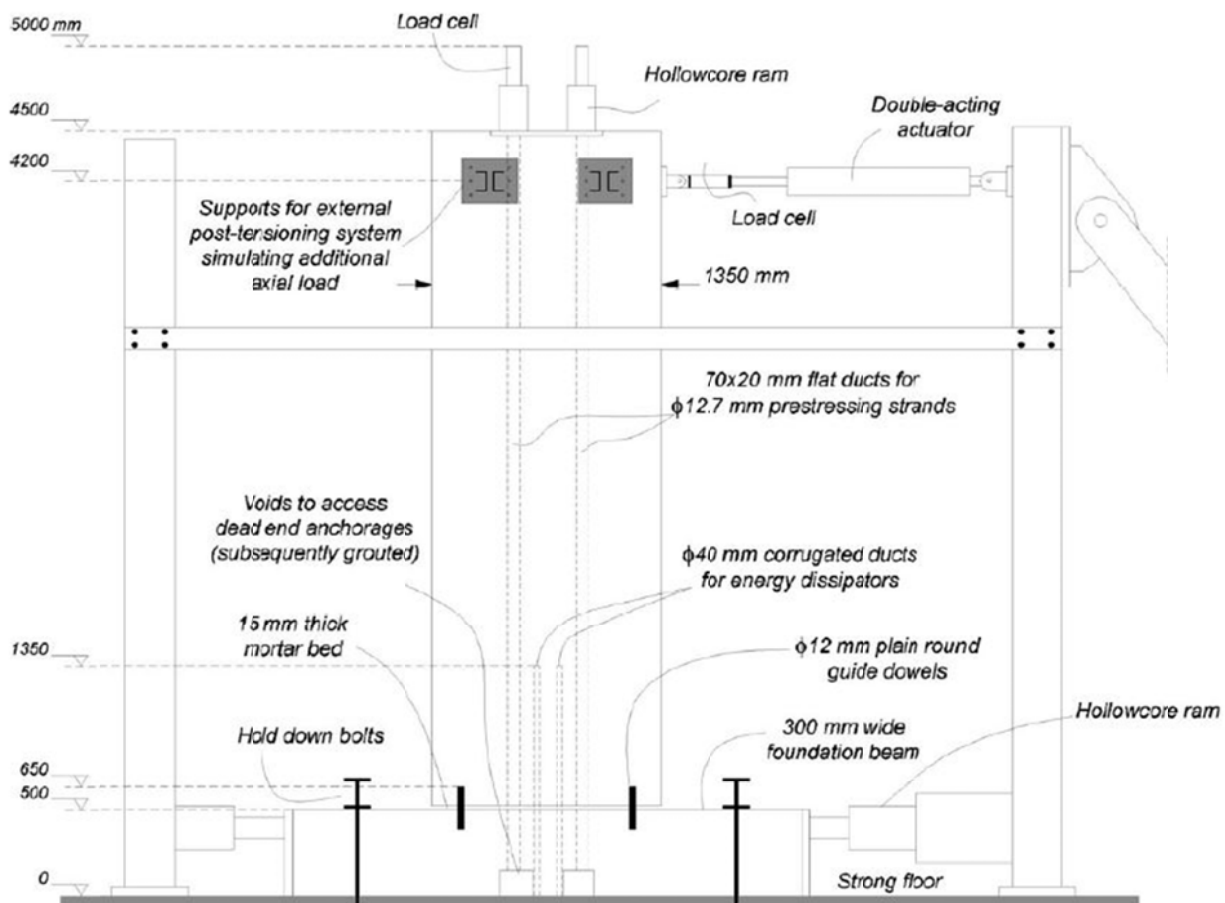
Figure 2.33 - Test setup of Restrepo and Rahman (2007)

Perez et al. (2013) tested five large-scale, isolated, multi story, unbounded post-tensioned (UPT), precast concrete walls under combined gravity and lateral loading (Figure 2.36). The results showed that the response of UPT precast concrete walls can be controlled by adjusting parameters such as the total area of post-tensioning steel and the level of prestressing. Authors studied the effect of four design parameters on the lateral load response of UPT precast concrete walls. Table 2.1 lists these parameters: 1) total PT steel area, A_p; 2) initial stress of the PT steel, f_{pi}; 3) initial concrete stress due to the post-tensioning, $f_{ci,p}$; and 4) confining reinforcement details at the boundary elements. Specimens were tested under cyclic lateral drift cycles up to 3% drift ratio.

The experimental parametric study concluded that certain design variables control the lateral load response of UPT precast concrete walls. Test results show that a reduction in the initial concrete stress ($f_{ci,p}$), by reduced initial PT prestressing (f_{pi}) (TW4 versus TW3), decreases the gap opening drift and the base shear at the spalling of cover concrete, increases the drift capacity of the wall and has no effect on the ultimate base shear capacity of the wall. Test results showed that a reduction in the $f_{ci,p}$ by reducing A_p while keeping f_{pi} constant (TW5 versus TW3) decreases the gap opening drift, the base shear at the spalling of cover concrete, and the ultimate base shear capacity of the wall, increases the ultimate drift capacity and has no effect on the

33

lateral drift at the yielding of PT steel.
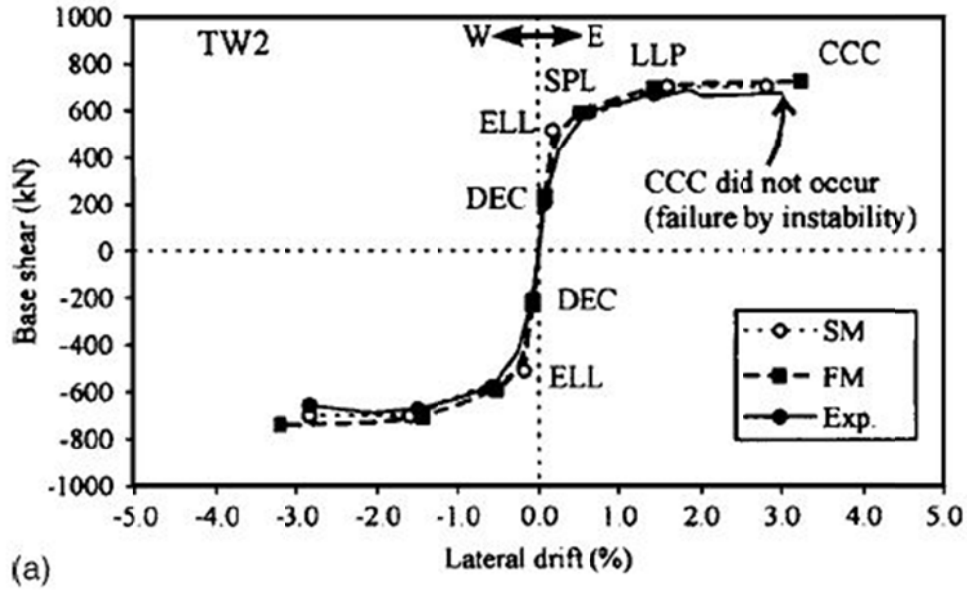
Figure 2.34 - Comparison of the cyclic loading response envelope and the analytical results under monotonic loading (Perez et al. 2007)
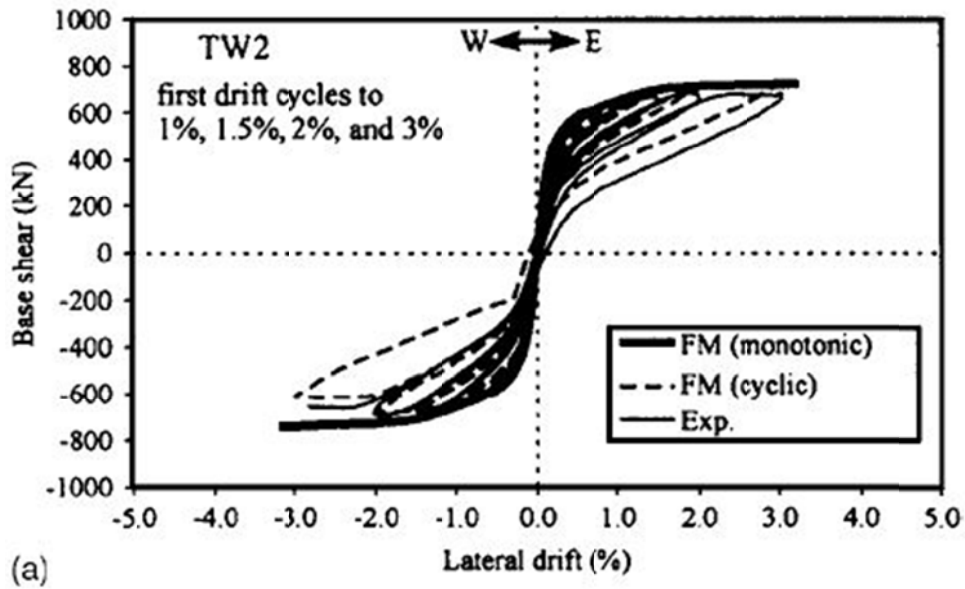
Figure 2.35 - Comparison of experimental and analytical results under cyclic loading (Perez et al. 2007)
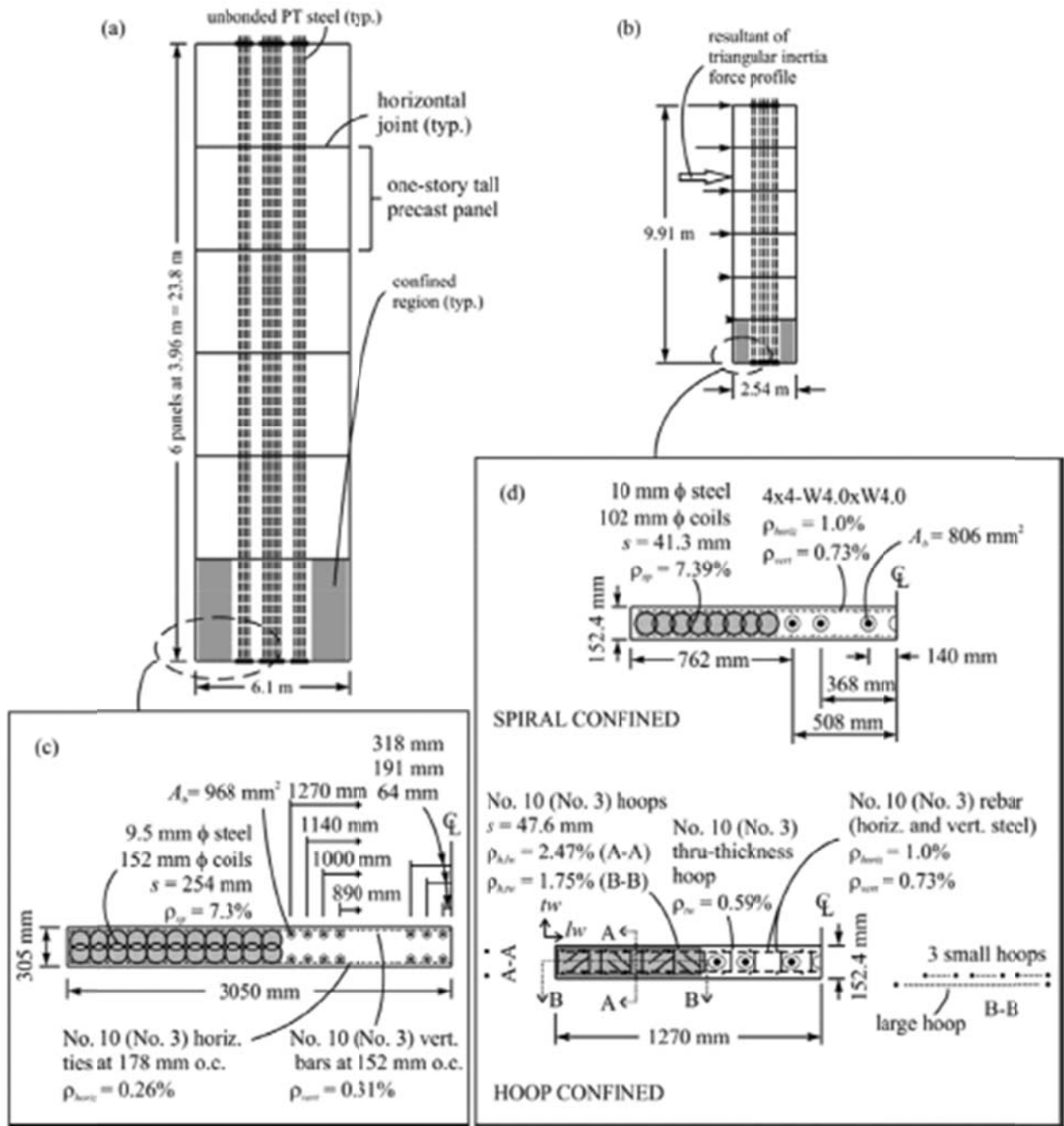
Figure 2.36 - Test specimens of Perez et al. (2013)

Primary research on self-centering systems in Japan began in 2000, with tests on hybrid column-beam joints with unbonded prestressing tendons and mild steel inside members (Sugata and Nakatsuka (2004)). This system was similar to the hybrid column-beam joint system previously tested in the United States. Sugata and Nakatsuka (2005) also proposed a numerical model to simulate flag shape hysteresis behavior exhibited by these connections. Niwa et al. (2005) studied unbonded PT precast beam-column joints with external damping devices under the beam. Ichioka et al. (2009) tested PT precast concrete portal frames with a corrugated steel

shear panel placed between the beam and the foundation beam. Maruta and Hamada (2010) conducted shaking table testing on reduced-scale (25%), three-story PT frames with bonded and unbonded beams. Test results demonstrated that PT precast concrete frames were very ductile, yet only minor damage was observed for ground motion velocities less than 50 Kine. However, due to the self-centering capability, the system displayed low energy dissipation capacity (no damping devices were used). Self-centering systems have been developed and tested for structural steel systems (Ikenaga et al. 2007; Ichioka et al. 2009); these systems have not yet been used in practice because design procedures have not been established to satisfy the Japanese Building Standard. In addition, the initial cost for the self-centering system is higher than conventional RC systems, and the potential long-term benefits of the system have not been sufficiently studied to assess if the higher initial cost is justified.

Table 2.1 - Test specimens and design parameters (Perez et al. 2013)

Test wall	Loading	A_p, cm^2	f_{pi}/f_{pu}	$f_{ci,p}$, MPa	Confinement type	PT bar arrangement*
TW1	Monotonic	48.4	0.553	8.20	Spirals	xx xox xx
TW2	Cyclic	48.4	0.553	8.20	Spirals	xx xox xx
TW3	Cyclic	48.4	0.553	8.20	Hoops	xx xox xx
TW4	Cyclic	48.4	0.277	4.07	Hoops	xx xox xx
TW5	Cyclic	24.2	0.553	4.07	Hoops	xo oxo ox

Chapter 3.   Collapse of a Concrete Wall Building in

the 2010 Chile Earthquake

3.1   Introduction

On 27 February 2010, at 03:34 local time (06:34 UTC), a M_w 8.8 earthquake occurred off the coast of central south Chile. The earthquake affected an area with population exceeding twelve million people, including five of the largest cities of Chile. The number of confirmed deaths stood at 525, with 25 people missing (Ministry of Interior, 2011).   The earthquake caused damage to buildings, highways, railroads, ports, and airports, including 81,000 destroyed residential structures (EERI, 2010). At least 50 multi-story reinforced concrete buildings were severely damaged and four collapsed partially or totally. Among these, the 15-story Alto Rio building in Concepción sustained failures near the base, overturned, and came to rest on its side, with eight fatalities (Figure 3.1). Details of the collapse, and analyses to understand it, are the subject of this chapter.

Figure 3.1 - Alto Rio building after the earthquake (from
http://skyscraperpage.com/cities/?buildingID=85186)

3.2   Research Significance

The failure of the Alto Rio building is significant for many reasons. It is the first shear wall building of its type to collapse by overturning during an earthquake. The failures suggest areas for which design and detailing practices could be improved. The analyses demonstrate a practical approach to assessing the collapse of a complex building subjected to earthquake shaking. The capabilities and shortcomings of the analyses to identify details of the failure mechanism are themselves important outcomes of the study.

3.3   Ground Motion Records in Concepción

The 2010 Chile earthquake had a moment magnitude of 8.8, which was the sixth largest earthquake ever to be recorded by a seismograph. According to the Seismological Service of the University of Chile, Concepción experienced strong ground shaking at Modified Mercalli Index IX (violent). Concepción was located 105 km (65.2 miles) from the estimated epicenter (35.909°S, 72.733°W; USGS 2010). Ground motions were recorded at Colegio Inmaculada Concepción (36.8281°S, 73.0483°W) (RENADIC 2010) in Concepción approximately 1.2 km (0.75 miles) from the Alto Rio site. Ramirez and Vivallos (2009) presents a study dividing Concepción into six different zones based on dominant periods and type of soil. This study shows that the Alto Rio building and Colegio Inmaculada Concepción sites are located in the same zone formed by alluvial deposits of the Bio-Bio River. The proximity of the sites and the similar site characteristics suggest that the motions at the two sites may be reasonably similar, although deviations due to different wave paths are to be expected. The records (Figure 3.2) show that shaking lasted more than 120 seconds, with peak ground accelerations of 0.402g and 0.397g in east-west (EW) and north-south (NS) directions, respectively. The east-west direction of the record corresponds to the transverse (short) axis of the building.
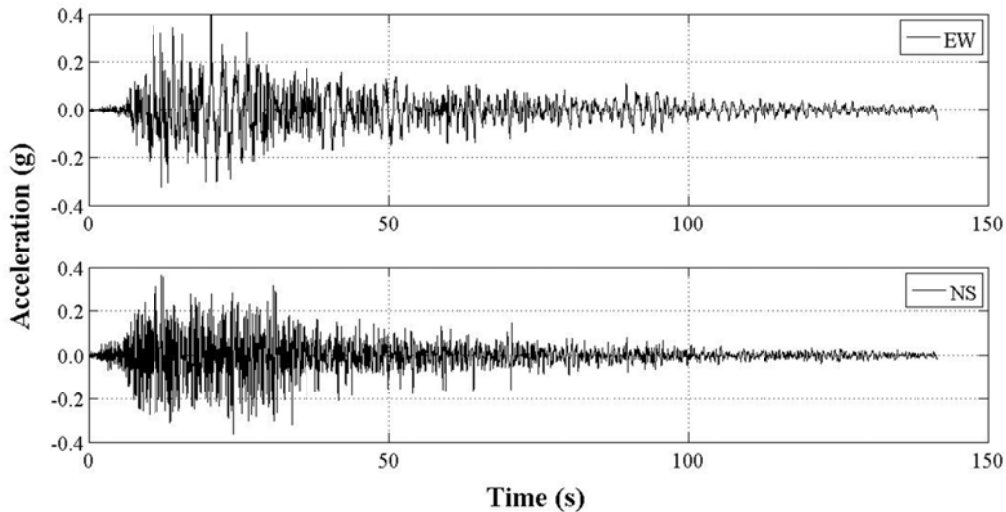
Figure 3.2 - Ground motion from Colegio Inmaculada Concepción

Figure 3.3 compares 5-percent-damped elastic response spectra computed using the records and design-level response spectra based on the Chilean code NCh433.Of96 for seismic zone 3 and building category C. Design response spectra are shown for two soil types. Soil Type II corresponds to stiff soil whereas Soil Type III corresponds to medium stiff soil. Soil Type II represents a dense gravel or clay with shear wave velocity larger than 400 m/s in the upper 10 m (32.2 ft), and Soil Type III is unsaturated gravel or clay with shear wave velocity less than 400 m/s (NCh433.Of96, 1996). Spectral accelerations for the earthquake are at or above the Type II soil design spectrum for almost all periods. The EW direction motions are particularly energetic in the approximate period range 1.5s to 2.5s.
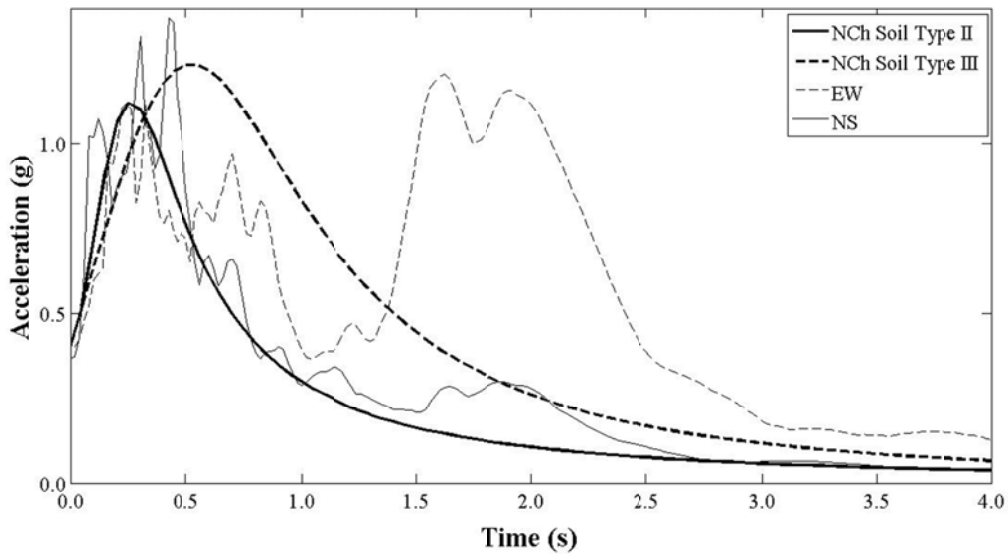
Figure 3.3 - Design-level response spectra and 5%-damped response spectra from the ground motion record in Concepción

3.4   Chilean Design Practice for RC Buildings

A long history of frequent strong earthquakes in Chile has resulted in the nearly universal use of bearing walls for mid-rise concrete residential construction. In a typical layout (Figure 3.4), corridor walls are flanked by transverse walls forming room partitions. A typical ratio of wall area to floor plan area is around three percent in each direction (Wallace and Moehle, 1992). This ratio has remained relatively constant over the years, but building heights have increased with time, leading on average to higher axial stresses at the building base. Wall thicknesses have also decreased over time; at the time of the earthquake, it was not unusual to find 15 to 20 cm (5.9 to 7.9 in) thick walls supporting 15 to 20-story tall buildings.

The Chilean Building Code NCh433.Of96 requires the use of ACI 318-95 for design of reinforced concrete structural elements intended to resist design seismic forces. However, based on satisfactory behavior of walls in past earthquakes, wall designs were not required to satisfy the ACI 318 requirements for confined boundary elements. The Chilean Reinforced Concrete

Code was modified in 2008 to require use of confined boundary elements. Several Chilean engineers have indicated, however, that this requirement was not always followed in design, and confinement, where specified, was not always implemented in construction.
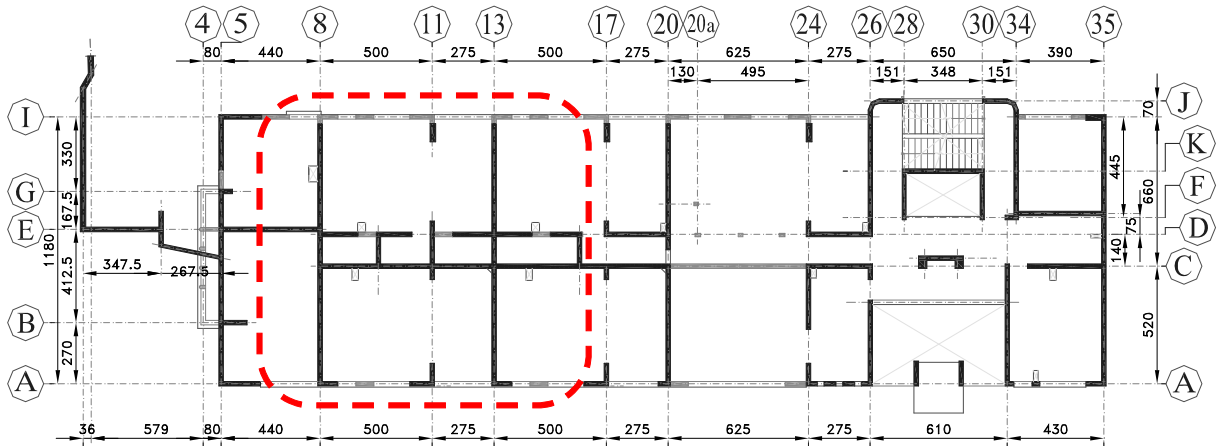
Figure 3.4 - Alto Rio building first-floor plan. Dashed line encloses portion of building modeled in the nonlinear static analysis (Unit: cm) (Note: 1 cm = 0.3937 in)
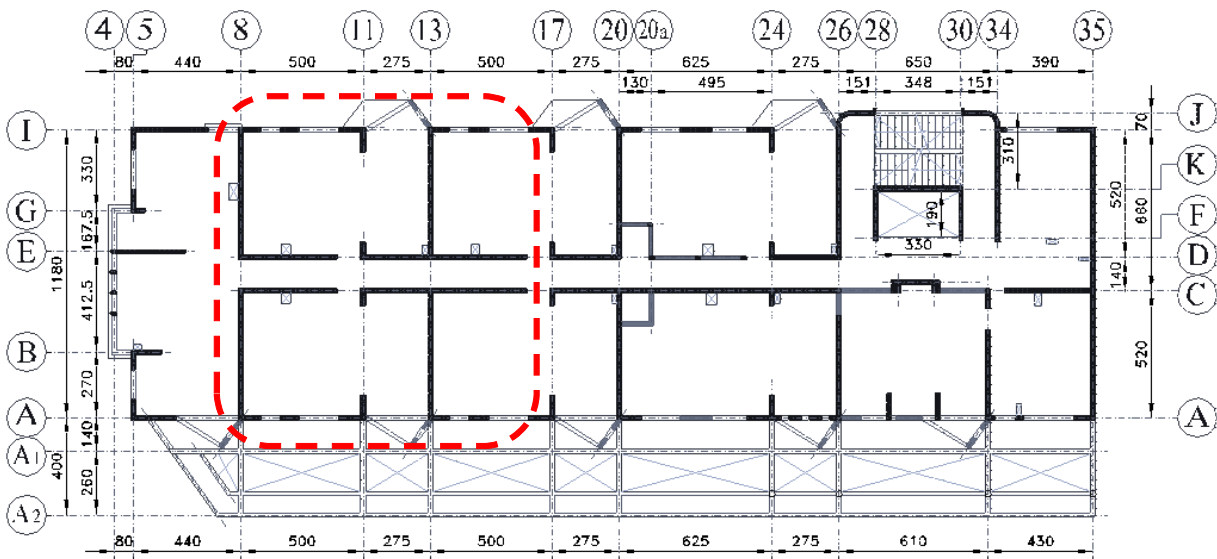
Figure 3.5 - Alto Rio building second-floor plan. Dashed line encloses portion of building modeled in the nonlinear static analysis (Unit: cm) (Note: 1 cm = 0.3937 in)

3.5   Alto Rio Building

The Alto Rio building was a 15-story reinforced concrete building with two additional subterranean levels. It had a nearly rectangular plan (Figure 3.4 and Figure 3.5) with the transverse (short) direction oriented on 60 degrees azimuth, which corresponds to the EW direction of the ground motion in Figure 3.2. The building plan dimensions were 40 m (131 ft) in the longitudinal direction and 12 m (39 ft) in the transverse direction. The building had stepped elevation at the roof, such that it was 12 stories tall at the north end and 15 stories tall at the south end, with maximum height of 38 m (125 ft). First-story height was 3.06 m (10 ft) and all other stories including subterranean levels were 2.52 m (8.3 ft) tall.

At the time of design in 2006, the applicable building code was NCh433.Of96, which referred to ACI 318-95. The building was designed using analysis and design procedures similar to those used in the US, including linear elastic response spectrum analysis using the computer program ETABS (CSI). Building construction was completed in 2009.

The seismic-force-resisting system comprised a pair of longitudinal corridor walls flanked by transverse walls, and interconnected by 150-mm (5-in.) thick floor slabs. Along axes 8, 13, and 20, the first-story transverse walls were continuous along the entire building width. Above the first story, a stack of 1.2 m (4 ft) wide corridor openings divided these into two separate walls coupled by floor slabs (Figure 3.6 and Figure 3.8). The easternmost edge of these walls, as well as the shorter walls along axes 11, 17, and 24, had another discontinuity at the second level where the first story was set back 40 cm (1.31 ft) from the upper stories on the east side of the building (Figure 3.7). Above the setback, the walls had a return at the exterior face of the building, exacerbating the vertical discontinuity in the framing system.

Figure 3.6 - Alto Rio building axis 8 elevation view (Unit: cm) (Note: 1 cm = 0.3937 in)

Figure 3.7 - Alto Rio building axis 11 elevation view (Unit: cm) (Note: 1 cm = 0.3937 in)

42
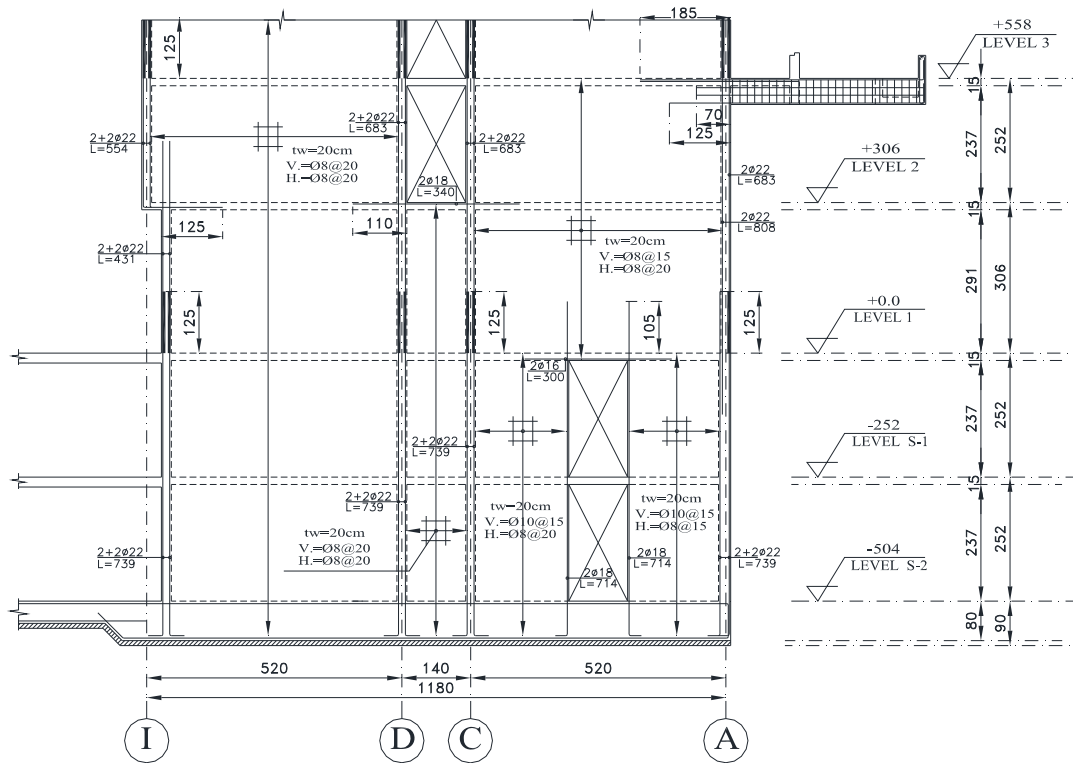
Figure 3.8 - Alto Rio building axis 13 elevation view (Unit: cm) (Note: 1 cm = 0.3937 in)

Walls were 20-cm (7.9 in) thick, except some underground walls were 25-cm (9.8 in) thick. Wall distributed reinforcement comprised either $\phi8$[1] or $\phi10$ with 15 or 20-cm (5.9 or 7.9 in) spacing. Larger diameter longitudinal bars ($\phi16$ to $\phi25$) were positioned at the wall boundaries. The structural drawings show wall transverse reinforcement detailed with 135-degree hooks anchored around wall boundary reinforcement with typical longitudinal (vertical) spacing of 20 cm (7.9 in). A field survey after collapse showed that transverse reinforcement was constructed with 90-degree hooks (IDIEM 2010). Wall longitudinal reinforcement was lap-spliced according to conventional practices, without special confining transverse reinforcement along the lap splices. For $\phi22$ mm and $\phi25$ bars, lap splice lengths of 125 cm (49 in) ($57d_b$) and 140 cm (55 in) ($56d_b$) are provided in design. The length required by ACI 318-11 equation 12-1 for a Class B lap splice (all the bars spliced at the same level) developing specified yield stress is $43d_b$. According to ACI 318-11 21.9.2.3, regions of special structural walls that are expected to yield are required to have development lengths of longitudinal reinforcement at least 1.25 times the values calculated for f_y in tension, or a lap splice length of $54d_b$. Therefore, lap splice lengths meet requirements of ACI 318. In US practice, however, a special structural wall might be expected to have more and better detailed transverse reinforcement than is typical in Chilean practice. Given the transverse reinforcement detailing in Alto Rio, it is reasonable to suspect the lap splices as a potential initiator of failure.

---

[1] The number following the symbol ϕ refers to nominal diameter in mm.

43

All reinforcement was specified S420 steel [minimum yield strength of 420MPa (60 ksi) and ultimate strength of 630MPa (90 ksi)]. Consistent with the specification, reinforcement samples taken from the collapsed building had mean yield and ultimate stresses of 484 MPa (70 ksi) and 727 MPa (105 ksi), respectively (IDIEM, 2010). From the base to the top of the second story, specified concrete compressive strength was 25 MPa (3600 psi); for the rest of the building specified compressive strength was 20 MPa (2900 psi). Thirty-three concrete cores taken from the structural walls after the earthquake showed mean compressive strength of 43 MPA (6200 psi), with somewhat lower strength in lower stories than upper stories. This result contrasts with the strength specification in that higher strengths were specified for the lower stories than upper stories.

The building was founded on alluvial deposits. Soil investigations reported by IDIEM (2010) indicate the building site had static strength parameters consistent with aspects of both Soil Type II and Type III (Table 3.1, Figure 3.9). Soil Type II corresponds to stiff soil whereas Soil Type III corresponds to medium stiff soil. Soil Type II represents a dense gravel or clay with shear wave velocity larger than 400 m/s in the upper 10 m (32 ft), and Soil Type III is unsaturated gravel or clay with shear wave velocity less than 400 m/s (NCh433.Of96, 1996). In order to be classified as Soil Type II, soil of that characteristic should have a minimum thickness of 20 m (65 ft); Soil Type III requires minimum thickness of 10 m (33 ft). Soil investigations reported by IDIEM (2010) indicate existence of both Soil Type II & III. However, all layers have shear wave velocities below 300 m/s, suggesting the soil should be classified as Type III.

The cross-sectional wall to floor area ratio was approximately 3% in the longitudinal direction and 4% in the transverse direction, resulting a total cross-sectional wall to floor area of 7%. Calculated wall axial load ratios ranged from 0.05 to 0.07 $P/f_c'A_g$, where P considers expected loads ($1.0D + 0.25L$), f_c' is the specified concrete compressive strength, and A_g is the gross cross-sectional area of the wall.

Table 3.1 - Soil properties of Alto Rio

(Note: 1 ft = 0.3048 m, 1 MPa = 145 psi)

Layer	Soil Characteristic	Test Result	Soil Type
1	Sandy Soil Layer	$(N_1)_{60} = 38$ / ft	III
2	Silty Soil Layer	$S_u = 0.12$ MPa	II
3	Sandy Soil Layer	$(N_1)_{60} = 36$ / ft	III
4	Sandy Soil Layer	$(N_1)_{60} > 50$ / ft	II

(a) View in transverse direction   (b) View in longitudinal direction
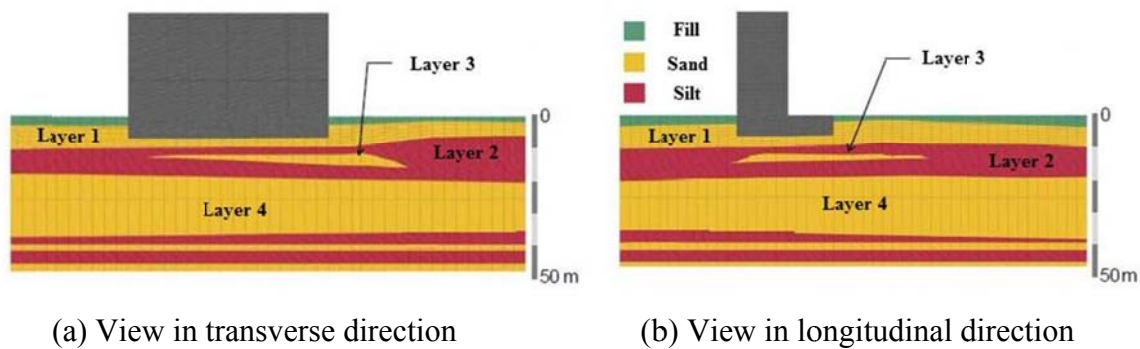
Figure 3.9 - Properties of Alto Rio building site (after IDIEM, 2010) (Note: 1 m = 3.28 ft)

3.6 Collapse

During the earthquake, the Alto Rio building overturned from the base level and came to rest on its east side (Figure 3.1). Examination of the building in its final resting place indicated that the main failure occurred in or near the first story, and that the building rotated approximately about the central corridor as it fell to the east. According to this mechanism, the west side of the building failed in tension whereas the east side failed in compression, with portions of the east side being thrust into the subterranean levels. A small amount of longitudinal movement was apparent where the building fractured at the base, but this appears to have occurred as the building collapsed, not beforehand (IDIEM, 2010). The building was also fractured at the ninth level, probably due to impact with the ground and walls of the adjacent parking structure, snapping the building in two as it hit the ground. Inspection of the foundation and soil did not identify significant damage.

Figure 3.10 and Figure 3.11 show damage maps identifying the principal fractures near the base of the building along axes 5, 8, 11, and 13, including:

- Walls along axes 8 and 13 show apparent compression failures on the east side near the first level. Detailed surveys showed both concrete crushing and longitudinal reinforcement buckling. Wall piers along axes 11, 17, and 24 suffered similar failures at the setback level (between first and second floor).

- Large horizontal cracks along axes 5 and 8 indicate that the wall on the west side near the first level sustained significant tension, consistent with actions expected as the building overturned toward the east. Photographs of the failure interface on the west side showed both fractured bars and failed lap splices. Similar damage was absent on the east side, although such damage would have been obscured by crushing failures on that side.

- The solid wall panels in the first story, just below the stack of corridor openings, sustained major damage (axes 5, 8, and 13). Damage in these panels may be due to large shear forces that result from opposing tension and compression forces in the wall boundaries adjacent to the corridor. Such "solid wall panels" have been damaged in past earthquakes (Naeim et al. (1990)).

45

Based on the damage inspection alone, the authors are unable to identify which of the major damage types (concrete crushing, reinforcement tension failure, or wall panel failure) occurred first or was the major trigger for the collapse. To gain further insight into the collapse, analytical studies were conducted, as described in the following sections.
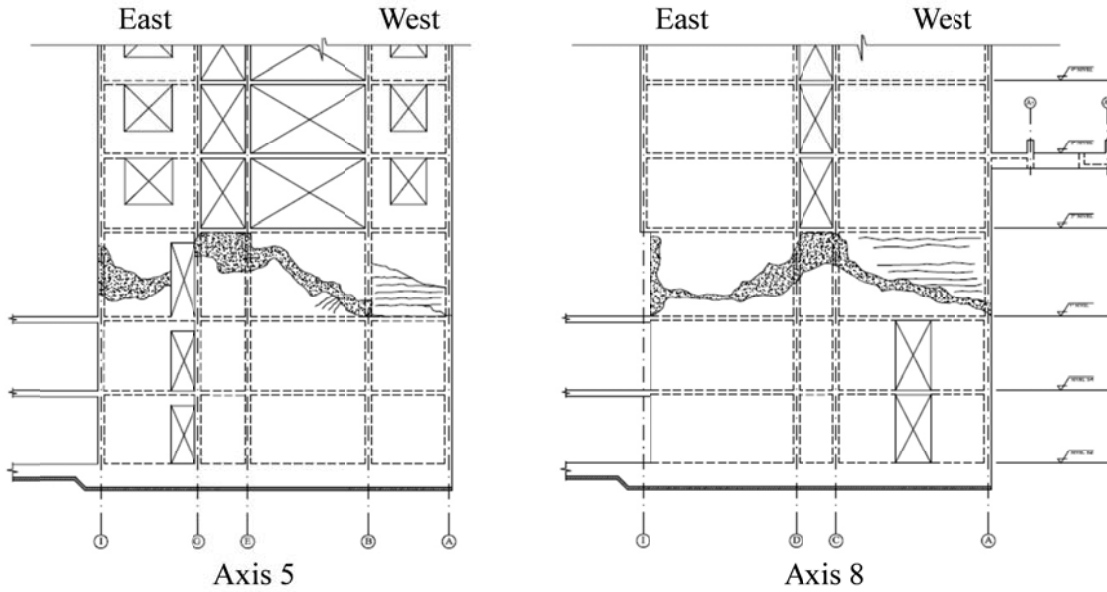
Figure 3.10 - Sketch of damage on axes 5 and 8 (after IDIEM, 2010)
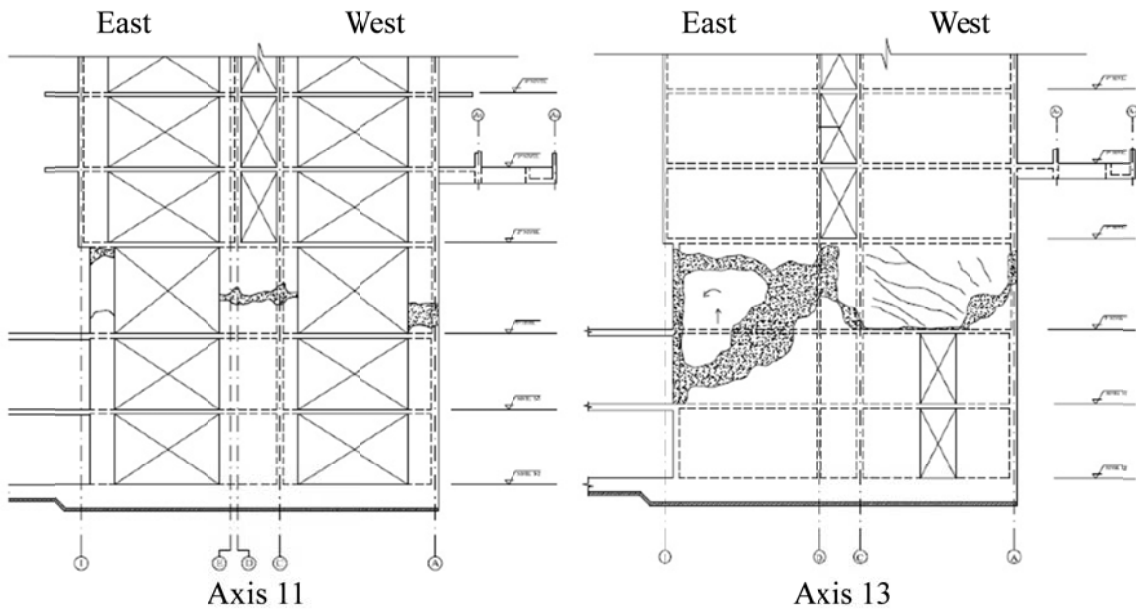
Figure 3.11 - Sketch of damage on axes 11 and 13 (after IDIEM, 2010)

3.7 Reconnaissance Data of the Post-Earthquake Damage

The reconnaissance data obtained from the post-earthquake investigations by IDIEM (2010) confirms the previous observations of the damage sketches. For more detailed understanding, the post-earthquake damage description of Axes 5, 8, 11 and 13 is included in this section with detailed pictures from the building site. The damage description is done starting from the Axis 5, corresponding to the north side, to the Axis 13 corresponding to the south side of the part of the building modeled and analyzed. The east side of the building was not accessible because of the nature of the collapse.

3.7.1 Axis 5

The damage develops at the base of the first story between the Axes A and B, showing failure of the cold joint. The damage gradually rises to the top of the first floor on Axis C and then down again (Figure 3.12). There is also evidence of compression failure starting from Axis B. The vertical reinforcement on Axes 5 and A showed evidence of fracture and lap splice failure apparently due to tensile forces (Figure 3.13).

Figure 3.12 - Post-earthquake picture of Axis 5 (after IDIEM, 2010)

Figure 3.13 - Post-earthquake picture of Axis 5 (after IDIEM, 2010)

3.7.2 Axis 8

The damage was observed at the base of the first story where the Axis 8 meets Axis A. Then the damage climbs diagonally to a height of 0.4 m around Axis B, and continues to the top of the first story with the same slope toward Axis C (Figure 3.14). Figure 3.15 shows apparent compression failure between Axes A and B. Figure 3.16 shows the twisted vertical reinforcement bars at the intersection of Axis 8 and C, which could be a result of compressive and shear forces at that location.

At west end of Axis 8 located on Axis A, lap splice failure of the boundary longitudinal reinforcement is clearly seen in Figure 3.17. Also, it is observed that the longitudinal web reinforcement is fractured under tensile loads in a similar manner. Figure 3.18 shows the detached horizontal reinforcement at Axis C.

Figure 3.14 - Post-earthquake picture of Axis 8(after IDIEM, 2010)

Figure 3.15 - Post-earthquake picture of Axis 8 (after IDIEM, 2010)

Figure 3.16 - Post-earthquake picture of Axis 8 (after IDIEM, 2010)

Figure 3.17 - Post-earthquake picture of Axis 8 (after IDIEM, 2010)

Figure 3.18 - Post-earthquake picture of Axis 8 (after IDIEM, 2010)

3.7.3 Axis 11

Similar to the previous axes, damage is observed horizontally in the base level of the first story at Axis A, and it climbs to 1.2m height at Axis C. Figure 3.19 shows the buckled lap-spliced longitudinal reinforcement at Axis C, possibly caused by the high compression that crushed the concrete or failed lap splices that then were subjected to high compression upon load reversal.

52

Figure 3.20 shows slip and horizontal movement of longitudinal reinforcement at the intersection of Axes 11 and A.

Figure 3.19 - Post-earthquake picture of Axis 11 (after IDIEM, 2010)

Figure 3.20 - Post-earthquake picture of Axis 11 (after IDIEM, 2010)

3.7.4   Axis 13

Damage at Axis 13 is observed at a height of 1.8 m at Axis A. The failure plane declines gradually until a height of 0.8 m at Axis C. It is noteworthy that the height 0.8 m corresponds to the height of lap splices (Figure 3.21, Figure 3.22, and Figure 3.23). Figure 3.24 and Figure 3.25 show the failure of confinement at the intersection of Axes 11 and A.

Failure of the shaft end wall 13-A at a height of about 1.8 m is observed, then goes back to a height of 0.8 m (coinciding with proximity of the end splices) and continuous basis until axis C. Also, it is observed that the slab on the ground floor is failed locally close to this location.

Figure 3.21 - Post-earthquake picture of Axis 13 (after IDIEM, 2010)

Figure 3.22 - Post-earthquake picture of Axis 13 (after IDIEM, 2010)

Figure 3.23 - Post-earthquake picture of Axis 13 (after IDIEM, 2010)

Figure 3.24 - Post-earthquake picture of Axis 13 (after IDIEM, 2010)

Figure 3.25 - Post-earthquake picture of Axis 13 (after IDIEM, 2010)

3.8 Linear Elastic Response Spectrum Analysis

A linear elastic model of the Alto Rio building was prepared using the computer program ETABS (CSI). Shear walls were modeled using shell elements. Effective flexural stiffness was defined as $E_c I_{eff} = 0.5 E_c I_g$ in accordance with ASCE 41-06, in which E_c = Young's modulus of concrete (assumed 30,820 MPa (4,470 ksi) for both C20 and C25 concretes), I_{eff} = effective second moment of inertia of the section, and I_g is the second moment of inertia of the gross section. Values of E_c are from ACI 318-11 using concrete strength values from the concrete core tests conducted after the earthquake (IDIEM, 2010). The same reduction factor (0.5) applies to shear and axial stiffness as well. Effective seismic mass on each floor was calculated as $m_s = m_d + 0.25 m_l$, in which m_d is mass of self-weight and dead loads, and m_l is mass corresponding to the design live load (2.0 kPa (0.29 psi) typically). Slabs had infinite in-plane stiffness with no out-of-plane flexural stiffness. The model includes flexibility of walls and columns extending below grade level, but lateral translational degrees of freedom are fixed at grade and subterranean levels, and vertical translational degrees of freedom are fixed at the lowest subterranean level.

Table 3.2 lists calculated periods and primary directions. The calculated fundamental periods in the transverse and longitudinal directions correspond to $N/19$ and $N/21$, respectively,

which are typical of values for Chilean shear wall buildings (Wallace and Moehle, 1989).

Table 3.2 - Calculated vibration periods

Mode	Period (s)	Direction
1	0.81	Transverse
2	0.71	Longitudinal
3	0.58	Torsional
4	0.19	Longitudinal
5	0.17	Transverse
6	0.14	Torsional

Response spectrum analysis was done using 2.5%-damped response spectra for the recorded Concepción ground motions, with results combined using the complete quadratic combination method (Der Kiureghian and Nakamura, 1993). The effective damping value was selected based on recommendations of PEER/ATC-72-1 (2010). Calculated roof displacements were $0.0070h$ and $0.0046h$ in the transverse and longitudinal directions, respectively, where $h =$ height from grade level to top of the roof at the 15th level. Maximum story drifts were $0.0090h_x$ and $0.0069h_x$ in the transverse and longitudinal directions, where $h_x =$ story height. As a point of reference, maximum permitted story drift ratio for this building type is $0.02h_x$ in ASCE 7-10. The linear model showed stress concentrations in the walls around the setback at level 2 and in the solid panels beneath the stacks of openings. Numerical values of stress were sensitive to mesh size, and are not reported here.

3.9   Nonlinear Static Analysis

To gain further understanding of the inelastic behavior of the building, a static lateral force analysis was conducted on an analytical model representing the inelastic material properties of a portion of the building in the transverse direction. Only the walls along axes 8 and 13 were modeled, as these were deemed representative of the main portion of the seismic-force-resisting system of the building. Contributions of the walls along axes 11 and 17 are ignored in the analysis, as these are not likely to contribute significantly to overall lateral resistance. Figure 3.4 and Figure 3.5 indicate the portion of the building included in the model.

An important first step in developing an inelastic model is to identify the likely modes of inelastic response. Inelastic flexural response of the walls is an obvious consideration. Typical of Chilean design practice, the Alto Rio building features a pair of longitudinal corridor walls flanked by transverse walls, resulting in a series of T and L-shaped wall cross sections (Figure

3.4 and Figure 3.5). Given the slender aspect ratio of the walls, the flanges can be assumed to be fully effective as either a compression or tension element, depending on the loading direction. Such walls are relatively strong but brittle for loading that puts the flange in tension and the stem in compression, and relatively weak but ductile for loading in the opposite direction. Figure 3.26 plots calculated moment-curvature relationships of a T-shaped shear wall along axis 13 for expected axial loads (1.0D + 0.25L), demonstrating the asymmetry in load-deformation response. Where two such walls are placed with their flanges back-to-back to create a corridor, the result is one T-wall that is strong and brittle while the other is weak and ductile. Under lateral load, the strong wall attracts greater force and degrades earlier than the other wall. These interactions can be monitored using a structural analysis model of the building that incorporates the inelastic flexural response characteristics.
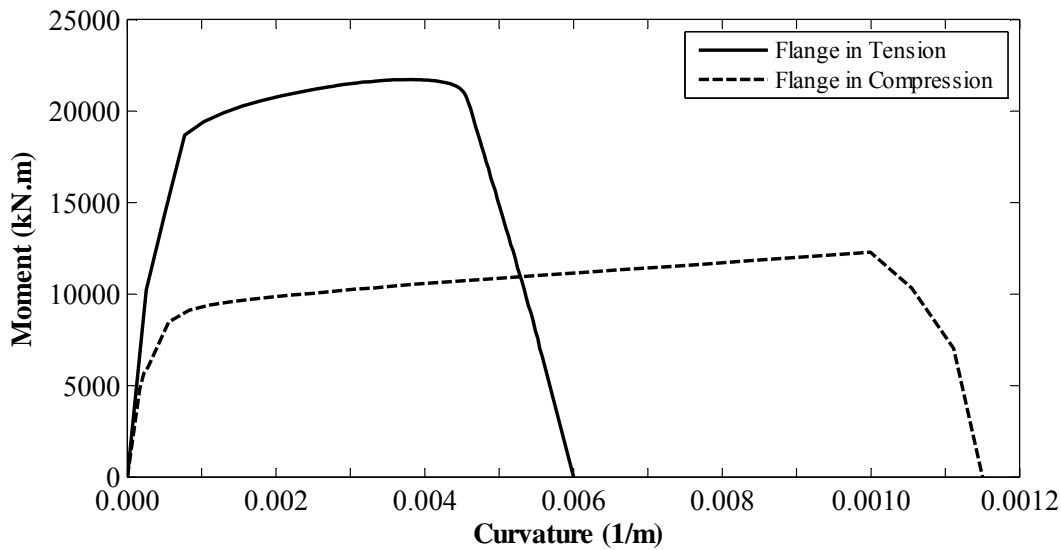
Figure 3.26 - Moment curvature analysis of the east wall on axis 13 (Note: 1 kN.m = 0.7375 kip.ft)

Another potential source of inelastic response results from the high shear stress that develops in the solid wall panel directly beneath a stack of openings. This stress is the result of opposing flexural tension and flexural compression forces in the boundaries of the walls on opposite sides of the opening (Figure 3.27). Studies (for example, Naeim et al., 1990) show that the majority of this force is resolved by panel zone shear stresses that occur within a short distance below the bottom of the stack of openings. The effect is analogous to the shear stress that develops in beam-column joints of moment-resisting frames. Studies of typical Chilean buildings show that this stress may reach the stress capacity of the panel (NIST GCR 14-917-25 (2014)). Therefore, a nonlinear model of the building should also represent this effect.

61
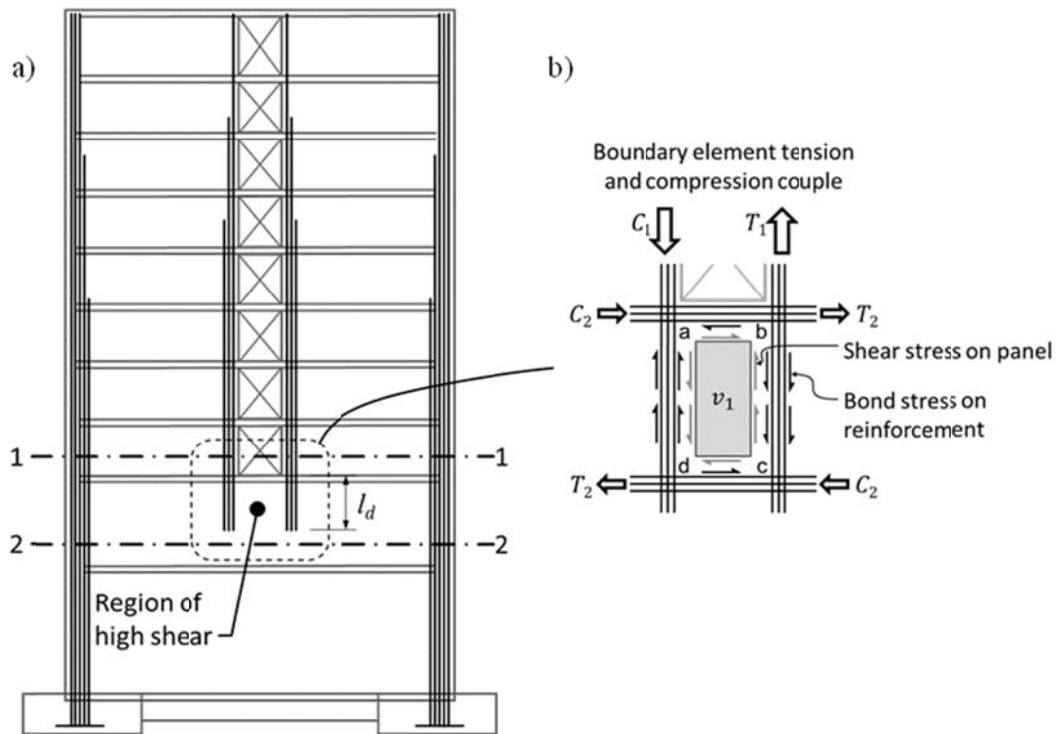
Figure 3.27 - (a) Region of high shear stress in solid wall panel below the stack of openings (b) Solid wall panel shear and tension/compression chords

Nonlinear static analysis was carried out using the computer program Perform3D (CSI). Structural walls were modeled using 4-noded "Shear Wall Elements" (CSI) with fiber cross sections. In this implementation, all interconnected planar wall segments at any level are assumed to remain plane when deformed. In the first and second floor, where inelastic actions were expected to concentrate, shear wall elements were meshed so that each element had a height of twice the wall web thickness. This value was established from post-earthquake observations of the typical height of spalled and crushed regions. For the rest of the building, larger-sized elements were used.

Figure 3.28 shows the 3D view of the numerical model in Perform 3D. Similarly, Figure 3.29 and Figure 3.30 how the elevation view of the Perform 3D model for Axis 8 and 13, respectively. Comparing these figures with Figure 3.6, Figure 3.7, and Figure 3.8, it can be seen that the Perform 3D model closely represents the geometric proportions and discontinuities.
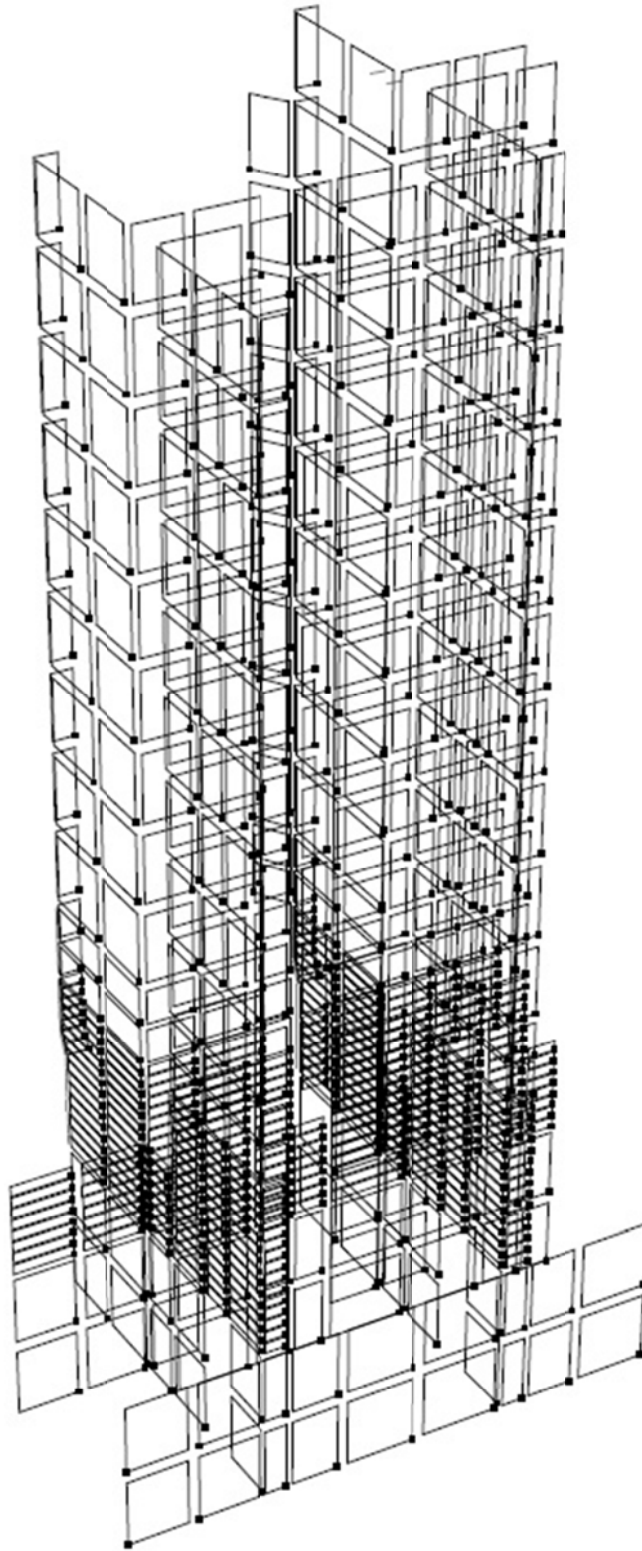
Figure 3.28 - 3D view of the numerical model in Perform 3D
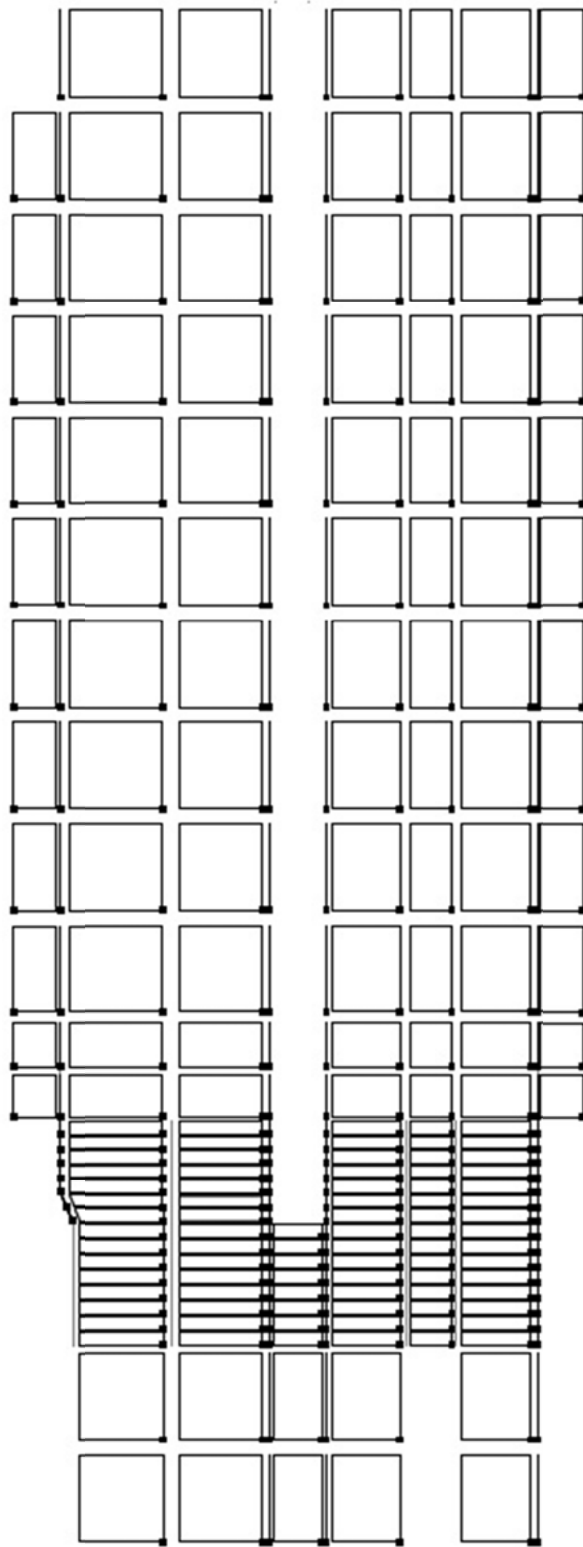
Figure 3.29 - Elevation view of Axis 8 of the numerical model in Perform 3D

64
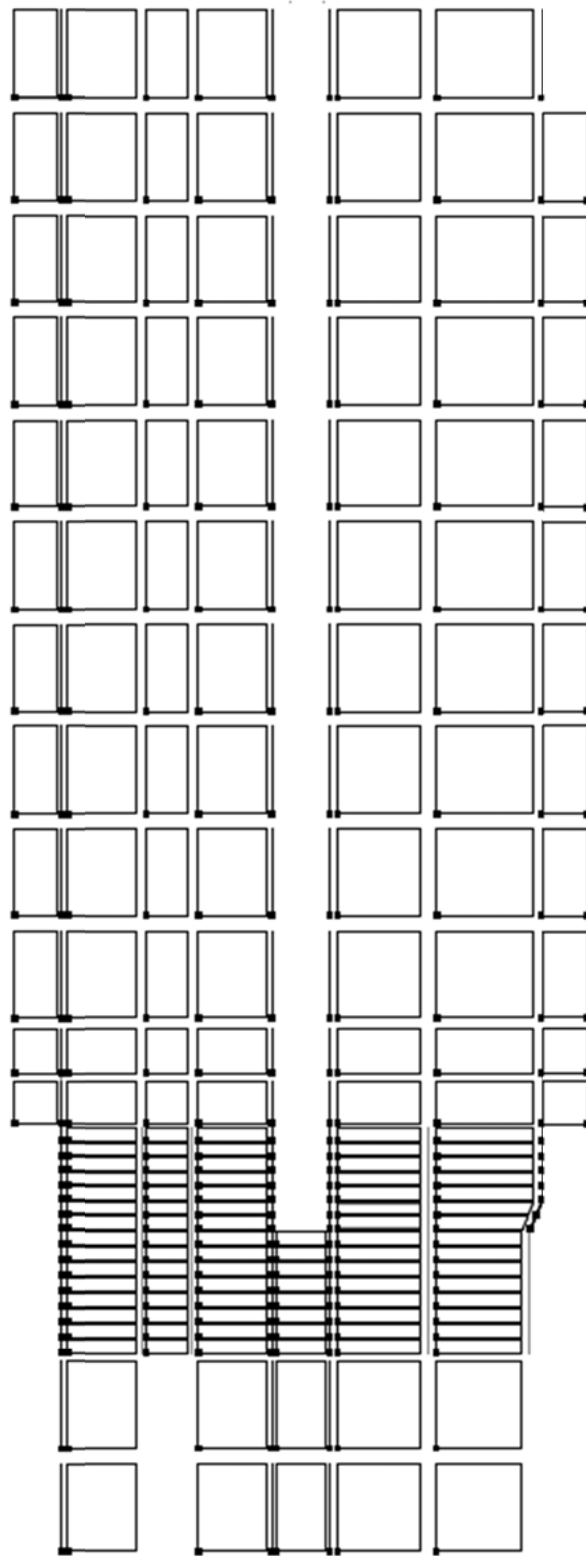
Figure 3.30 - Elevation view of Axis 13 of the numerical model in Perform 3D

Figure 3.31 and Figure 3.32 show the plan view of the Perform 3D numerical model of the second floor (and above) and first floor, respectively. These figures can be compared to the highlighted portions of Figure 3.4 and Figure 3.5 for clarity.
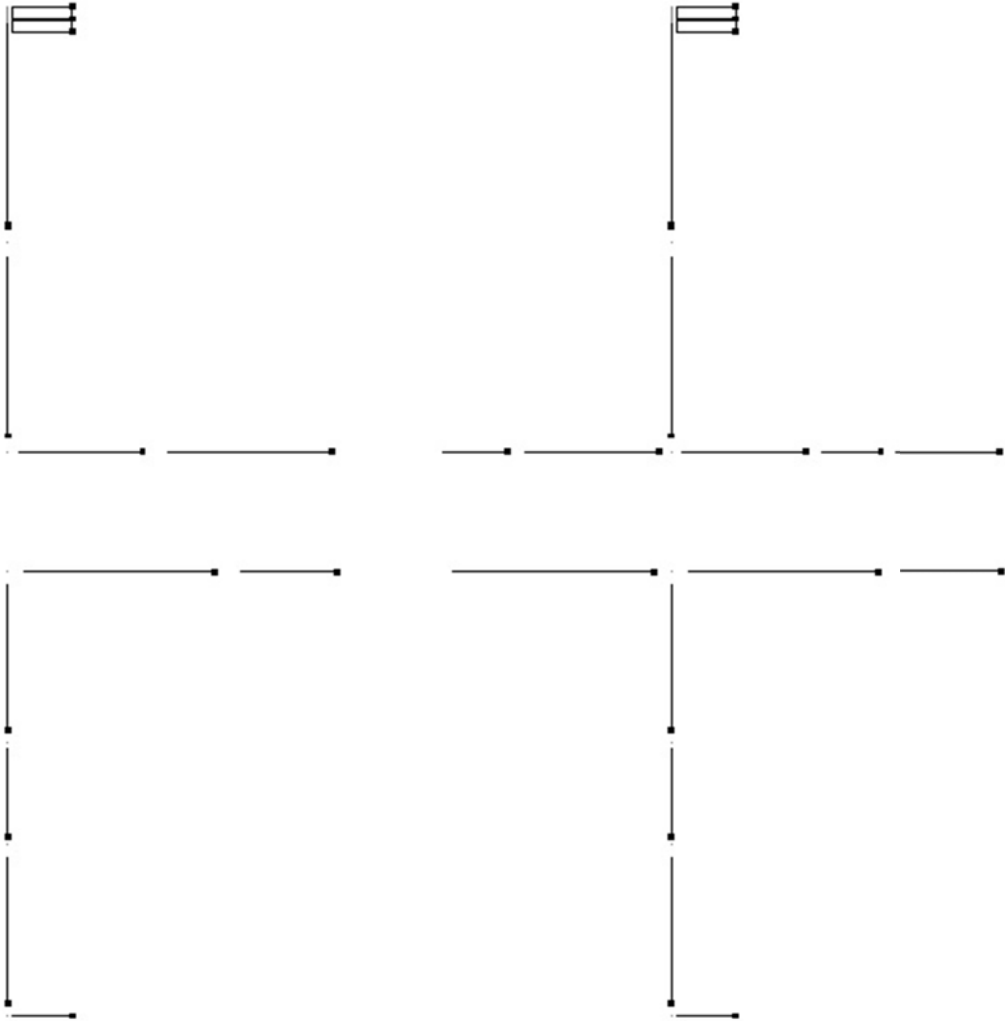
Figure 3.31 - Second story (and above) plan view of the numerical model in Perform 3D
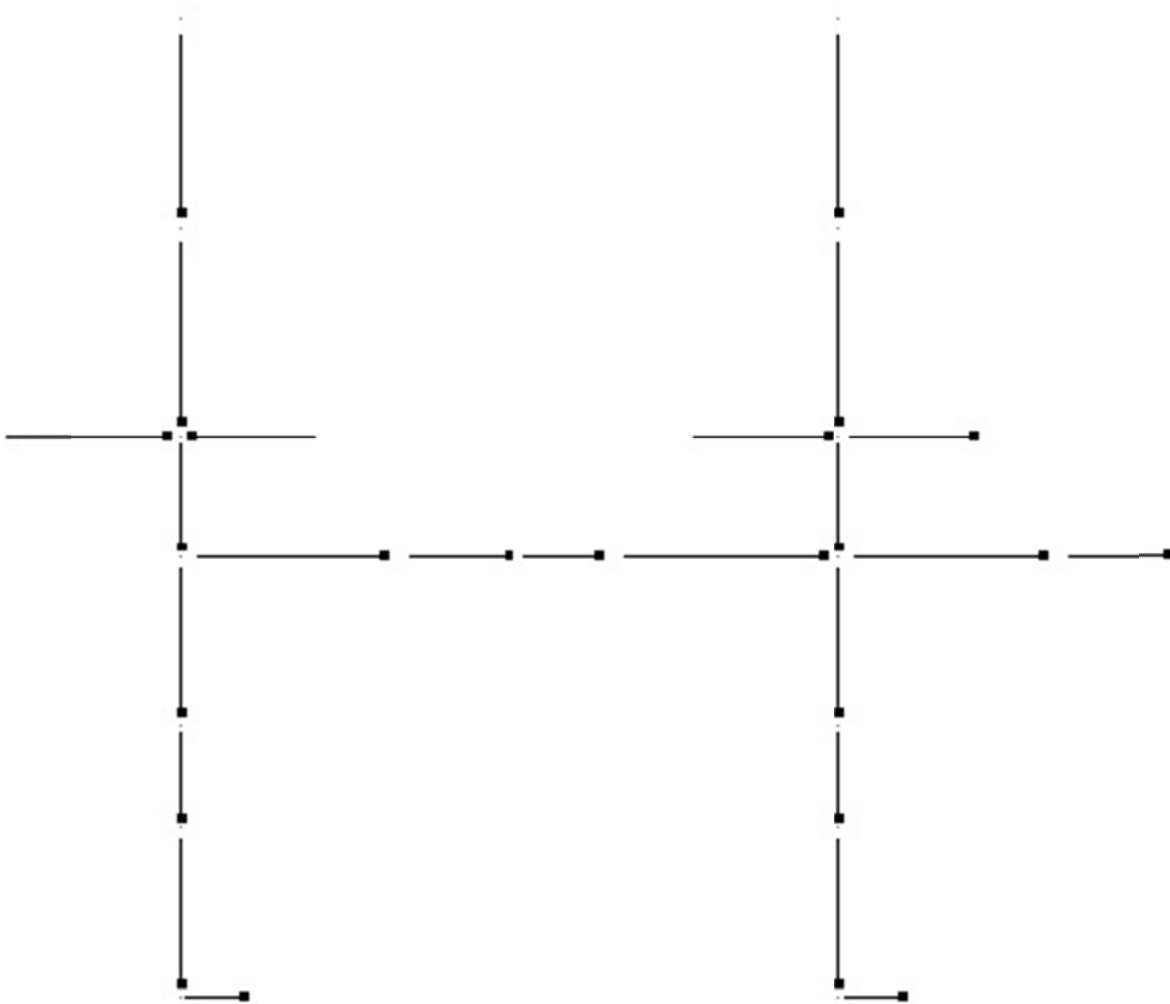
Figure 3.32 - First story plan view of the numerical model in Perform 3D

Materials for the fiber elements were modeled based on the mean test results from coupons taken after the earthquake. The concrete stress-strain relation for compression was a trilinear relation with a descending portion (Figure 3.33). Concrete was assumed to be unconfined because of the wide spacing and 90-degree hooks on the transverse reinforcement. It was assumed that concrete has no tension resistance.

67
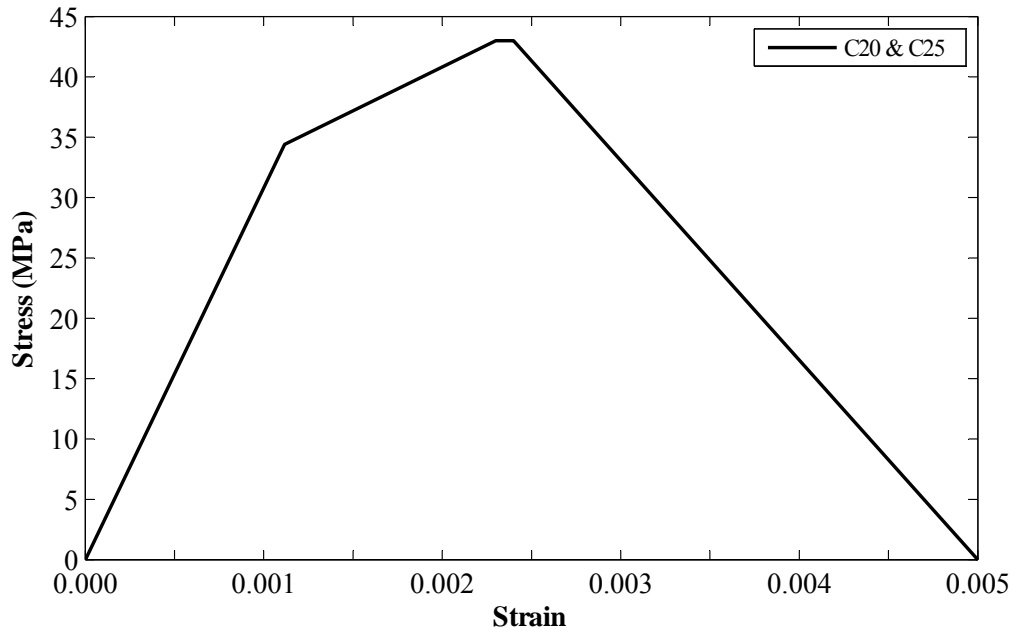
Figure 3.33 - Concrete stress-strain relation (positive values are compressive) (Note: 1 MPa = 145 psi)

The reinforcing steel stress-strain relation for the fiber elements was modeled using the relation shown in Figure 3.34. The ultimate strain in tension was limited to 0.05 in consideration of low-cyclic fatigue (PEER/ATC-72-1). Behavior in compression was varied according to the ratio s/d_b (s = spacing of transverse reinforcement and d_b = diameter of longitudinal bar) in consideration of longitudinal bar buckling (Monti and Nuti, 1992). It was assumed that bar buckling could not trigger spalling, but instead buckling could occur only following spalling of cover concrete at assumed compressive strain of 0.005. Some ongoing research suggests that reinforcement buckling can initiate spalling under some circumstances, but this possibility was not modeled.

An inelastic shear material was used for the walls, with nominal shear strength of $1.5V_n$, in which V_n is the nominal shear strength defined in ACI 318-11, that is, $V_n = \left(0.17\sqrt{f_c'} + \rho_t f_{yt}\right)A_{cv}$ (MPa) $\left[\left(2\sqrt{f_c'} + \rho_t f_{yt}\right)A_{cv}$ (psi)$\right]$, in which ρ_t = transverse reinforcement ratio, f_{yt} = yield stress of transverse reinforcement, and A_{cv} = web area of wall. The solid wall panels beneath the stack of openings were modeled in two different ways. In one model, the regions were modeled with an elastic shear material having effective shear stiffness defined as $0.4E_cA_{cv}/20$ (PEER/ATC-72-1), in which $0.4E_c$ approximates the shear modulus G_c and the divisor 20 represents stiffness reduction associated with concrete cracking. In a second model, the solid wall panels were modeled using a trilinear shear material having initial stiffness $0.4E_cA_{cv}$, with the first break point at shear equal to $0.33\sqrt{f_c'}A_{cv}$ (MPa) $\left[4\sqrt{f_c'}A_{cv}$ (psi)$\right]$, followed by a strain-hardening branch to a point defined by the intersection of a shear force of $1.5V_n$ and a secant from the origin at a slope of $2.5\rho_t nG_c$, in which ρ_t is the ratio of the area of horizontal reinforcement to the area of concrete, $n = E_s/E_c$ is defined as the modular ratio, and G_c

68

is the shear modulus of concrete (= $0.4E_c$). The shear model degrades after reaching shear force $1.5V_n$. This model was based on the recommendation in Sozen et al. (1992) and was found to correlate well with the test results of similar wall panels reported in Vecchio and Collins (1986). The force transfer between the panel zone and the adjacent walls is achieved through the assumption of the perfect bond of the boundary element reinforcement from the walls into the solid segment.
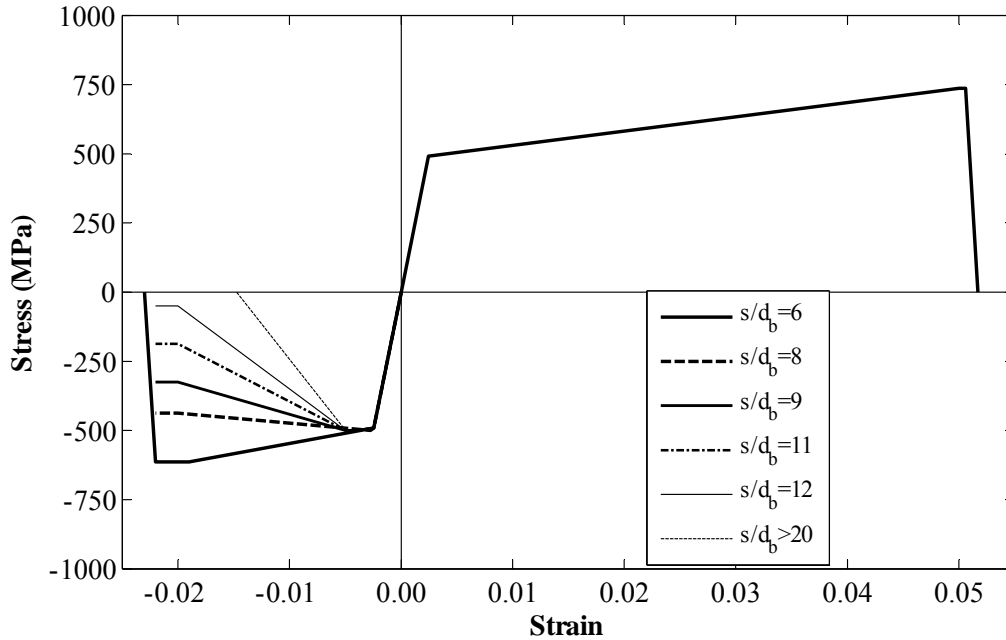
Figure 3.34 - Reinforcing steel stress-strain relation (positive values are tensile) (Note: 1 MPa = 145 psi)

The analytical model was subjected first to gravity loads and then to progressively increasing lateral forces. Gravity loads were estimated based on tributary areas for the various walls, considering $1.0D + 0.25L$ (D = dead load and L = specified live load). For lateral analysis, an inverted triangular force pattern was applied at the center of mass of each floor of the modeled part of the building. Due to the tendency for some torsional response for this loading, rotations about a vertical axis were artificially prevented.

Figure 3.35 shows calculated relations between base shear and roof displacement for east and west loading directions of the model with nonlinear shear stress-strain relationships assigned to the solid panel beneath the corridor openings and the rest of the model. For loading the model to the east, the direction in which collapse occurred, the first significant event is crushing of the wall boundary at the east edge of the east wall along axis 13 at around 0.72% roof drift ratio, followed by similar crushing of the east part of wall 8 at around 1% roof drift ratio. The crushing occurs at the transition between levels 1 and 2, apparently because of the wall vertical discontinuities at that level (the setback between stories 1 and 2 and beginning of the stacked openings along the corridor). Compression failure of the east side of the walls along axes 13 and 8 resulted in numerical instability of the model. It is noteworthy that at the roof drift

69

corresponding to the crushing of W8-E, the model indicates boundary reinforcement tensile strain of 5 to 14 times the yield strain. Thus, it plausible that the lap splices may have sustained some yielding and strength degradation before this point.
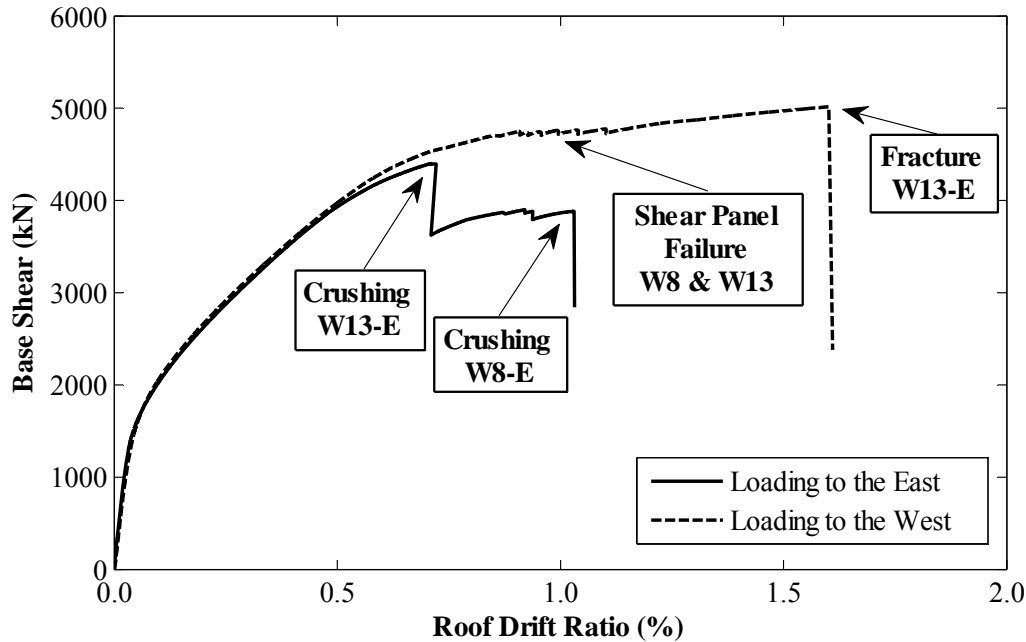
Figure 3.35 - Base shear – drift relationship of nonlinear static analysis (Note: 1 kN = 0.2248 kips)

For lateral load to the west, the first significant events are failure of the solid wall panels below the stack of openings between coupled walls along axes 8 and 13 at around 1.0% roof drift ratio. "Failure" is arbitrarily defined as onset of strength degradation after reaching shear strength $1.5V_n$. This is followed by fracture of the longitudinal reinforcement at the east side of the east walls along Axis 13 at 1.6% roof drift ratio. (The drift estimates corresponding to fracture are likely to be low because of the small element size, which can result in strain concentration in the reinforcing steel model. Sensitivity studies have been done in order to investigate the effect of mesh size on the response. There was no significant relationship observed between element sizes and drift ratios corresponding to the fracture of reinforcing steel.) It is noteworthy that crushing failure is not calculated to occur for loading in this direction, at least not within the drift range of interest. Apparently, the absence of the setback and the short returns on the walls result in sufficient compression area to avoid crushing failure for loading to the west. In the absence of splice failure, compressive failure seems unlikely in this direction. However, compression failure could occur if the wall edges are previously damaged by splice failure.

The calculated maximum shear force resisted by the walls along axes 8 and 13 is 4400 kN (990 kips) for loading to the east and around 5000 kN (1125 kips) for loading to the west. Nominal shear strength V_n calculated according to ACI 318-11 is 9300 kN (2090 kips). Shear

forces could increase for alternative lateral loading patterns, especially where building response extends well past the effectively linear range of response (Rejec et al., 2011). Crushing of the walls, however, effectively preempts development of ductile flexural response, thereby reducing the likely shear force amplification. Therefore, it seems highly unlikely that the shear demands reached the shear capacity, or that wall shear failure was a primary initiator of the collapse. The single exception is the solid wall panel immediately below the stack of openings.

Figure 3.36 shows the calculated relations between roof drift ratio and (a) average shear stress in the solid wall panel below the stack of openings (solid line) and (b) average shear stress across the entire wall length (dashed line). The results are for the model loaded in the collapse direction, with the solid wall panel below the stack of openings modeled as linearly-elastic. The average stress in the solid wall panel below the stack of openings is approximately three times the average stress acting across the entire wall section. This result is consistent with the results reported by Naeim et al. (1990).
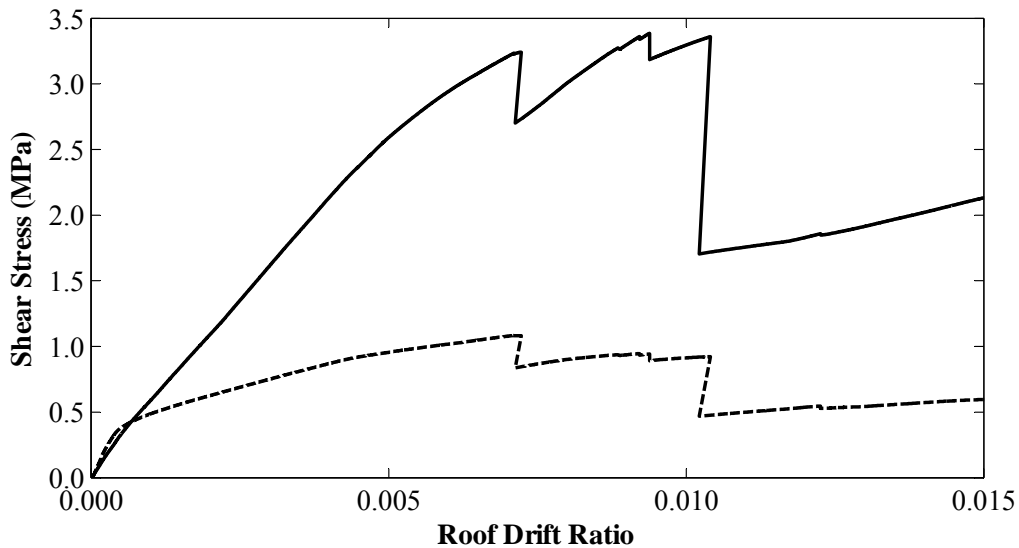
Figure 3.36 - Shear stress – roof drift ratio relationship for solid wall panel below the stack of openings and for entire wall in story 1, using a linear model for the solid wall panel. Stress for the solid wall panel is the average value over the height of the story below the stack of openings. (Note: 1 MPa = 145 psi)

Figure 3.37 shows the calculated relation between shear stress and shear strain in the solid wall panel below the stack of openings for the model in which the solid wall panel is modeled using an inelastic shear material, as described previously. Lateral loading is toward the east. Inelastic response of the region is apparent. More significant inelastic response of the solid wall panel is obtained for loading toward the west (not shown). Overall, the calculated results are consistent with reported damage, which shows cracking or destruction of the solid wall panel below the stack of openings (see Figure 3.10 & Figure 3.11).

It is noteworthy that wall crushing damage and solid wall panel shear damage are estimated to occur for roof drift ratio in the range 0.007 to 0.010 for loading toward the east, with similar

effects at higher drifts for loading toward the west (Figure 3.35, Figure 3.37). As reported previously in this paper, linear response spectrum analysis indicates that the roof drift ratio demand was approximately 0.007 in the transverse direction, similar to the drift at onset of critical damage. To better understand dynamic response, a series of simplified nonlinear dynamic models were studied. The results of these studies will be presented later in this chapter.
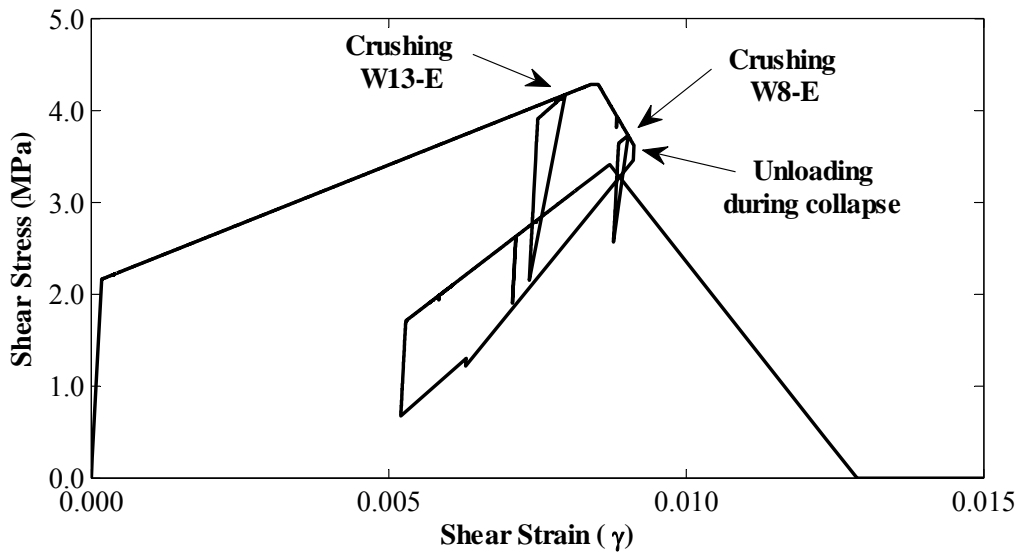
Figure 3.37 - Shear stress – strain relationship of the solid wall panel below the stack of openings along axis 13 of the Alto Río building (Note: 1 MPa = 145 psi)

Figure 3.38 and Figure 3.39 show the deformation concentrations of the Perform 3D model under the loading to the east at 0.75% roof drift ratio. These figures represent the deformations at specific elements right after the "Concrete Crushing of W13-E". The wall on the right side (wall on Axis 13) of the figure had localized deformations at the top of the first story due to the compression failure.

Similarly, Figure 3.40 and Figure 3.41 show the deformation concentrations of the Perform 3D model under the loading to the east at 1.1% roof drift ratio. These figures represent the deformations at specific elements right after the "Concrete Crushing of W8-E". It is worth noting that the wall on Axis 8 (the wall on the left) also experienced the concentrated compression failure right below the setbacks at the top of the first story.

Figure 3.42 and Figure 3.43 show the deformation concentrations of the Perform 3D model under the loading to the west at 1.6% roof drift ratio. This deformation corresponds to the "Tensile Fracture of W13-E". The calculated damage of the bar fracture is located at the bottom of the first story of the wall on Axis 13 (the wall on the right) as can be seen in the figures. It is also apparent that the damage is distributed throughout the first story due to the ductile nature of the tensile failure.

72
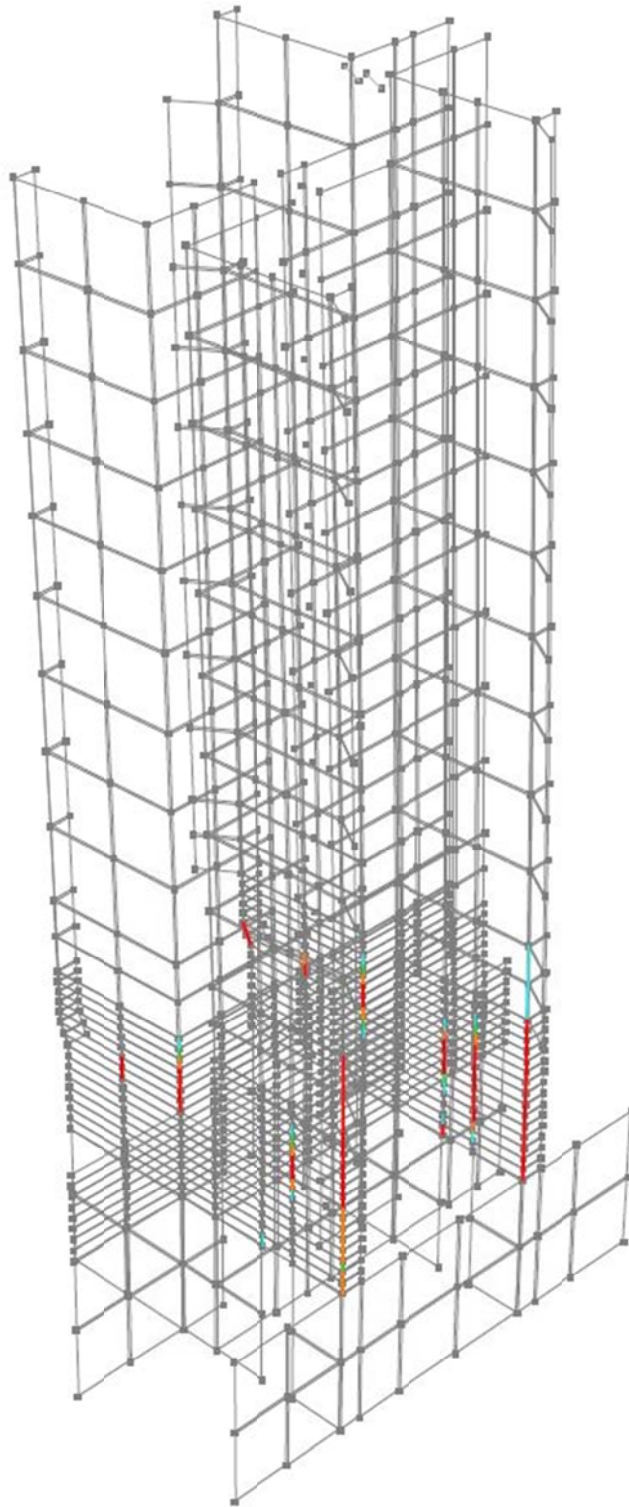
Figure 3.38 – Deformation concentrations of the Perform 3D model under loading to the east at roof drift of 0.75% after "Concrete Crushing W13-E"
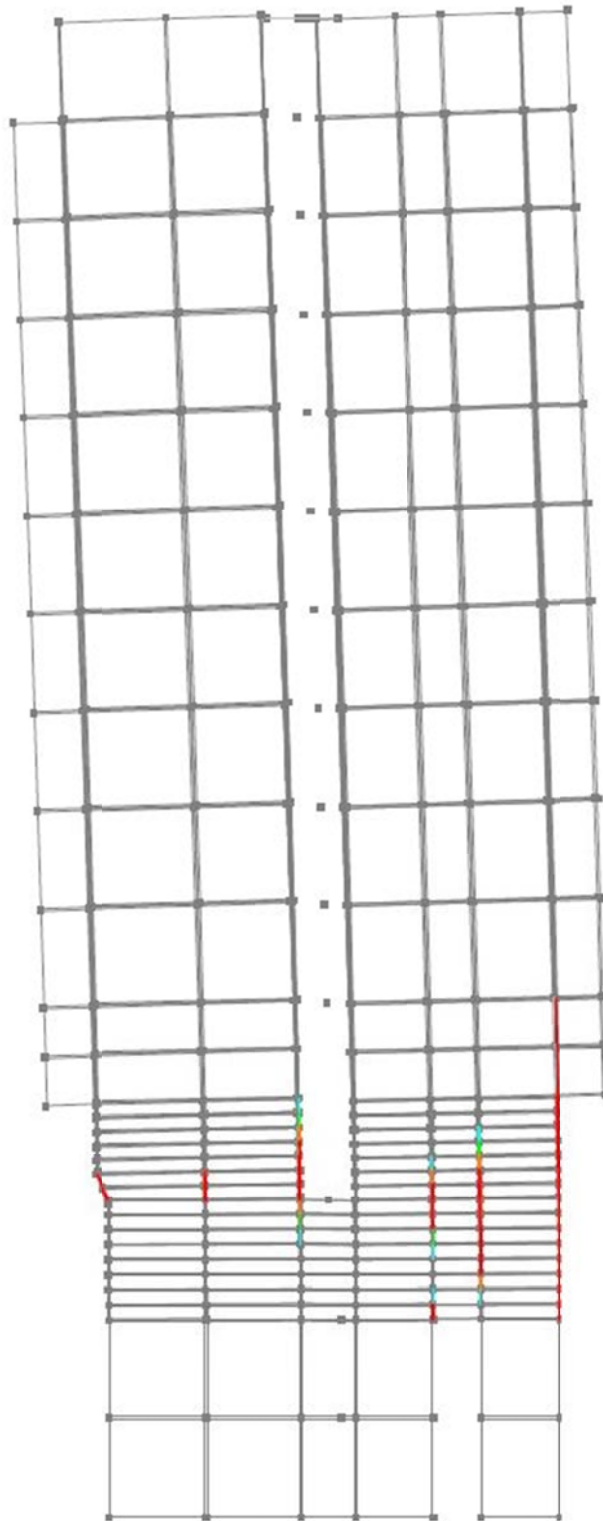
Figure 3.39 - Deformation concentrations of the Perform 3D model under loading to the east at roof drift of 0.75% after "Concrete Crushing W13-E"
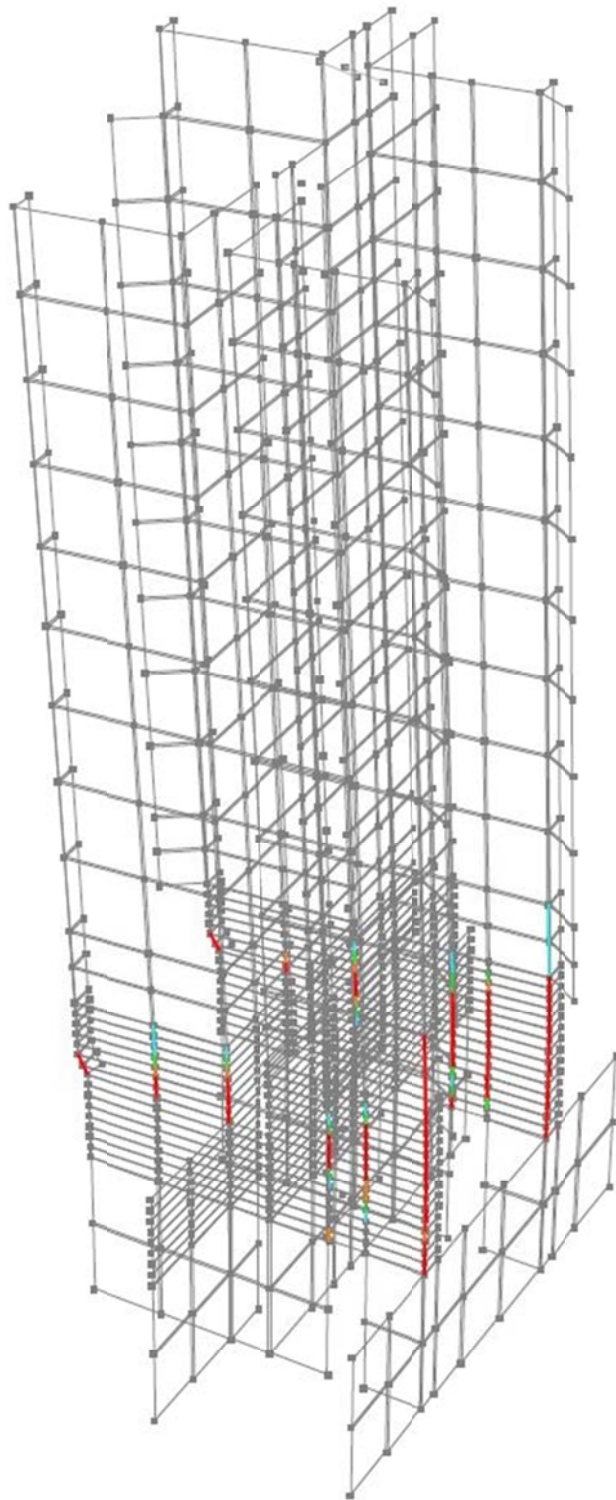
Figure 3.40 - Deformation concentrations of the Perform 3D model under loading to the east at roof drift of 1.1% after "Concrete Crushing W8-E"
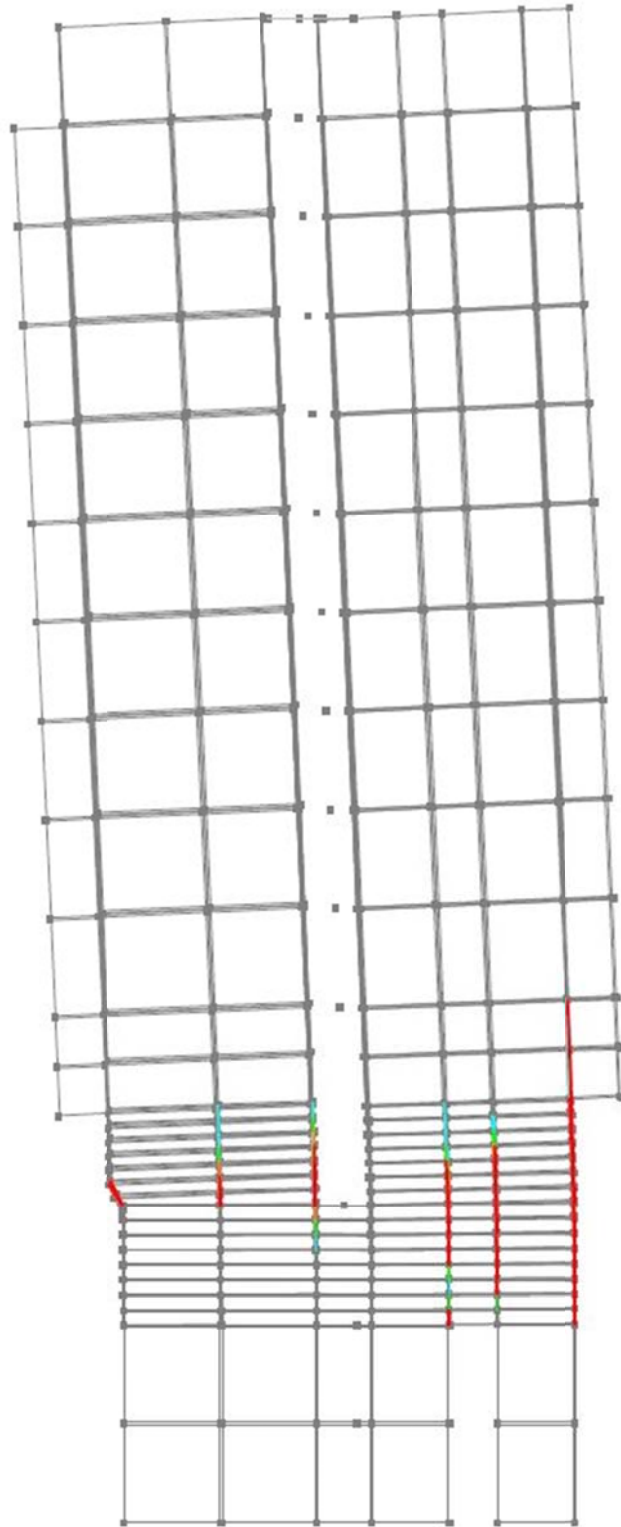
Figure 3.41 - Deformation concentrations of the Perform 3D model under loading to the east at roof drift of 1.1% after "Concrete Crushing W8-E"

76
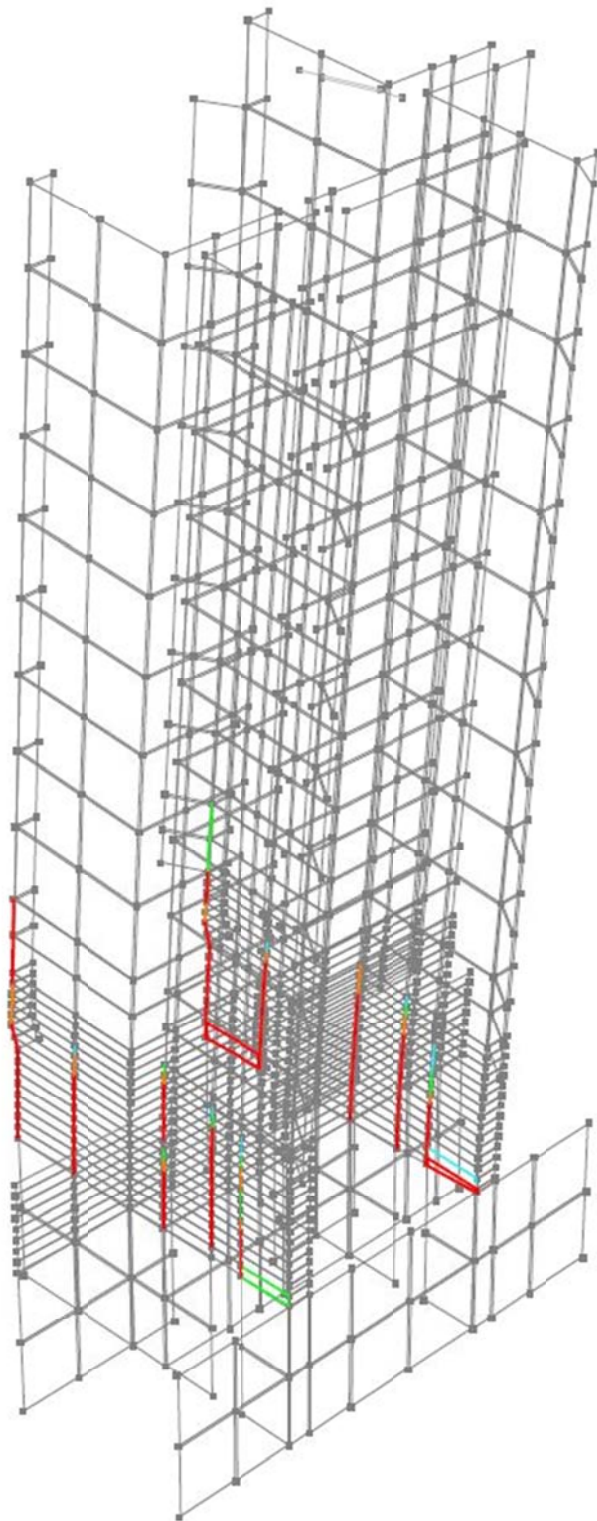
Figure 3.42 - Deformation concentrations of the Perform 3D model under loading to the west at roof drift of 1.6% after "Tensile Fracture W13-E"
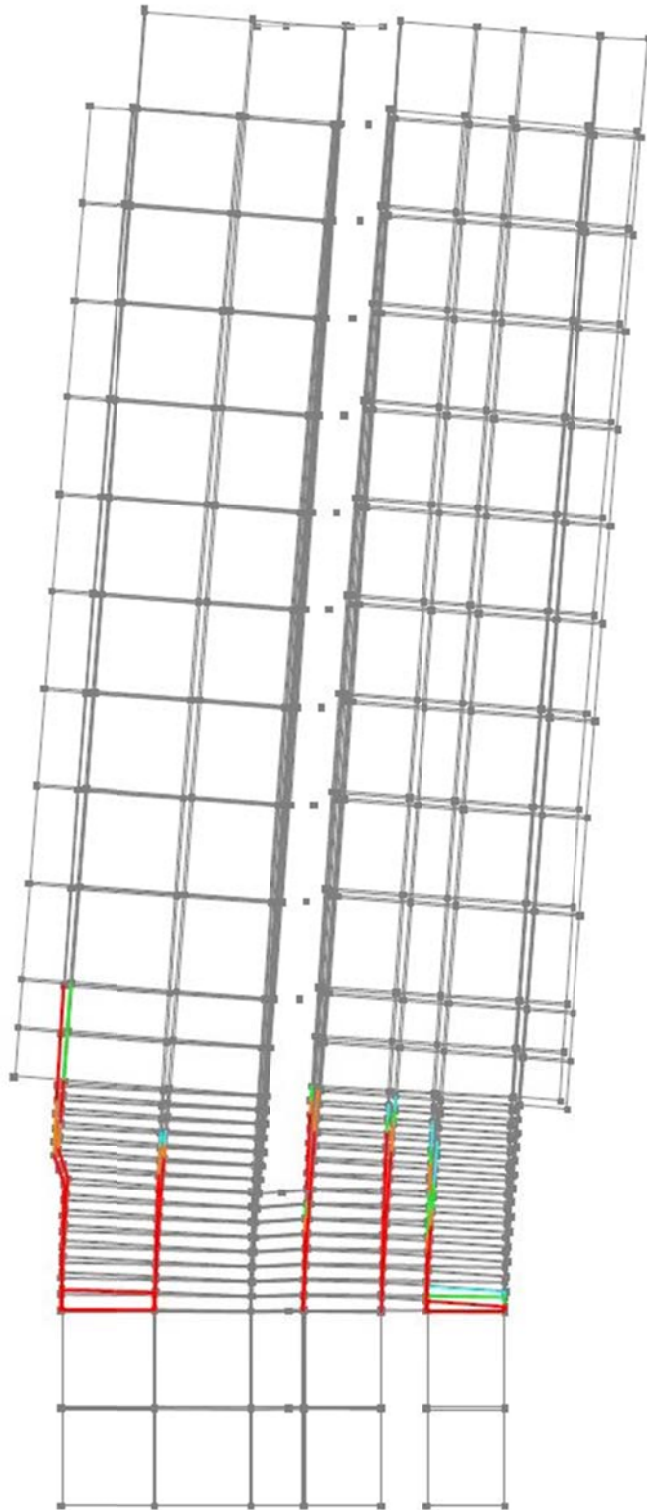
Figure 3.43 - Deformation concentrations of the Perform 3D model under loading to the west at roof drift of 1.6% after "Tensile Fracture W13-E"

3.10   Effect of the Shear Material Model on Response

As mentioned before, an inelastic shear material was used for the walls, with nominal shear strength of $1.5V_n$, in which V_n is the nominal shear strength defined in ACI 318-11, that is, $V_n = \left(0.17\sqrt{f_c'} + \rho_t f_{yt}\right)A_{cv}$ (MPa) $\left[\left(2\sqrt{f_c'} + \rho_t f_{yt}\right)A_{cv}$ (psi)$\right]$, in which ρ_t = transverse reinforcement ratio, f_{yt} = yield stress of transverse reinforcement, and A_{cv} = web area of wall. Figure 3.35, shows the calculated relation between base shear and roof displacement for the model with nonlinear shear stress-strain relationships assigned for the whole model including the shear panel region.

Although these modeling parameters are validated against the results of similar wall panels from the study of Vecchio and Collins (1986), there are some other possible modeling techniques currently popular among structural engineering community. One of these modeling assumptions is modeling shear behavior with an equivalent linear elastic model. To assess the effects of such a modeling decision, a model with an elastic shear material having effective shear stiffness defined as $0.4E_cA_{cv}/20$ (PEER/ATC-72-1), in which $0.4E_c$ approximates the shear modulus G_c and the divisor 20 represents stiffness reduction associated with concrete cracking.

Figure 3.44 shows the comparison of the calculated base shear – drift relationship of nonlinear static analysis of two models of the Alto Rio building. The solid and dashed black lines represent the results for the model with the inelastic shear material. These are the same curves as those presented in Figure 3.35. The solid and dashed red lines represent the results of the model with elastic shear material. There is an apparent difference in the overall stiffness of these two models. Because the elastic shear material model represents the cracked concrete properties, the stiffness of this model is relatively lower than the model with inelastic shear material. A stiffer behavior is expected form the inelastic shear material model because of the stiffer initial slope of the shear stress strain curve shown in Figure 3.37.

The lower stiffness of the model with the elastic shear material results into delayed failures. For lateral loading to the east, crushing of east side of the wall 13 happens at 0.8% roof drift ratio compared to 0.7% of the previous model. Similarly, crushing of the east side of the wall 8 happens at 1.2% roof drift ratio, which was at a 1.0% roof drift ratio for the model with inelastic shear material model. However, it should be noted that the sequence of failures observed didn't change with a change of the shear material model.

For the lateral load to the west, the first difference in the damage modes is observed. As expected, the failure of the shear panel of the walls 8 and 13 is not observed, due to the elastic model of the shear material. On the other hand, the fracture of the longitudinal reinforcement at the east side of the east walls along Axis 13 is observed at 2.0% roof drift ratio rather than the 1.6% observed in the inelastic shear material model.

Another observation of the comparison of the results of these two models is the overall strength of the pushover curves. For the lateral loading to the east, the results of the elastic shear material model have slightly lower strength. On the other hand, for the lateral loading to the west, the nonlinear static analysis of the elastic shear material model results with a higher strength. This inverse effect should be investigated further.

The preceding results indicate that modeling the behavior is important to correctly

understanding; (a) stiffness of the structural system, (b) the types of failures that can occur, including failure of the panel zone, and (c) understanding the drifts at which different failures occur.
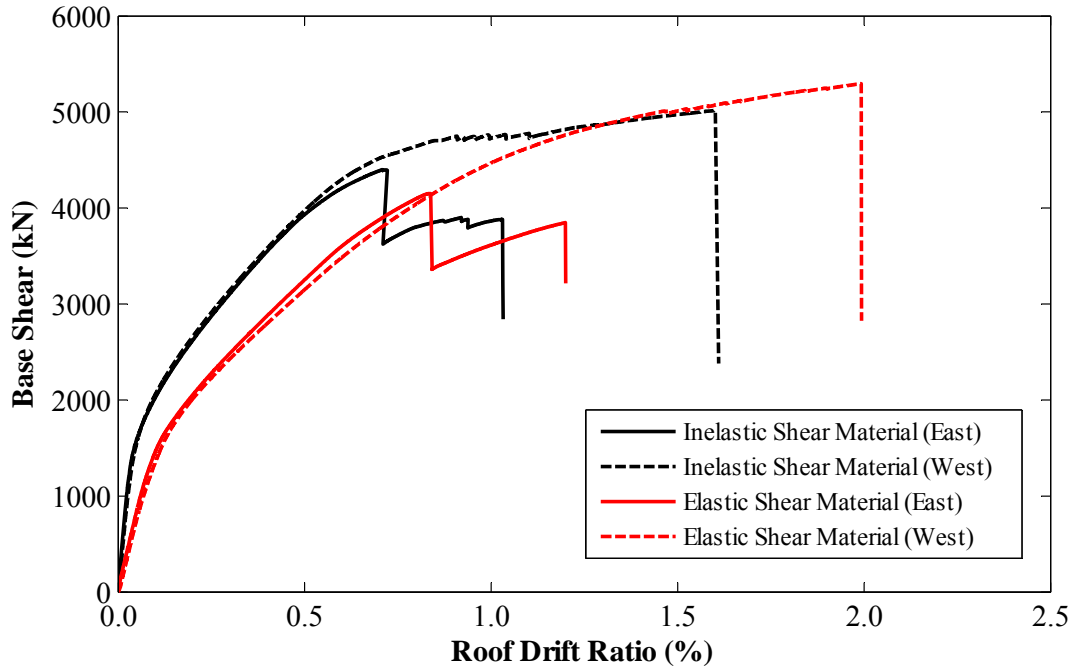
Figure 3.44 - Comparison of the base shear – drift relationship of nonlinear static analysis for elastic and inelastic shear material models (Note: 1 kN = 0.2248 kips)

3.11 Dynamic SDOF Analysis

A single-degree-of-freedom (SDOF) model was established to represent the effective first translational mode response of the Alto Rio building in the transverse direction. The SDOF model was implemented in Perform3D with a nonlinear rotational spring at the base, a massless rigid bar, and a mass at the top. Mass and height of the rigid bar are effective modal mass, M_1^*, and effective modal height, h_1^*, of the fundamental vibration mode (Chopra 2011), defined by:

$$M_1^* = \frac{\sum_{r=1}^{j}(m_r\varphi_r)^2}{\sum_{r=1}^{j}m_r\varphi_r^2} \qquad\qquad 3.1$$

80

$$h_1^* = \frac{\sum_{r=1}^{j} m_r \varphi_r h_r}{\sum_{r=1}^{j} m_r \varphi_r}$$

3.2

in which φ_r is the rth story value of the first-mode shape, m_r is the mass matrix value of the rth story, h_r is the height of rth story level from the base level, and j is the number of stories.

The moment-rotation relationship of the rotational spring is based on the base moment versus roof drift relationship resulting from the nonlinear static analysis of the structure (Figure 3.45). Because the nonlinear static analysis results are only for a representative part of the structure, they should be adjusted to represent the response characteristics of the entire building. Recognizing the approximate nature of the scaling process, we simply scaled the moment values of the relationship by the ratio of seismic mass of the whole building to the seismic mass of the portion of the structure included in the nonlinear static analysis. The initial slope of the moment-rotation response was selected to match the fundamental vibration period calculated using ETABS, described previously. Other parameters of the simplified trilinear moment-rotation relation were adjusted to approximate the relation obtained with the scaled nonlinear static analysis, as shown in Figure 3.45. Hysteresis rules governing unloading and reloading stiffness and energy dissipation per cycle were implemented to approximate the approach presented by Saiidi and Sozen (1981). The SDOF model was excited with the east-west direction of the ground motions recorded at Colegio Inmaculada Concepción site.

Calculated moment-drift relations and displacement response histories of the SDOF model subjected to the Concepción motion are plotted in Figure 3.46 and Figure 3.47. It is worth noting that after a deformation cycle as large as 1.3% roof drift ratio in the west direction, the SDOF model collapses to the east (collapse) direction at around 22 seconds of the excitation. Based on the calculated damage from the PERFORM nonlinear static analyses presented previously, it is expected that the building would sustain concrete crushing failures for both walls on Axes 8 and 13 during the cycle to the east at around 20 seconds. Immediately after that, the loading cycle changes direction. The amplitude of response is consistent with the occurrence of shear damage to the shear panels on both Axes 8 and 13 at around 21 seconds. This is followed by a large cycle to the east direction around 22 seconds, where the nonlinear dynamic model becomes permanently displaced to the east. This permanent displacement of the model is also an indicator of the collapse to the east direction. The final result of the dynamic SDOF analysis is consistent with the observed damage and collapse of the building.
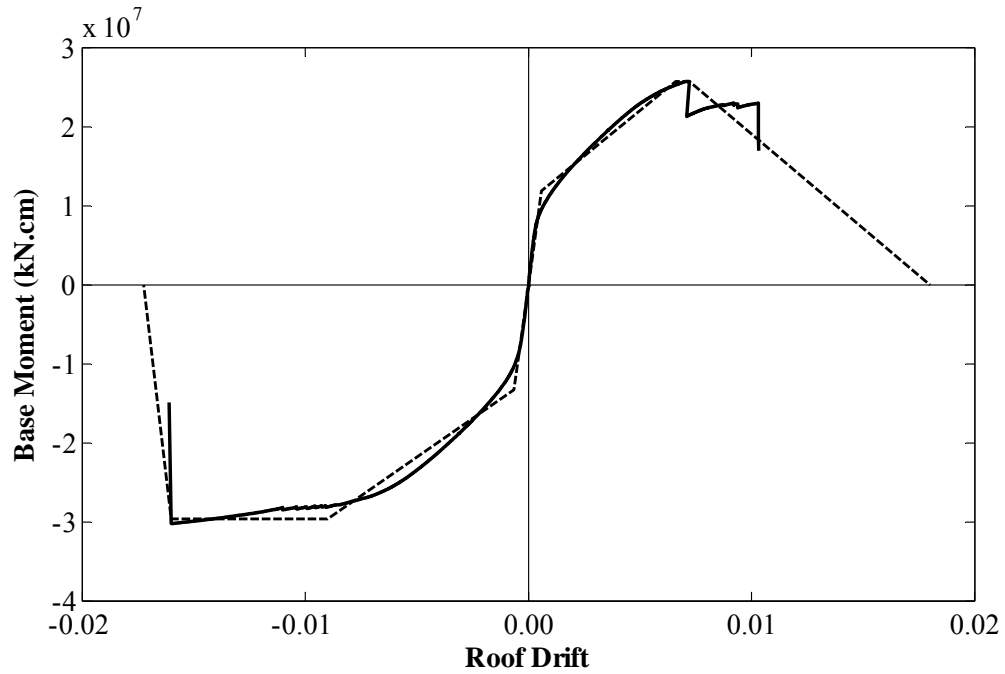
Figure 3.45 - Comparison of moment-rotation relations for the SDOF model and the scaled nonlinear static analysis (Note: 1 kN.m = 0.7375 kip.ft)
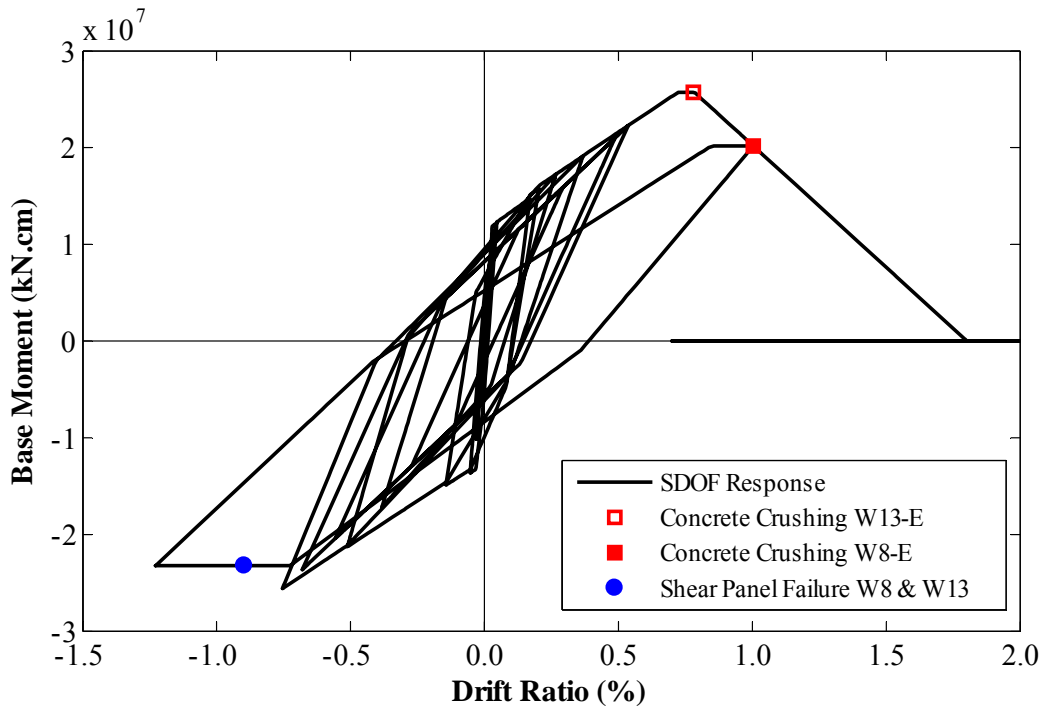
Figure 3.46 - Moment–drift ratio response of the SDOF model under the Concepción ground motion (Note: 1 kN.m = 0.7375 kip.ft)
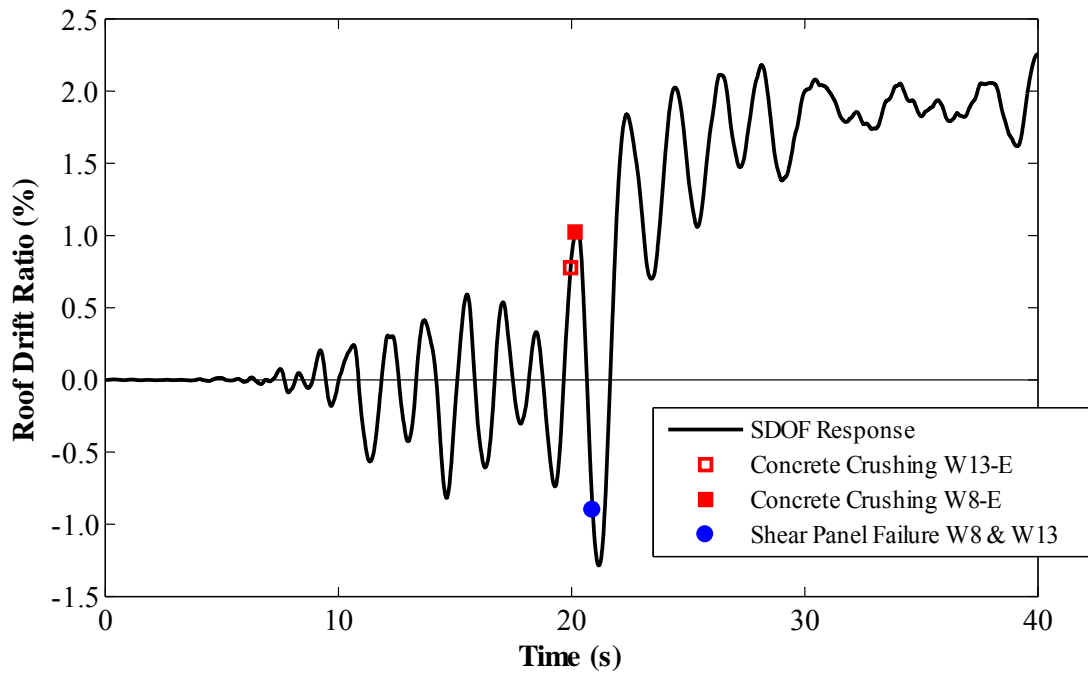
Figure 3.47 - Roof drift ratio response history of the SDOF model subjected to the Concepción ground motion

To assess the influences of fundamental period and base moment capacity of the SDOF model on the calculated response, a sensitivity study was conducted. Varying values of fundamental periods from 0.4 seconds to 1.2 seconds (increments of 0.1 seconds), and values of base moment capacity from 0.5 to 1.5 (increments of 0.1) times the calculated moment capacity were used in the analysis. All combinations resulted in collapse of SDOF model in the east (collapse) direction. This result suggests that the collapse was insensitive to strength and stiffness, and instead was driven by the brittle and asymmetric behavior of the structure.

3.12 Effect of the Softening Slope of the Concrete Stress-Strain Relationship

As mentioned before, the concrete stress-strain relation for compression was a trilinear relation with a descending portion (Figure 3.33). Concrete was assumed to be unconfined because of the wide spacing and 90-degree hooks on the transverse reinforcement. It was assumed that concrete has no tension resistance. The slope of the descending portion of the concrete stress-strain relationship after the ultimate strength point (f_c'), is decided according to the recommendations of the document PEER/ATC-72-1. PEER/ATC-72-1 recommends the value of the concrete ultimate strain (ε_u) to be 0.005 for normal strength concrete. The analyses reported previously in this study were done with this assumption. To explore the effect of these assumptions, additional

83

analyses were carried out using adjusted concrete models.

Figure 3.48 shows the four different concrete stress-strain relationships used in this study with the only difference of the ultimate concrete strain (ε_u) values. The first stress-strain relationship is the model recommended in PEER/ATC-72-1, plotted as the black solid line. As previously mentioned, this model is assumed to have an ultimate compressive strain of 0.005. A second stress-strain relationship is the model by Roy and Sozen (1965) plotted with dashed green line in Figure 3.48. This study recommends an empirical formula for the stress-strain relationship of concrete under compressive forces and results into a smaller ultimate strain (ε_u) value of 0.0043. This model is selected to be a lower bound of values can be selected for the ultimate strain of concrete under compression. This value of the ultimate strain is also approximately equal to the two times of the strain at the peak stress value (ε_o), which is a value that is being used to estimate the ultimate strain value. A third model using the model of Mander et al. (1988) is plotted with the dashed blue line. It should be noted that the Mander et al (1988) stress-strain relationship for concrete results an ultimate strain (ε_u) value of 0.01. This value seems to be higher than the strain that unconfined concrete can achieve under cyclic loading conditions. This value is selected to be an upper bound for the ultimate compressive strain of concrete under cyclic loading conditions.

Lastly, a fourth concrete compressive stress-strain relationship is modeled using the proposed regularization technique against loss of objectivity by Coleman and Spacone (2001). That study proposes a regularization technique for softening sections that requires knowledge of the compression fracture energy for the concrete used in the structure. This parameter supplements the concrete stress-strain relation to maintain a constant stress-displacement relation in the post-peak. Coleman and Spacone (2001) focus on the likelihood of the strain-softening type behaviors that can promote localization in one integration point only. This can occur when the number of integration points increases, as when the element size gets smaller in Perform 3D. This will cause the local base section moment-curvature response and the global base shear-displacement response to lose objectivity. Coleman and Spacone (2001) use the concept of constant fracture energy in tension, which is used widely to regularize mesh-sensitive smeared crack displacement-based elements in continuum finite-element analysis. The main idea of the regularization process is to assume that the uniaxial stress-strain relation for concrete is supplemented by an additional parameter, the fracture energy in compression G_f^c, defined as;

$$G_f^c = \int \sigma \, du_i \qquad\qquad 3.3$$

where σ is the concrete stress and u_i is the inelastic displacement. To adapt the fracture energy concept case in terms of stress and strain, Equation 3.3 may be written as;

$$G_f^c = h \int \sigma \, d\varepsilon_i = L_p \int \sigma \, d\varepsilon_i \qquad\qquad 3.4$$

where ε_i indicates inelastic strain and L_p is the plastic hinge length.

The regularization in their study is applied to the Kent and Park (1971) law used for the

concrete fibers of the fiber cross-section. The pre-peak behavior is given by a parabola, followed by a linear post-peak softening branch until a stress of 20% f'_c is reached at a prescribed strain labeled ε_{20}. The value of ε_{20} must be calibrated to maintain a constant energy release. Assuming that G^c_f is known for unconfined concrete, leads to the following expression:

$$\varepsilon_{20} = \frac{G^c_f}{0.6f'_c L_p} - \frac{0.8f'_c}{E} + \varepsilon_0 \qquad\qquad 3.5$$

where E is Young's modulus and ε_0 is the strain corresponding to peak stress of concrete under compression. Plugging in values of G^c_f equal to 20 N/mm for unconfined concrete, f'_c equal to 43 MPa, L_p to be 40 cm, E to be 30820 MPa, and, ε_0 equal to 0.0023, Equation 5 results in an ε_{20} value of 0.0052 and a ε_0 value of 0.0058. These parameters representing the Coleman and Spacone approach (2001) are plotted with a red dashed line in Figure 1.23.
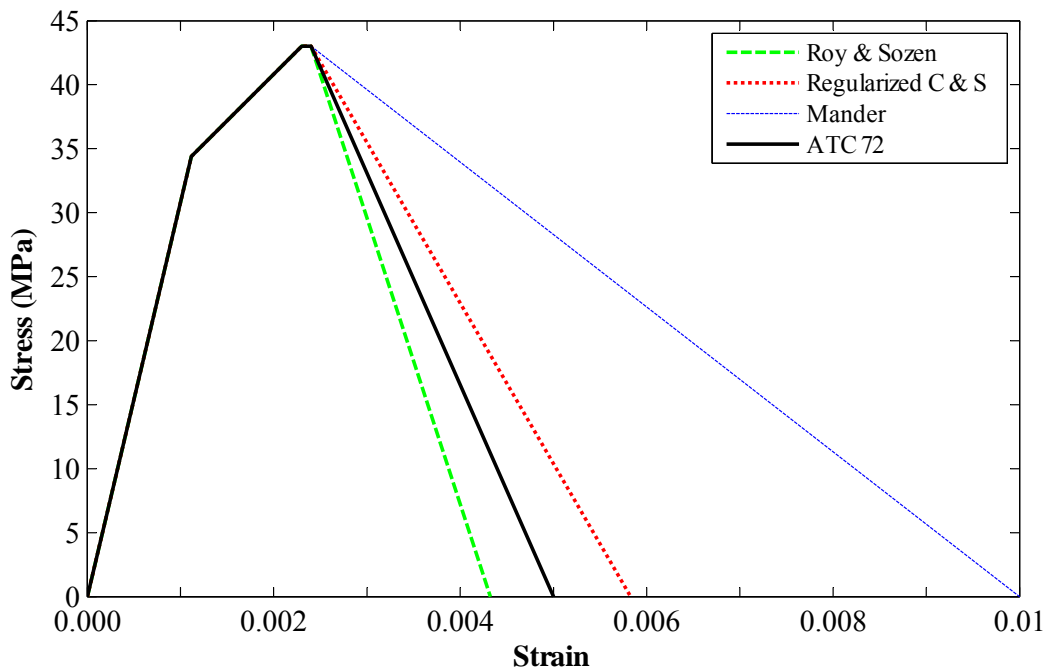
Figure 3.48 - Concrete stress-strain relationships for the sensitivity study (Note: 1 MPa = 145 psi)

Figure 3.49 shows the comparison of the calculated relations between base shear and roof drift for east loading direction of models with different concrete stress-strain relationships. The calculated results of the analysis are plotted with the same line colors with the material models plotted in Figure 3.48. The green line represents the model with concrete stress-strain relationship using Roy and Sozen (1965), the black line represents the model with concrete

85

stress-strain relationship by PEER/ATC-72-1, red line represents the model with concrete stress-strain relationship regularized by Coleman and Spacone (2001), and the blue line represents the model with concrete stress-strain relationship using Mander et al (1988). In Figure 3.49 the black line with the PEER/ATC-72-1 material model is the same curve previously shown in Figure 3.35. As expected, there is no difference in the overall stiffness of the responses in either case. Differences in results are observed after the roof drift ratio of 0.7%. It should be noted that the order of failures observed didn't change with a change of the concrete material model. However, the drift capacity of the different models is notably dependent of the concrete ultimate strain value (ε_u). This is not surprising considering the failure mode of the Alto Rio in this direction is controlled by concrete crushing.
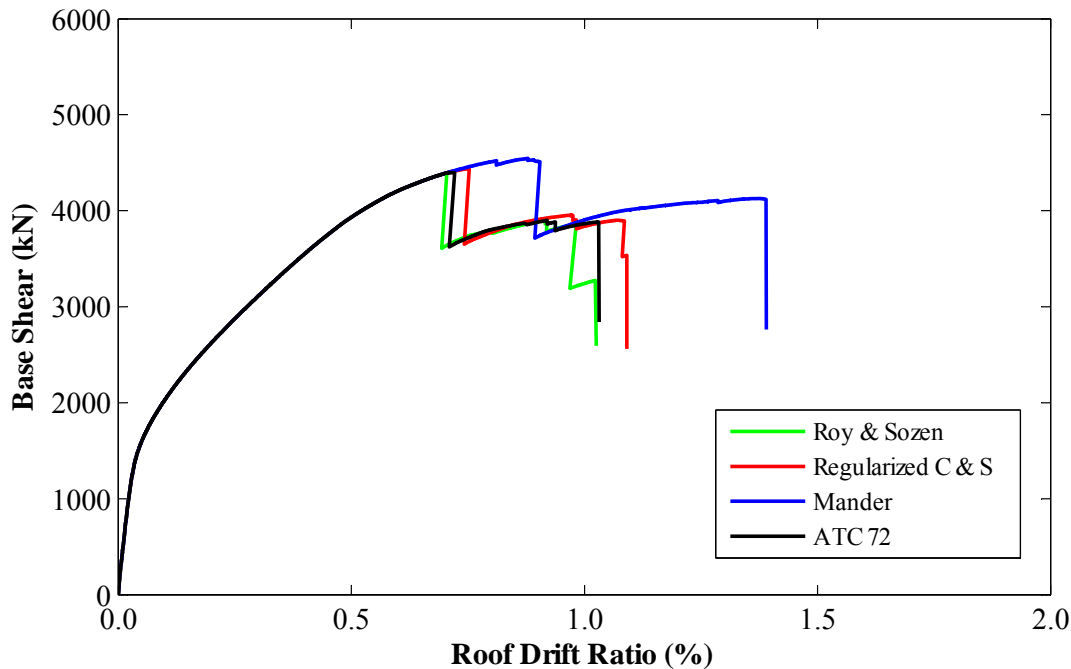
Figure 3.49 - Comparison base shear – drift relationship of nonlinear static analysis for different concrete stress-strain models (loading to the east) (Note: 1 kN = 0.2248 kips)

For all of the different concrete material models considered, crushing of east side of wall 13 happens first, followed by crushing of the east side of the wall 8. The crushing of the east side of wall 13 happens at 0.7% drift ratio for Roy and Sozen (1965), 0.72% for PEER/ATC-72-1, 0.75% for regularized Coleman and Spacone (2001) and 0.9% for Mander et al (1988). Similar order is seen for the crushing of the east side of wall 8, which happens at 0.98% for Roy and Sozen (1965), 1.0% for PEER/ATC-72-1, 1.1% for regularized Coleman and Spacone (2001), and 1.4% for Mander et al (1988). The trend shows that the higher value of the ultimate concrete compressive strain (ε_u) assigned for the model, the higher drift capacity is observed in the analysis. It seems like the analysis results are sensitive to the assumptions of the material level stress-strain relationships, in this case for concrete under compressive loading. However, for values of concrete ultimate strain in accordance with Roy and Sozen (1965), PEER/ATC-72-1, and regularized Coleman and Spacone (2001), the model predicts the first strength degradation at

a small interval of 0.7 to 0.75% roof drift ratio.

Figure 3.50 shows the comparison of the calculated relations between base shear and roof drift for the west loading direction of models with different concrete stress-strain relationships. The calculated results of the analysis are plotted with the same line colors with the material models plotted in Figure 3.48 and Figure 3.49. For lateral load to the west, the first significant event is failure of the longitudinal reinforcement at the east side if the east walls along Axis 13 at 1.55% for Roy and Sozen (1965), 1.60% for PEER/ATC-72-1, 1.65% for regularized Coleman and Spacone (2001), and 1.97% for Mander et al (1988). The trend shows that the higher value of the ultimate concrete compressive strain (ε_u) assigned for the model, the higher drift capacity is observed in the analysis. This is unexpected since the controlling failure mechanism in this direction of loading is tensile failure of reinforcement rather than the concrete crushing. It seems that the analysis results are sensitive to the assumptions of the material level stress-strain relationships, in this case for concrete under compressive loading. However, for values of concrete ultimate strain in accordance with Roy and Sozen (1965), PEER/ATC-72-1, and regularized Coleman and Spacone (2001), the model predicts the first strength degradation at a small interval of 1.55 to 1.65% roof drift ratio.
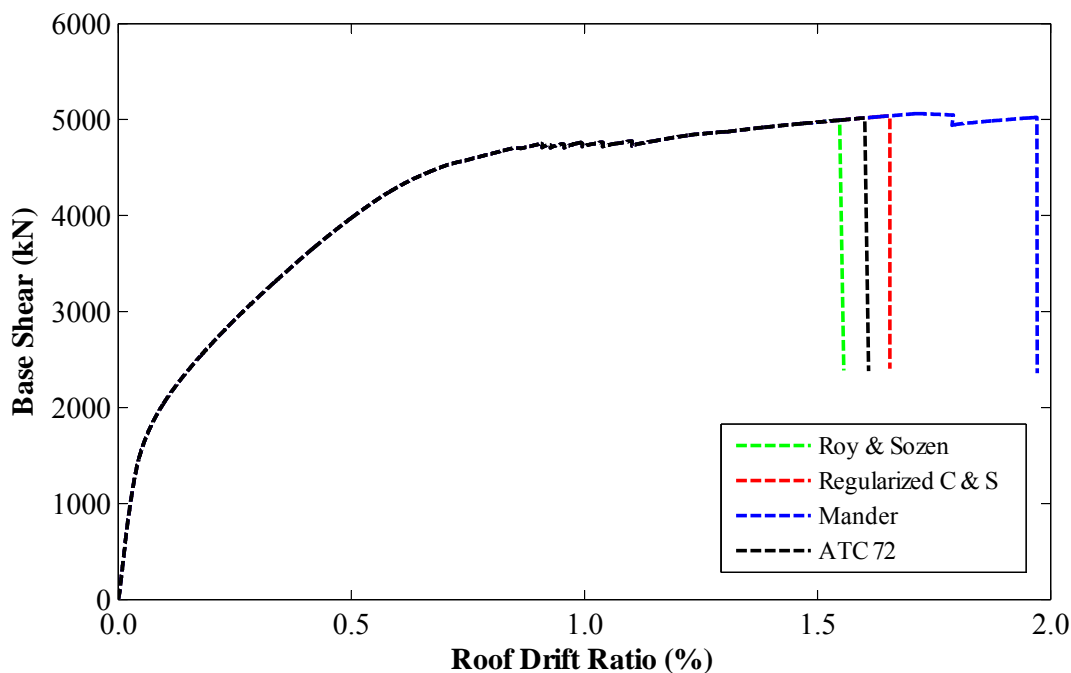
Figure 3.50 - Comparison base shear – drift relationship of nonlinear static analysis for different concrete stress-strain models (loading to the west)

Results of this sensitivity study conclude that the material level stress-strain curve has an important effect of the overall behavior of the numerical model. Therefore, practicing engineers should be cautious for the selection of element size and material stress-strain relationships for possible effects on model behavior. The approach of Coleman and Spacone (2001) is recommended for addressing this issue.

3.13 Effect of Lap Splices to the Modeling and the Response

The provided lap splice lengths in design of the Alto Rio building exceed the required lengths of ACI 318-95. Thus, the analytical models reported previously assumed that the lap splices were adequate and did not require modeling. However, a recent study done by Hardisty et al. (2014) showed that behavior of lap splice in unconfined structural walls cannot be ignored, especially in the plastic hinge regions.

Hardisty et al. (2014) studied six beams with unconfined lap splices and reinforcement layouts similar to the detailing of the Alto Rio building. The test setup simulated the nearly constant-moment region of the lap splices at boundary elements of the Alto Rio building (Figure 3.51). The study also tested two structural walls with similar detailing, which had large moment gradients. It was concluded that boundary elements in constant-moment regions may fail in bond while similar boundary elements subject to large moment gradients may be adequate. They also observed that results from test of scaled structural walls with large-scale lap splices couldn't always be projected directly to full-scale walls. Therefore, the test results of beams with unconfined lap splices in Hardisty et al. (2014) could be used as a guide to understand the behavior of the lap splices of the Alto Rio building.

Figure 3.52, Figure 3.53, and Figure 3.54 show the cross-sections and stirrup details of the beams tested by Hardisty et al. (2014). Four #8 ($\phi 25$ in SI units) longitudinal reinforcing bars were spliced at the top of the beam. Similarly sized $\phi 22$ and $\phi 25$ bars were lap spliced at the boundary elements of the Alto Rio building. The spacing and cover of longitudinal reinforcement of the test beams is also similar to that used in the Alto Rio walls. In Hardisty et al. (2014), #3 ($\phi 9$) stirrups had spacing of $5d_b$, $8d_b$ and $11d_b$, which compares with $\phi 8$ stirrups with 20 cm spacing used in the Alto Rio building.

The lap splice length in all of the beam tests was $60d_b$. In Alto Rio, for $\phi 22$ mm and $\phi 25$ bars, lap splice lengths of 125 cm (49 in) ($57d_b$) and 140 cm (55 in) ($56d_b$) are called out in the design. The length required by ACI 318-11 equation 12-1 for a Class B lap splice (all the bars spliced at the same level) developing specified yield stress is $43d_b$. According to ACI 318-11 21.9.2.3, regions of special structural walls that are expected to yield are required to have development lengths of longitudinal reinforcement at least 1.25 times the values calculated for f_y in tension, or a lap splice length of $54d_b$. Therefore, lap splice lengths in both Alto Rio building and the tested beams meet requirements of ACI 318.
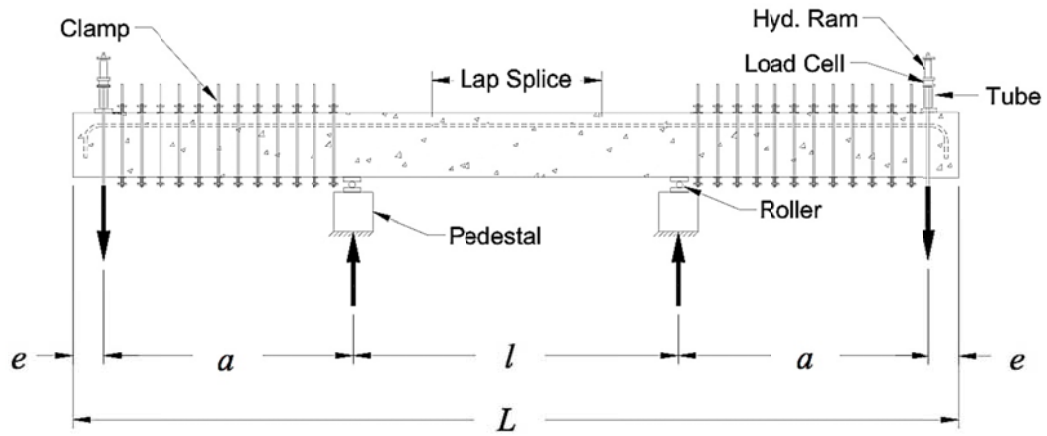
Figure 3.51 - Test setup of Hardisty et al. (2014)
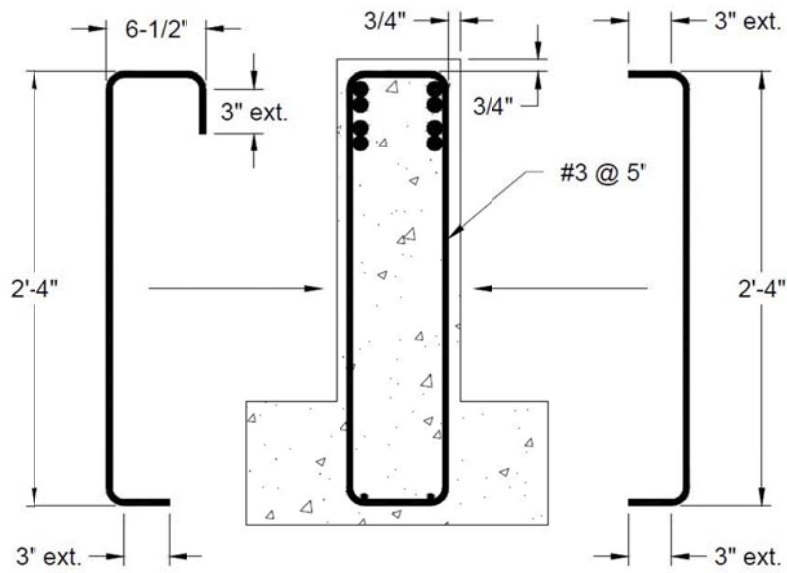
Figure 3.52 - Type-I stirrups (beams T-60-8-B and E) of Hardisty et al. (2014) (1 in = 2.54 cm)
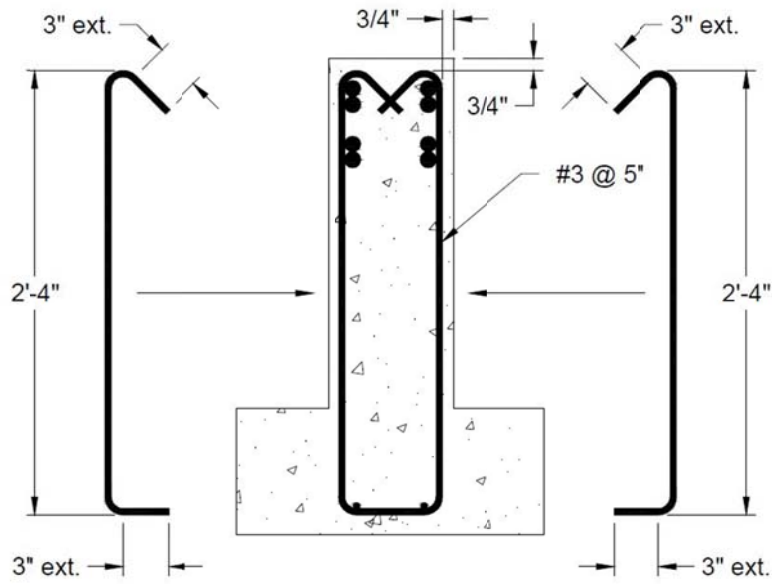
Figure 3.53 - Type-II stirrups (beams T-60-8-A) of Hardisty et al. (2014) (1 in = 2.54 cm)
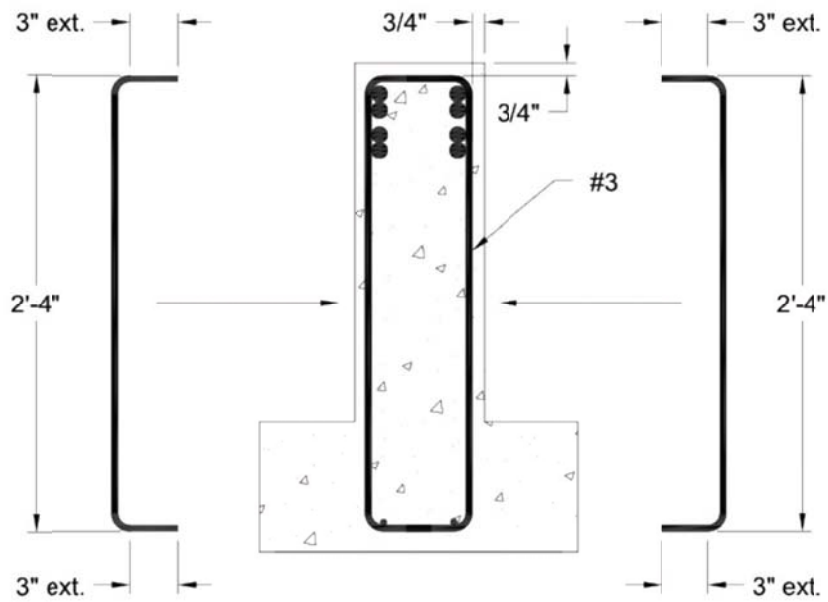
Figure 3.54 - Type-III stirrups (beams T-60-8-D and F) of Hardisty et al. (2014) (1 in = 2.54 cm)

Table 3.3 - Results of Hardisty et al. (2014)

Designation	R	V_1 kip (kN)	V_2 kip (kN)	V_3 kip (kN)	V_u kip (kN)	Δ_u in. (cm)	Δ_y in. (cm)	Δ_u/Δ_y	Δ_u/L_{CL} %	Δ_y/L_{CL} %
T-60-8-A	15	55.0 (244.7)	57.0 (253.5)	59.0 (262.4)	59.4 (264.2)	0.78 (1.98)	0.20 (0.51)	3.9	1.30	0.33
T-60-8-B	4	56.5 (251.3)	- -	- -	56.7 (252.2)	0.33 (0.84)	0.21 (0.53)	1.6	0.55	0.35
T-60-8-C[1]	0	- -	- -	- -	42.2 (187.7)	0.17 (0.43)	- -	-	0.28	-
T-60-8-D	12	56.0 (249.1)	65.0 (239.1)	-	64.8 (288.2)	0.58 (1.47)	0.26 (0.66)	2.2	0.97	0.43
T-60-8-E	17	58.0 (258.0)	66.0 (293.6)	-	66.1 (294.0)	0.62 (1.57)	0.28 (0.71)	2.2	1.03	0.47
T-60-8-F	12	58.0 (258.0)	65.0 (239.1)	-	64.8 (288.2)	0.56 (1.42)	0.29 (0.74)	1.9	0.93	0.48

[1]: Specimen did not reach yield

Table 3.3 shows the test results of the six beams reported Hardisty et al. (2014). It is noteworthy that, with similar longitudinal reinforcement bar diameter, number and spacing, and different stirrup detailing and spacing, the ratio of Δ_u/Δ_y are staying around the value of 2.0 for all cases. Here Δ_u refers to the ultimate displacement at the midspan of the tested beam, and Δ_y refers to the midspan displacement at the yield strength. It is also reasonable to assume that, in the case of a tension controlled beam (like the tested ones), the ratio of Δ_u/Δ_y is directly proportional to the ratio of the ultimate strain (ε_u) to the yield strain (ε_y) of the reinforcing steel. Thus, it would be reasonable to deduce that the strain capacity of the reinforcement was approximately twice the yield strain at the onset of splice failure.

In light of the results of Hardisty et al. (2014), the Perform 3D model was modified to account for the possible effects of lap splice failure on building collapse. Figure 3.55 shows the assumed stress-strain relationships of reinforcing bars with and without the consideration of lap splices. The modification done was the change in the ultimate strain (ε_u) value in the tension loading side. Results of Hardisty et al. (2014) suggested that a value of $2\varepsilon_y$ would be a good approximation for the ultimate strain (ε_u) capacity of unconfined lap splices under cyclic loading. The modified stress-strain relationship is show in red dashed line in Figure 3.55.

Figure 3.56 shows calculated relations between base shear and roof displacement for east and west loading directions of the model with modified reinforcing steel stress-strain relationships for spliced reinforcing bars. Figure 3.56 also shows the base shear and roof displacement relationship for the model without accounting for the effects of lap splices. For loading the model to the east, the direction in which collapse occurred, similar to the previous model, crushing of the wall boundary at the east edge of the east wall along axis 13 at around 0.72% roof drift ratio, followed by similar crushing of the east part of wall 8 at around 1% roof

drift ratio. However, there is relatively higher strength degradation after the crushing of the wall along axis 13. It can be seen that, even though the crushing of the wall on axis 8 is at the same displacement, overall strength of the building at 1% roof drift ratio is lower than the model not accounting for lap splice effects.

For lateral load to the west, unlike the previous results, the first significant event is the failure of shear panel on the Axis 13 at 0.62% roof drift ratio. It is followed by the failure of the longitudinal reinforcement lap splices at the east side of the east walls along Axis 13 at 0.82% roof drift ratio. This shows that the modifications done to account for lap splice affects the tension-controlled failure dramatically, decreasing the drift capacity of the building to half of the previous model. It is noteworthy that crushing failure is still not calculated to occur for loading in this direction, similar to the previous model. This conclusion about crushing failure is based on the assumption that the boundary is not previously damaged by some other action such as the lap splice failure.
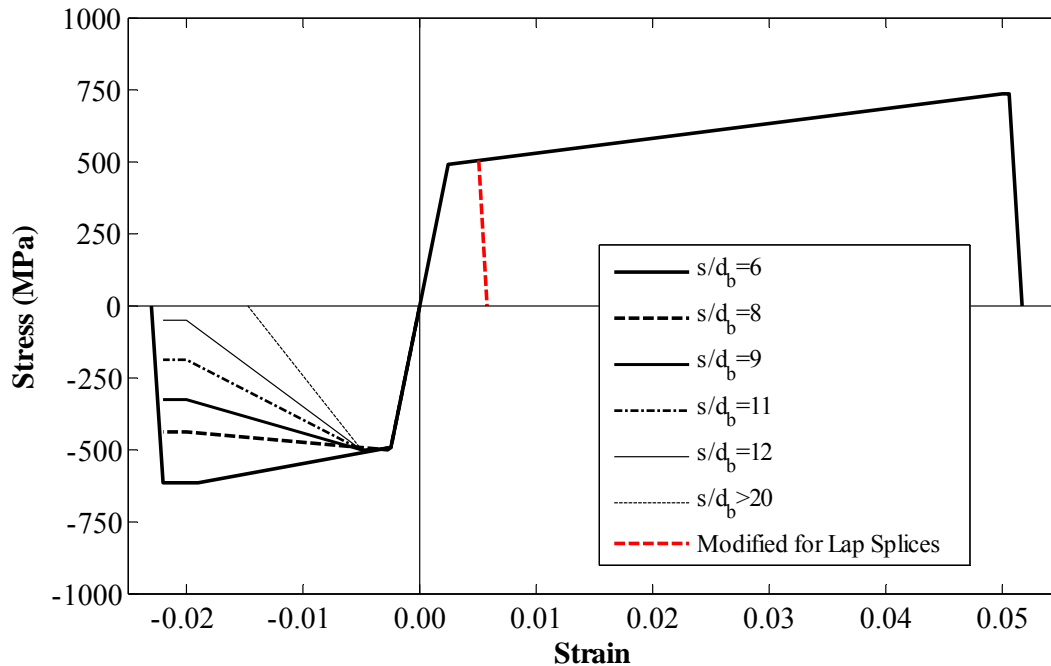
Figure 3.55 - Reinforcing steel stress-strain relation with modifications for lap splices (positive values are tensile) (Note: 1 MPa = 145 psi)

92
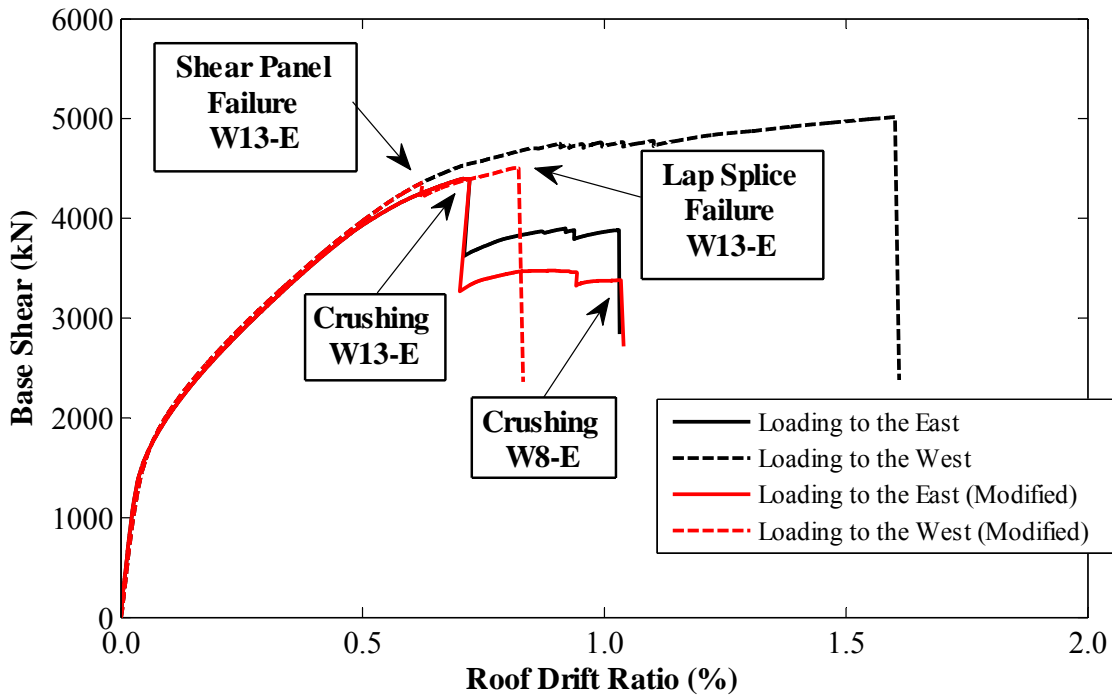
Figure 3.56 - Base shear – drift relationship of nonlinear static analysis with modifications for lap splices (Note: 1 kN = 0.2248 kips)

Similar to the previous analysis, a second single-degree-of-freedom (SDOF) model was established to represent the effective first translational mode response of the Alto Rio building in the transverse direction, accounting for the lap splice effects. The SDOF model was implemented in Perform3D with a nonlinear rotational spring at the base, a massless rigid bar, and a mass at the top, using a procedure similar to the previous model. Parameters of the simplified trilinear moment-rotation relation of the modified SDOF were adjusted to approximate the relation obtained with the scaled nonlinear static analysis, as shown in Figure 3.57. The SDOF model was excited with the east-west direction of the ground motions recorded at Colegio Inmaculada Concepción site.
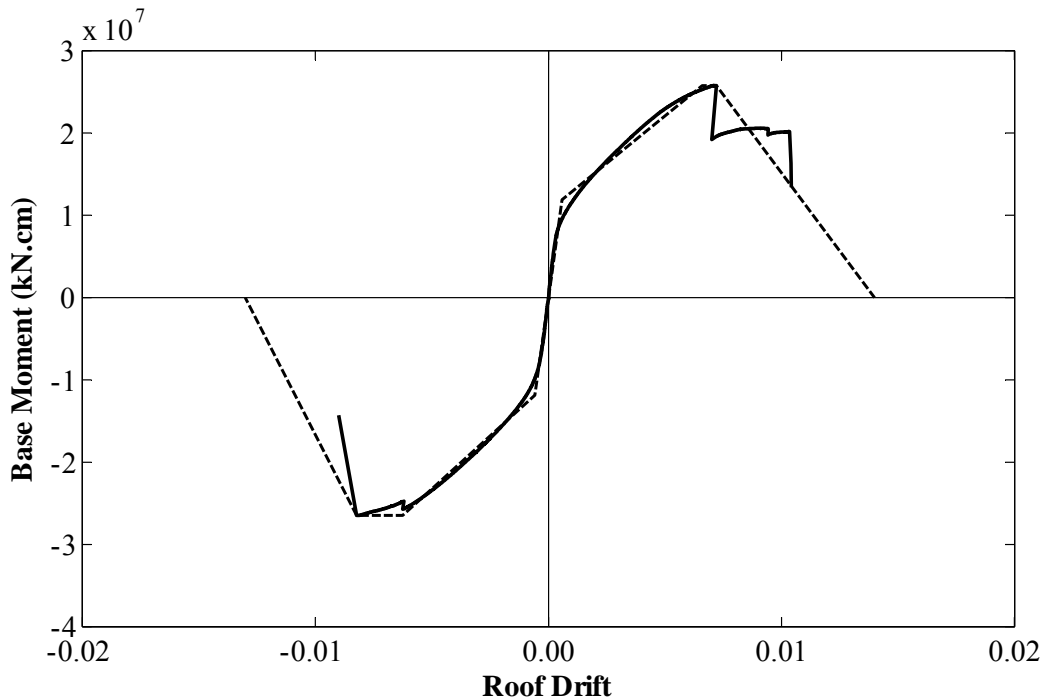
Figure 3.57 - Comparison of moment-rotation relations for the modified SDOF model and the scaled nonlinear static analysis (Note: 1 kN.m = 0.7375 kip.ft)

Calculated moment-drift relations and displacement response histories of the modified SDOF model subjected to the Concepción motion are plotted in Figure 3.58, Figure 3.59, and Figure 3.60. It is worth noting that after a deformation cycle as large as 1.2% roof drift ratio in the west direction, the SDOF model collapses to the east (collapse) direction at around 22 seconds of the excitation. First significant event of the structure response under dynamic analysis is the damage at the shear panel on the Axis 13 in a cycle to the west around 15 seconds. In the cycle to the east at around 20 seconds, concrete crushes under compression for both walls on Axes 13 and 8, respectively. Right after that the loading cycle changes direction to the west and causes the failure of the lap splices on the east side of the east wall on Axis 13 at around 21 seconds. It is followed by a large cycle to the east direction around 22 seconds, where structure permanently displaced to the east. This permanent displacement of the model is also an indicator of the collapse to the east direction.

Figure 3.60 compares the displacement response histories of the original and SDOF model modified for the lap splice effects. The results of the dynamic analysis of the modified SDOF system are very close to the analysis of the original model. The final result of the dynamic SDOF analysis is consistent with the observed damage and collapse of the building. This suggests that although the possible effects of the lap splices can change the nonlinear static analysis results of the Alto Rio building, it neither had a dramatic effect on the dynamic SDOF analysis, nor changed the mode of collapse.

94
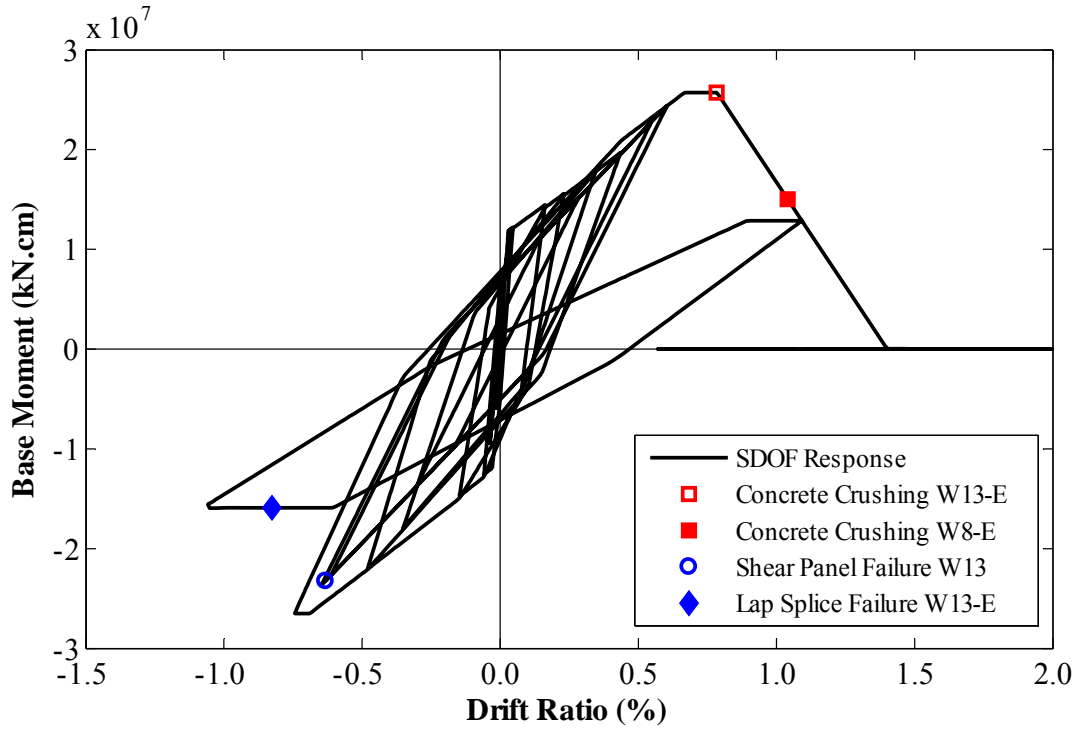
Figure 3.58 - Moment–drift ratio response of the modified SDOF model under the Concepción ground motion (Note: 1 kN.m = 0.7375 kip.ft)
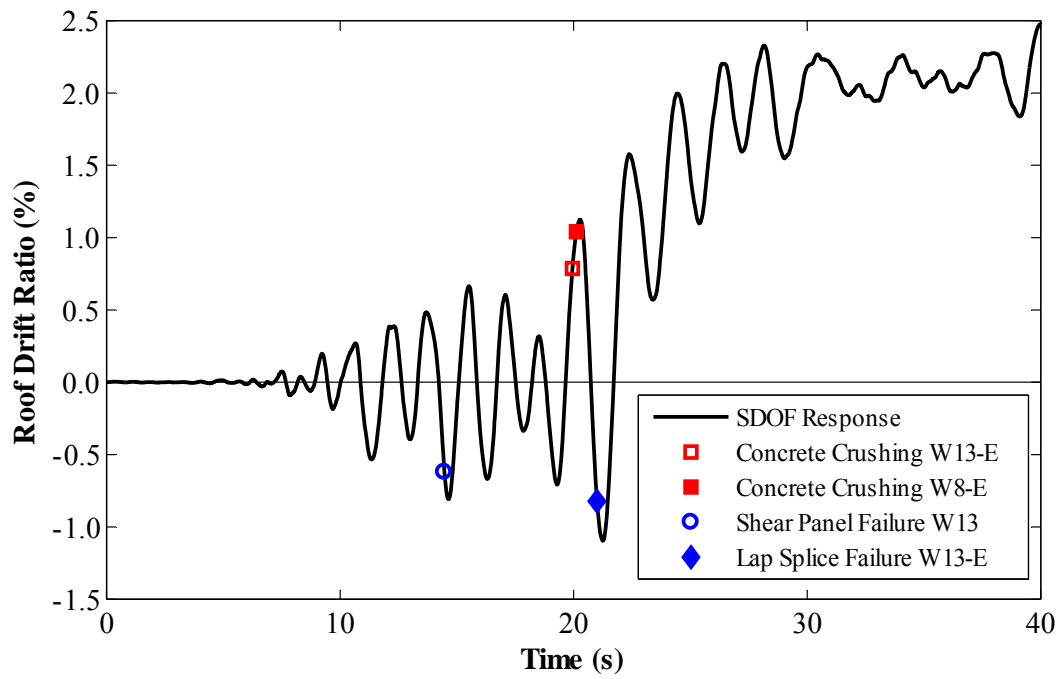
Figure 3.59 - Roof drift ratio response history of the modified SDOF model subjected to the Concepción ground motion

95
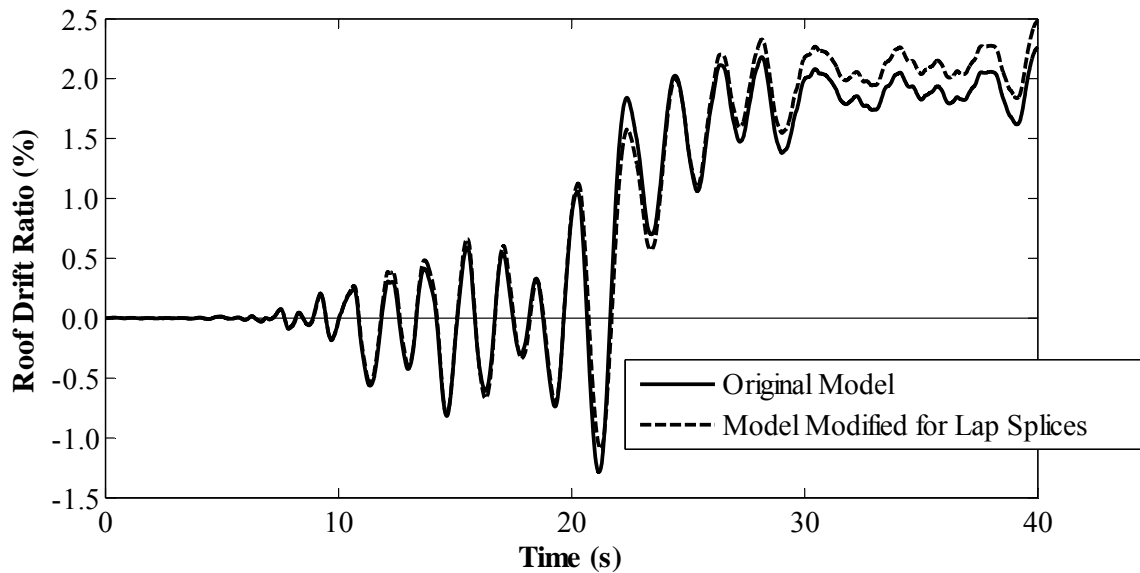
Figure 3.60 - Roof drift ratio response history of the modified SDOF model subjected to the Concepción ground motion

The nonlinear static and dynamic SDOF analysis results demonstrate that the Alto Rio building was susceptible to collapse to the east direction. The main factors contributing to the failure include: the configuration of T and L-shaped wall cross sections, vertical discontinuities at the east side of the building, and high shear stresses in the solid wall panels below the stack of openings. The structural drawings and reconnaissance data suggest that the absence of confined boundary elements and the occurrence of lap splices of longitudinal bars without sufficient transverse reinforcement could be other factors that contributed to the collapse. However, the analysis of models modified according to the behavior of lap splices showed that lap splices have a very minor effect on the overall behavior of the building under this specific earthquake motion. The specific analyses reported in this paper indicate one plausible failure sequence, that is, initiation of shear damage in the solid wall panel immediately below the stack of openings, crushing and buckling failure of the walls at the discontinuity between the first and second stories on the east side of the building, and subsequent failure of the tension chord on the west side of the building as it collapsed toward the east. Other failure sequences are also plausible, depending on details of the ground motion and structural model, but these were not indicated by the present study. Observed damage after the earthquake (IDIEM, 2010) is consistent with the findings of the analysis results.

Figure 3.61 and Figure 3.62 show the deformation concentrations of the Perform 3D model modified according to the behavior of lap splices under the loading to the east at 0.75% roof drift ratio. These figures represent the deformations at specific elements right after the "Concrete Crushing of W13-E". The wall on the right side (wall on Axis 13) of the figure had localized deformations at the top of the first floor due to the compression failure. This damage state is very similar to the damage state presented in Figure 3.38 for the model ignoring lap splices. The effect of lap splices for this deformation state is negligible.

96

Similarly, Figure 3.63 and Figure 3.64 show the deformation concentrations of the Perform 3D model modified according to the behavior of lap splices under the loading to the east at 1.1% roof drift ratio. These figures represent the deformations at specific elements right after the "Concrete Crushing of W8-E". It is worth noting that the wall on Axis 8 (the wall on the left) also experienced the concentrated compression failure right below the setbacks at the top of the first floor. Similar to the previous damage state, this damage state is very similar to the damage state presented in Figure 3.39 for the model ignoring lap splices. The effect of lap splices for this deformation state is also negligible.

Figure 3.65 and Figure 3.66 show the deformation concentrations of Perform 3D model modified according to the behavior of lap splices under the loading to the west at 0.86% roof drift ratio. This deformation corresponds to the "Lap Splice Failure of W13-E". The damage concentrated at the bottom of the first floor level wall on Axis 13 (the wall on the right) can be seen. Similar damage is also seen at the bottom of the first floor level of the wall on Axis 8 (the wall on the left side). For this failure mode, the lap splices actually shortened the deformation capacity of the whole model. The deformations of this failure mode is very concentrated when compared to another tensile (however rather ductile) failure mode shown in Figure 3.42. For this mode of damage, the change in lap splice behavior affects the response and deformation concentrations in the model dramatically.
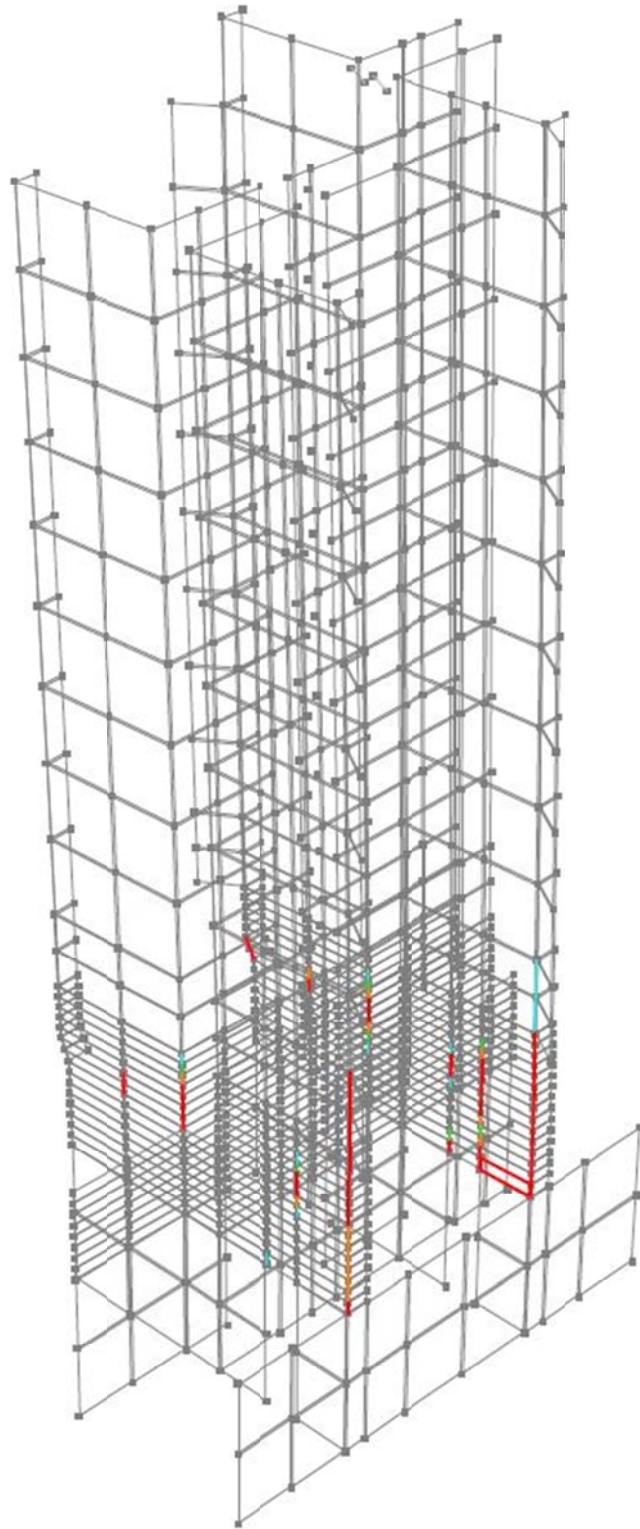
Figure 3.61 - Deformation concentrations of the modified Perform 3D model under loading to the east at roof drift of 0.75% after "Concrete Crushing W13-E"
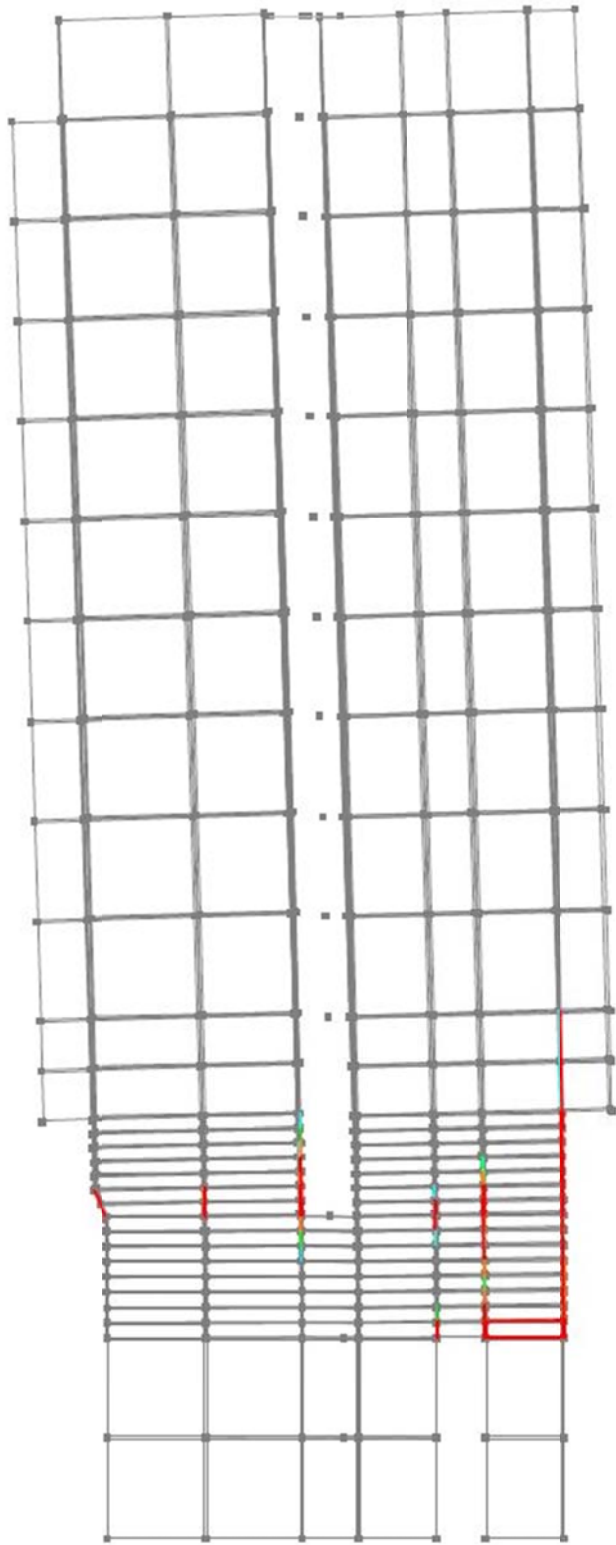
Figure 3.62 - Deformation concentrations of the modified Perform 3D model under loading to the east at roof drift of 0.75% after "Concrete Crushing W13-E"
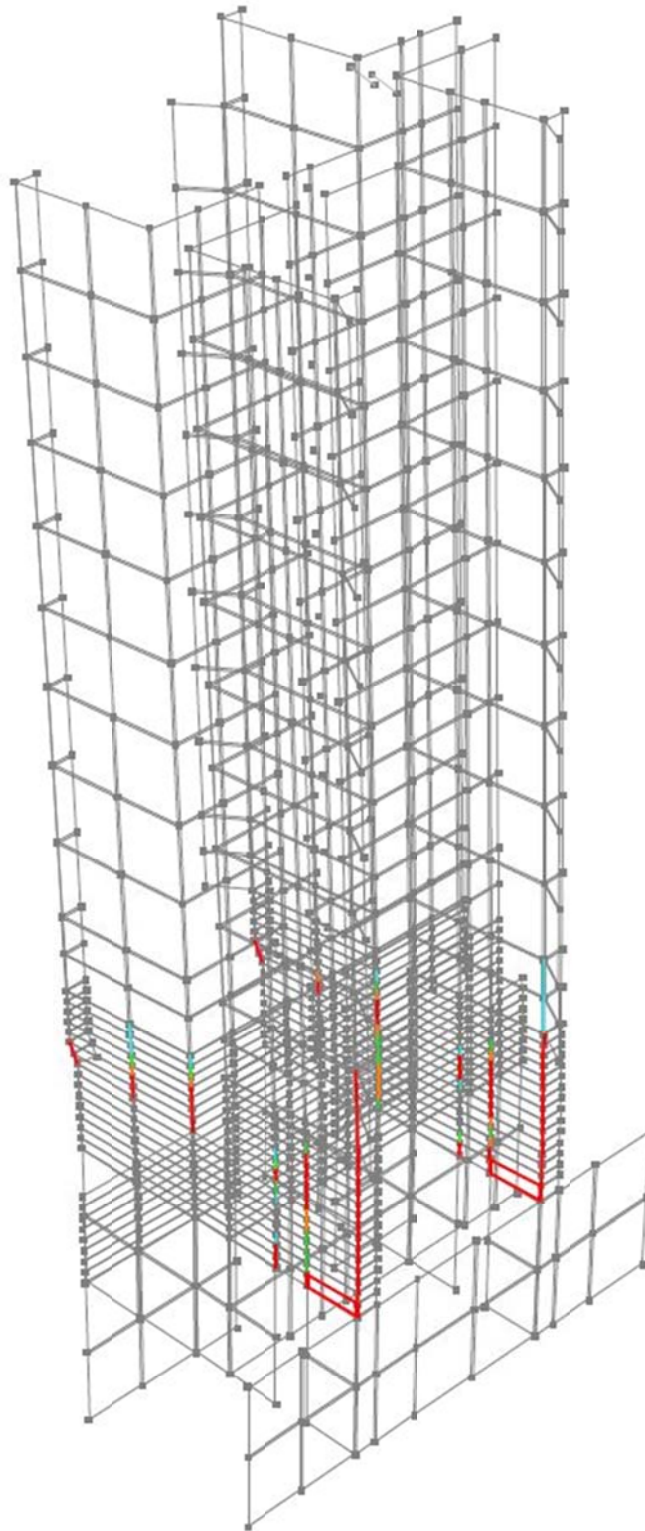
Figure 3.63 - Deformation concentrations of the modified Perform 3D model under loading to the east at roof drift of 1.1% after "Concrete Crushing W8-E"
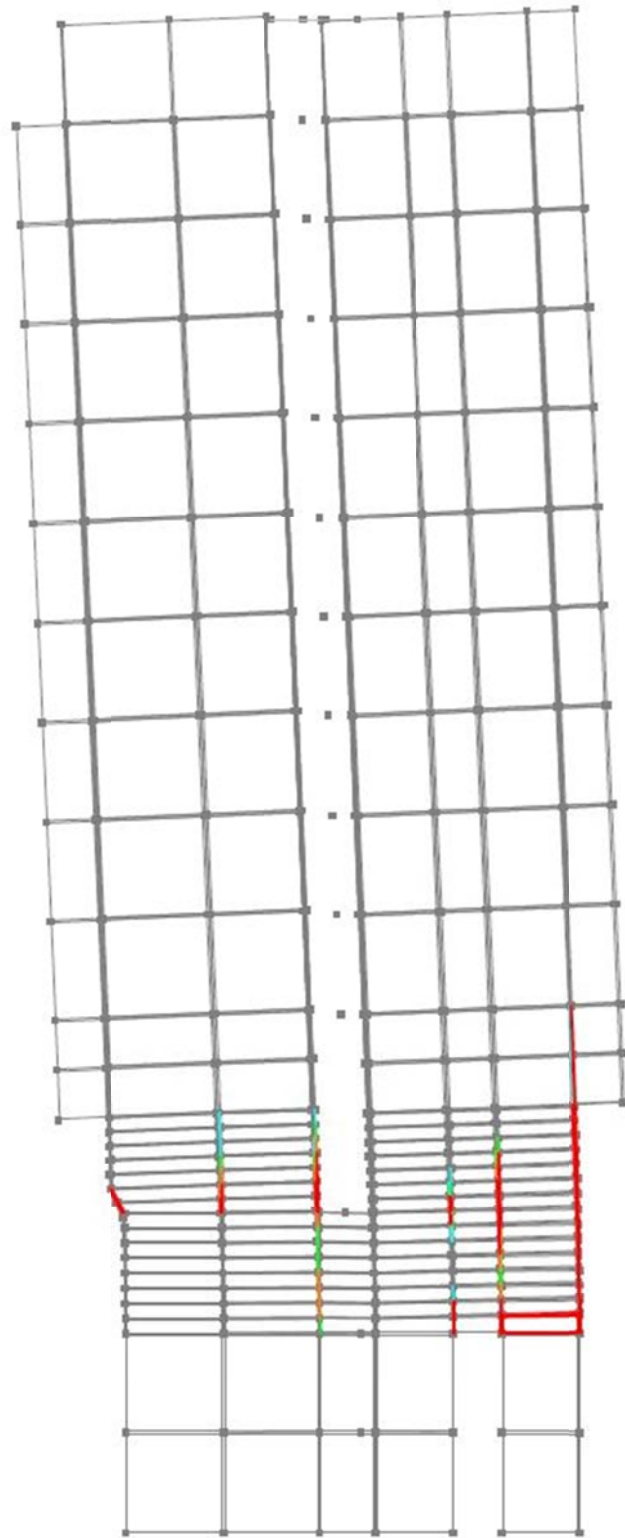
Figure 3.64 - Deformation concentrations of the modified Perform 3D model under loading to the east at roof drift of 1.1% after "Concrete Crushing W8-E"

101
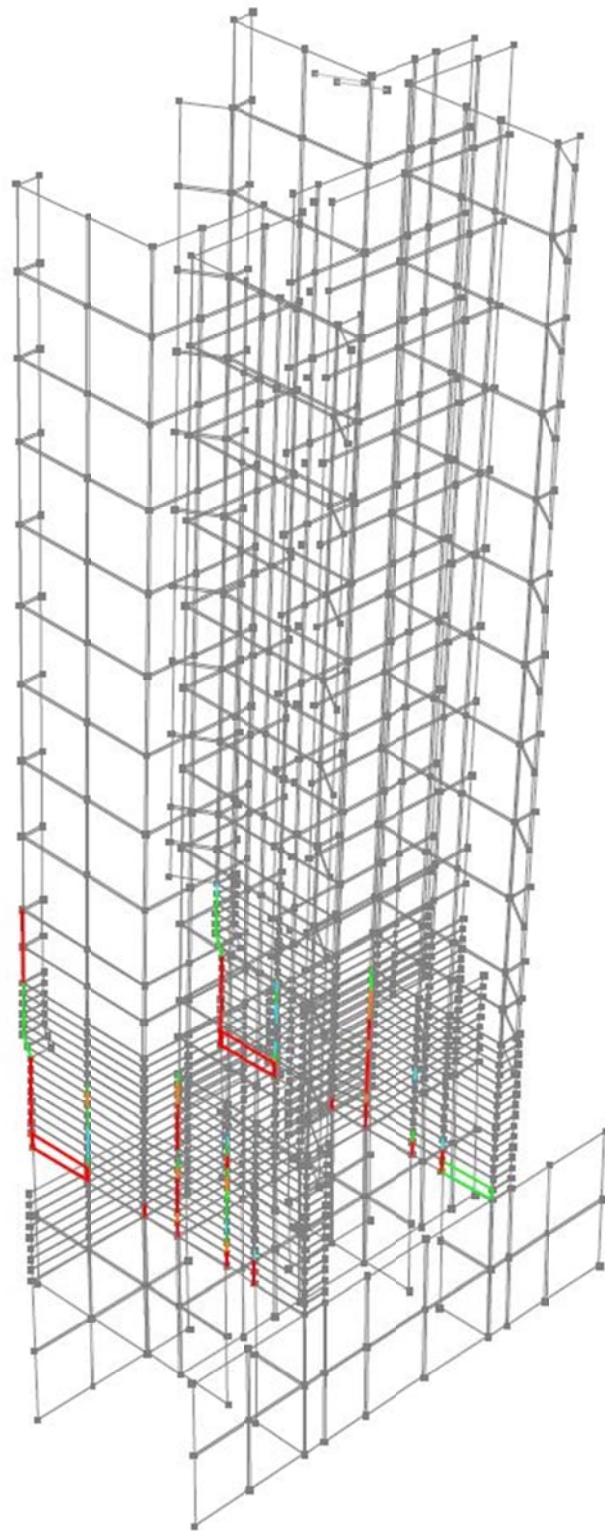
Figure 3.65 - Deformation concentrations of the modified Perform 3D model under loading to the west at roof drift of 0.86% after "Lap Splice Failure W13-E"

102
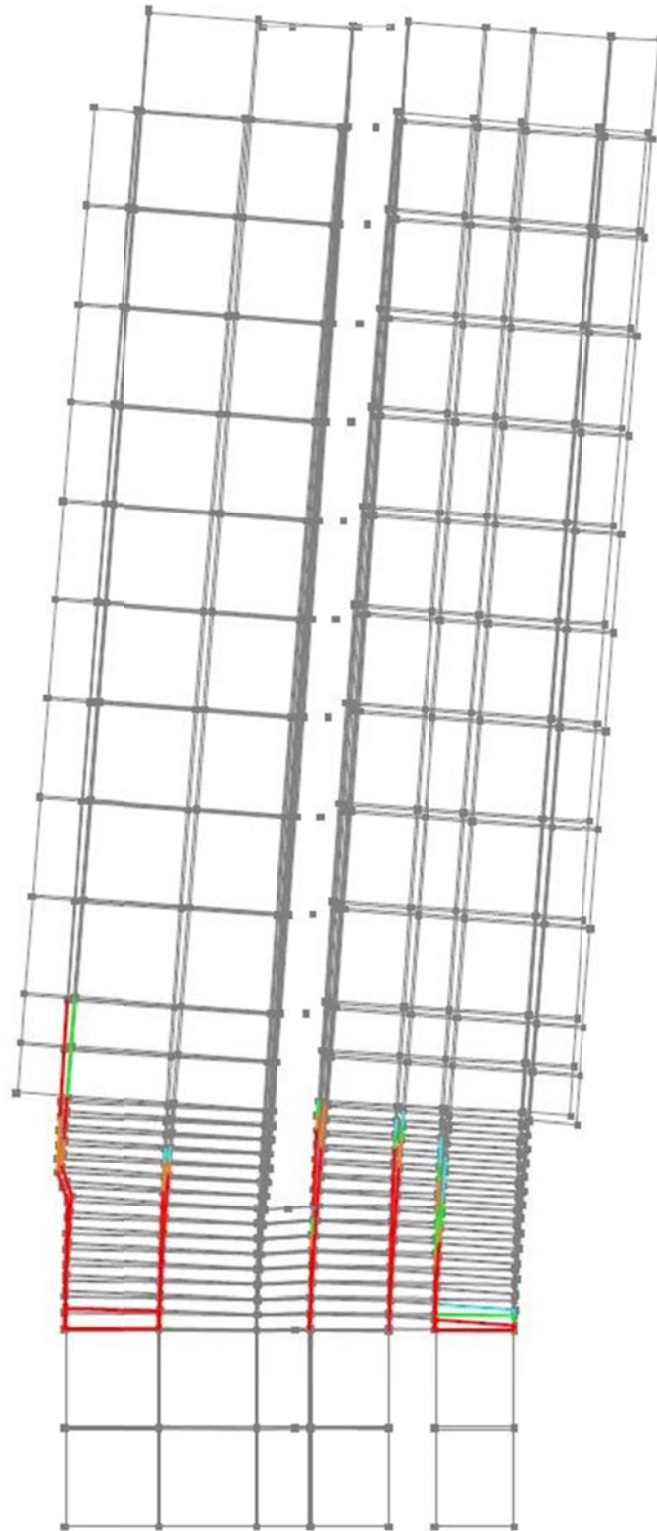
Figure 3.66 - Deformation concentrations of the modified Perform 3D model under loading to the west at roof drift of 0.86% after "Lap Splice Failure W13-E"

3.14 Investigation of Lateral Buckling of Reinforced Concrete Walls on the Response

Lateral buckling of walls is the overall lateral instability of the concrete wall section over a portion of wall height. Lateral buckling of walls or wall-like elements has been observed in several laboratory tests, including Chai and Elayer (1999), Thomsen and Wallace (2004), Paulay and Priestley (1993), and Corley, W.G., A.E. Fiorato, and R.G. Oesterle (1981). Recently, lateral (overall) buckling of reinforced concrete walls are also observed following 2010 Maule (Chile) earthquake and 2011 Christchurch (New Zealand) earthquake. Figure 3.67 shows the Alto Huerto building, one of the buildings that experienced lateral wall buckling after the 2010 Chile earthquake.

Slenderness of the concrete walls is one of the major factors of wall buckling. Design practice globally has resulted in more slender walls. In the case of Chile, it has been common to find rectangular wall sections having a thickness of 6 to 8 inches (150mm to 200mm), and floor-to-floor slenderness ratios (h_u/b) of 16 or greater, where h_u is the clear story height and b is the wall thickness. This increase in the slenderness ratio can make walls more susceptible to buckling. There are two hypotheses for the lateral wall buckling. One of these hypotheses (Paulay and Priestley, 1993; Chai and Elayer, 1999) is that the tensile yielding for loading in one direction softens the boundary for the subsequent loading cycle in the opposite direction, causing the lateral instability of the wall in compression. Although the lateral buckling of the wall is under the compression cycle, it is strongly influenced by the prior tensile strains in the opposite loading direction. Another hypothesis (ATC 94 report) is that the wall crushes under the compression cycle, making the cross-section smaller and irregular. The smaller cross-section becomes vulnerable to lateral buckling under the same or subsequent compression cycles.

(a) Elevation view   (b) Lateral wall buckling along Axis Ñ

Figure 3.67 – Alto Huerto building
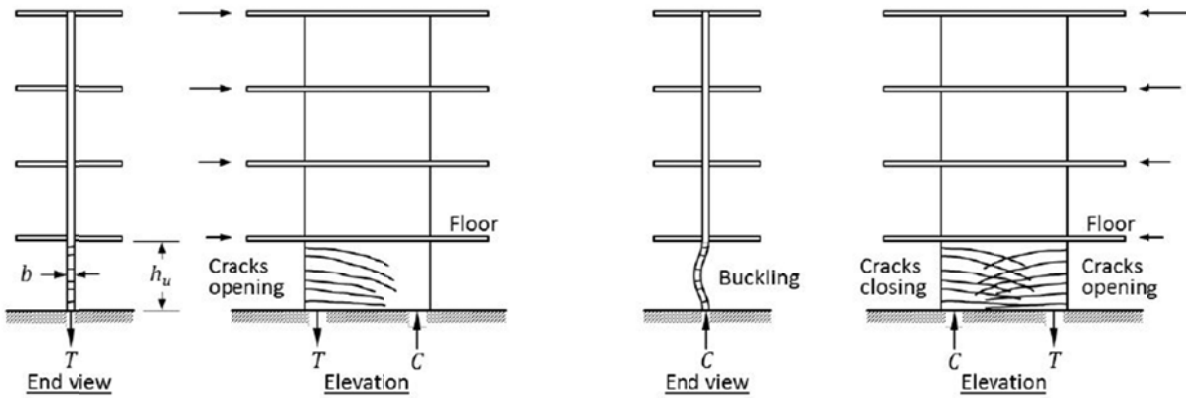
(a) Crack opening under tension cycle   (b) Closing cracks under compression cycle

Figure 3.68 – Lateral instability of wall boundary previously yielded in tension (after Chai and Elayer, 1999; and Parra and Moehle, 2014)

Parra and Moehle (2014) presents a theory for buckling of walls subjected to inelastic tension and compression strain cycles for a multistory wall shown in Figure 3.68 and Figure 3.69. The foundation and floor diaphragms provide lateral support at each level. Therefore, the clear story height h_u is chosen for the unsupported height of the wall boundary. An effective length of kh_u is defined based on the rotational restraint at each floor level. For slender walls (like Alto Rio building) with rotational restraint from the floor system at the top and bottom of the unsupported length, k can be approximated as 0.5 (fixed-fixed condition).
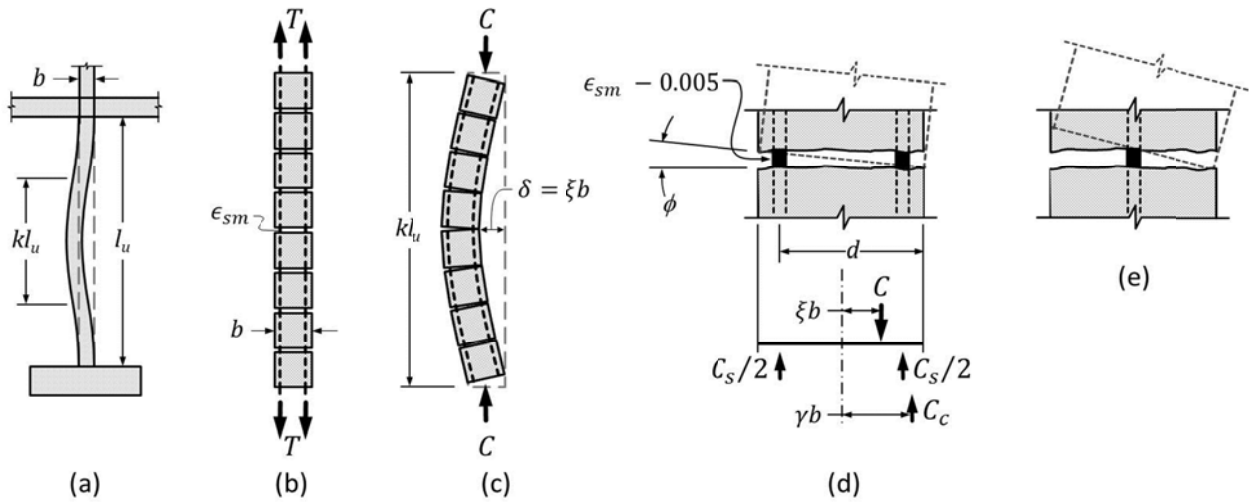
Figure 3.69 – Lateral instability of wall boundary previously yielded in tension (after Moehle, 2014)

Consistent with the work of Paulay and Priestley (1993), Parra and Moehle (2014) assumes that under alternating tension and compression cycles in an earthquake, the crack widths caused by the boundary element yielding in tension is dependent on the value of the longitudinal reinforcement tensile strain in the previous cycle, ε_{sm}. In case of a wall yielded in tension, closure of cracks may cause yielding of reinforcement in compression. Parra and Moehle (2014) suggests that any asymmetry in the reinforcement in a wall with two curtains of reinforcement will result in one curtain yield before the other, and lead to an out-of-plane curvature. In the case of a structural wall with single curtain of reinforcement, out-of-plane curvature is even more pronounced. The vulnerability of the wall against lateral buckling depends on the prior tensile strain amplitude, ε_{sm}, and the wall slenderness ratio measured with the parameter, kh_u/b, where b is the wall thickness. According to the derivation of the wall instability relationship in Parra and Moehle (2014), Equation 3-6 relates the critical slenderness ratio to the maximum tensile strain in the prior cycle.

$$\frac{b}{kh_u} = \frac{1}{\pi}\sqrt{\frac{\varepsilon_{sm} - 0.005}{\kappa\xi}} \qquad \text{3-6}$$

Here κ is a parameter introduced for the effective depth of the wall section in the out-of-plane direction. The parameter κ can be taken as 0.8 for walls with two curtains of reinforcement and 0.5 for the walls with single curtain. Solving the Equation 3-6 for the parameter ξ gives:

$$\xi \leq 0.5\left(1 + \frac{2m}{0.85} - \sqrt{\left(\frac{2m}{0.85}\right)^2 + \frac{4m}{0.85}}\right) \qquad \text{3-7}$$

106

where m is defined as $\rho f_y / f_c'$ and called mechanical reinforcement ratio. It is noted that for design practice values of ξ ranges from 0.4 to 0.6. For practical applications, Parra and Moehle simplify Equation 3-6 by taking κ equals to 0.8 and ξ equals to 0.5, which becomes:

$$\frac{h_u}{b} = \frac{1}{0.7k\sqrt{\varepsilon_{sm}-0.005}}$$

3-8

Figure 3.70 shows the relation between the critical slenderness ratio, h_u/b, and the maximum tensile strain ε_{sm}, according to the Equation 3-8 for the parameter k being equal to 0.5. Considering the effect of low-cycle fatigue, the ultimate tensile strain for the reinforcing steel was assumed to be 0.05 under cyclic loading conditions and hence it is an upper bound. Given the slenderness ratio of the wall one is interested in, Figure 3.70 shows the maximum tensile strain can that wall undergo before experiencing lateral buckling.
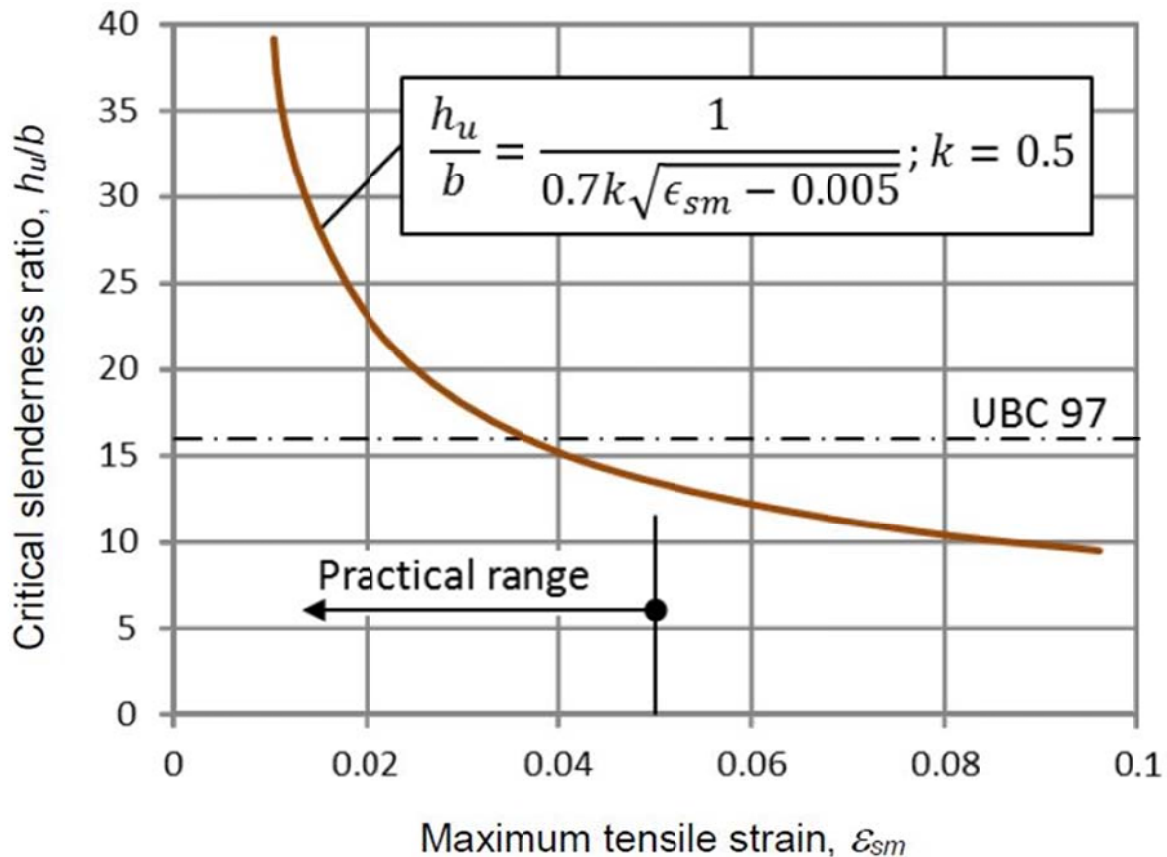
Figure 3.70 – Critical slenderness ratio as a function of maximum tensile strain (after NIST GCR 14-917-25, 2014)

This theory is applied on the walls on the Axes 8 and 13 of the Alto Rio building, in order to investigate the possible effect of lateral wall buckling to the collapse. These two walls had the same parameters concerning the lateral buckling theory. Both walls had a clear story height of h_u = 291 cm (114.5 in), a thickness of b = 20 cm (8 in), and a spalled thickness of $b_{spalled}$ = 17 cm (6.7 in). Plugging in these values for two possible wall thickness cases in to the Equation 3-8, results in to a maximum tensile strain value of ε_{sm} = 0.043 for the full wall thickness and $\varepsilon_{sm,spalled}$ = 0.032 for the spalled wall thickness.

The values of maximum tensile strains calculated for the two possible cases are reasonable strain values for walls like the ones in the Alto Rio building. In the case of the Alto Rio building, the locations of concern for lateral buckling coincide with the locations of lap splices, as shown in Figure 3.6 and Figure 3.8. According to the findings of Section 3.13, and the study done by Hardisty et al. (2014), a value of $2\varepsilon_y$ would be a good approximation for the ultimate strain, (ε_u), capacity of unconfined lap splices under cyclic loading. The assumed stress-strain relationship for unconfined lap splices is show in red dashed line in Figure 3.55. The value of $2\varepsilon_y$ is around 0.0042, if a value of 0.0021 is assumed for the value of ε_y. According to this finding, the ultimate strain that unconfined lap splices can go through under cyclic excitation is in the order of $2\varepsilon_y$ or 0.0042. The maximum tensile strain values calculated with the lateral wall buckling theory of Parra and Moehle (2014) (ε_{sm} = 0.043 and $\varepsilon_{sm,spalled}$ = 0.032) are in the order of tenfold of the ultimate tensile strain. Having the maximum tensile strain values for lateral wall buckling to be tenfold greater than the ultimate strain capacity of the lap splices located at the same wall edge, it can be concluded that the lateral wall buckling of walls on the Axes 8 and 13 are highly unlikely and most probably is not a major factor contributed to the collapse of the Alto Rio building. Spalling of the wall could leave a reduced effective core area that would be more prone to buckling. However, absent confinement reinforcement to define a confined core, the stability of a crushed boundary seems questionable, and does not warrant further consideration.

The structural wall tests done by Villalobos (2014) have similar findings for the possible effects of lap splices on the lateral wall buckling (case of Alto Rio building). Villalobos (2014) tested six wall specimens to study the effects of lap splices of longitudinal reinforcement. From these six specimens, two walls are interesting for the investigation of the lateral wall buckling where lap splices are present. Specimens W-MC-N and W-60-N, is designed similar to the construction practice in Chile with light reinforcement ratios and non-confined boundary elements (Figure 3.71 and Figure 3.72). The only difference between these two specimens where that the W-MC-N had mechanical couplers at the foundation level of the wall, where W-60-N had lap splices with a length of $60d_b$ at the bottom of the wall specimen. It is worth noting that the $60d_b$ lap splice length is very close to the lap splice length provided in Alto Rio building ($58d_b$).

Both wall specimens were tested under identical displacement cycles in the same test setup. These two walls having identical properties except the lap splices on the bottom level of the wall, had different failure modes. Figure 3.73 shows the failure modes of two walls. The wall W-MC-N failed in lateral wall buckling, on the other hand the wall W-60-N failed with the buckling of longitudinal reinforcements. It was reported that there was a strain concentration at the lap splices of W-60-N, this and the difference in the response might be caused by the similar effect of the ultimate strain limitation of the unconfined lap splices (similar to Alto Rio building). Test results of Villalobos (2014) support the conclusion of the previous investigation of lateral wall buckling in Alto Rio building. Considering previous analysis and test results, the occurrence of

lateral wall buckling as a primary cause of failure seems to be highly unlikely in Alto Rio building.
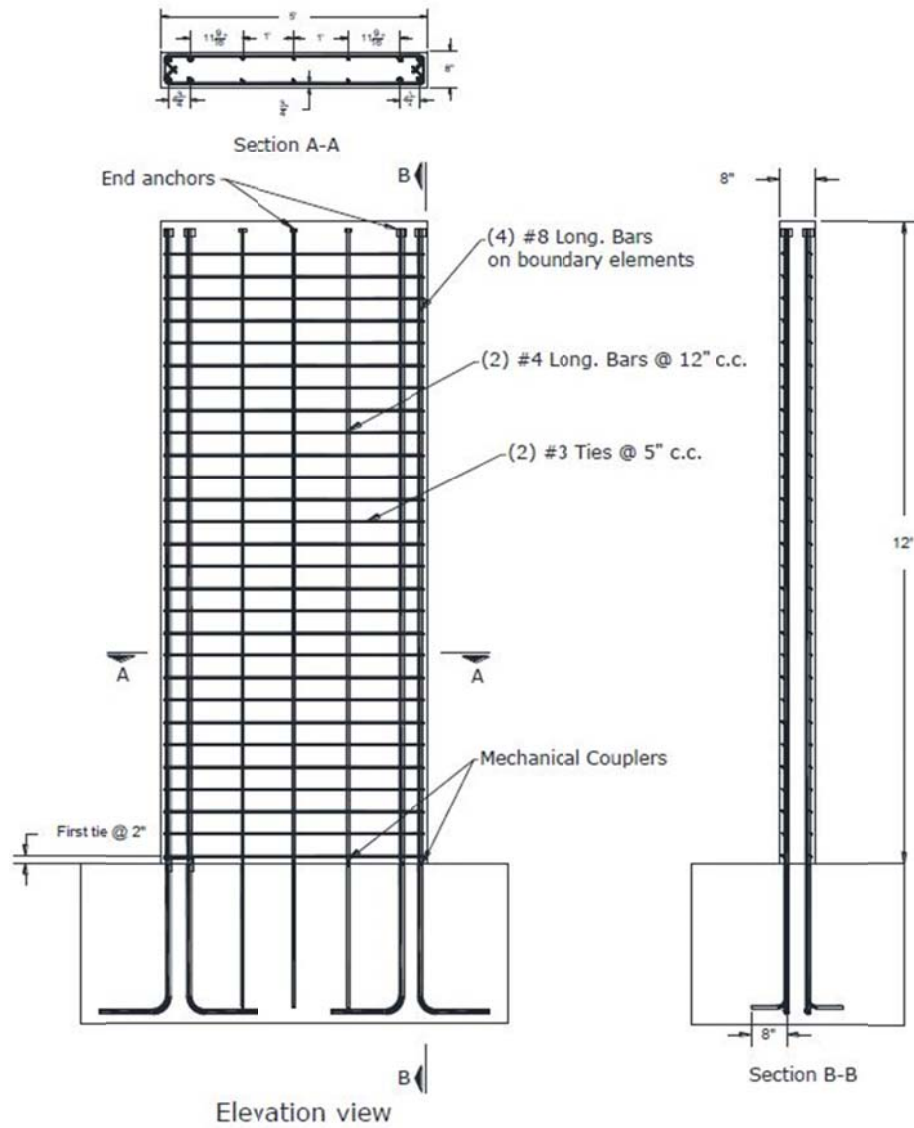
Figure 3.71 – Test specimen with mechanical couplers (W-MC-N) of Villalobos (2014)

Section A-A

(4) #8 Long. Bars
on boundary elements

(2) #4 Long. Bars @ 12" c.c.

(2) #3 Ties @ 5" c.c.

60" Lap Splice for #8 Bars

30" Lap Splice for #4 Bars

First tie @ 2"

Elevation view

Section B-B
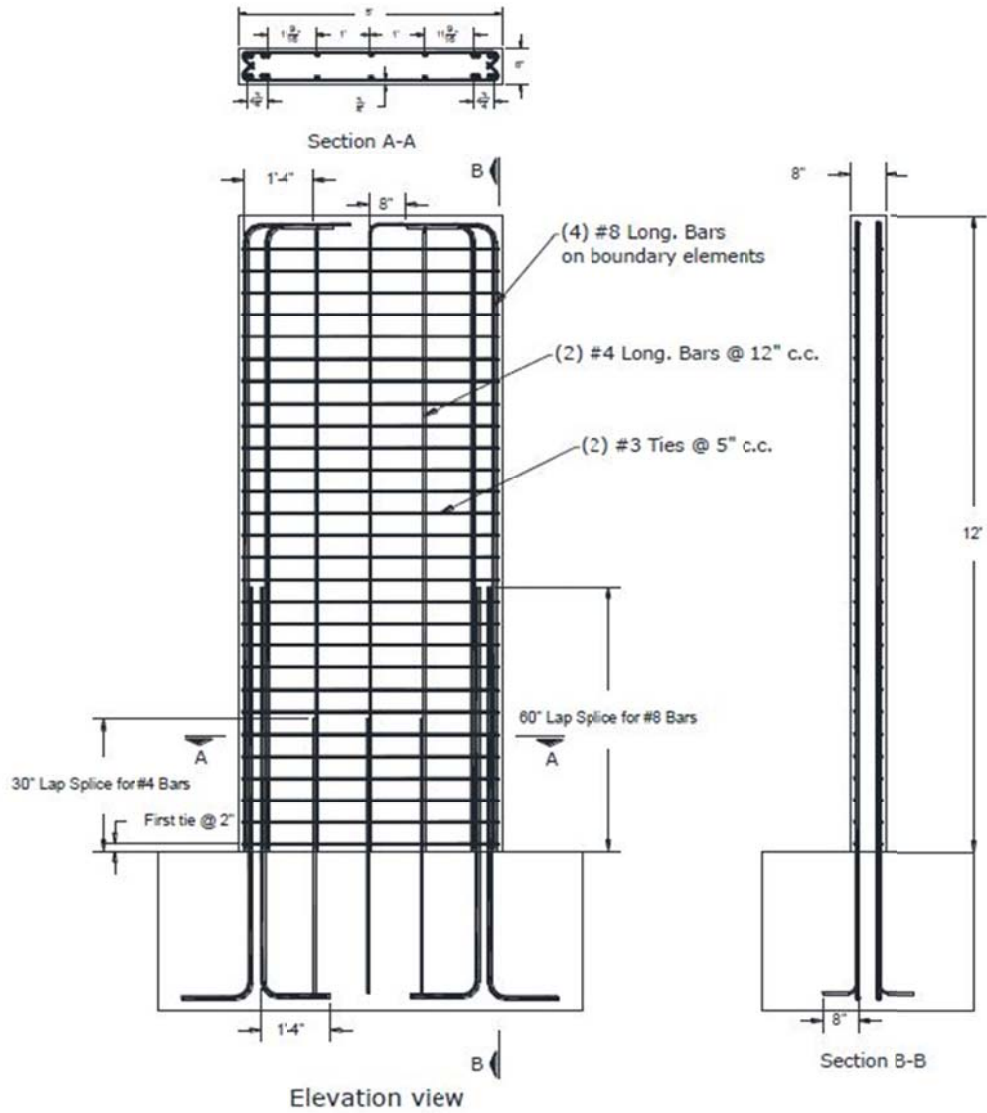
Figure 3.72 – Test specimen with lap splices (W-60- N) of Villalobos (2014)

110
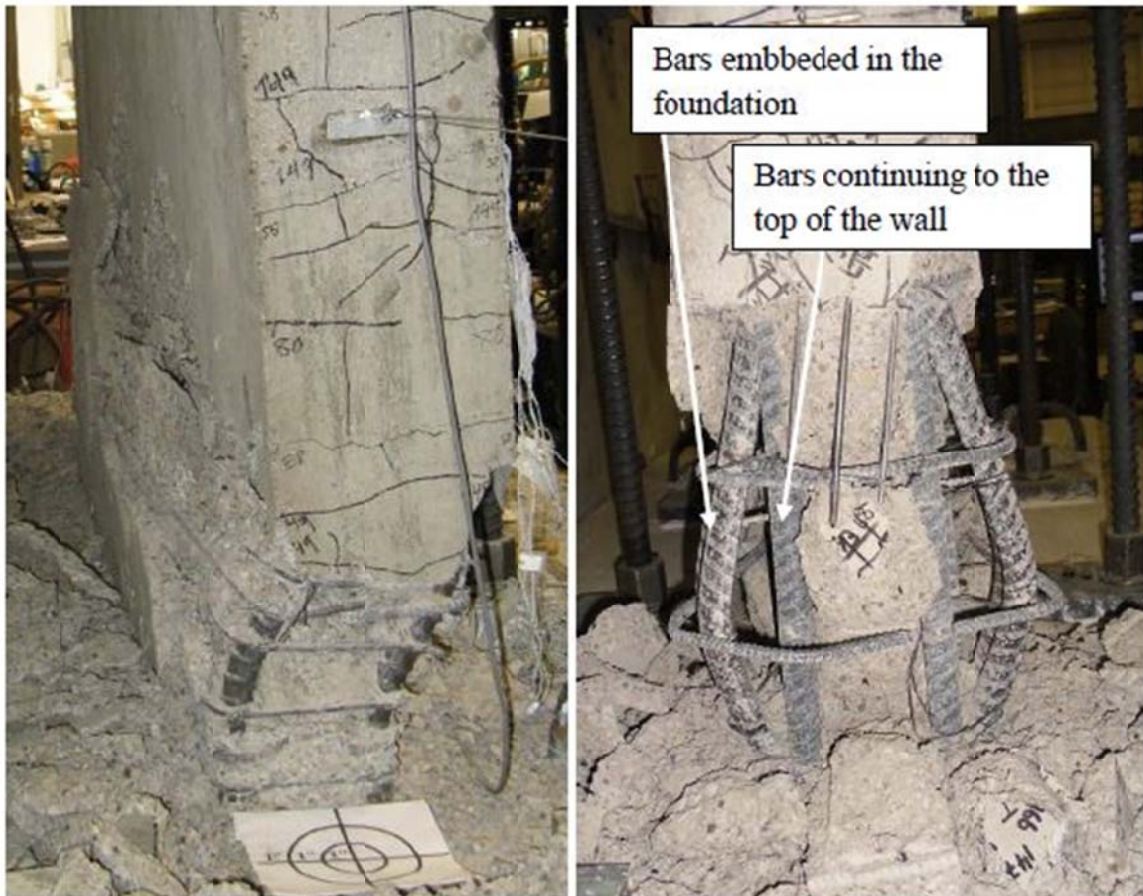
(a) W-MC-N (lateral wall buckling) (b) W-60-N (longitudinal bar buckling)

Figure 3.73 – Failure modes of specimens W-MC-N and W-60-N of Villalobos (2014)

3.15   Summary and Conclusions

The M_w 8.8 2010 Maule Chile earthquake affected over twelve million people in central south Chile, severely damaging more than 50 multi-story reinforced concrete buildings and causing partial or total collapse of four other such buildings. Among these, the 15-story residential Alto Rio building stands out as the first modern shear wall building to collapse by overturning during an earthquake. The recorded ground motions approximately 1.2 km (0.75 miles) away from Alto Rio show that shaking lasted more than 120 seconds with peak ground accelerations of 0.402g and 0.397g in east-west and north-south directions, respectively. Using the building plans and a post-earthquake reconnaissance report, reasons of collapse are investigated with linear elastic, nonlinear static, and nonlinear dynamic analyses.

A linear elastic model of the whole Alto Rio building was prepared using effective (cracked) section properties of the structural elements. The fundamental periods in transverse

and longitudinal directions were typical of values for Chilean wall buildings, with values of $N/18$ and $N/20$, respectively, where N = number of stories. Calculated wall axial load ratios ranged from 0.05 to 0.07 $P/f_c'A_g$, where P considers expected loads (1.0D + 0.25L).

A nonlinear static analysis was conducted on an analytical model representing inelastic material properties of walls along axes 8 and 13 in the building transverse direction; this portion was deemed representative of the seismic-force-resisting system of the building. The model was loaded with an inverted triangular lateral force pattern. For loading to the east (collapse) direction, critical lateral strength degradation occurred due to crushing of the wall boundary at the east edge of the east wall along axis 13 at around 0.7% roof drift ratio, followed by similar crushing of the east part of wall along axis 8 around 1.0% roof drift ratio. The crushing zone occurred adjacent to a vertical discontinuity in the wall cross section. Solid wall panels beneath the stack of openings were calculated to undergo cracking and inelastic response, without failure, for loading in this direction. For lateral load toward the west, those same solid wall panels sustained shear failures, as indicated by initiation of shear strength degradation, at approximately 0.9% roof drift ratio. This was followed by fracture of the longitudinal reinforcement at the east side of the east walls along Axis 13 at 1.6% roof drift ratio. Apart from the isolated shear failure of the solid panel beneath the stack of openings, analyses indicate that shear failure was not an initiator of building failure.

The effect of modeling decisions such as modeling of shear behavior of walls and the softening slope of the concrete material stress-strain relationship are also investigated for understanding of the model sensitivity for these parameters. Nonlinear static analysis of a model with linear elastic shear stress-strain relationship assigned for the whole model was conducted and compared with the previous model with nonlinear shear behavior. There was an apparent difference in the overall stiffness of these two models. Because the elastic shear material model represents the cracked concrete properties, the stiffness of this model was relatively lower than the model with inelastic shear material. The lower stiffness of the model with the elastic shear material results into delayed failures. For lateral loading to the east, crushing of east side of the wall 13 happens at 0.8% roof drift ratio compared to 0.7% of the previous model. Similarly, crushing of the east side of the wall 8 happens at 1.2% roof drift ratio, which was at a 1.0% roof drift ratio for the model with inelastic shear material model. However, it should be noted that the order of failures observed didn't change with a change of the shear material model. For the lateral load to the west, the first difference in the damage modes is observed. As expected, the failure of the shear panel of the walls 8 and 13 is not observed, due to the elastic model of the shear material. On the other hand, the fracture of the longitudinal reinforcement at the east side of the east walls along Axis 13 is observed at 2.0% roof drift ratio rather than the 1.6% observed in the inelastic shear material model. It showed that the failure modes except the failure of shear panels are calculated with the same order with the inelastic shear material model .However; there were some discrepancies in drift capacities and strength of the model that can be critical to the dynamic response of such models. It was concluded that the inelastic modeling of shear should be employed by practicing engineers.

Another parametric study was done to investigate the possible effects of the softening slope of the concrete material stress-strain relationship to the response of the model. Four different concrete stress-strain relationships used in this study with the only difference of the ultimate concrete strain (ε_u) values. The first stress-strain relationship was the model recommended in PEER/ATC-72-1, and this model was assumed to have an ultimate compressive

strain of 0.005. A second stress-strain relationship was the model by Roy and Sozen (1965) with a smaller ultimate strain (ε_u) value of 0.0043. The third model using the Mander et al. (1988) resulted in an ultimate strain (ε_u) value of 0.01. Lastly, a fourth concrete compressive stress-strain relationship was modeled using the proposed regularization technique against loss of objectivity by Coleman and Spacone (2001) with a value of ultimate strain (ε_u) equals to 0.0058. As expected, there was no difference in the overall stiffness of the responses in either case. The order of failures observed didn't change with a change of the concrete material model. The drift capacity of the different models was dramatically dependent of the concrete ultimate strain value (ε_u). This is not surprising considering the failure mode of the Alto Rio in this direction is controlled by concrete crushing. The trend showed that the higher value of the ultimate concrete compressive strain (ε_u) assigned for the model, the higher drift capacity is observed in the analysis. It seems like the analysis results are sensitive to the assumptions of the material level stress-strain relationships, in this case for concrete under compressive loading. The analysis results showed that the higher value of the ultimate concrete compressive strain (ε_u) assigned for the model, the higher drift capacity is observed in the analysis. It is concluded that the material stress-strain relationship has an important effect on the overall model behavior, and practicing engineers should be cautious of the element size and material model selection. Tackling possible pitfalls can be achieved using the regularization of the post peak behavior of the concrete stress-stain relationship according to Coleman and Spacone (2001).

Dynamic analysis of a single-degree-of-freedom (SDOF) model was established to represent the effective first translational mode response of the Alto Rio building in the transverse direction. The SDOF model was excited by the ground motions recorded in Concepción, 1.2 km (0.75 miles) away from Alto Rio. The proximity of the sites and the similar site characteristics according to Ramirez and Vivallos (2009) suggest that the motions at the two sites may be reasonably similar, although deviations due to different wave paths are to be expected. Studies using this model indicate that building collapse would occur toward the east at around 22 seconds into the ground motion, as observed following the earthquake, and that this result was relatively insensitive to the properties of the SDOF model. After a deformation cycle as large as 1.3% roof drift ratio in the west direction, the SDOF model collapses to the east (collapse) direction at around 22 seconds of the excitation. In the cycle to the east at around 20 seconds, concrete crushes under compression for both walls on Axes 13 and 8, respectively. Right after that the loading cycle changes direction and damages the shear panels on both Axes 8 and 13 at around 21 seconds. It is followed by a large cycle to the east direction around 22 seconds, where structure permanently displaced to the east. This permanent displacement of the model is also an indicator of the collapse to the east direction. The final result of the dynamic SDOF analysis is consistent with the observed damage and collapse of the building.

In another nonlinear static analysis the effects of lap splices to the response are investigated. The provided lap splice lengths in design of the Alto Rio building were more than the required amount by ACI 318-95.However, a recent study done by Hardisty et al. (2014) showed that unconfined lap splices will have limited deformation capacity, even though the splice lengths required by ACI 318-95 provided. In light of the results of Hardisty et al. (2014), Perform 3D model was modified to account for the lap splices with the modification done was the change in the ultimate strain (ε_u) value in the tension loading side. Results of Hardisty et al. (2014) suggested that a value of $2\varepsilon_y$ would be a good approximation for the ultimate strain (ε_u) capacity of unconfined lap splices under cyclic loading. For loading the model to the east, the

direction in which collapse occurred, similar to the previous model, crushing of the wall boundary at the east edge of the east wall along axis 13 at around 0.72% roof drift ratio, followed by similar crushing of the east part of wall 8 at around 1% roof drift ratio. However, there is relatively higher strength degradation after the crushing of the wall along axis 13. It can be seen that, even though the crushing of the wall on axis 8 is at the same displacement, overall strength of the building at 1% roof drift ratio is lower than the model not accounting for lap splice effects. For lateral load to the west, unlike the previous results, the first significant event is the failure of shear panel on the Axis 13 at 0.62% roof drift ratio. It is followed by the failure of the longitudinal reinforcement lap splices at the east side of the east walls along Axis 13 at 0.82% roof drift ratio. This shows that the modifications done to account for lap splices affect the tension controlled failure dramatically, decreasing the drift capacity of the building to half of the previous model.

Similar to the previous analysis, a second single-degree-of-freedom (SDOF) model was established to represent the effective first translational mode response of the Alto Rio building in the transverse direction, accounting for the lap splice effects. After a deformation cycle as large as 1.2% roof drift ratio in the west direction, the SDOF model collapses to the east (collapse) direction at around 22 seconds of the excitation. First significant event of the structure response under dynamic analysis is the damage at the shear panel on the Axis 13 in a cycle to the west around 15 seconds. In the cycle to the east at around 20 seconds, concrete crushes under compression for both walls on Axes 13 and 8, respectively. Right after that the loading cycle changes direction to the west and causes the failure of the lap splices on the east side of the east wall on Axis 13 at around 21 seconds. It is followed by a large cycle to the east direction around 22 seconds, where structure permanently displaced to the east. This permanent displacement of the model is also an indicator of the collapse to the east direction. The results of the dynamic analysis of the modified SDOF system are very close to the analysis of the original model. This demonstrates that although the possible effects of the lap splices can change the nonlinear static analysis results of the Alto Rio building, it neither had a dramatic effect on the dynamic SDOF analysis, nor changed the mode of collapse.

The possible effect of lateral wall buckling to the collapse of Alto Rio building was also investigated using the theory presented in Parra and Moehle (2014). The maximum tensile strain values for the lateral wall buckling to occur was $\varepsilon_{sm} = 0.043$ and $\varepsilon_{sm,spalled} = 0.032$ for full wall thickness and the spalled wall thickness, respectively. Altough, these maximum tensile strain values are reasonable for shear walls, in the case of the Alto Rio building, the locations of concern for lateral buckling coincide with the locations of lap splices. Since the maximum tensile strain values for lateral wall buckling is tenfold of the ultimate tensile strain capacity of the unconfined lap splices ($2\varepsilon_y$) according to Hardisty et al. (2014), it can be concluded that the lateral wall buckling of walls on the Axes 8 and 13 are highly unlikely and most probably is not a major factor contributed to the collapse of the Alto Rio building.

The results of this study suggest that the Alto Rio building was susceptible to collapse to the east direction due to the following main factors:

1. The configuration of T and L-shaped wall cross sections resulted in low deformation capacity for loading that placed the flange in tension and the stem in compression.

2. Vertical discontinuities at the east side of the building created stress concentration at the top of the first story, with corresponding damage concentration.

114

3. The solid wall panels below the stack of corridor openings were susceptible to high shear demands and shear damage.

4. The absence of confined boundary elements limited the deformation capacity of the walls and caused damage concentrations at the boundary elements.

5. The presence of lap-spliced longitudinal reinforcement without confining transverse reinforcement reduced the tensile deformation capacity of lap splices, and further reduced the deformation capacity of the structural system.

The nonlinear static and dynamic SDOF analysis results demonstrate that the Alto Rio building was susceptible to collapse to the east direction. The main factors contributing to the failure include: the configuration of T and L-shaped wall cross sections, vertical discontinuities at the east side of the building, and high shear stresses in the solid wall panels below the stack of openings. The structural drawings and reconnaissance data suggest that the absence of confined boundary elements and the occurrence of lap splices of longitudinal bars without sufficient transverse reinforcement could be other factors that contributed to the collapse. However, the analysis of models modified according to the behavior of lap splices demonstrated that lap splices have a very minor effect on the overall behavior of the building under this specific earthquake motion. The specific analyses reported in this paper indicate one plausible failure sequence, that is, initiation of shear damage in the solid wall panel immediately below the stack of openings, crushing and buckling failure of the walls at the discontinuity between the first and second stories on the east side of the building, and subsequent failure of the tension chord on the west side of the building as it collapsed toward the east. Figure 3.74 shows the modes of failure that analyses resulted at the suspected locations of the building. Other failure sequences are also plausible, depending on details of the ground motion and structural model, but these were not indicated by the present study. Observed damage after the earthquake (IDIEM, 2010) is consistent with the findings of the analysis results.
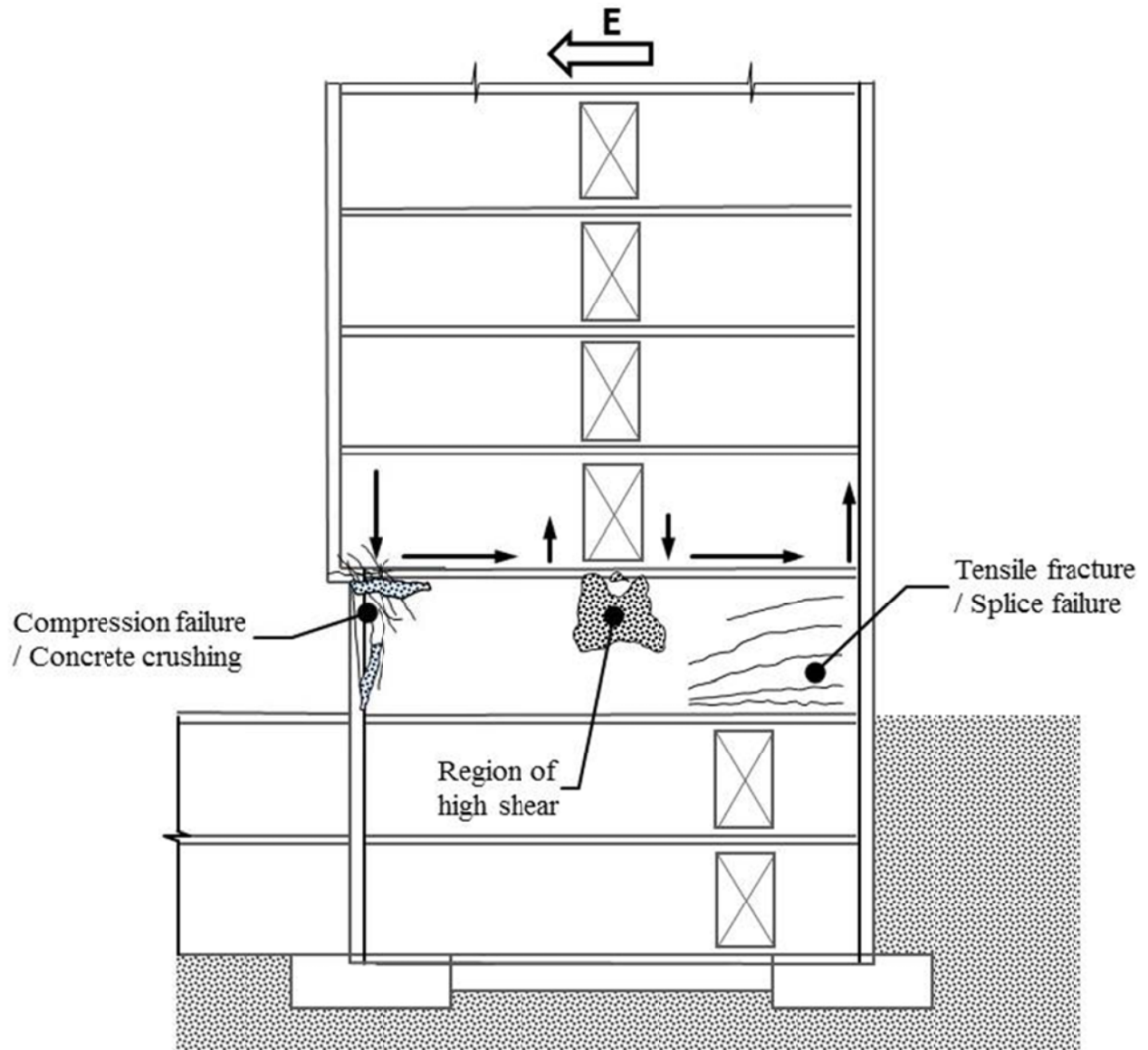
Figure 3.74 – Damage sketch of the Alto Rio building according to the analyses results

Chapter 4. Seismic Performance and Modeling of

Post-Tensioned Precast Concrete Shear Walls

4.1   Introduction

Past earthquakes have shown examples of unsatisfactory performance of buildings using reinforced concrete structural walls as the primary lateral-force-resisting system. In the 1994 Northridge earthquake, examples can be found where walls possessed too much overstrength, leading to unintended failure of collectors and floor systems, including precast and post-tensioned construction. In the 2010 Chile earthquake, many structural wall buildings sustained severe damage. Although Chilean design standards result in different reinforcement detailing than is common in U.S. walls, the failure patterns raise concerns about how well conventionally reinforced structural walls in U.S. buildings will perform during the next earthquake. Past research efforts, including the PRESSS program (Priestley et al. 1999) and subsequent studies, have explored alternative design approaches using post-tensioned precast structural walls to better control yielding mechanisms and promote self-centering behavior. These studies have provided excellent guidance on design and construction requirements, but examples of full-scale, three-dimensional dynamic tests to demonstrate behavior in realistic structural systems have been lacking. Such demonstrations are important to identify complex interactions that occur in complete building structures. Such demonstrations also are useful to serve as a vehicle for acceptance by the engineering community.

In December 2010, the National Research Institute for Earth Science and Disaster Prevention (NIED) in Japan conducted a three-dimensional earthquake simulation test on a full-scale, four-story building using the E-Defense shaking table (Figure 4.1). Design, instrumentation, preliminary analytical studies, and testing of the building were a collaboration among researchers from Japan and the U.S. (lead researchers in the U.S. were J. Moehle, W. Ghannoum, R. Sause, and J. Wallace). The seismic-force-resisting system of the test building comprised two PT frames in one direction and two unbonded PT precast walls in the other direction. The building was designed using the latest code requirements and design recommendations available both in Japan and the U.S., including the ACI ITG-5.2-09. The test building was subjected to several earthquake ground motions, ranging from serviceability level to near collapse.

Analytical studies were carried out as part of the overall research program. The studies, which are reported here, aim to develop practical structural engineering models, to conduct analytical simulations to test the capability of the structural models to replicate behaviors important to structural engineers, and to assess whether available analysis tools are sufficient to model dynamic behavior that results when a full-scale building is subjected to realistic

earthquake ground shaking. Measured response data from such an outstanding test provides an opportunity to fully understand the response characteristics of PT walls and assess the ability of nonlinear analytical models to reproduce important global and local responses, including three-dimensional system interactions, both prior to and after loss of significant lateral strength. Moreover, this study to assess behavior and system interaction of PT walls leads to improvements of the current design ideas and performance expectations.

4.2   Overview of the Test

4.2.1   Background

In December 2010, two full-scale, four-story buildings were tested simultaneously on the NIED E-Defense shaking table (Figure 4.1). The two buildings were designed to have the same height and floor plan; one of the buildings used a conventional reinforced concrete (RC) structural system with shear walls in one direction and moment frames in the other direction, whereas the other building used the same systems constructed with post-tensioned (PT) precast concrete members. This study focuses on the PT building only.

The test was conducted on the world's largest shaking table facility, E-Defense. The E-Defense shaking table has plan dimensions of 20 m x 15 m (Figure 4.2). The table can produce a velocity of 2.0 m/s and displacement of 1.0 m simultaneously in two horizontal directions, and accommodate specimens weighing up to 1200 metric tons. The two buildings were almost identical in geometry and configuration, and were tested simultaneously, as shown in Figure 4.3. Each building weighed approximately 5900 kN; therefore, the total weight of the two buildings was 98% of E-Defense table capacity.

Figure 4.1 - Picture of the specimens at the E-Defense shaking table
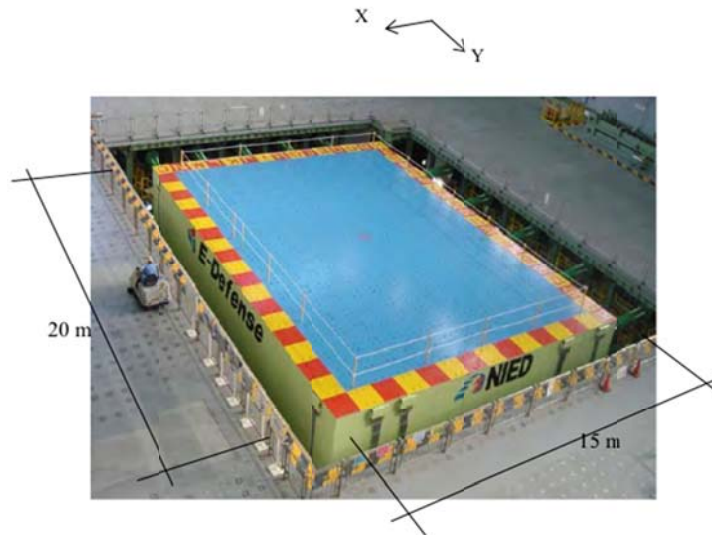
Figure 4.2 - E-Defense shaking table
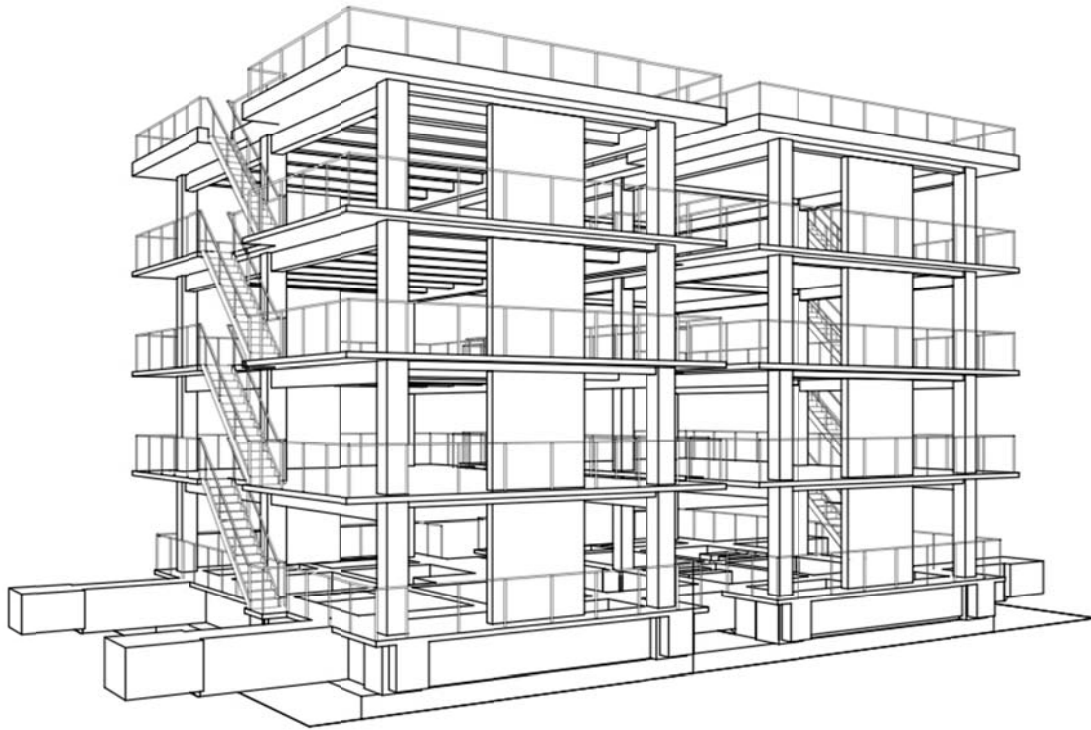
Figure 4.3 - Overview of the test setup

4.2.2 Test Specimen

The test specimen was a full-scale, four-story, post-tensioned precast concrete building. It had a rectangular plan (Figure 4.4), with dimensions 7.2 m in the Y (transverse) direction and 14.4 m in the X (longitudinal) direction. The height of each floor was 3 m, resulting in a total building height of 12 m. The lateral-load-resisting system in the Y-direction was two precast unbonded PT shear walls and one bay unbonded PT center moment frame at the B Axis (Figure 4.5.b and Figure 4.5.c). In the X-direction, the structural system consisted of two-bay bonded PT moment frames (Figure 4.5.a). All structural elements were precast off-site and installed and post-tensioned on-site. Post-tensioning tendons of beams and columns in the X-direction were bonded with grouting after installation. On the other hand, PT tendons of shear walls and beams in the Y-direction were constructed to be unbonded from the concrete.
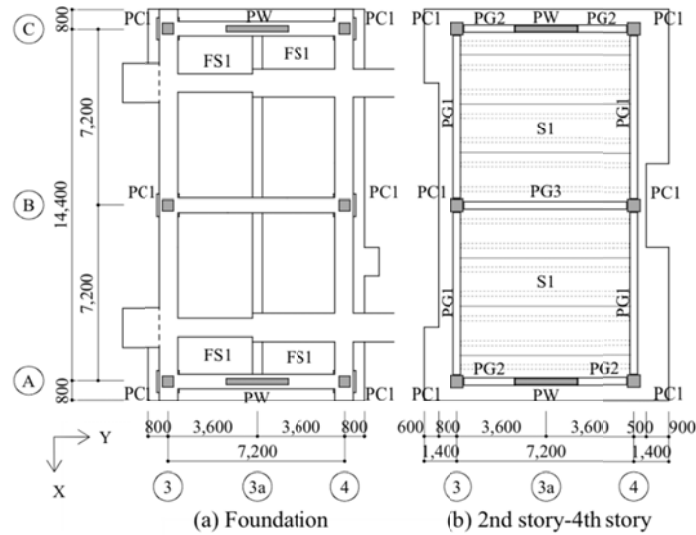
Figure 4.4 - Floor plan of the specimen (Unit: mm)
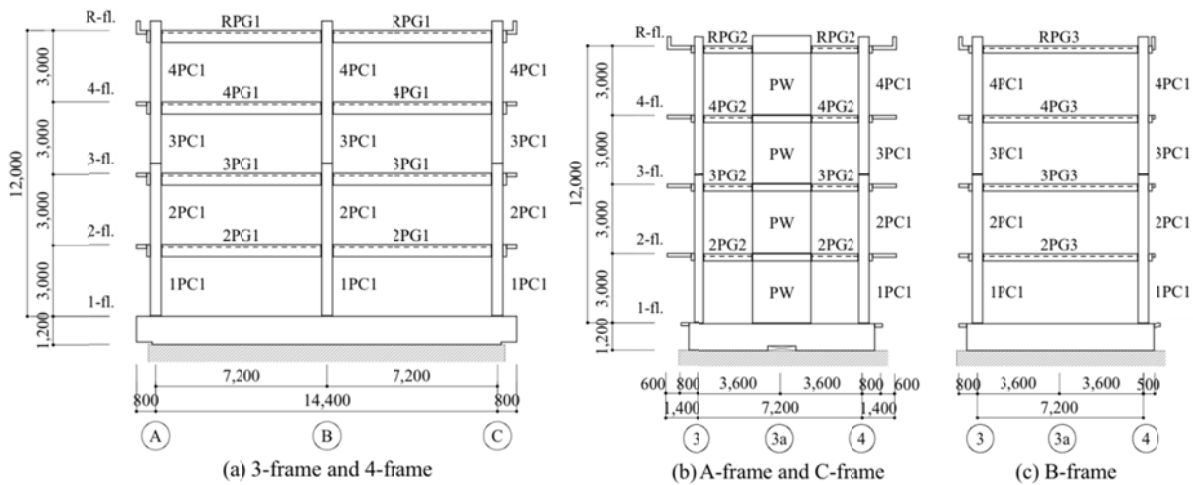
Figure 4.5 - Elevation view of the specimen (Unit: mm)
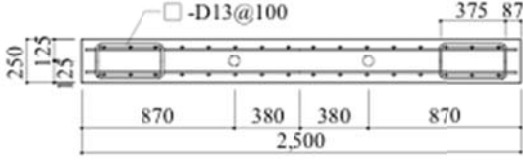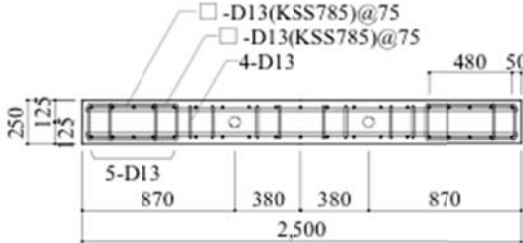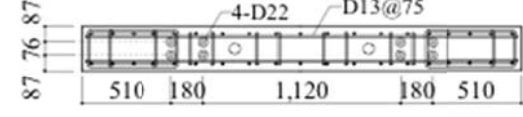
Shear walls had a rectangular cross section with a length (l_w) of 2500 mm and a thickness (t_w) of 250 mm with a cross-sectional aspect ratio l_w/t_w of 10. PT walls were 12 m high, and therefore had a slenderness ratio of $H_w/l_w = 4.8$, where H_w is the height of the wall, and l_w is the length of the wall. Shear walls were prefabricated as 3-meter high panels and assembled in place. Therefore, shear walls consisted of 4 precast panels placed on top of each other and post-tensioned from roof to foundation level. The fourth story wall panel was extended 450 mm above the roof slab. The extended part of the wall was thickened to 400 mm in order to accommodate anchorage stresses for the post-tensioning reinforcement. The first two floors of the north wall were constructed using FRCC (fiber reinforced cement composite); the south wall was constructed using conventional Portland cement concrete mix. The concrete design strength was 60 MPa for precast walls. Grout mortar was injected between the precast wall panels. The design strength of the grout mortar was 60 MPa.

121

Table 4.1 shows the cross section of the wall panels. The first floor cross section was different than the other three floors. However, the same cross section was used for floors 2 thru 4. The first floor cross section had well-confined boundary elements at the two ends of the wall. The total confinement length ratio l_c/l_w was 0.4, where l_c is the total confinement length, and l_w is the length of the wall. The volumetric ratio of confinement steel to confined concrete core in the lengthwise direction was $\rho_x = 1.7$ %, whereas it was $\rho_y = 1.8$ % in the transverse direction. The overall confinement steel ratio was $\rho_s = 3.5$ %. The two-way mesh of reinforcing steel was D13 SD295, which had a nominal design strength of 345 MPa. Transverse reinforcement of the wall boundary elements was high-strength steel bars with a nominal strength of 785 MPa.

Wall panels were post-tensioned at the roof level with two bundles of *10 – D15.2 SWPR7B* tendons. Post-tensioning tendons were located with an eccentricity of 380 mm from the center of the cross section (Figure 4.7 - Reinforcement details of wall base (Unit: mm)). PT tendons were placed inside 85 mm diameter polyethylene ducts without bonding surrounded by concrete over the full wall height. The area of the post-tensioning tendons were $A_{spt} = 1387$ mm^2, which corresponds to a post-tensioning reinforcement ratio $\rho_{pt} = 0.44$ %. Tendons were initially prestressed to 60 % of f_{py}, where f_{py} is the design yield strength of the PT tendons. Initial prestressing of wall panels resulted in an initial concrete compressive stress of $f_{ci,pt} = 4.3$ MPa. PT strands used in the walls had design strength of 1600 MPa. Figure 2.6 shows reinforcement details of the PT walls and the wall-to-beam joint details. Post-tensioning tendon locations throughout the wall height are shown in Figure 4.9.b.

Eight D22 (22 mm diameter) unbonded mild steel bars (four on each side) were placed with 540 mm eccentricity from the center of the wall cross section (Figure 4.7). These bars were unbonded through the lower 1.5 m of the first story and connected to the foundation with mechanical couplers. Unbonded mild reinforcement was placed across the interface of the wall base and the foundation to provide a mechanism for concentrating the inelastic action on these bars and dissipating energy.

Table 4.1 - Wall cross sections

Figure 4.6 - Reinforcement details of wall base (Unit: mm)
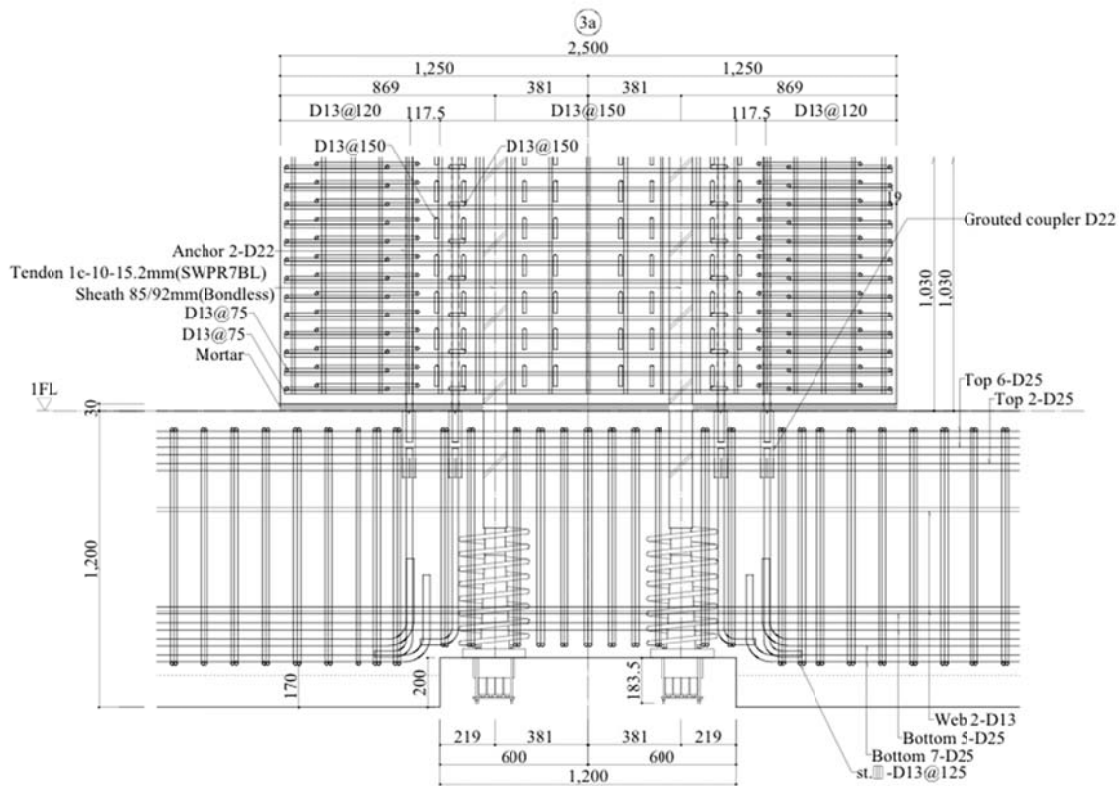
Figure 4.7 - Reinforcement details of wall base (Unit: mm)

Only one generic column cross section is used for all of the columns throughout the test building. Columns (PC1) were square and dimensioned 450 mm by 450 mm (Table 4.2). One precast column member was two-stories high. Four D19 SD345 reinforcing bars were used as longitudinal reinforcement. Columns were post-tensioned using eight bundles of 21mm diameter SBPR 1080/1230 tendons (Figure 4.9, see Table 4.3 for material properties). Effective prestressing of the PT tendon was 0.8 times the yield strength for PC1 columns. PT tendons in columns were bonded to concrete by grouting them after post-tensioning. Two legs of D10 SD295A bars with 100 mm spacing were used as transverse reinforcement. The amount of transverse reinforcement was adequate for the typical Japanese practice for post-tensioned moment frames. However, this transverse reinforcement choice was not enough to confine high strength concrete in the core of the columns. This issue will be discussed in more detail in Section 4.3.
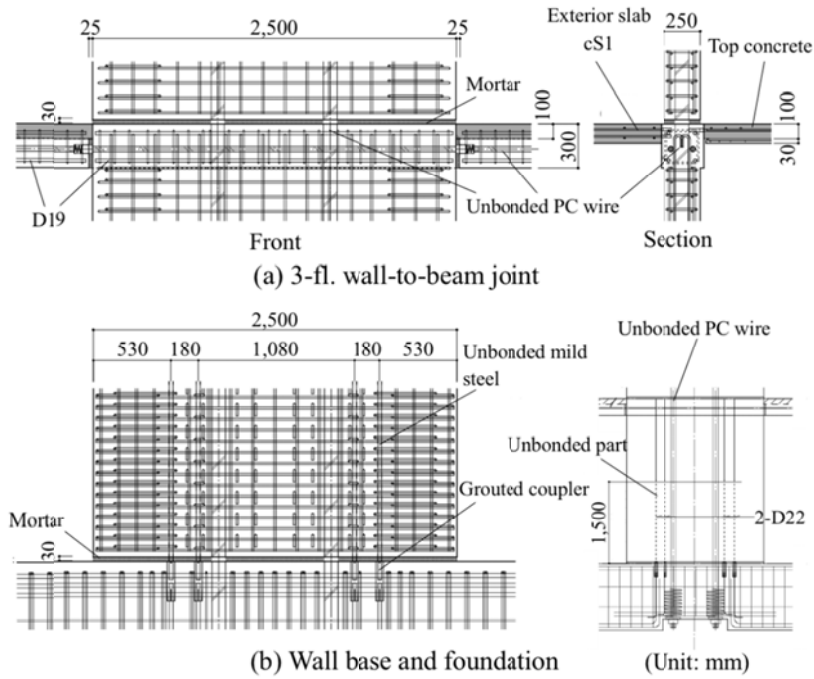
Figure 4.8 - Reinforcement details of walls (Unit: mm)
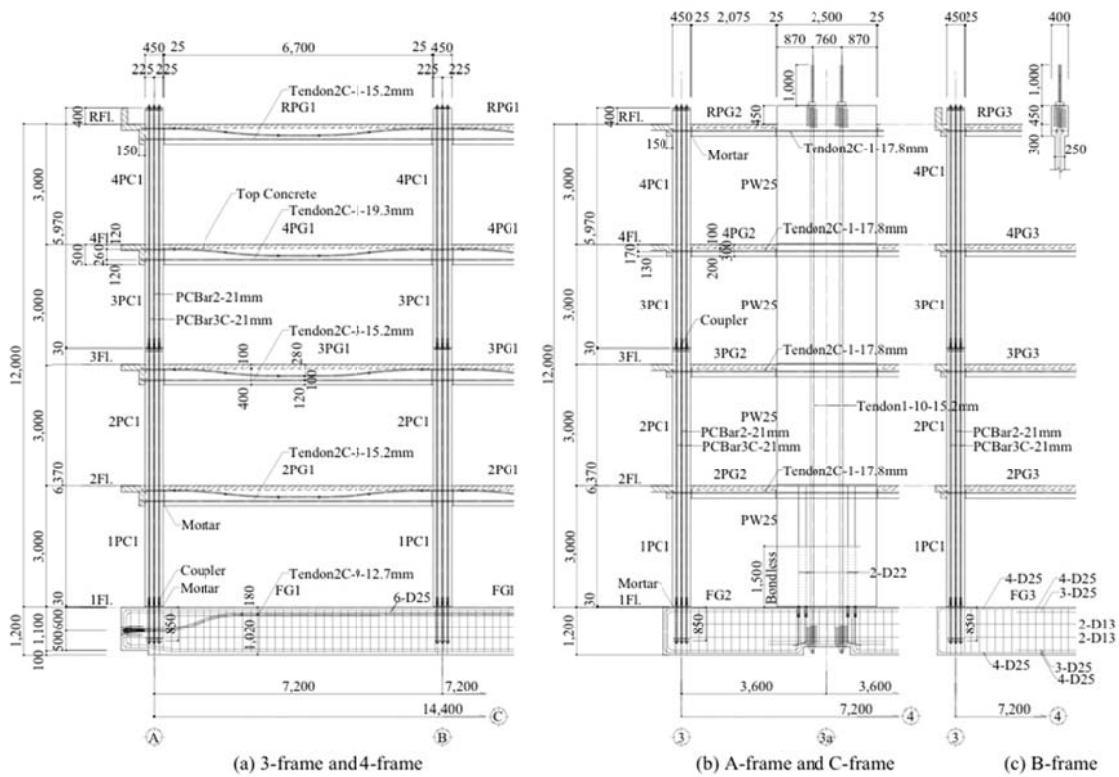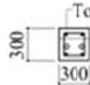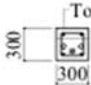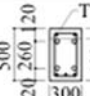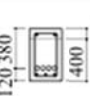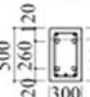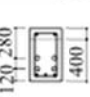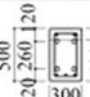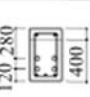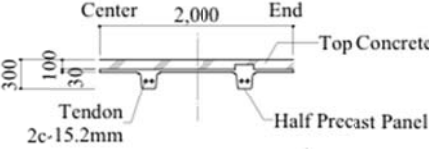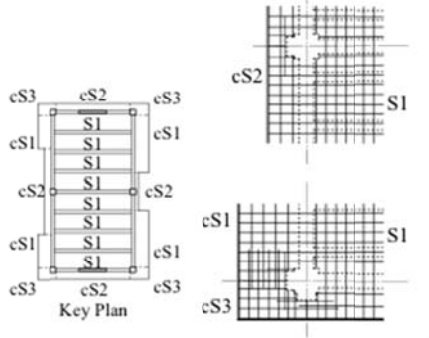
Figure 4.9 - Post-tensioning tendon details

125

Table 4.2: Beam, column and slab cross sections

List of Column		
		PC1
All	Section	450
	Tendon	8-21mm(SBPR1080/1230)
	Rebar	4-D19
	Hoop	D10@100

List of Girder			
		PG2	PG3
All	Section	300 × 300 Top Concrete	300 × 300 Top Concrete
	Tendon	2C-1-17.8mm(SWPR19L)	2C-1-17.8mm(SWPR19L) 1C-17mm(SBPR930/1080)
	Top	2 - D19	2 - D19
	Bottom	2 - D19	2 - D19
	Stirrup	2-D10@100(KSS785)	2-D10@150

List of Girder			
		PG1	
	Location	End	Center
R-fl.	Section	Top Concrete	
	Tendon	4C-1-17.8mm(SWPR19L)	
	Top	2 - D19	
	Bottom	3 - D19	
	Stirrup	2-D10@150	2-D10@200
4-fl.	Section		
	Tendon	4C-1-19.3mm(SWPR7BL)	
	Top	2 - D19	
	Bottom	3 - D19	
	Stirrup	2-D10@100	2-D10@200
3-fl. 2-fl.	Section		
	Tendon	4C-3-15.2mm(SWPR7BL)	
	Top	2 - D19	
	Bottom	3 - D19	
	Stirrup	2-D10@90	2-D10@200

List of Slab   Depth: 130mm

Center 2,000 End
Top Concrete
Tendon 2c-15.2mm
Half Precast Panel

Key Plan

		Shorter direction	Longer direction
S1		D10@200	D10@200
cS1	Top	D13@200	D10@250
	Bottom	D10@200	D10@250
cS2	Top	D10@200	D10@250
	Bottom	D10@200	D10@250
cS3	Top	D13@200	D13@200
	Bottom	D10@200	D10@200

126

Beams in the wall direction (PG2 & PG3) were partially precast, with the top 100 mm of the 300mm by 300 mm section cast-in-place with the slab (Table 4.2). Four D19 SD345 longitudinal reinforcement bars were used for both beam cross sections. Both beams were post-tensioned with 2 bundles of 17.8 mm diameter SWPR19L unbonded tendons. However, beams on frame B had an additional 17 mm SBPR930/1080 tendon prestressed in fabrication. Beam PG2 had two hoops of D10 KSS785 (high strength steel, Table 4.3) transverse reinforcement with 100 mm spacing. On the other hand, beam PG3 had two hoops of D10 SD295A with 150 mm spacing. Effective prestressing of the PT tendon was 0.6 times the yield strength for PG2 beams and 0.8 times the yield strength for PG3 beams. A typical beam-column joint is shown in Figure 4.10. Beams in the longitudinal direction (PG1) were not the interest of this study and not covered here in detail. However, detailed information about these beams can be found in Table 4.2.
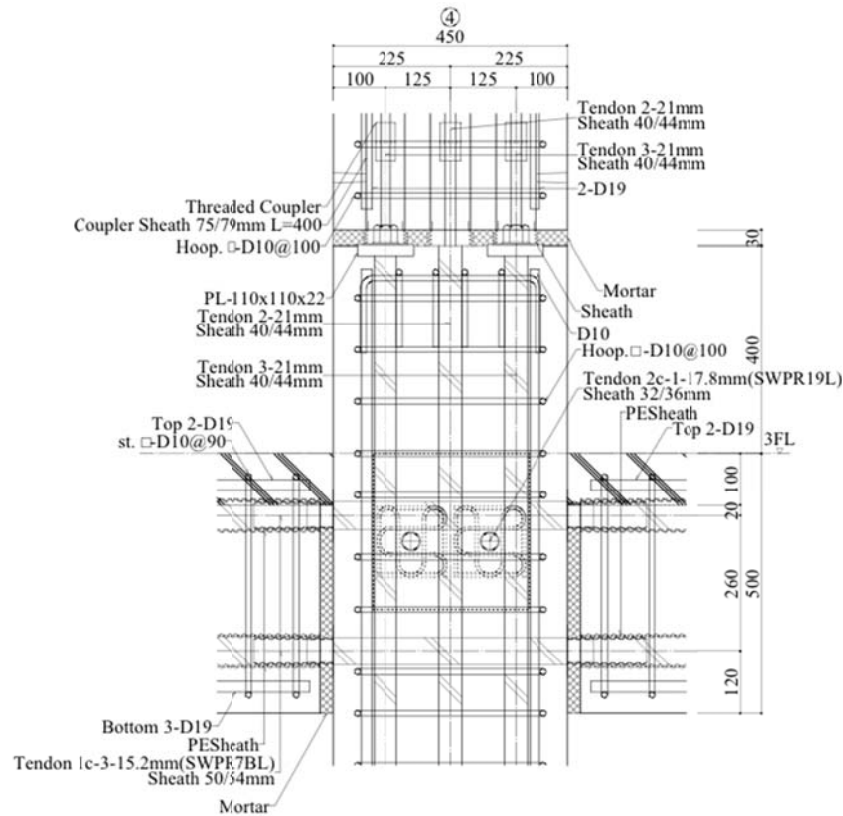
Figure 4.10 - Details of the beam column joint (Unit: mm)

The slab comprised of half-precast 2 meter wide double-tee sections. The slab was supported by pretensioned joists with 1 m interval in the transverse direction. Each joist was pretensioned using 2 bundles of 15.2 mm tendons. The slab was 130 mm thick with the top 100 mm cast on site monolithically with the beams. Table 4.2 shows the reinforcement details of the slab.

The concrete design strength was 60 MPa for precast parts and 30 MPa for cast-in-place parts. The design strength of the grout mortar was 60 MPa. Nominal strength of the generic steel bar was 345 MPa. Transverse reinforcement of beams and walls in the Y-direction was high strength steel bars with a nominal strength of 785 MPa. PT rods of columns were high strength steel with a design strength of 1080 MPa. PT strands used in walls and beams had a design strength of 1600 MPa. Test results of the materials are shown in Table 4.3.

Table 4.3 - Material test results

(a) Concrete

	σ_B [N/mm^2]
PCa	83.2
PCa (F)	85.5
Top	40.9

(b) Grout

	σ_B [N/mm^2]
Mortar	135.6
Mortar (F)	120.3
Milk cement	63.4

(c) Steel

	σ_y [N/mm^2]	σ_t [N/mm^2]
PC bar φ21 (Column, SBPR1080/1230)	1194	1277
D22 (Wall, SD345)	385	563
D19 (Column and beam, SD345)	389	561
D13 (Wall, SD295A)	347	501
D13 (Slab, SD295A)	372	522
D10 (Column and beam, SD295A)	361	518
D10 (Slab, SD295A)	388	513
D13 (Wall and PG2, KSS785)	938	1107

	F_y [kN]	F_t [kN]
PC wire φ15.2 (Wall, SWPR7BL)	250	277
PC wire φ15.2 (Beam, SWPR7BL)	255	279
PC wire φ17.8 (Beam, SWPR19L)	356	404
PC wire φ19.3 (Beam, SWPR7BL)	429	481

The total weight of the specimen was 5592 kN. The weight of each floor was 996 kN for the roof, 813 kN for the 3rd floor, 806 kN for the 2nd floor, and 804 kN for the 1st floor. The detailed distribution of building weight is shown in Table 4.4.

Table 4.4 - Weight distribution of the building

Structural		PT				2.4 t/m^3	
		RFL	4FL	3FL	2FL	Base	
RC	Column	4.40	8.70	8.70	8.70	4.40	
	Girder	14.20	14.20	14.20	14.20	200.20	
	Wall	4.10	8.10	8.10	8.10	4.10	
	Slab	52.60	43.70	43.30	42.90	10.60	
	Beam	5.50	5.50	5.50	5.50	0.00	
	Parapet	7.90	0.00	0.00	0.00	0.00	
Steel	Temp. Girder	0.00	0.00	0.00	0.00	0.30	
Sum		88.70	80.30	79.90	79.40	219.40	[t]
Non-Structural		PT					
		RFL	4FL	3FL	2FL	Base	
Steel	Stair	330.00	360.00	360.00	360.00	0.00	
	Measurement	0.00	300.00	1750.00	2030.00	2030.00	
	Handrail	244.00	271.00	271.00	271.00	197.00	
Machine	on the slab	5610.00	671.00	0.00	0.00	0.00	
	under the slab	0.00	0.00	0.00	0.00	0.00	
	RC Base	6798.00	1107.00	0.00	0.00	0.00	
Ceiling	under the slab	0.00	0.00	0.00	0.00	0.00	
Duct	under the slab	0.00	0.00	0.00	0.00	0.00	
Sum		12982.00	2709.00	2381.00	2661.00	2227.00	[kg]
Total		PT					
		RFL	4FL	3FL	2FL	Base	TOTAL
Sum		101.60	83.00	82.20	82.10	221.60	570.60 [t]
Sum in Kips		224.00	183.00	181.00	181.00	488.50	1258.00 k

4.2.3 Input Motions

The input ground motions were scaled JMA-Kobe and JR-Takatori records from the 1995 Hyogoken-Nanbu earthquake. Excitation was applied in two horizontal and vertical directions simultaneously. The NS-direction wave, EW-direction wave, and UD-direction wave were input to the Y-direction, X-direction, and vertical direction of the specimen, respectively. Firstly, the JMA-Kobe motion was applied with a wave amplitude magnification of 25%, 50%, and 100%, respectively. Lastly, 40% and 60% scaled JR-Takatori motions were applied to the test specimen. In this study, only the 25%, 50% and 100% excitations are considered.

Figure 4.11 shows the time series of the 100% scaled Kobe and 60% scaled Takatori motions.

Table 4.5 shows the maximum accelerations recorded on the shaking table for all applied input motions. Target and actual acceleration response spectra of all applied motions are shown in Figure 4.12. Peak spectral accelerations observed on the shaking table were 0.58g at 25%, 1.18g at 50%, and 2.79g at 100% JMA-Kobe in the X-direction; and 0.89g at 25%, 1.58g at 50%, and 3.42g at 100% JMA-Kobe in the Y-direction. Moreover, in the X-direction, peak spectral accelerations were 1.11g for 40% and 1.72g for 60% scaled Takatori motion; and in the Y-

129

direction, peak spectral accelerations were 0.99g for 40% and 1.51g for 60% Takatori motion. Prior to application of earthquake motions, the test building was excited with white noise. Fundamental periods of the building were 0.29 s in the Y-direction and 0.45 s in the X-direction.
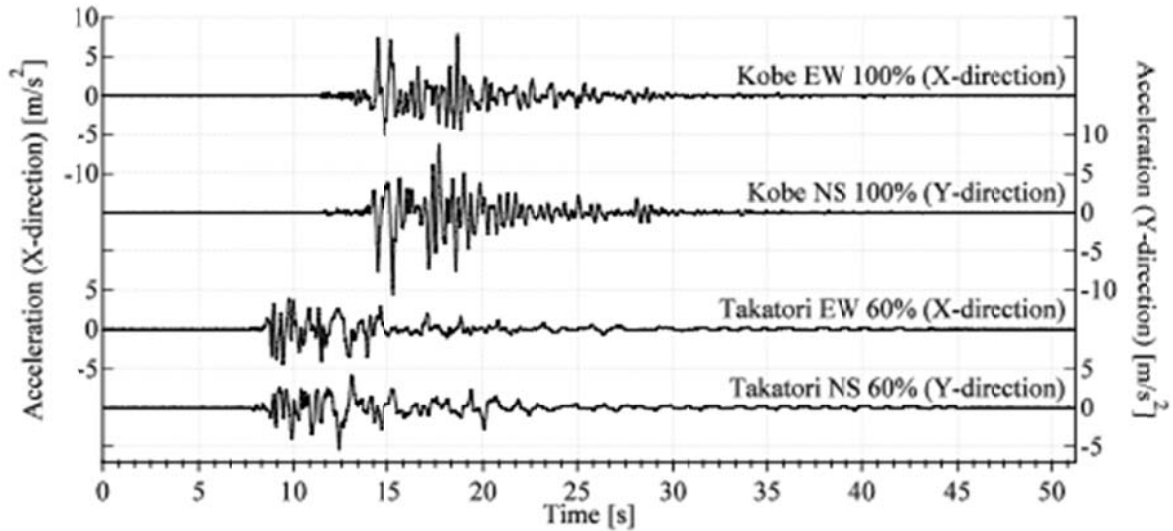
Figure 4.11 - Time series of the input motions
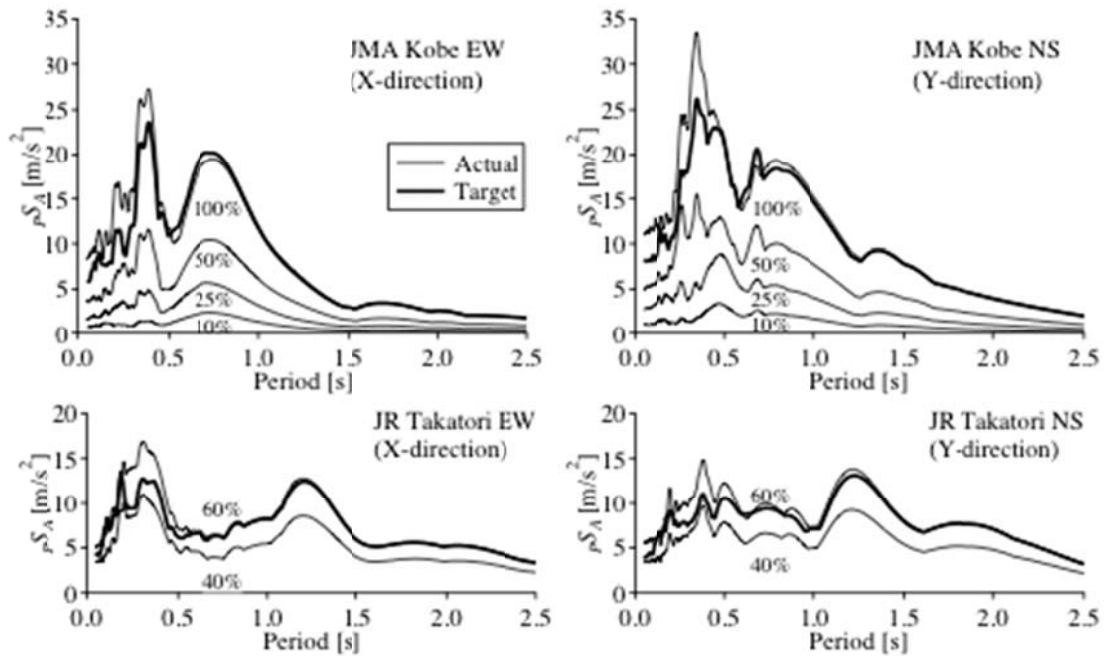
Figure 4.12 - Acceleration response spectra of input motions (Damping ratio = 5%)

Table 4.5 - Maximum acceleration recorded on shaking table

No.	Input wave	Maximum acceleration [m/s^2]		
		X-direction	Y-direction	Z-direction
1	JMA-Kobe-10%	0.69	0.98	0.35
2	JMA-Kobe-25%	1.66	2.69	0.96
3	JMA-Kobe-50%	3.49	4.66	1.98
4	JMA-Kobe-100%	7.88	10.67	4.15
5	JR-Takatori-40%	3.05	3.34	1.15
6	JR-Takatori-60%	4.54	5.46	1.69

4.2.4 Instrumentation

A total of 609 channels of data were collected during the tests for the RC and PT specimens, including 48 accelerometers, 202 displacement transducers, and 235 strain gauges. The accelerometers were placed on the foundation and on each floor slab to record accelerations in three directions. Displacement transducers were arranged to measure story displacements, beam end rotations, column end rotations, and base wall rotations. Strain gauges were glued to the longitudinal and transverse reinforcement of beams, columns, and walls. Strain gauges were largely used for the RC specimen, whereas displacement transducers were used for the PT specimen (to measure member end rotations). Video cameras were used to record the tests and included overall views of the test specimens, as well as close up views of regions where yielding and damage were anticipated. Data acquisition was accomplished using 24 bit A/D converters using a sample rate of 0.001 sec (1000 Hz).

4.2.5 Accelerometers

Accelerometers were used to record accelerations at each floor. Figure 4.13 shows the locations of accelerometers.

131
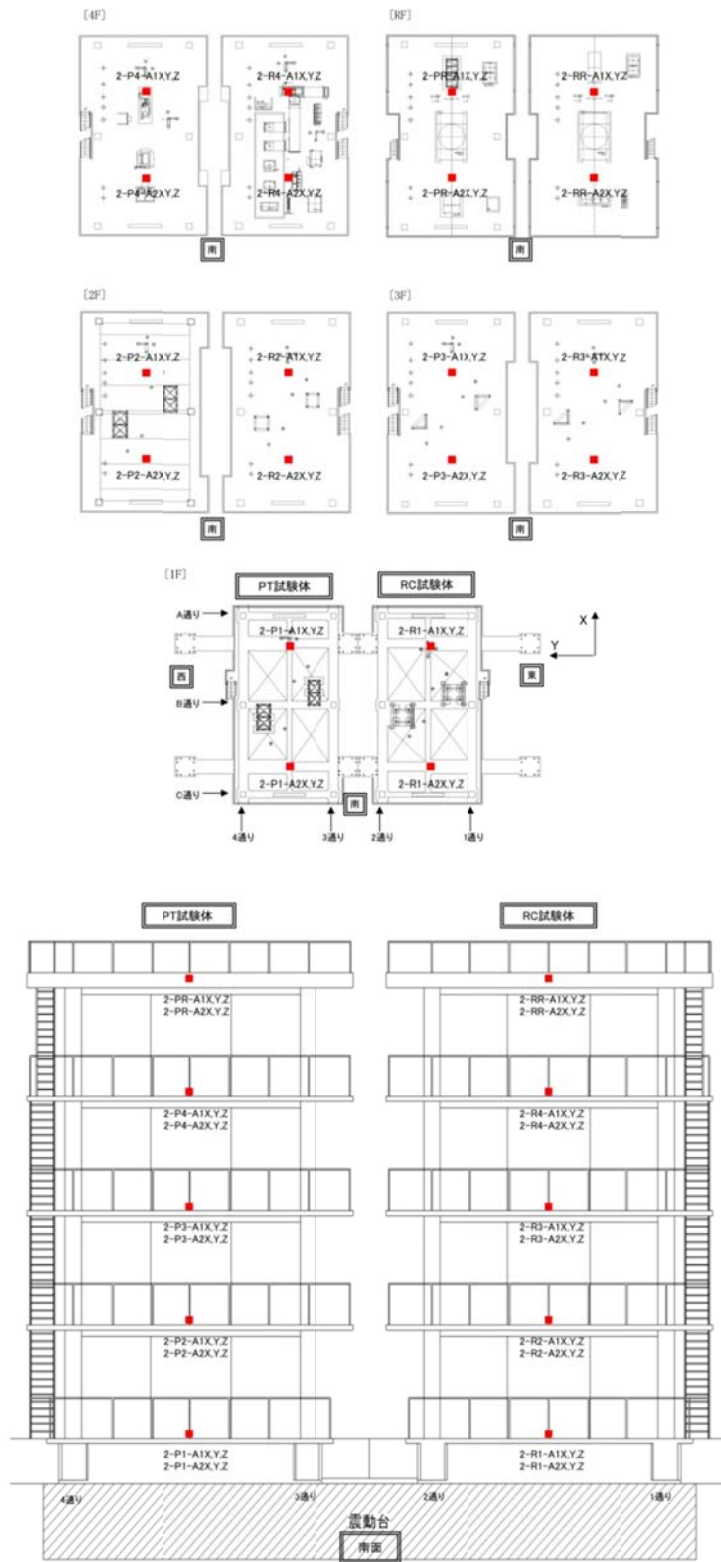
Figure 4.13 - Locations of accelerometers

4.2.6 Displacement Transducers

A total of 202 displacement transducers were used for the tests, including wire potentiometers, laser-type displacement transducers, and linear variable differential transducers (LVDTs). The transducers were attached to the test specimens to measure horizontal and vertical displacements, lateral story displacements and drifts, average concrete strains over gauge lengths, pullout/gapping at member ends, and sliding at the base of the shear walls. Locations of wire and laser transducers are shown in Figure 4.14 and Figure 4.15. A majority of the LVDTs were provided by NIED; however, some of the displacements transducers were provided by NEES@UCLA, IOWA State University, and the Earthquake Research Institute at the University of Tokyo; this enabled more detailed measurements of wall deformations (Figure 4.16). Four transducers were used over a gauge length of 540 mm at the base of the walls to enable the curvature along the wall length (depth) to be determined (Figure 4.16); additional displacement transducers were provided at each wall boundary over the entire height of the building (Figure 4.16). Two pairs of diagonally-oriented displacement transducers were used over the first-story height to enable the determination of shear deformations.
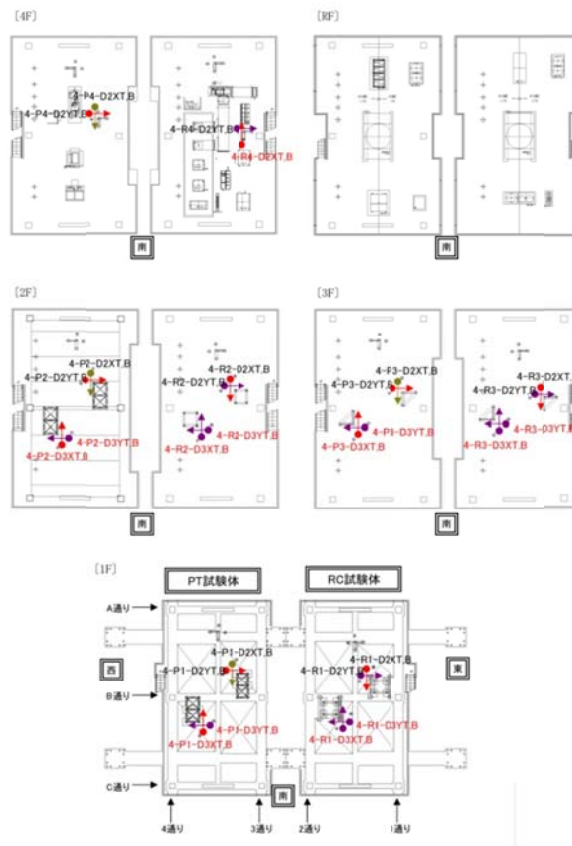
Figure 4.14 - Locations of displacement transducers

133
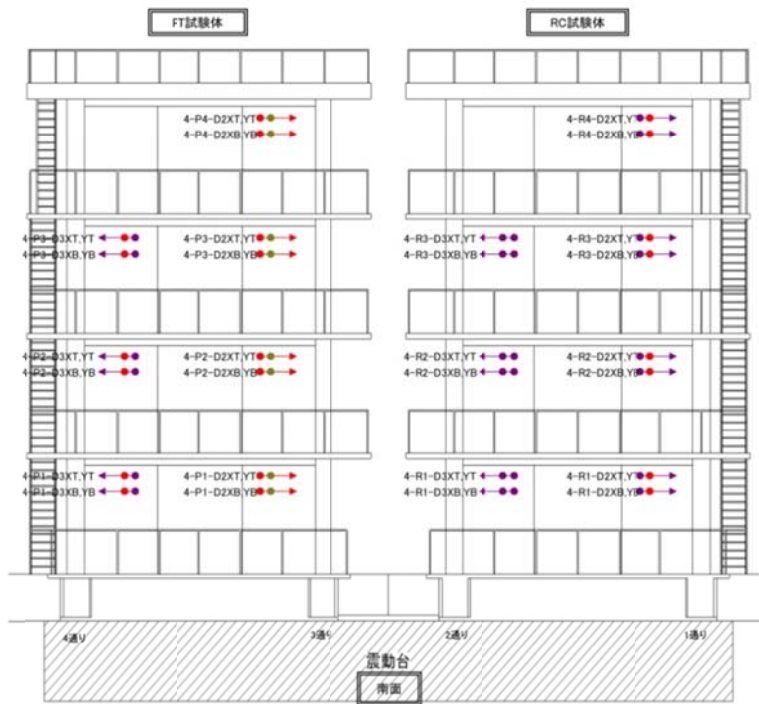
Figure 4.15 - Locations of displacement transducers
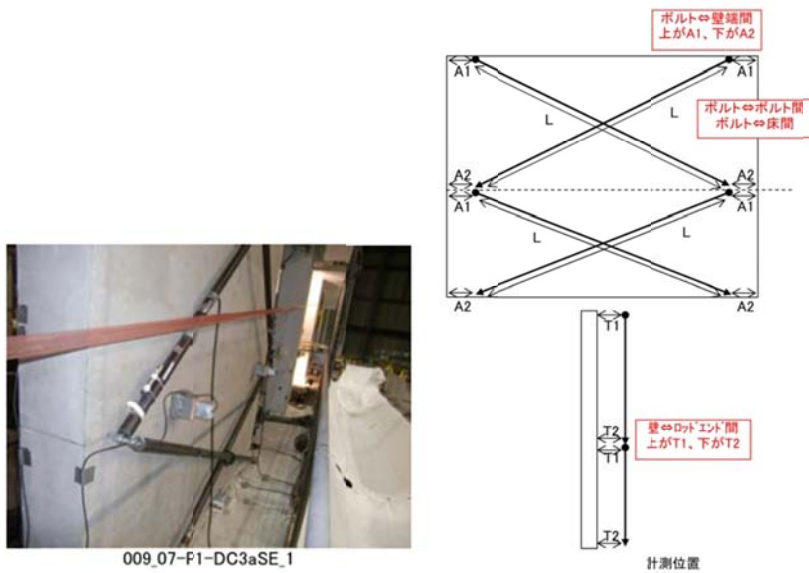
Figure 4.16 - Diagonal LVDT configuration

4.3   Test Results

Table 4.6 shows the maximum story drift ratios recorded in building for each direction and for different levels of excitation. The fundamental vibration periods measured using White Noise excitations prior to the applied ground motions, are also reported in Table 4.6. Figure 4.17 shows the maximum story drift ratio distribution of Axes 3a and B over the building height. For the 50% Kobe motion, the maximum story drift ratio was 0.004 for the X-direction and 0.006 for the Y-direction. Under the 100% Kobe motion, the maximum story drift values became 0.039 for the X-direction and 0.017 for the Y-direction. The height distribution of the story drifts in Figure 4.17.a show that the moment frame in the X-direction has a concentrated drift distribution at the first floor level, which is a typical mechanism for frame systems. On the other hand, the drift distribution shown in Figure 4.17.b, exhibits a uniform story drift distribution for the Y-direction. The uniform drift distribution is expected due to the structural walls and the rocking behavior. For the 60% Takatori motion, similar drift distributions are observed in both X and Y-directions. The maximum story drift ratio for this motion was 0.058 for the X-direction and 0.016 for the Y-direction. The measured fundamental period of the building was 0.45 seconds in the X-direction and 0.31 seconds in the Y-direction, after the 25% Kobe excitation. After the application of the 100% Kobe motion, the fundamental period of the building was measured to be 0.69 seconds in the X-direction and 0.52 seconds in the Y-direction. The fundamental period of the test specimen was measured to be 0.84 seconds for the X-direction and 0.55 seconds for the Y-direction after the 60% Takatori motion.

Table 4.6 - Maximum story drift ratio and fundamental vibration period (after Nagae et al. (2011))

No.	Input wave	Maximum story drift angle [rad]		Period [sec]	
		X-direction	Y-direction	X-direction	Y-direction
1	JMA-Kobe-10%	-	-	0.45	0.29
2	JMA-Kobe-25%	0.002	0.002	0.45	0.31
3	JMA-Kobe-50%	0.004	0.006	0.44	0.37
4	JMA-Kobe-100%	0.039	0.017	0.69	0.52
5	JR-Takatori-40%	0.014	0.009	0.68	0.51
6	JR-Takatori-60%	0.058	0.016	0.84	0.55
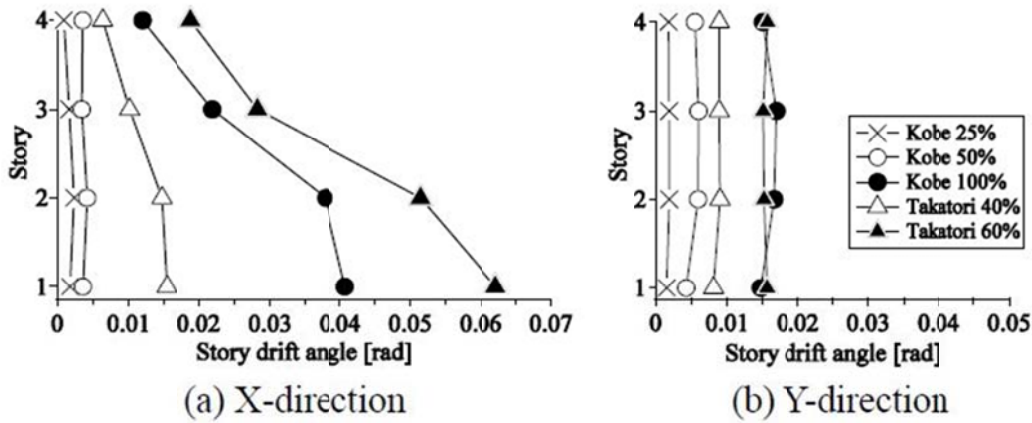
Figure 4.17 - Maximum story drift ratio distributions for each building directions (after Nagae et al. (2011))

The time variation of the roof drift ratio at difference axes of X and Y-directions are plotted on Figure 4.18, for the 100% Kobe motion. Figure 4.18.a shows that the roof drift ratio values of different axes in X-direction are substantially equal with a small variation in the 100% Kobe motion. On the other hand, the roof drift ratio measurements of the Y-direction show some variation in the different axes (Figure 4.18.b). Between 19-21 seconds of the motion, Axis A reaches around 0.01, whereas Axis C reaches a value of 0.02. This difference is possibly caused by the use of the steel fiber reinforced mortar in the first and second stories of the wall on Axis A. The use of the steel fiber reinforced mortar increased the stiffness of the wall on Axis A, causing a torsional response of the building.
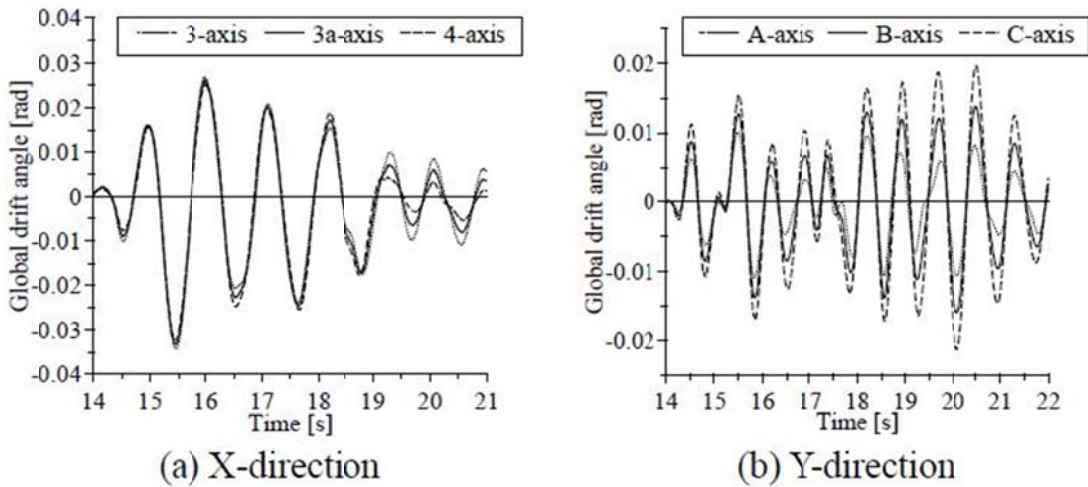
Figure 4.18 - Roof drift ratio–time relationship of each axes in Kobe 100% motion (after Nagae et al. (2011))

Figure 4.19 shows the damage at the first floor interior column base and at a second floor

136

interior joint after the 100% Kobe motion. The damage at the column base was concentrated at a height of 0.5 times the column dimension. Figure 4.20 shows the measurement locations and angle notations of the moment frame. Comparison of the exterior column base rotation to the first floor story drift for 50% and 100% Kobe motions are shown in the Figure 4.21. For the 50% Kobe motion, the column base reaches a rotation of 0.004, which is less than the first story drift measurements. For the 100% Kobe motion, shown in Figure 4.21.b, the first floor story drift reaches to a value of 0.04, and the column base rotation angle is almost equal to the story drift measurements. This deformation concentration might be caused by the concentrated damage at the column base.

(a) Interior column base   (b) Interior joint of 2-fl.
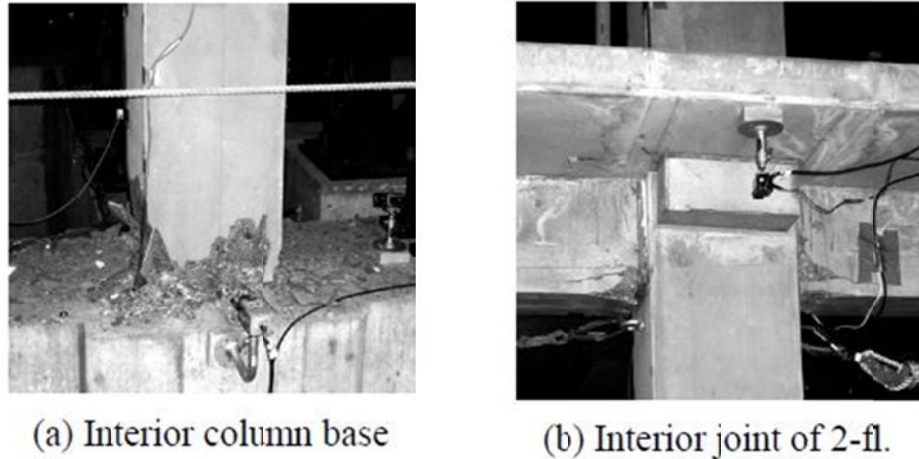
Figure 4.19 - Damage at the X-direction after 100% Kobe motion (after Nagae et al. (2011))
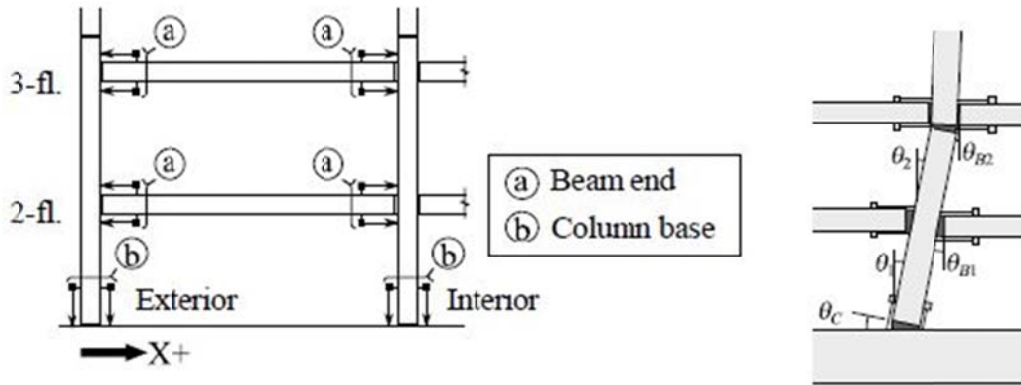
Figure 4.20 - Moment frame deformations (after Nagae et al. (2011))
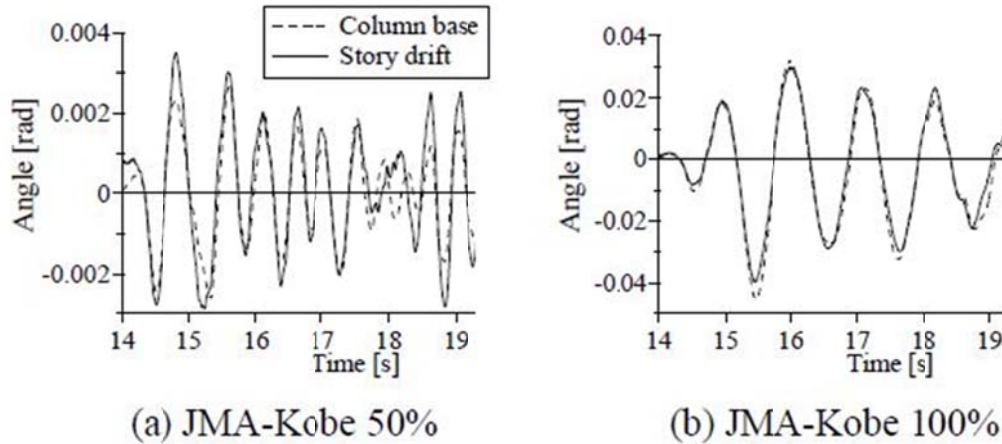
Figure 4.21 - Exterior column base rotation (after Nagae et al. (2011))

The maximum story drift ratios and the beam end rotation values are plotted in Figure 4.22 for 50% and 100% Kobe motions. For the 50% Kobe motion, the beam end rotation was 0.65 times of the story drift ratio values. For the 100% Kobe excitation, the story drift ratio and the beam end rotation angle have almost the same value of 0.04 rad for the first floor. However, the third floor beam end rotation is only 0.5 times of the second story drift ratio. This difference is caused by the aforementioned damage concentration in the frame system.

Figure 4.23 shows the damage of the wall in the Y-direction of the building after the 100% Kobe motion. The concrete cover at the boundary regions was spalled at the wall base. This wall damage had a height of approximately one wall thickness. Figure 4.24 shows the wall deformations and measurements of the rotation angles, and the wall slip. The wall base rotation angle and slip measurements are plotted against story drift values under the 100% Kobe motion in Figure 4.25. The story drift ratio and base rotation angle values are almost identical during the excitation, and measured wall base slip is ignorable compared to the other values. Figure 4.26 shows the ratios of the wall deformation contributions of wall base rotation and wall slip. In all motions the wall rotation angle of the first floor is larger than the upper floors. Especially, at 100% Kobe motion the first floor rotation becomes very dominant. Similar to the previous findings, the contribution of wall slip is very small.
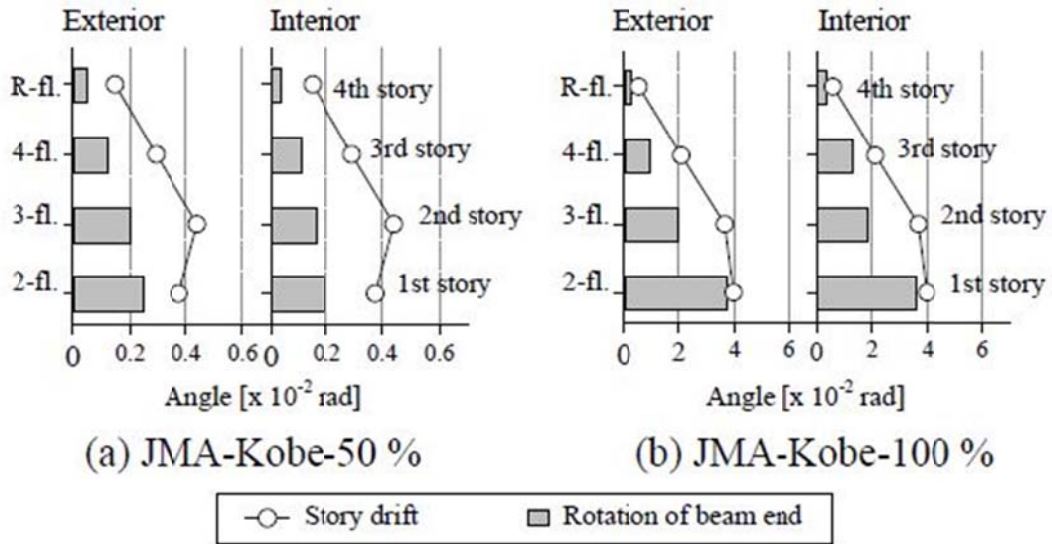
Figure 4.22 - Beam end rotation and story drifts (after Nagae et al. (2011))

Figure 4.23 - Y-direction damage after 100% Kobe motion (after Nagae et al. (2011))
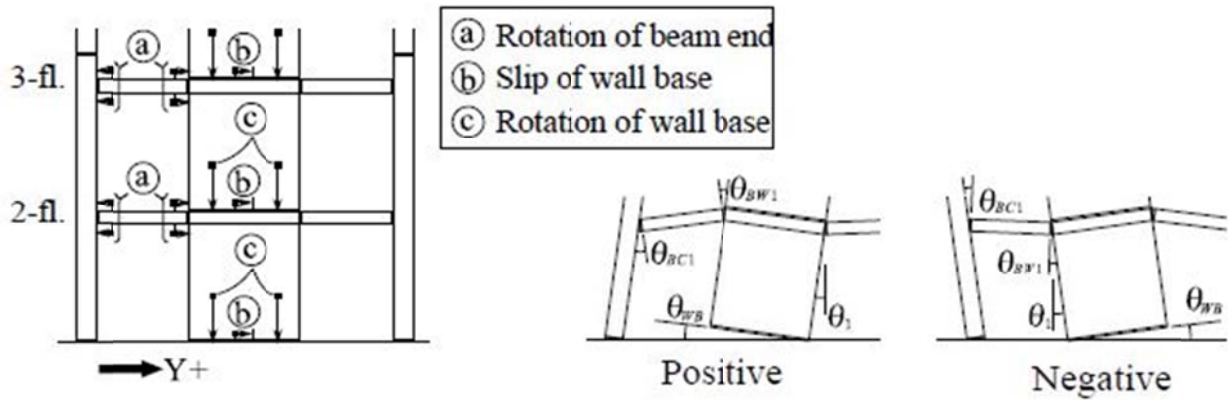
Figure 4.24 - Wall deformations (after Nagae et al. (2011))
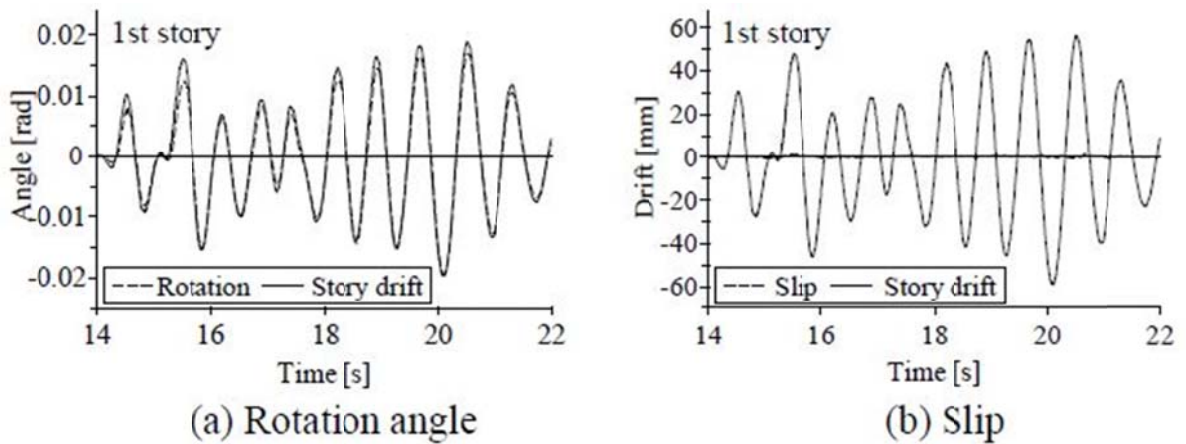
Figure 4.25 - Wall base deformations for 100% Kobe motion (after Nagae et al. (2011))
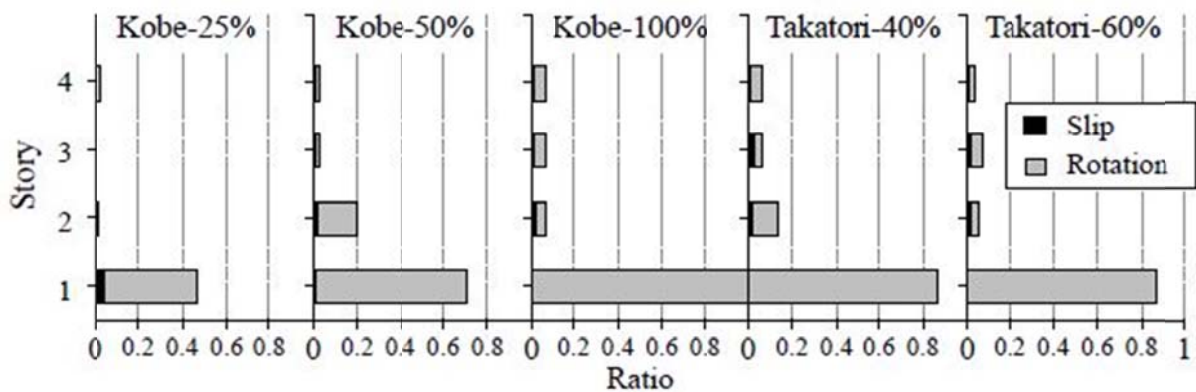
Figure 4.26 - Wall deformation ratios of rotation and slip (after Nagae et al. (2011))

Figure 4.27 and Figure 4.28 show the base shear-roof drift ratio and the time variation of the base shear force X and Y-directions for the 50% and 100% Kobe motions, respectively. For the 50% scaled Kobe motion the response seems almost linearly elastic with no significant decrease in the stiffness for both building directions. On the other hand, for the 100% Kobe excitation, both X and Y-directions experienced stiffness deterioration due to the damage. In the X-direction, the large BC cycle reaching 0.03 rad caused significant stiffness deterioration. In the Y-direction, the maximum base shear values are achieved at the cycle AB. After this cycle the stiffness slowly degraded in cycles CF, and reached a drift ratio of 0.017.

Figure 4.29 shows the distribution of the maximum story shear to the first story shear ratio. The solid lines show the absolute maximum values of the story shear for each floor. The dashed lines represent the story shear distribution at the moment of the peak base shear during the excitation. The Ai distribution represents the design shear distribution according to the Japanese code. The design shear distribution has a good match with the separate maximum shear values. In the X-direction, the maximum base shear distributions are uniform for all excitations.
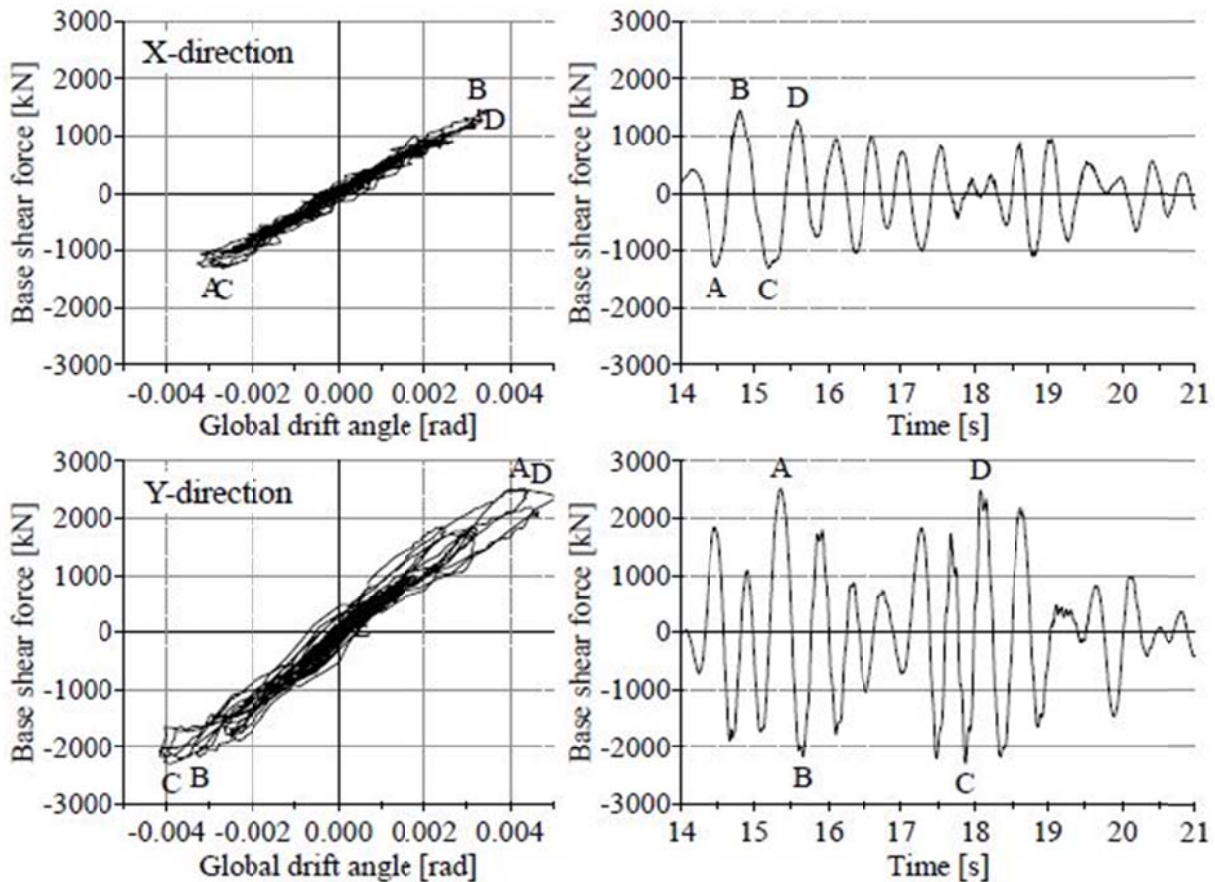
Figure 4.27 - Global response for 50% Kobe motion (after Nagae et al. (2011))

141
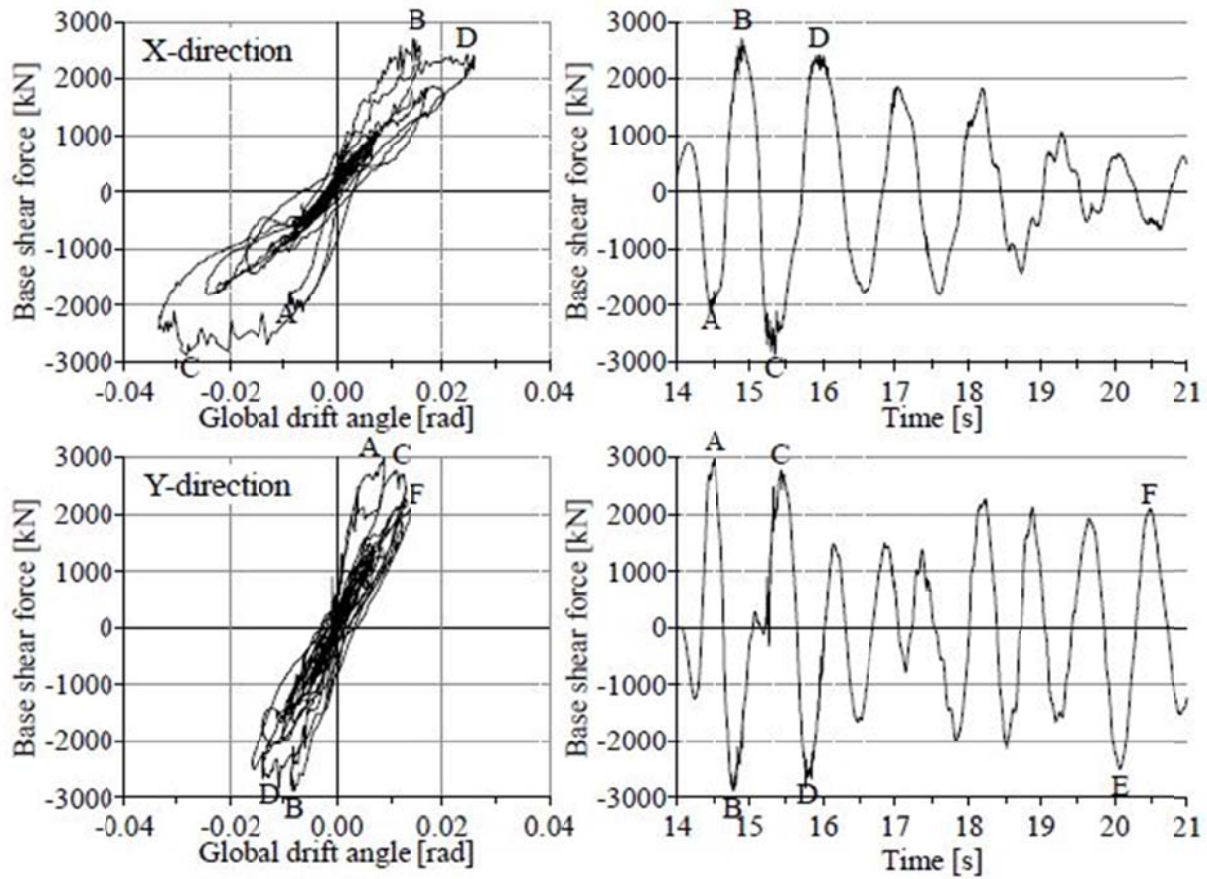
Figure 4.28 - Global response for 100% Kobe motion (after Nagae et al. (2011))
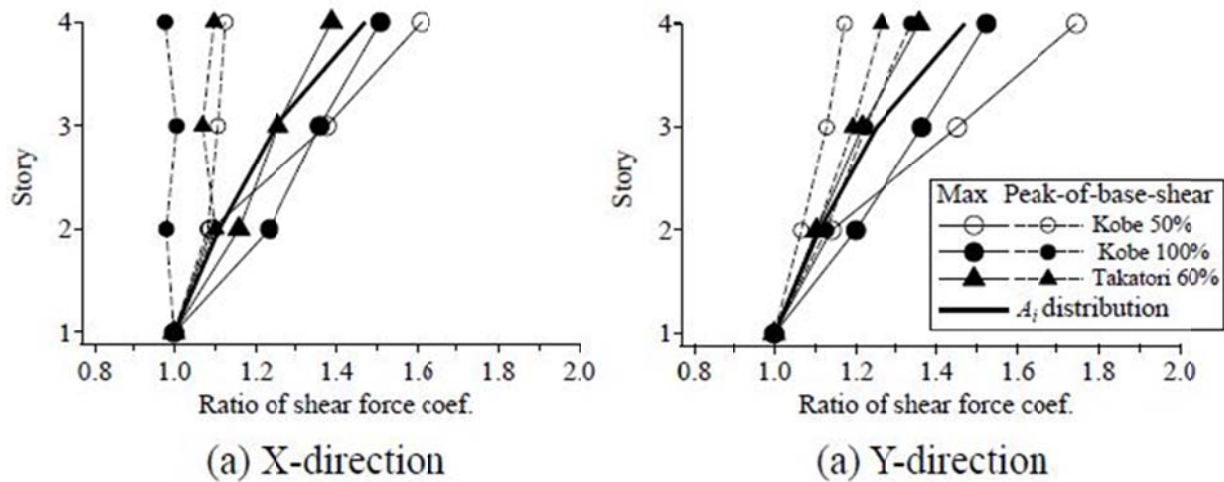
Figure 4.29 - Maximum shear force distribution through the height (after Nagae et al. (2011))

The analytical study presented in this chapter focuses on the response and modeling of the Y-direction of the building with an interest in the rocking precast post-tensioned shear wall. For convenience the base shear-roof drift ratio relationship of the building in Y-direction is plotted for 25%, 50% and 100% Kobe motions in Figure 4.1. Figure 4.31, Figure 4.32, and Figure 4.33 show the time variation of the roof drift ratio response of the test specimen in Y-direction for 25%, 50%, and 100% Kobe motions, respectively. Similarly, Figure 4.34, Figure 4.35, and Figure 4.36 show the time variation of the base shear force of the Y-direction for 25%, 50%, and 100% Kobe motions, respectively.
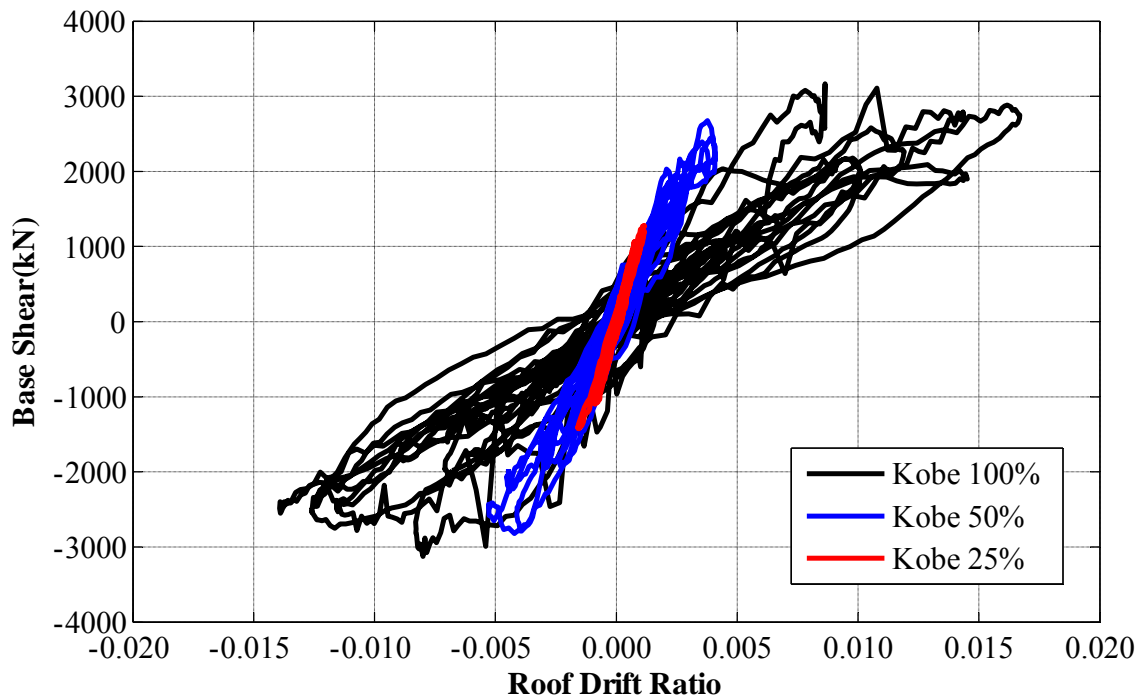
Figure 4.30 - Base shear-roof drift ratio relationship of test results for 25%, 50%, and 100% Kobe motions
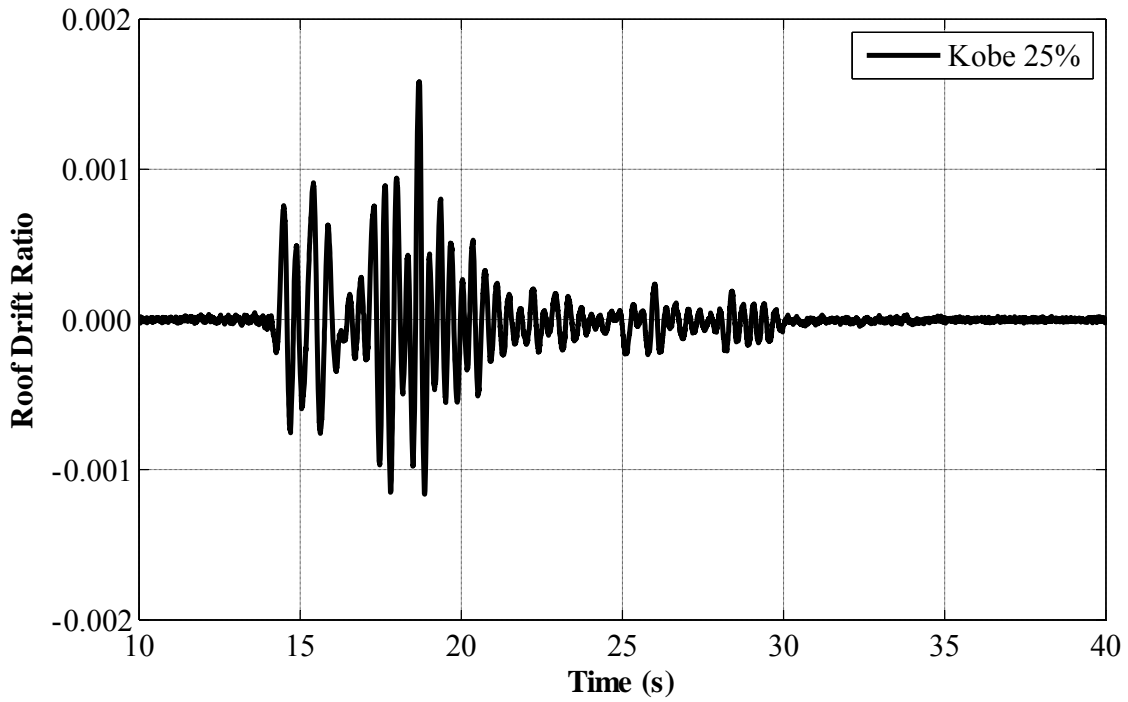
Figure 4.31 - Roof drift ratio-time comparison of results for 25% Kobe motion
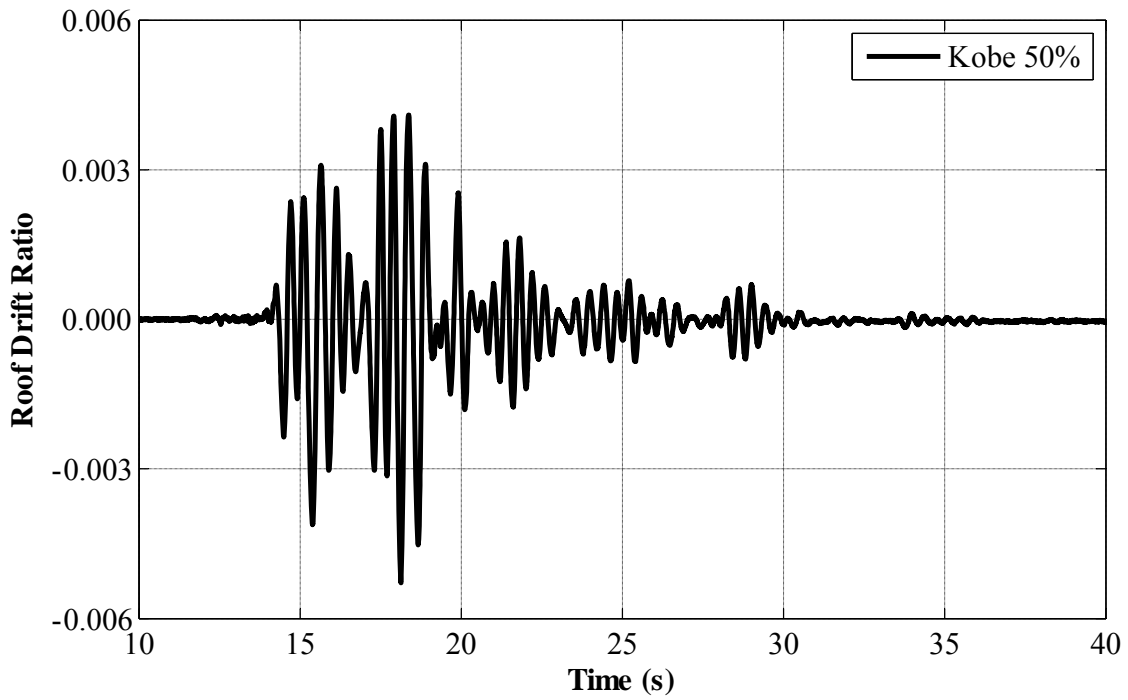
Figure 4.32 - Roof drift ratio-time comparison of results for 50% Kobe motion

144
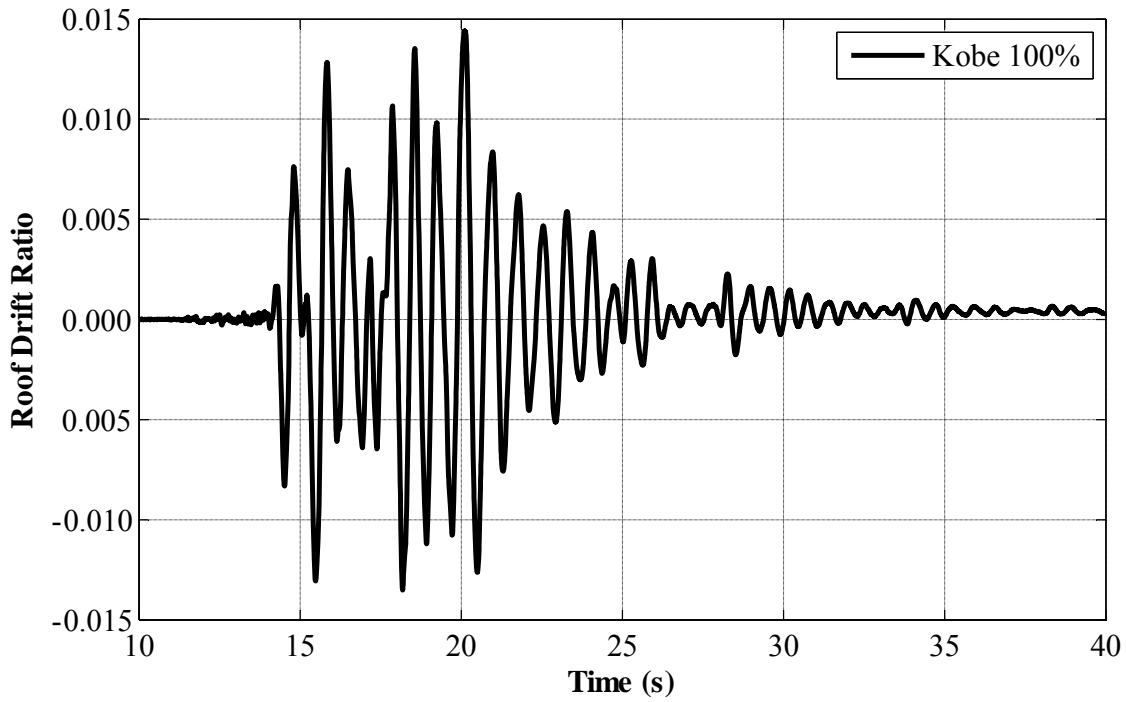
Figure 4.33 - Roof drift ratio-time comparison of results for 100% Kobe motion
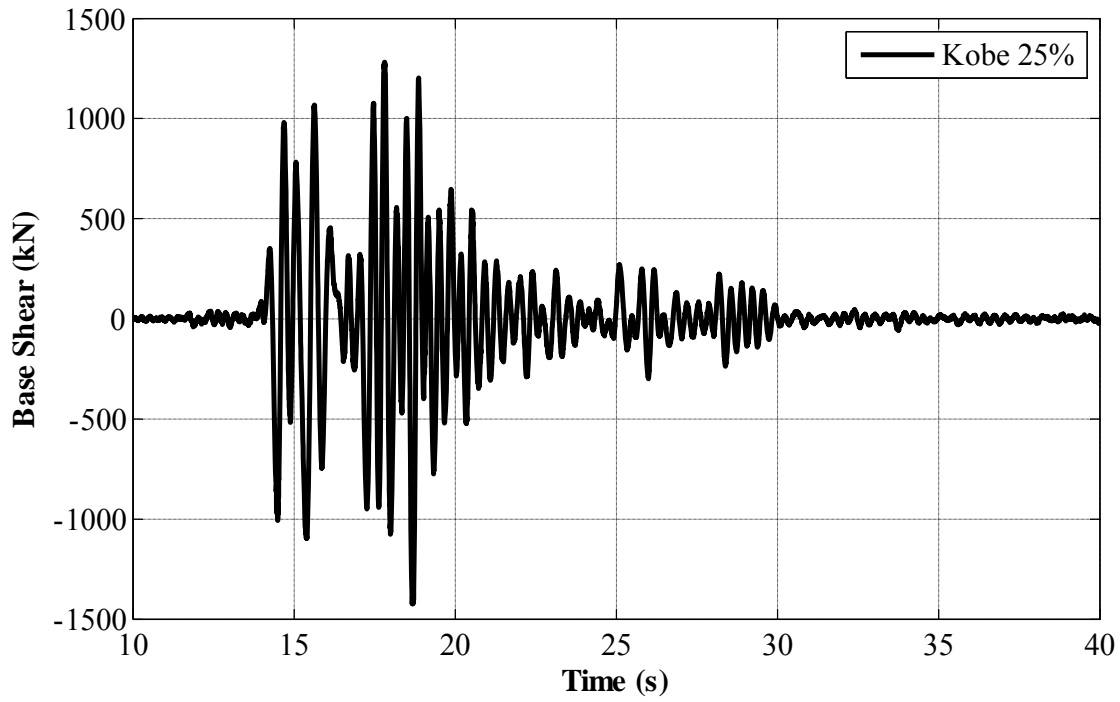
Figure 4.34 - Base shear-time comparison of results for 25% Kobe motion

145
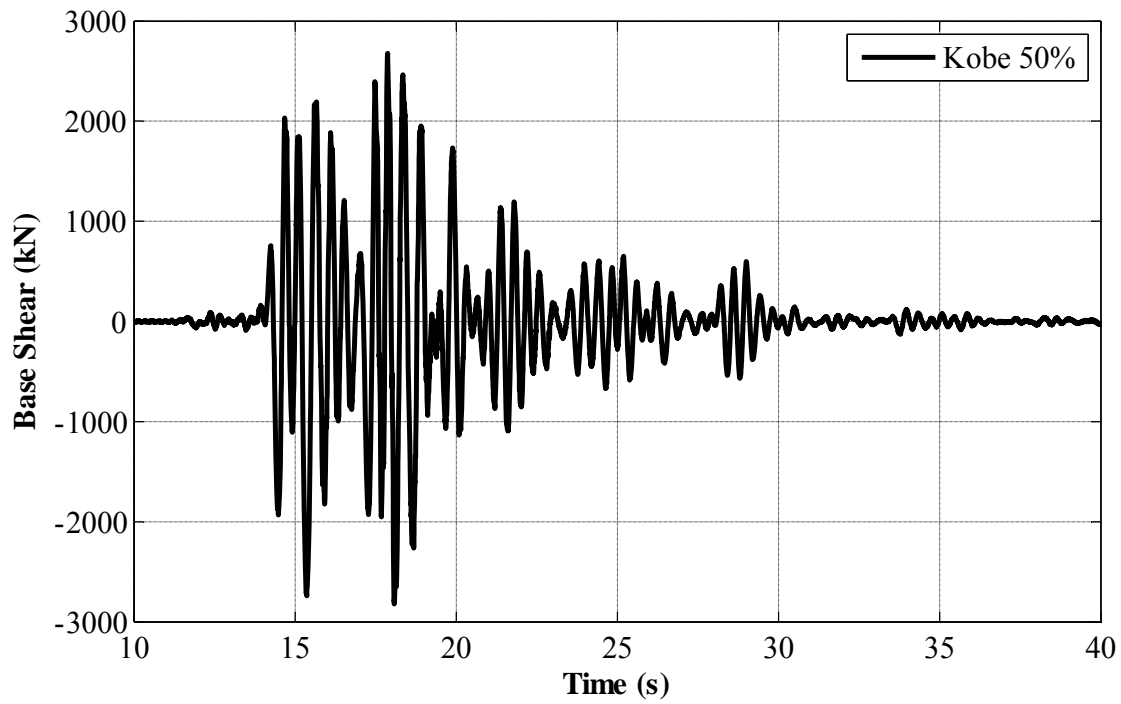
Figure 4.35 - Base shear-time comparison of results for 50% Kobe motion
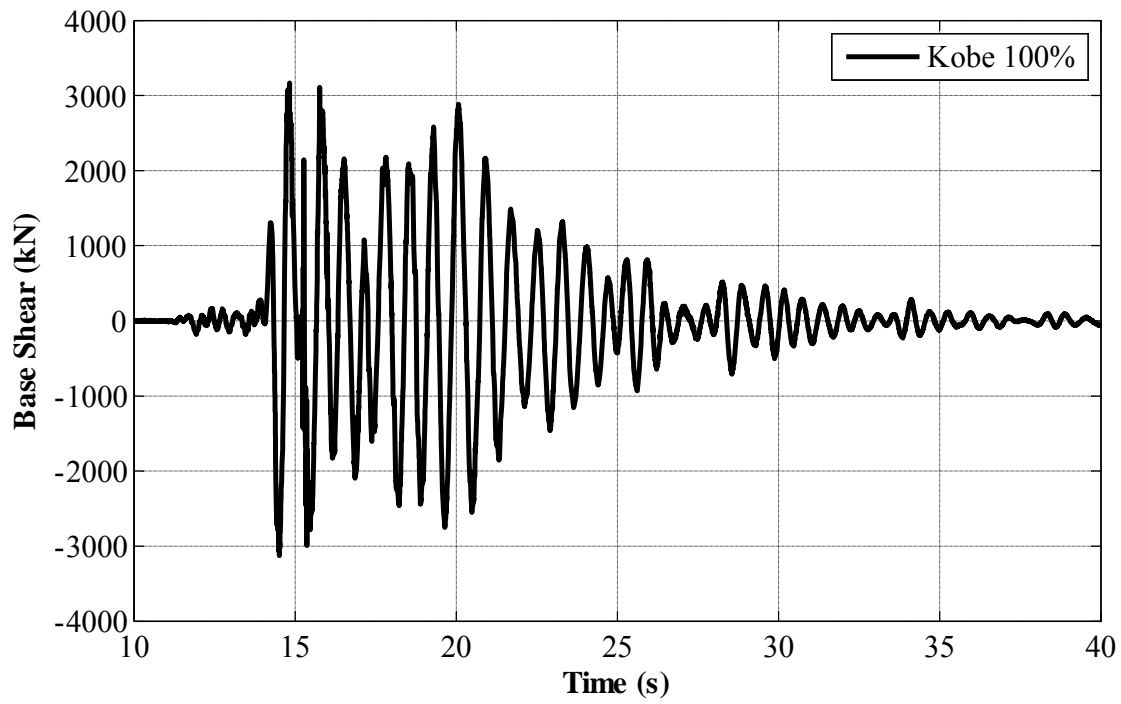
Figure 4.36 - Base shear-time comparison of results for 100% Kobe motion

146

4.4   Analytical Simulation

A three-dimensional analytical model of the Y-direction of the specimen was implemented using the computer program Perform 3D (CSI).

4.4.1   Perform 3D

PERFORM-3D *Nonlinear Analysis and Performance Assessment for 3D Structures* (Computers and Structures, Incorporated) is a commercially available modeling and analysis software useful for the performance assessment of structural systems. Figure 4.37 shows the component-level force-deformation relationships available in the program. This tri-linear force-deformation relationship with strength loss can be used at the material level to represent stress-strain relationships or at the section level to represent concentrated plasticity springs in moment-rotation relationships. Strength and stiffness degradation may be modeled during cyclic response (Figure 4.38). Geometric nonlinearity can also be accounted for in the analysis.
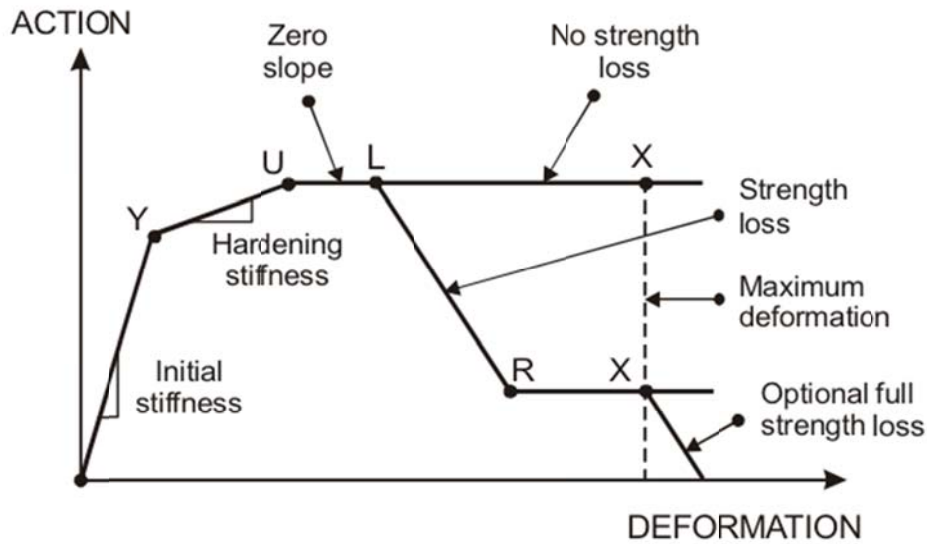
Figure 4.37 - Perform 3D general force-deformation relationship

147
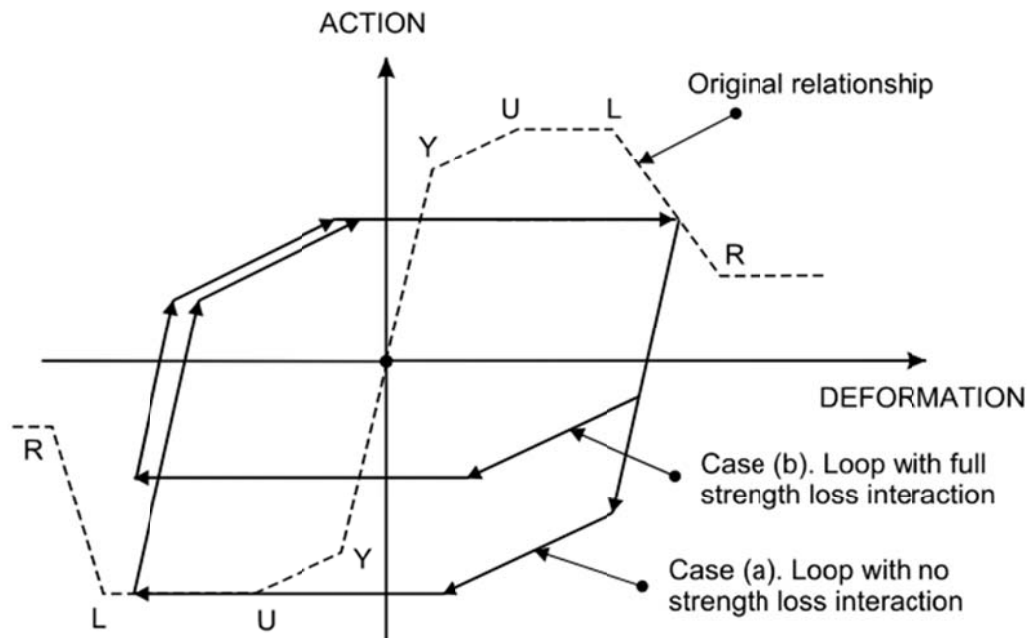
Figure 4.38 - Perform 3D strength loss interaction

4.4.2 Shear Wall Model

Structural walls were modeled using four-noded "Shear Wall Elements" (CSI). The axial forces and bending moments on axis 2 are resisted by fiber cross sections (Figure 4.39.a). In this implementation, all interconnected planar wall segments at any level are assumed to remain plane when deformed. Shear forces on the element can be resisted by either a concrete shear option (Figure 4.39.c) or a combination of diagonal compression and fiber cross sections on axis 3 (Figure 4.39.e and Figure 4.39.b). All of the aforementioned layers are acting in parallel. Material properties assigned to the fibers are uniaxial properties and the shear layer is uncoupled from the axial loads or bending moments acting on the element. Ignoring this interaction can lead to misleading results. However, in the case of PT walls in this test, shear deformations were essentially linearly-elastic such that the interaction can be neglected. Out-of-plane bending of the element is assumed to be linearly-elastic.

In the first story, where inelastic actions were expected to concentrate, shear wall elements were meshed so that each element had a height of $2b_w$ (b_w = wall thickness). This value is established from post-earthquake observations of the typical height of spalled regions from the 2010 Chile and New Zealand earthquakes. For the rest of the building, larger sized elements are used. From the second to the fourth floor, two elements per story height are used.
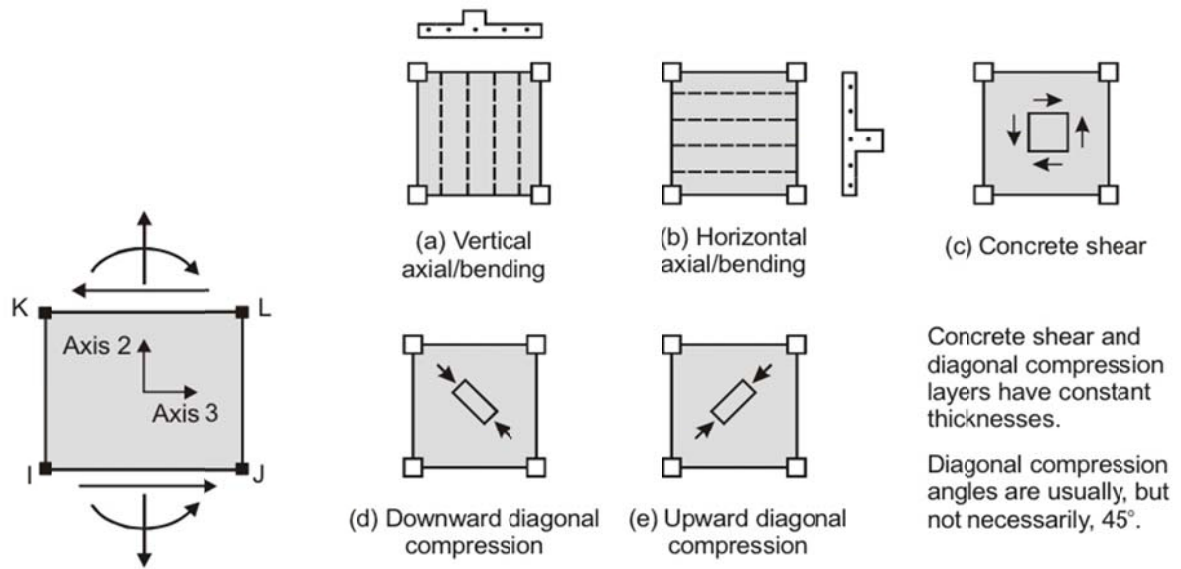
Figure 4.39 - Shear wall element (CSI)

The constitutive material model for concrete is an idealization of material tests using a trilinear curve with a descending portion (Figure 4.40). The stress-strain relationship for confined concrete is implemented using the confinement model for high-strength concrete developed by Razvi & Saatcioglu (1999). Tension resistance of concrete is modeled except for the rocking sections. Similarly, the reinforcing steel stress-strain relation was a simplified trilinear curve with a descending portion (Figure 4.41).
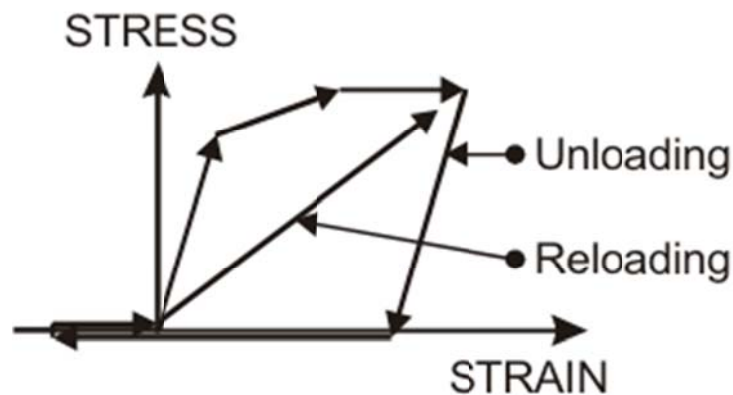
Figure 4.40 - Concrete material in Perform 3D (CSI)
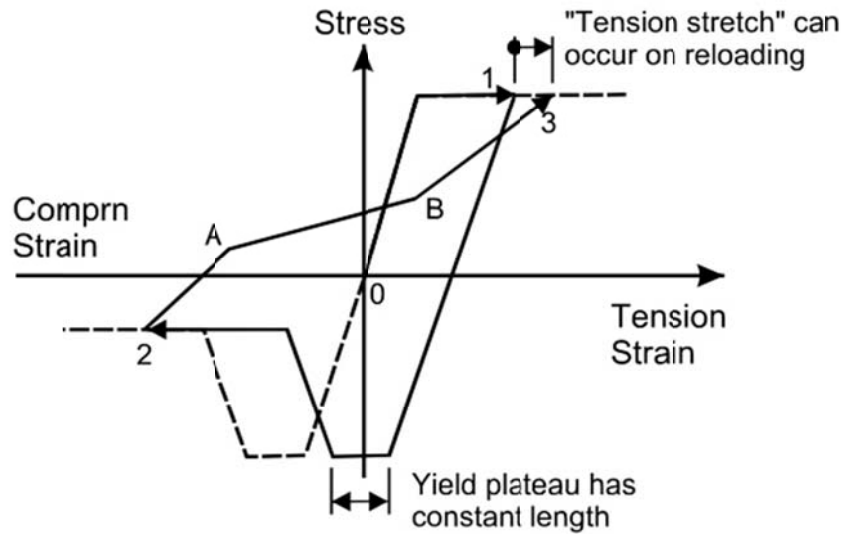
Figure 4.41 - Steel material in Perform 3D (CSI)

The shear wall element available in Perform 3D allows the maximum number of fibers to be defined as sixteen in a cross section. As a result, there was a need to divide the wall cross section into multiple elements. Walls had a symmetrical cross section with respect to the center-line of the wall. For each floor, different fiber cross sections were used to represent the boundary elements and the rest of the cross section. In the structural engineering community of the West Coast of the United States, it is a common practice to ignore the cover concrete of the walls, due to the fact that the shear wall element of Perform 3D allows only one row of fibers to be defined. For this study, the effect of cover concrete is not insignificant, and should be modeled. Every cross section was divided into cover and core concrete parts, and cover concrete portions of the cross section were assigned to a parallel element. The in-plane second moment of inertia of the section is calculated accurately with this modeling method; however the calculated out-of-plane second moment of inertia is not correct. Figure 4.42 shows the fiber cross sections of parallel "core" and "cover" elements for the first-story boundary element. Concrete and steel stress-strain relationships used for the first-story boundary element cross sections are shown in Figure 4.43 and Figure 4.44. Unconfined and confined concrete properties were used for "cover" and "core" elements respectively. The stress-strain relationship for confined concrete is implemented using the confinement model for high-strength concrete developed by Razvi & Saatcioglu (1999). The ultimate strain of reinforcing steel in tension was limited to 0.05 in consideration of cyclic fatigue (PEER/ATC-72-1). Behavior in compression was checked according to the ratio s/d_b (s = spacing of transverse reinforcement and d_b = diameter of longitudinal bar) in consideration of longitudinal bar buckling (Monti and Nuti, 1992). The adequately small s/d_b ratio is such that reinforcing bars are unlikely to buckle prematurely. The ultimate strain of reinforcing steel under compression is limited to 0.02 (PEER/ATC-72-1). Material stress-strain relationship properties were decided according to the material sample test results (Table 4.3).
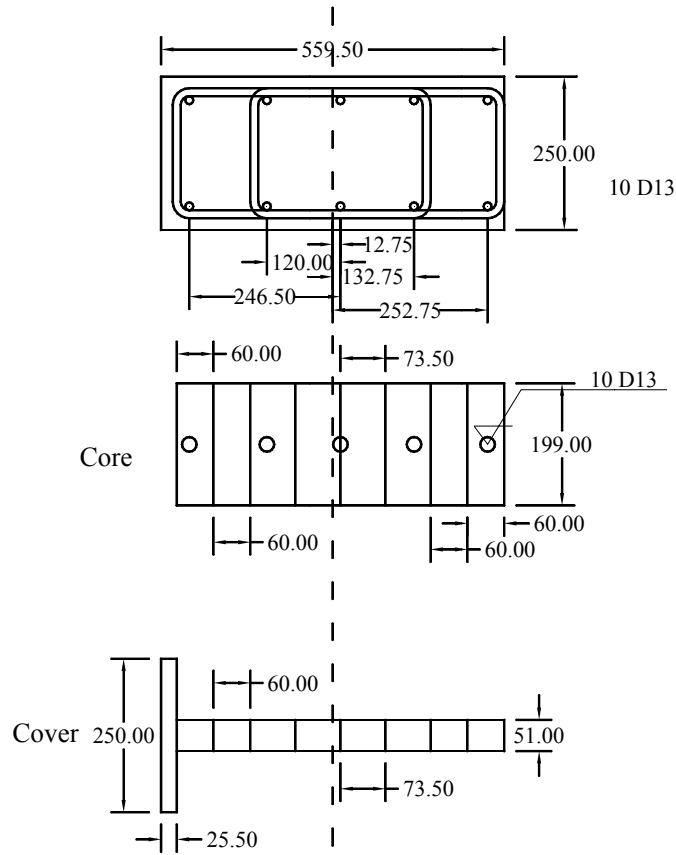
Figure 4.42 - First-story boundary element cross section (Units: mm)
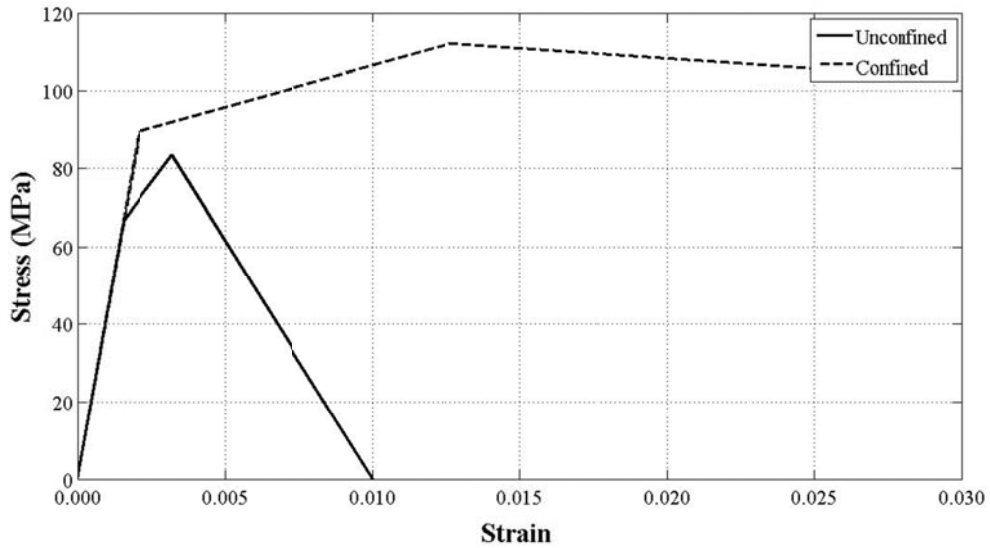
Figure 4.43 - Concrete stress-strain relationships used for 1st story boundary element

151
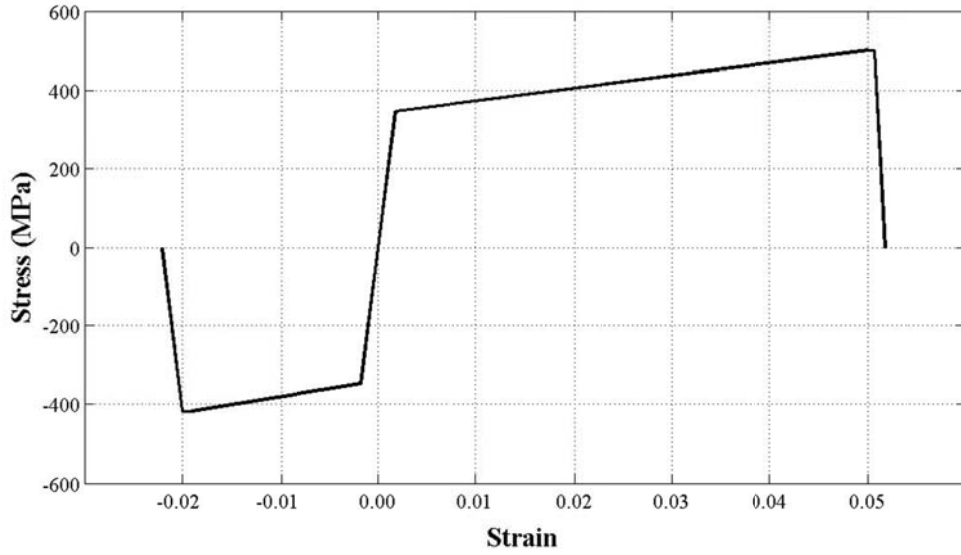
Figure 4.44 - Steel stress-strain relationships used for 1st story boundary element
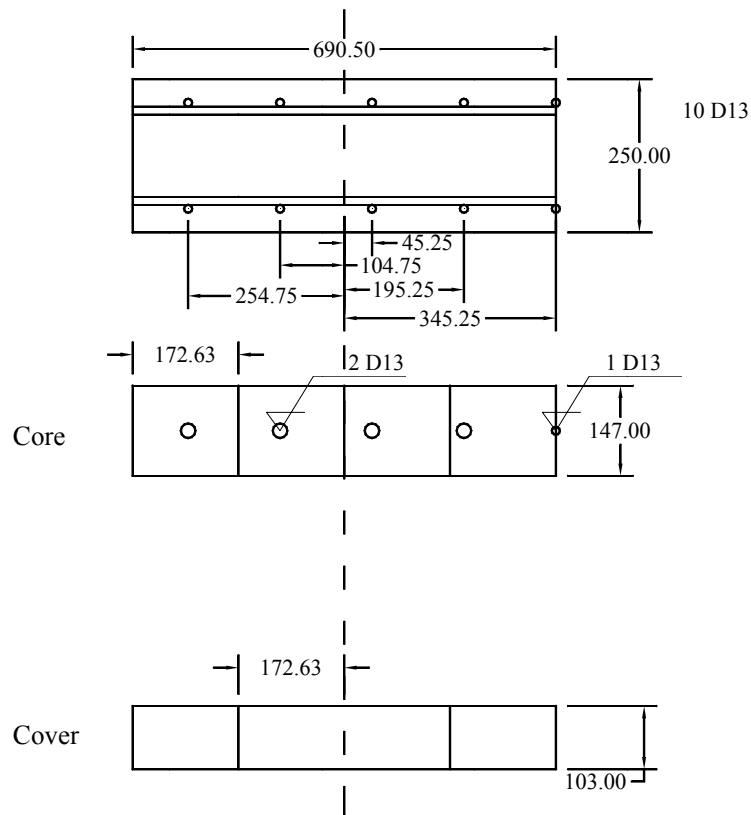
Figure 4.45 - First-story mid-section element cross section (Units: mm)

Similarly, Figure 4.45 shows the "core" and "cover" sections for the first-story mid-section of the wall. Concrete and steel material stress-strain relationships are shown in Figure 4.46 and

Figure 4.47. Similar plots are shown for the second-story boundary section and second-story mid-section in Figure 4.48,Figure 4.49 and Figure 4.50, and in Figure 4.51, Figure 4.52 and Figure 4.53, respectively.
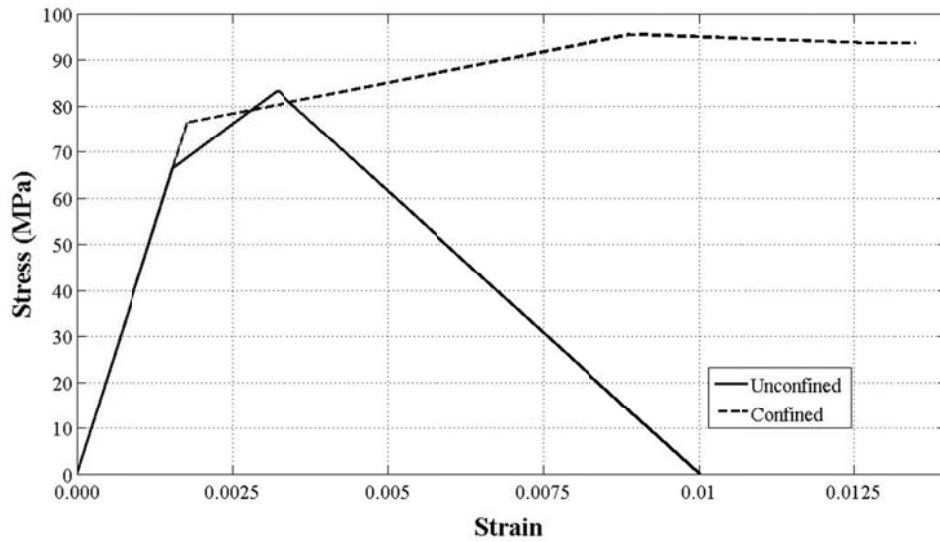
Figure 4.46 - Concrete stress-strain relationships used for 1st story boundary element
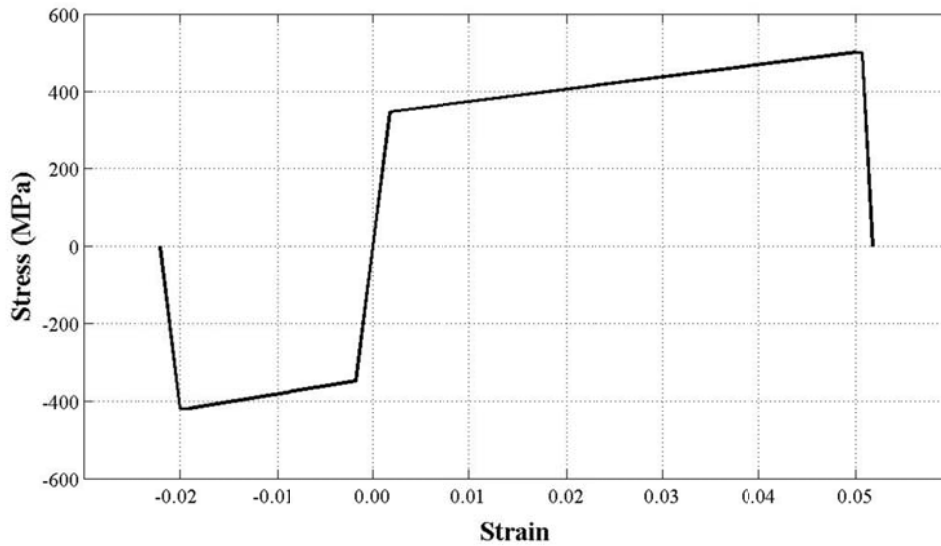
Figure 4.47 - Steel stress-strain relationships used for 1st story boundary element

153
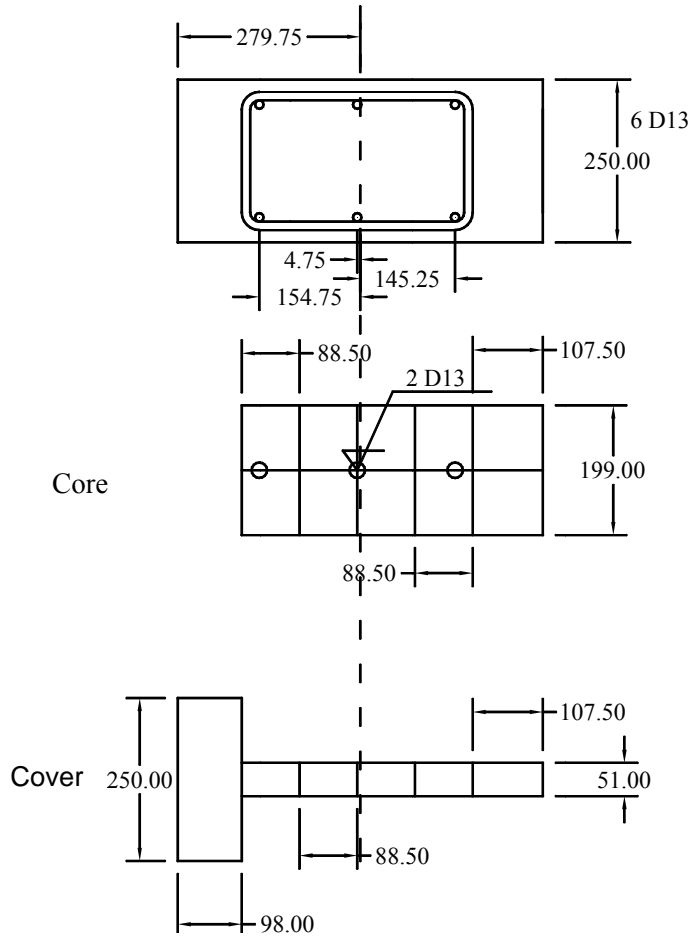
Figure 4.48 - Second-story boundary element cross section (Units: mm)
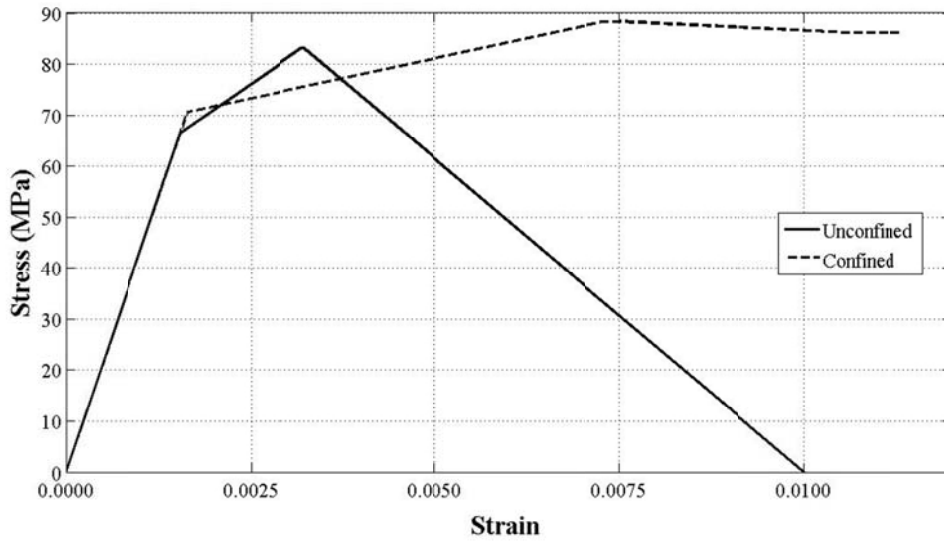
Figure 4.49 - Concrete stress-strain relationships used for 1st story boundary element

154
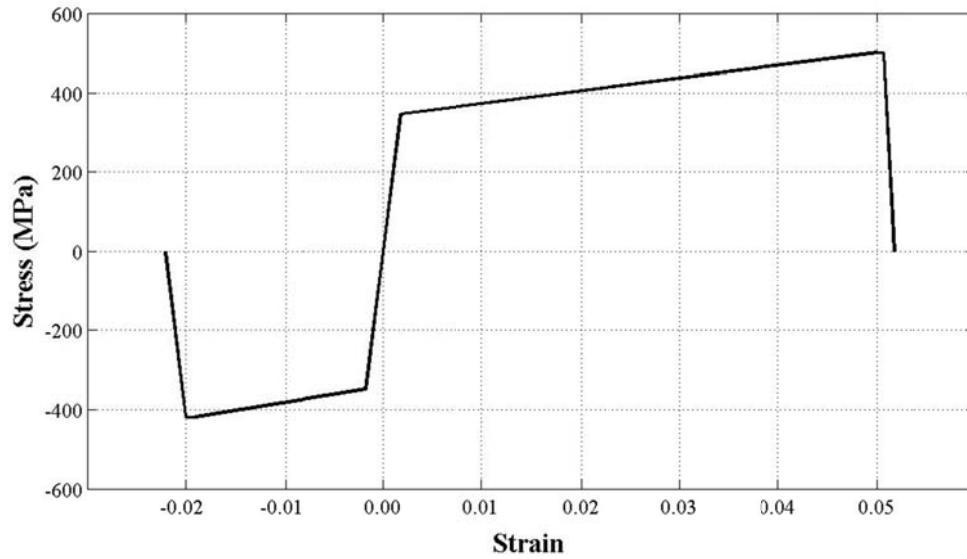
Figure 4.50 - Steel stress-strain relationships used for 2nd story boundary element
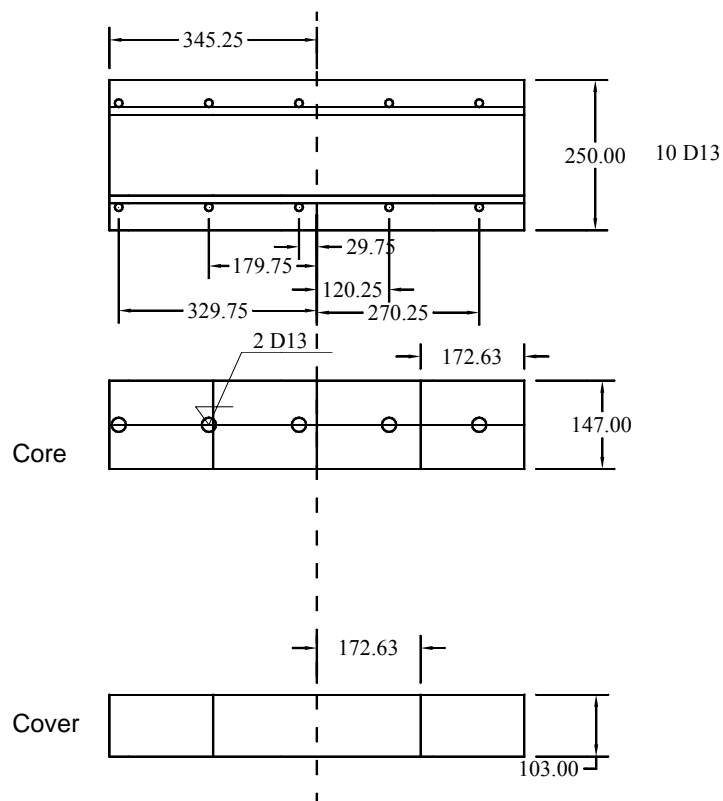
Figure 4.51 - Second-story mid-section element cross section (Units: mm)

155
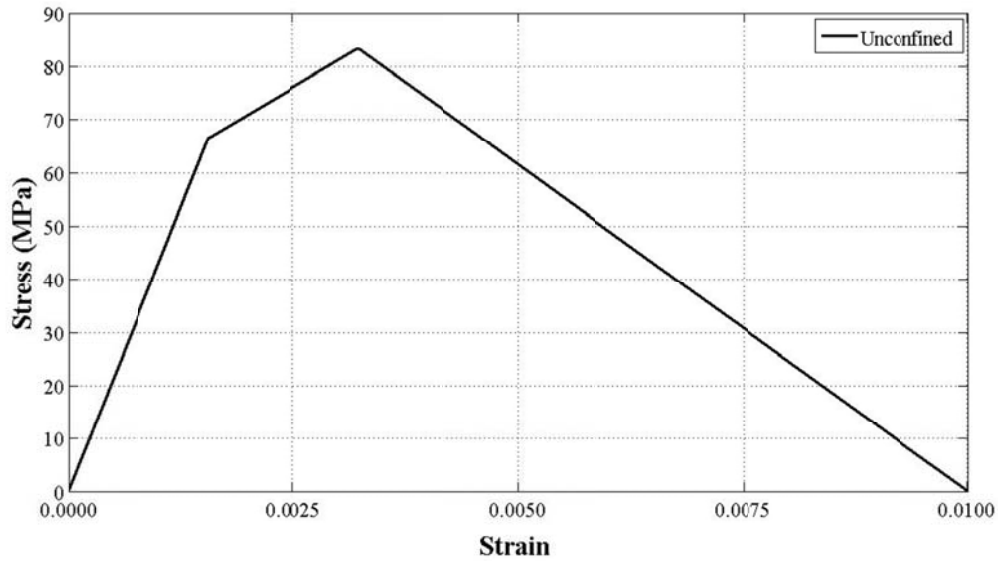
Figure 4.52 - Concrete stress-strain relationships used for 1st story boundary element
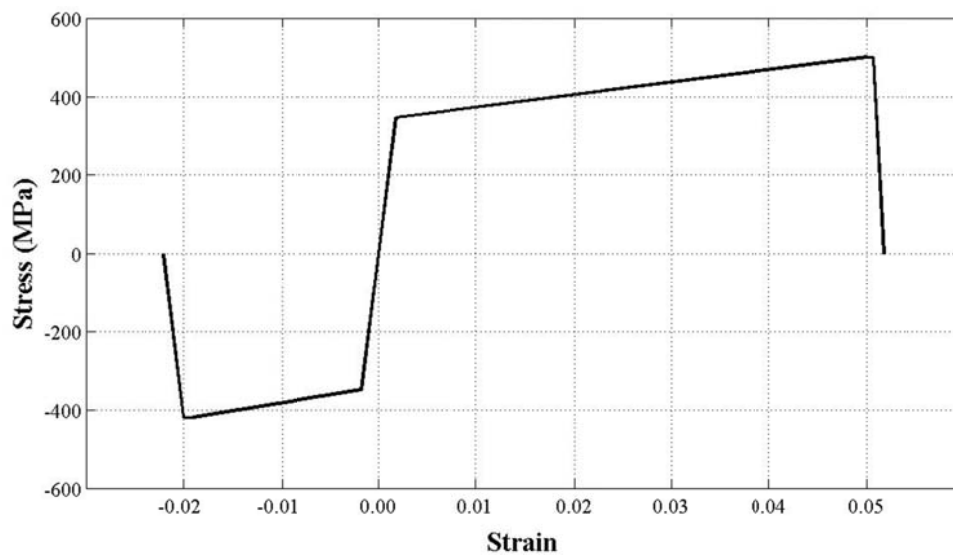
Figure 4.53 - Steel stress-strain relationships used for 2nd floor mid-section element

Due to anticipated low shear demands, an elastic shear material was used for walls (concrete shear layer Figure 4.39.c), with effective shear stiffness defined as $G_cA_w = 0.4E_cA_w/20$ (PEER/ATC- 72-1), in which $0.4E_c$ approximates the shear modulus G_c, E_c is Young's modulus of concrete (taken as $4700\sqrt{f_c'}$, MPa, where f_c' is the specified concrete compressive strength), and A_w is web area, and the divisor 20 represents stiffness reduction associated with concrete cracking.
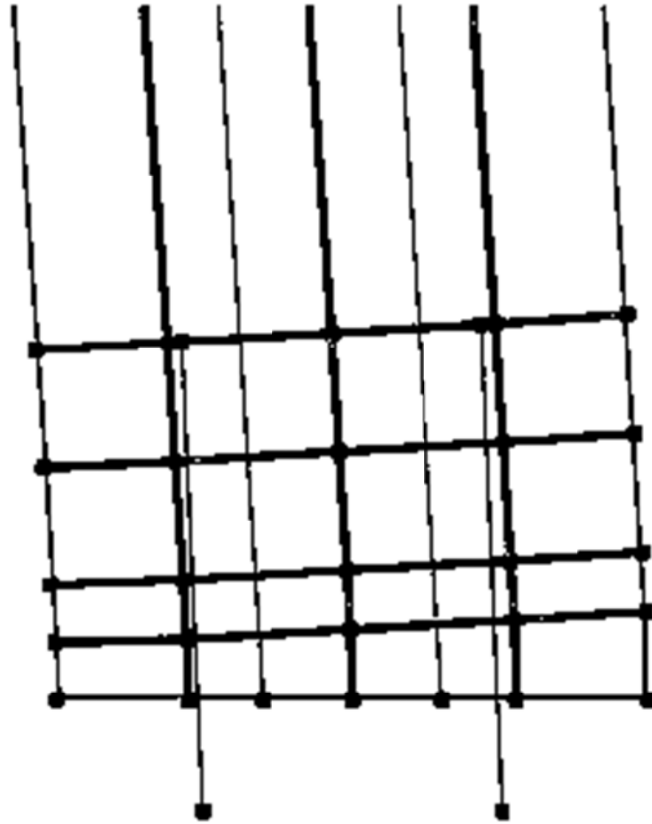
Figure 4.54 - Rocking section at foundation level

Although mortar was used between wall panels at each floor level and foundation level, gap openings between wall panels was observed during the test. Therefore, rocking behavior of wall segments is implemented for wall elements at each floor level (Figure 4.54). These "rocking" wall elements had a height of b_w (b_w = wall thickness). The selected element height was the smallest number within reason given possible convergence issues. However, there was no further investigation done on the effect of element height to the response. This behavior is achieved through modifying material models assigned to fiber sections to have no tension resistance, keeping the compression stress-strain relationship the same (Figure 4.55 and Figure 4.56). Figure 4.54 shows the elements rocking at the foundation level. It is worth noting that Perform 3D assumes linear strain distribution in fiber cross sections, and this assumption is not true for a rocking concrete surface. Moreover, this behavior causes large displacements in small sized elements, which can cause numerical problems. However, there were no numerical problems encountered during analyses of the test structure.

157
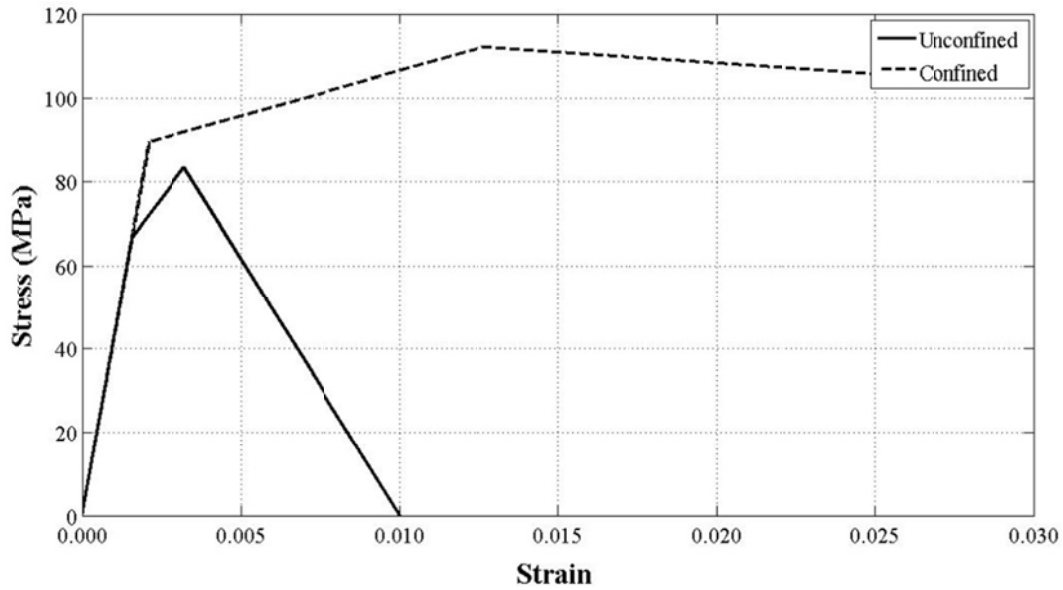
Figure 4.55 - Concrete stress-strain relationships used for 2nd floor mid-section element
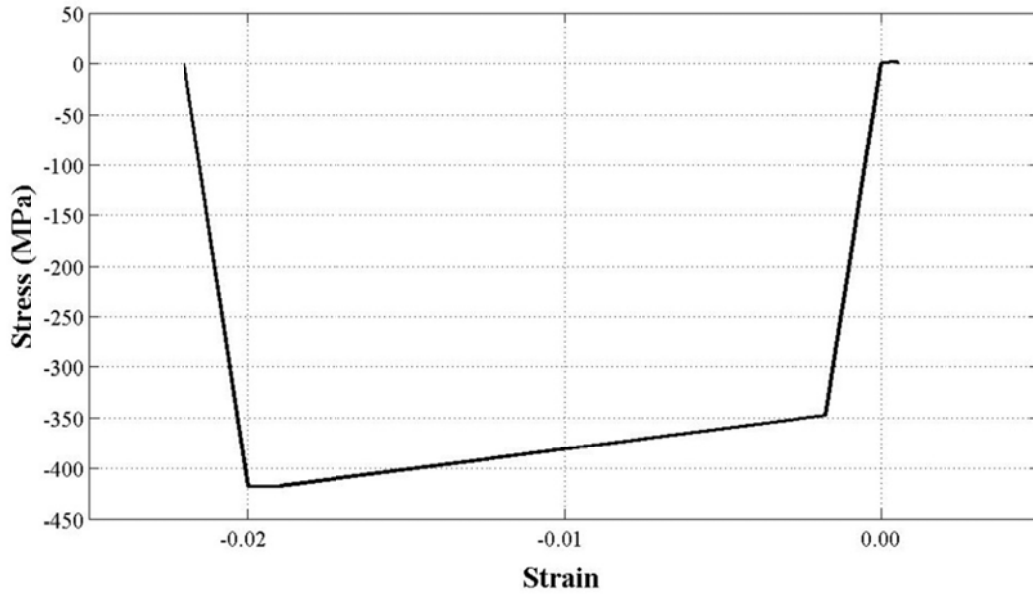
Figure 4.56 - Material stress-strain relationships used for rocking cross section

PT tendons and energy dissipation (ED) bars are modeled using truss elements with nonlinear material properties, although PT tendons stayed elastic throughout the tests. Truss elements are connected to shear wall elements through rigid beams extending to locations of tendons and ED bars in section. Lateral displacements of PT tendons are slaved to shear wall elements at each floor level, which is analogous to the effect of tendon ducts. Truss elements representing ED bars are modeled along the unbonded length of the bars. Four ED bars are lumped into one truss element on each side of the wall due to the spacing limitation between

158

nodes in Perform 3D. Figure 4.59 shows the locations of the nonlinear truss elements on the model. Material stress-strain relationships for the PT tendons and ED bars are simplified bilinear approximations of the test results (Table 4.3). Figure 4.57 and Figure 4.58 show the simplified stress-strain relationship for PT strands and ED bars, respectively. PT tendons had an initial prestressing of 60% of f_{py}, where f_{py} is the specified yield strength of the PT strands. Post-tensioning loads on tendons are applied as initial strains concurrently with gravity loads in the analysis.
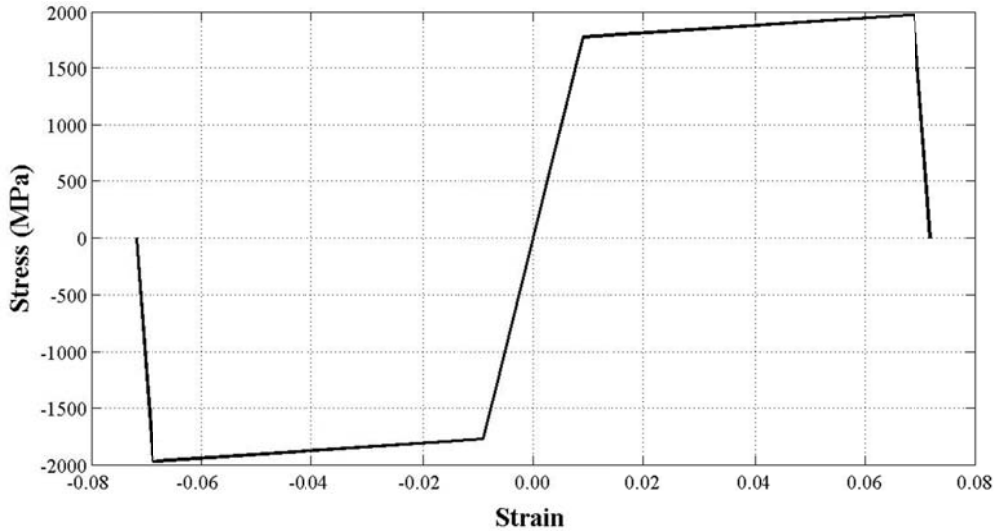
Figure 4.57 - Stress-strain relationship for PT tendons
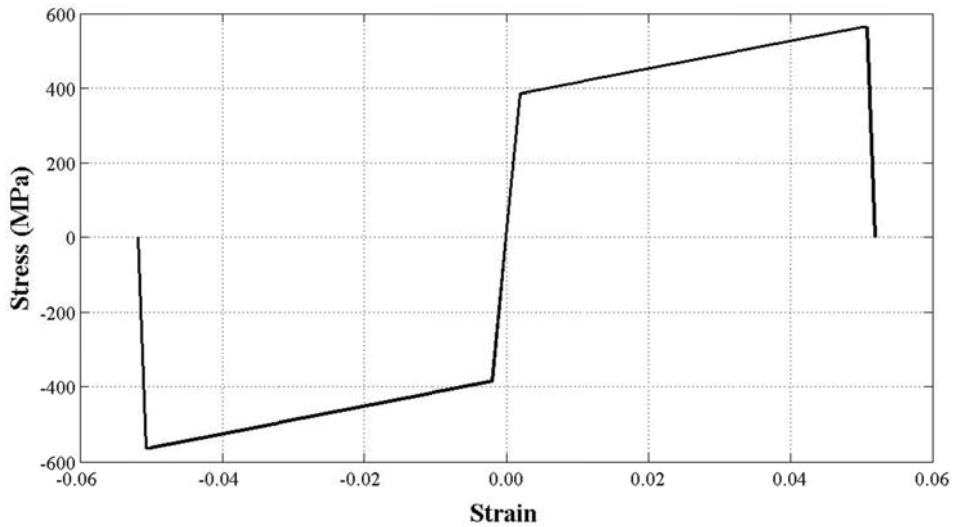
Figure 4.58 - Stress-strain relationship for ED bars

For post-tensioned, precast concrete shear walls having longitudinal reinforcement (ED

159

bars in this case) anchored into the foundation, additional flexibility is introduced due to rigid-body rotations that result from slip of the tensile ED longitudinal reinforcement from the anchorage (Figure 4.59). The reinforcement enters the foundation in tension and transfers force through bond stress to the surrounding concrete. Consequently, the tension force gradually decreases until distance l_d into the anchoring foundation, at which point the tension force reaches zero. Assuming the concrete to be rigid, the reinforcement must slip from the surrounding concrete by an amount equal to the total bar elongation within the anchorage. Bar elongation from the point of zero tension force to the face of the anchorage can be calculated as the integral of the strain along the anchorage length (Moehle, 2013).

Bar slip (strain penetration) effects are considered for modeling of ED bars. ED bar trusses are extended below the top of the foundation to mimic the extra elongation caused by the slip of ED bars. Bar slip is calculated equating the total bond force between steel and concrete to the force at the yielding strength of the steel bar, as shown in Figure 4.59. Since bars deform beyond the yield point, a bond stress of $6\sqrt{f_c'}$ was assumed, where f_c' is the specified concrete compressive strength. Equating the bar force and the bond force determines the required extension length of the bar, shown as:

$$\pi \frac{d_b^2}{4} f_y = \pi d_b l_d u \tag{1.9}$$

$$l_d = \frac{f_y d_b}{4u} \tag{1.10}$$

in which d_b is the bar diameter, f_y is the specified yield strength of the steel bar, u is the assumed bond stress, l_d is the length of the bar from the point of zero stress to the point where stress f_y is calculated. Stresses on the steel bar have a triangular distribution (from zero to f_y), whereas bond stresses are assumed to be constant throughout the length l_d. To simulate extra deformation caused by the bar slip, the truss element should be extended with a length of $l_d / 2$ on both sides. For practical modeling purposes, ED trusses were extended with a length of l_d at the foundation level. Calculations resulted into a l_d value of 46.6 cm.
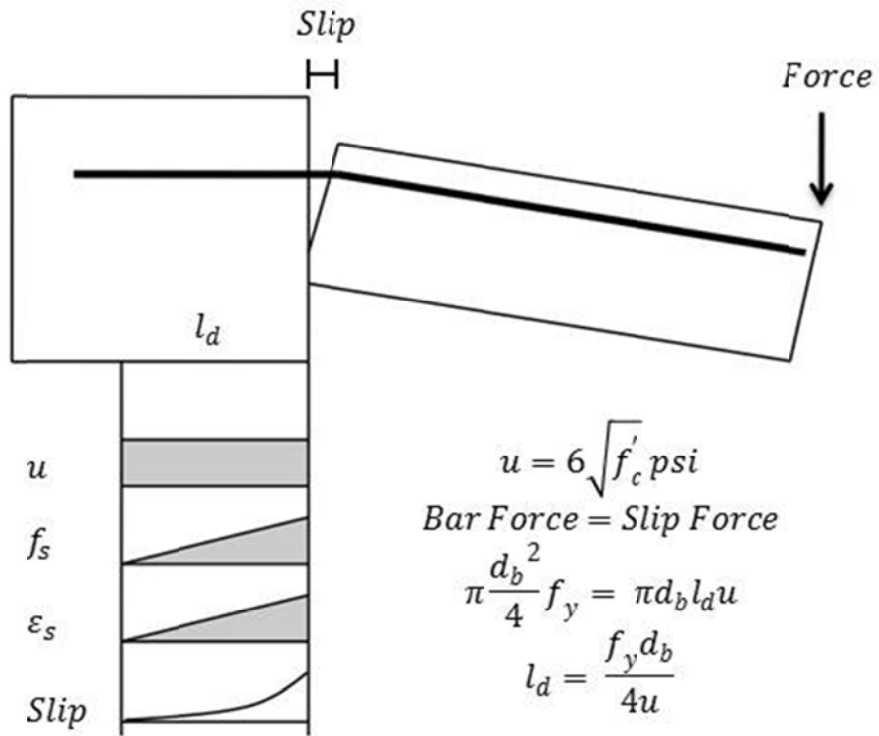
Figure 4.59 - Bar slip (strain penetration) phenomena
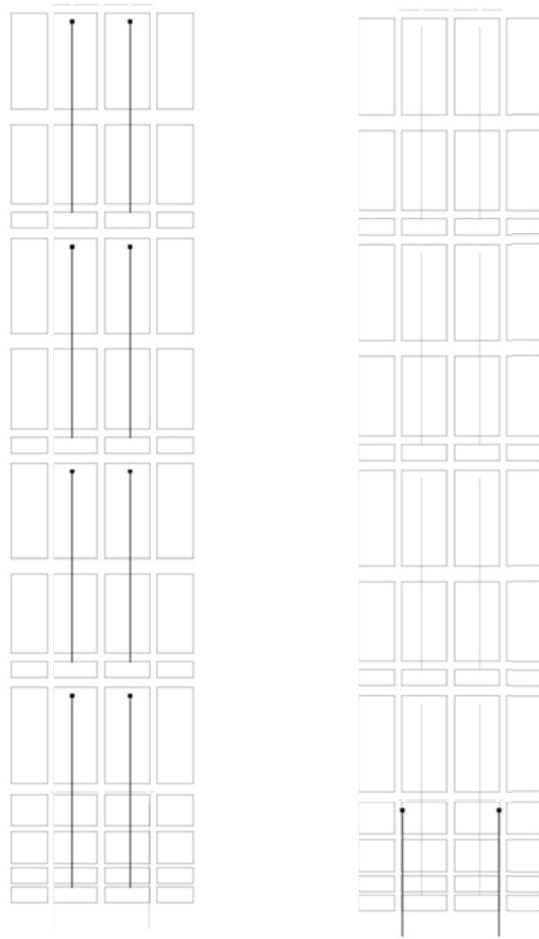
(a) PT tendons   (b) ED bars

Figure 4.60 - Nonlinear truss elements

4.4.2.1   Miscellaneous Notes on the Analytical Model

Rayleigh damping is used for nonlinear response history analysis, with parameters set to produce 2 percent damping at periods $0.2T_1$ and T_1, where $T_1 = 0.45$ seconds. Figure 4.61 shows the relationship of the damping ratio to the period ratio, where period ratio is defined as the period divided by the fundamental period. All analyses were in the Y-direction; therefore, X-direction displacements of all nodes are restrained. After the application of gravity and prestressing loads, the model is excited with 25%, 50%, and 100% Kobe motions, respectively.
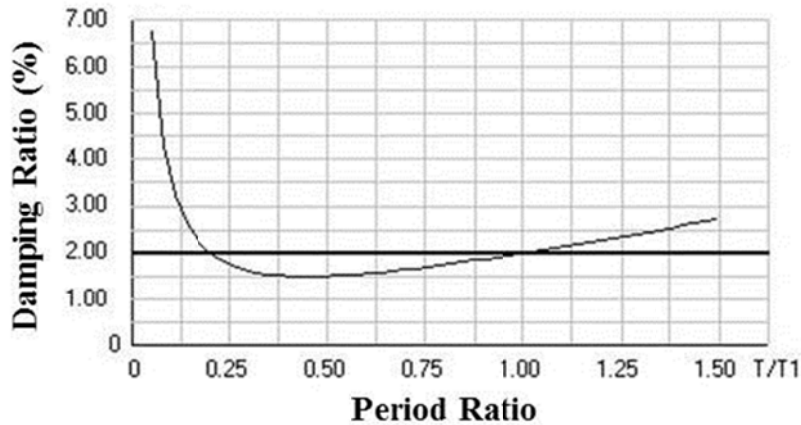
Figure 4.61 - Damping ratio-period ratio relationship for Rayleigh damping

4.4.2.2   Comparison of Wall Simulation and Test Results

Base shear versus roof drift ratio responses of the analytical model and test specimen under 25%, 50%, 100% Kobe excitations are shown in Figure 4.62, Figure 4.64, and Figure 4.66. Comparisons of the roof drift ratio versus time responses of analytical model and test specimen are shown in Figure 4.63, Figure 4.65, and Figure 4.67. Flag-shaped hysteresis typical of unbonded post-tensioned concrete is apparent. The initial stiffness of the analytical model does not match the test results (Figure 4.62). For all excitations, maximum base shear is under-estimated. Maximum roof drift ratio values are over-estimated in all excitations except after 17 s of 100% Kobe motion. These results suggest that the contribution of the PT frames in the Y-direction may be significant and should be modeled for successful estimations of response. It is noteworthy that there is a good match of roof drift ratio versus time for 100% Kobe motion after 17 s. This good estimation could be a result of strength loss caused by heavy damage of the frames, where the response mainly depends on the walls.

163

Figure 4.62 - Base shear-roof drift ratio comparison of results for 25% Kobe motion

Figure 4.63 - Roof drift ratio-time comparison of results for 25% Kobe motion

164

Figure 4.64 - Base shear-roof drift ratio comparison of results for 50% Kobe motion

Figure 4.65 - Roof drift ratio-time comparison of results for 50% Kobe motion

Figure 4.66 - Base shear-roof drift ratio comparison of results for 100% Kobe motion

Figure 4.67 - Roof drift ratio-time comparison of results for 100% Kobe motion

4.4.3 Modeling of Frames

The significant difference of the analytical simulation of the walls and test results (Section 3.2.2) suggested that it would be necessary to include the frames in the building analytical model if more accurate response simulations were to be achieved in the Y-direction. Therefore, a modified building model was developed that modeled the frame members on Axes A, B, and C, in addition to the walls. Frames in Axes A and C were coupled to the walls. The frame in the B axis was a one bay frame. Beams in the Y-direction were precast members post-tensioned using unbonded PT tendons. All columns were post-tensioned with bonded tendons.

4.4.3.1   Beam and Column Models

Beams and columns are modeled using nonlinear beam column elements with rigid end zones. Nonlinear fiber sections are assigned through the length of the elements with distributed plasticity (Figure 4.68). Similar to the shear wall elements, a simplified trilinear curve with a descending portion is used to model concrete and steel materials. Similar to rocking sections of wall elements, opening between precast elements is simulated by assigning a "rocking section" to the necessary integration points of elements (i.e., closest integration point of a beam element to a wall or column). The aforementioned "rocking section" has the same cross section and fiber locations as the other integration points. However, materials assigned to this section are modified to have no tension resistance, keeping the compression response unchanged.
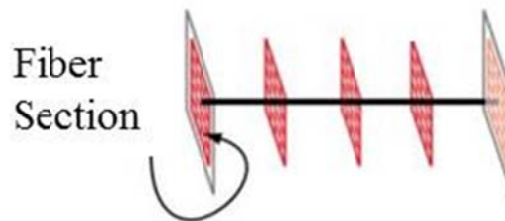
Figure 4.68 - Nonlinear beam column element with distributed plasticity

Upper portions of half-precast beams were cast monolithically with slabs. Beam effective flange widths are calculated using ACI 318 equations. The governing case for effective flange width was one-quarter of the span length of the beam. In Perform 3D, beam elements can only resist axial and bending forces with fibers in the major axis of bending only. Therefore, beam cross sections are discretized into fibers in one row as shown in Figure 4.69. This discretization didn't include the empty post-tensioning steel ducts; with the assumption of these ducts have inconsequential effect on the overall behavior and response of these members. A similar assumption is made for the reinforcing bars. Bending stiffness of the minor bending axis is defined with effective bending stiffness as $0.5E_cI_g$, in which I_g is the gross section moment of inertia according to the minor bending axis (Elwood et al. 2007).
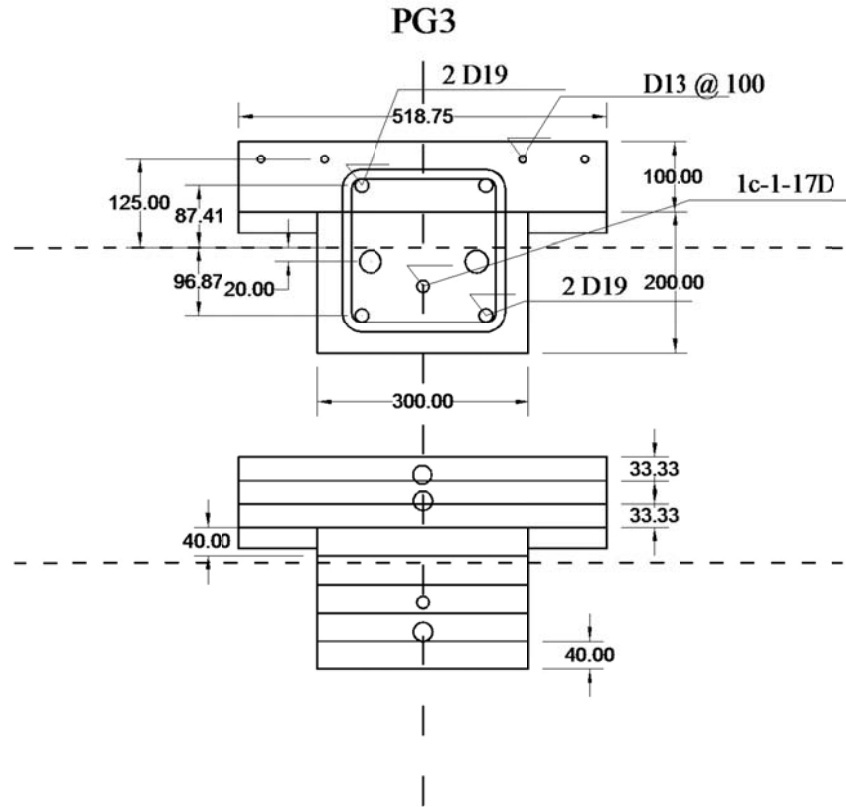
Figure 4.69 - Beam fiber cross section

Unlike beam elements, column elements in Perform 3D can resist axial and bending forces using fiber cross sections in both bending directions. The column cross sections are discretized into fibers in a mesh as shown in Figure 4.70. Similar to the beam models, this discretization didn't include the empty post-tensioning steel ducts; with the assumption of these ducts have negligible effect on the overall behavior and response of these members. A similar assumption is made for the reinforcing bars.

168
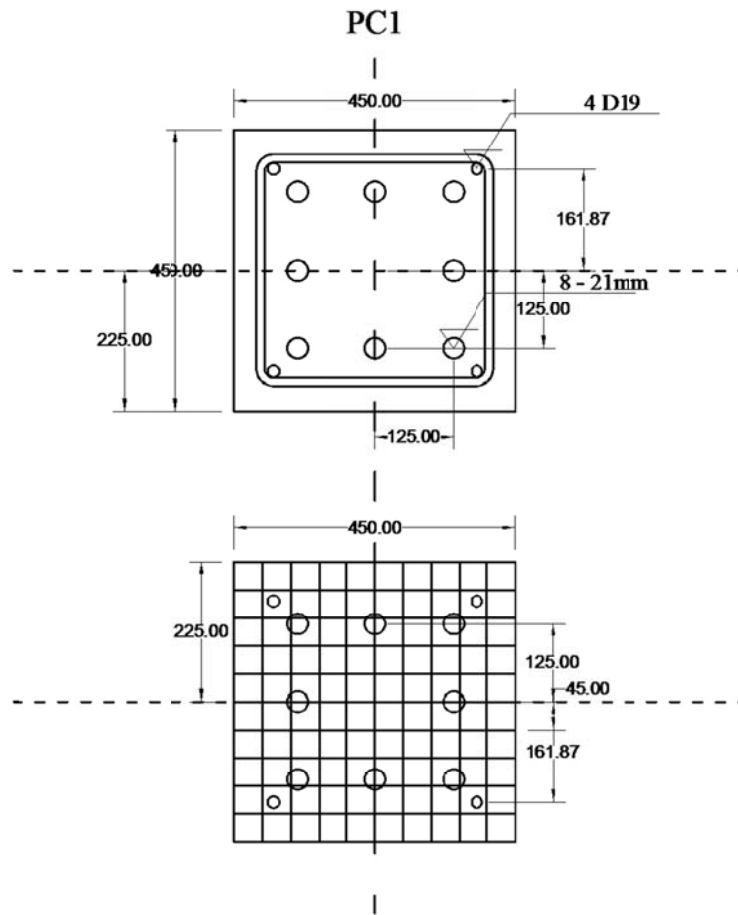
Figure 4.70 - Column fiber cross section

Due to adequate shear design of the members, a linearly-elastic shear material was used for beams and columns, with effective shear stiffness defined as $G_cA_w = 0.4E_cA_w$ (Elwood et al. 2007).

Unbonded PT tendons of beams (PG2 & PG3) are modeled with parallel truss elements with nonlinear material properties. Their vertical displacements through beams and walls are slaved to parallel elements similar to modeling of ducts for walls. Similar to PT tendons of walls, post-tensioning loads on tendons are applied as initial strains. In contrast, bonded PT rods of columns (PC1) are included in the fiber cross section. Post-tensioning loads on columns are approximated by applied point loads (in the same direction with gravity).

4.4.3.2   Miscellaneous Notes on the Analytical Model

Figure 4.71 shows a 3D view of the final analytical model including walls and frames modeled together. An elevation view of the transverse direction of the analytical model is shown

169

in Figure 4.72. Rayleigh damping is used for nonlinear response history analysis, with parameters set to produce 2 percent damping at periods $T_1/8$ and $1.25T_1$, where $T_1 = 0.29$ seconds. Figure 4.73 shows the relationship of the damping ratio and the period ratio. All analyses were in the Y-direction; therefore X-direction displacements of all nodes are restrained. After the application of gravity and prestressing loads, the model is excited with 25%, 50%, and 100% Kobe motions, respectively.
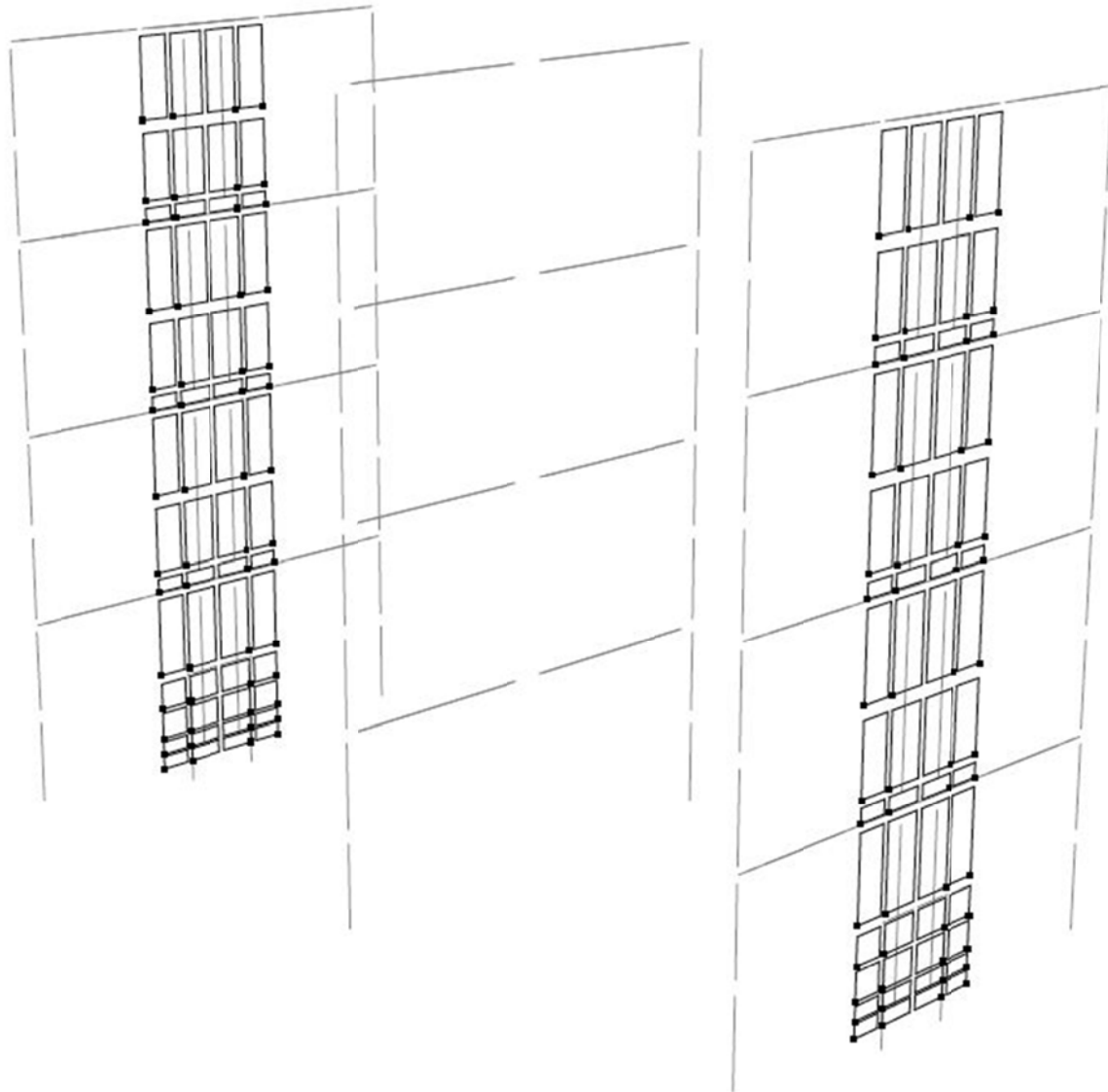
Figure 4.71 - 3D view of the Perform 3D model
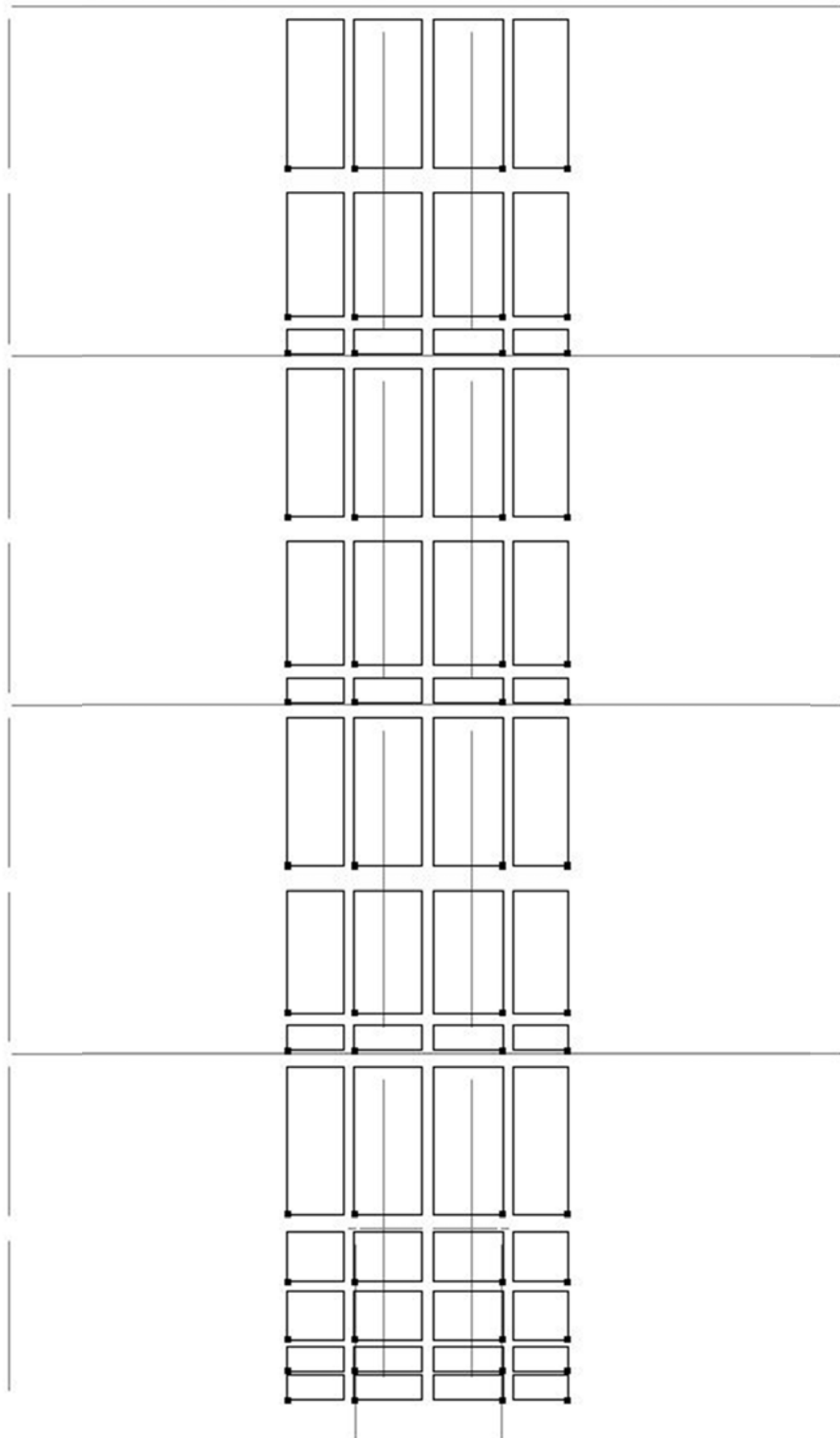
Figure 4.72 - Elevation view of the Perform 3D model

171
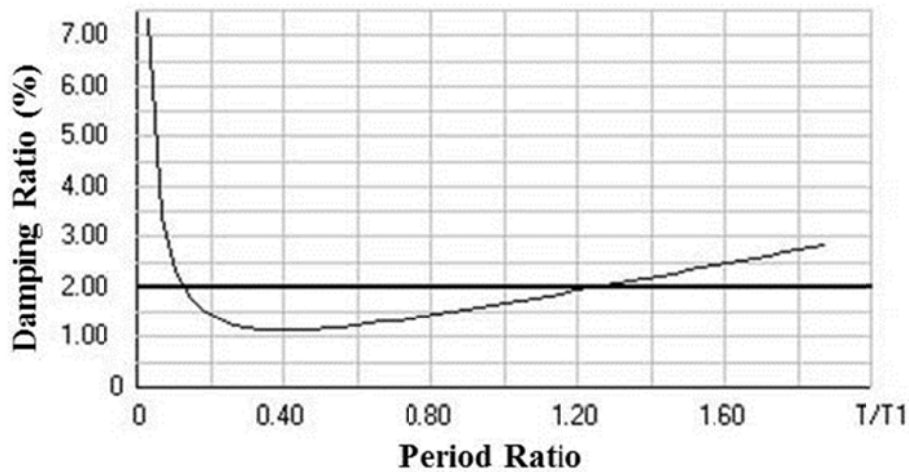
Figure 4.73 - Damping ratio-period ratio relationship for Rayleigh damping

4.5 Comparison of Simulation and Test Results

Prior to application of earthquake motions, the test building was excited with white noise. Fundamental periods of the building were 0.29 s in the Y-direction and 0.45 s in the X-direction. Modal analysis of the analytical model resulted in a fundamental period of 0.29 s in the Y-direction. Therefore the numerical model was able to match the fundamental period of the test building accurately.

Base shear versus roof drift ratio responses of the analytical model and test specimen under 25%, 50%, 100% Kobe excitations are shown in Figure 4.75, Figure 4.78, and Figure 4.81. Comparisons of roof drift ratio versus time responses of analytical model and test specimen are shown in Figure 4.76, Figure 4.79, and Figure 4.82. Figure 4.74,Figure 4.77, and Figure 4.80 show the time variations of the rood drift ratio of the test building along the whole duration of the excitation for 25%, 50%, and 100% Kobe motions, respectively.
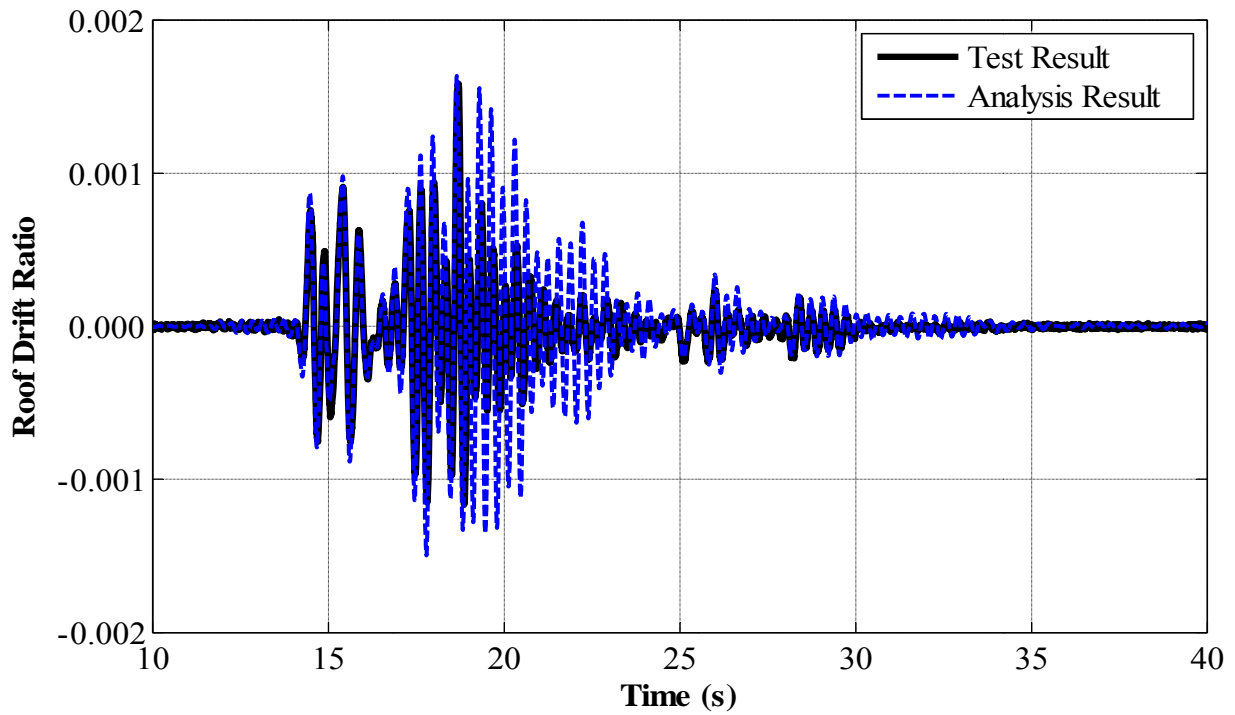
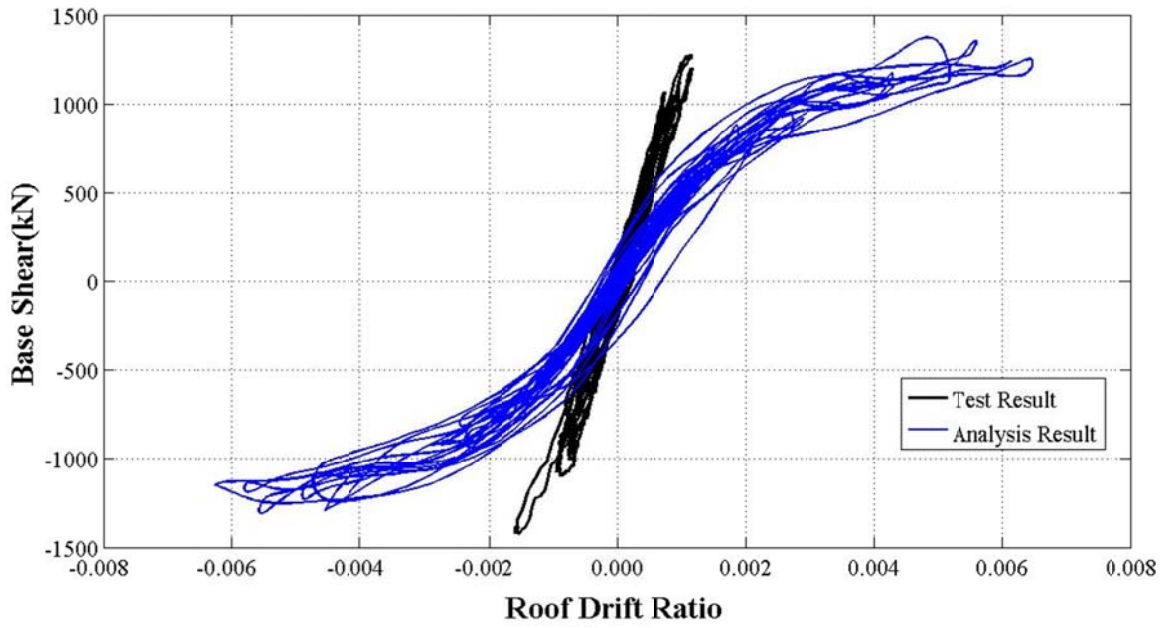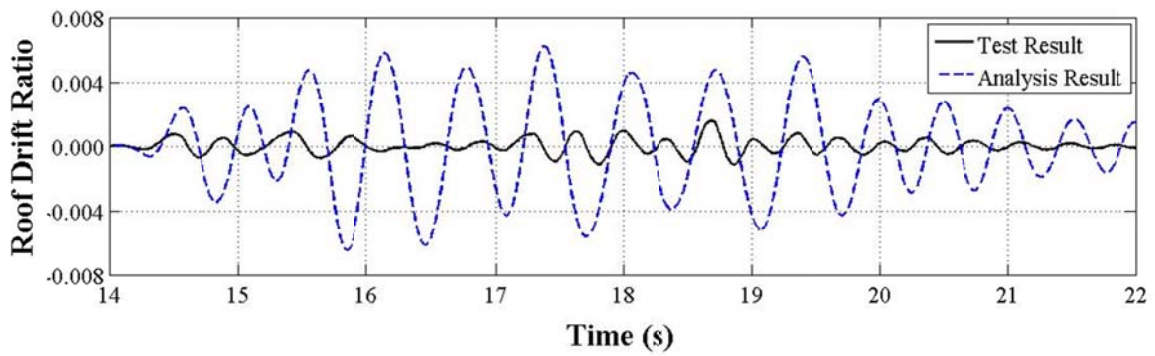**Figure 4.74 - Roof drift ratio-time comparison of results for 25% Kobe motion**
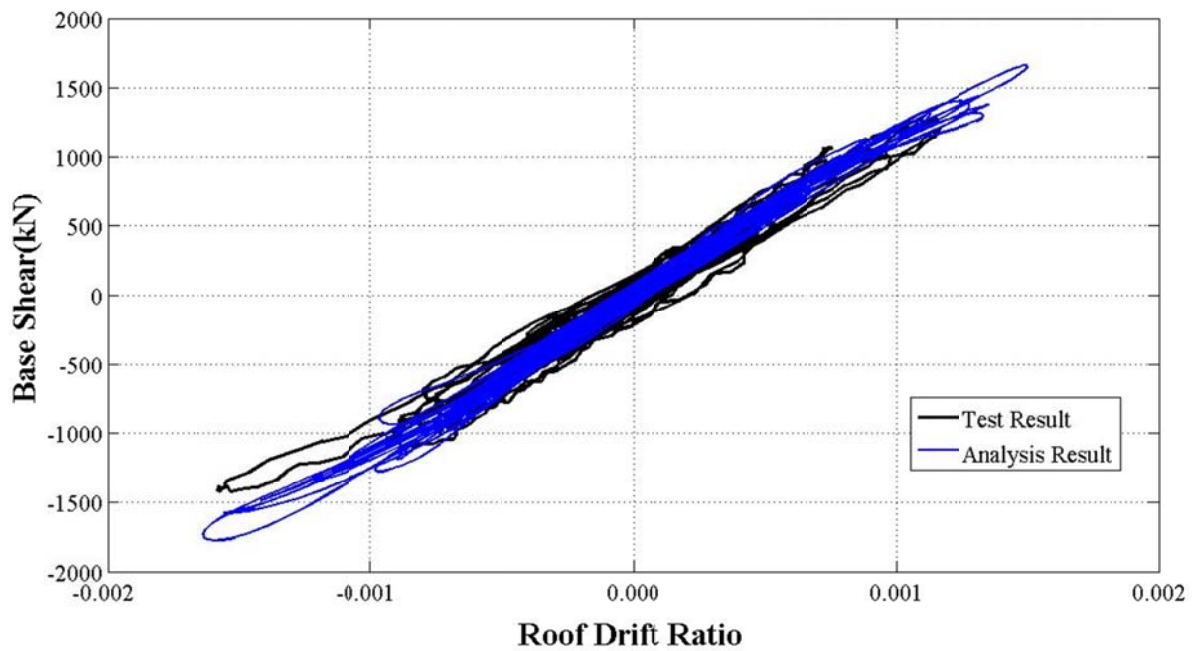
Figure 4.75 - Base shear-roof drift ratio comparison of results for 25% Kobe motion
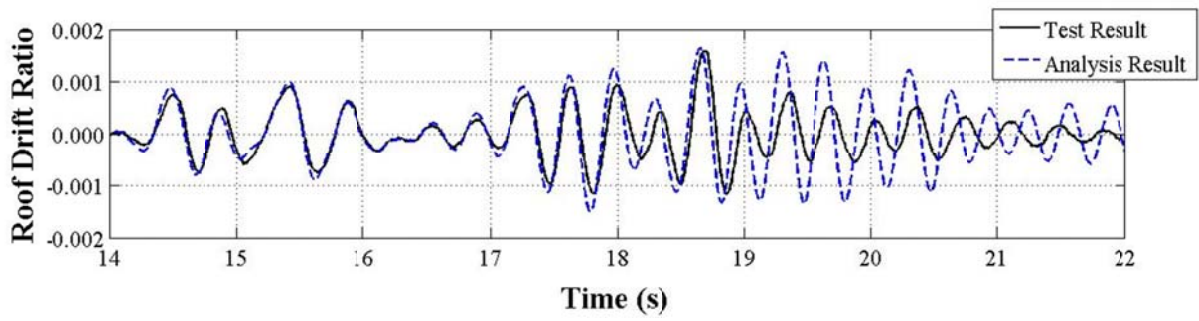
Figure 4.76 - Roof drift ratio-time comparison of results for 25% Kobe motion
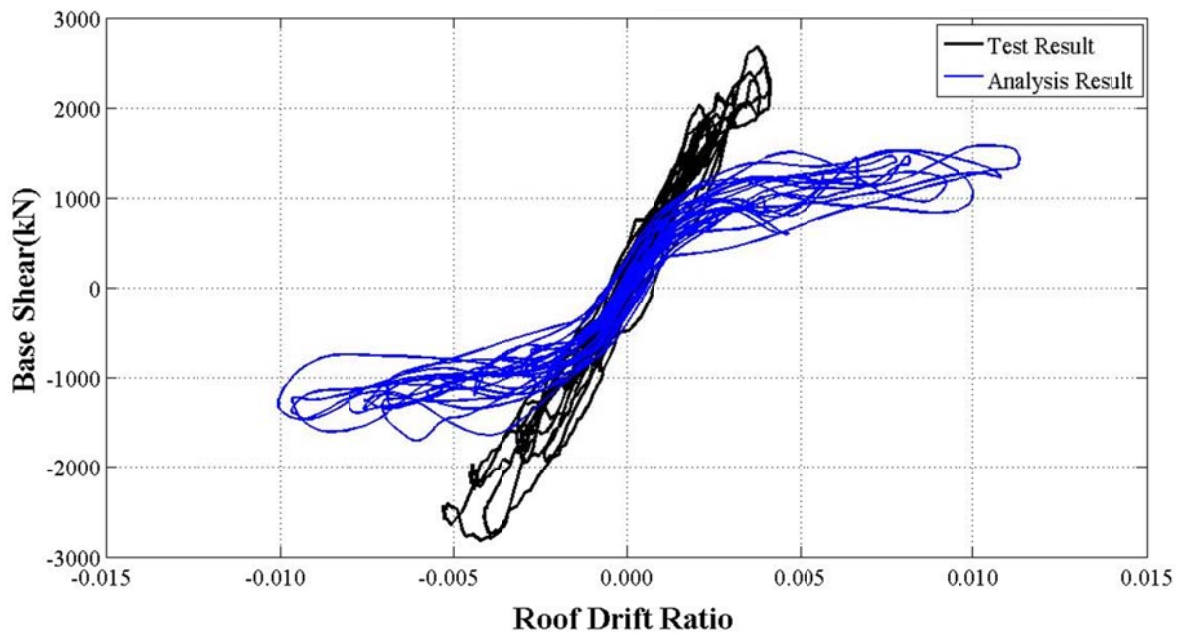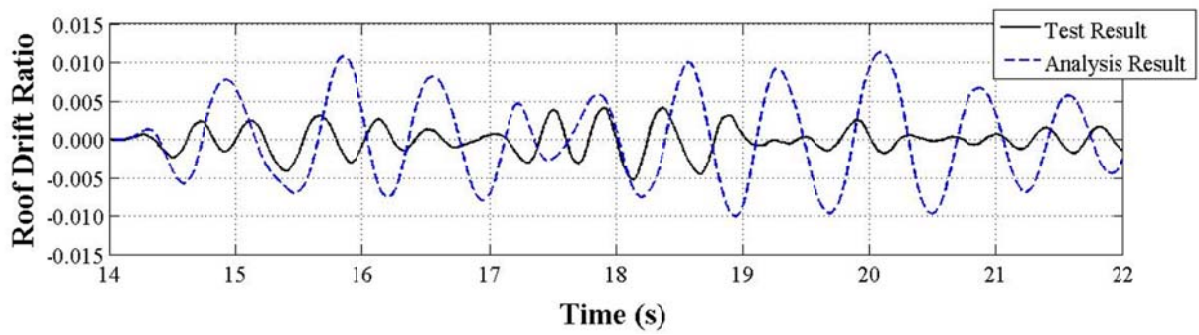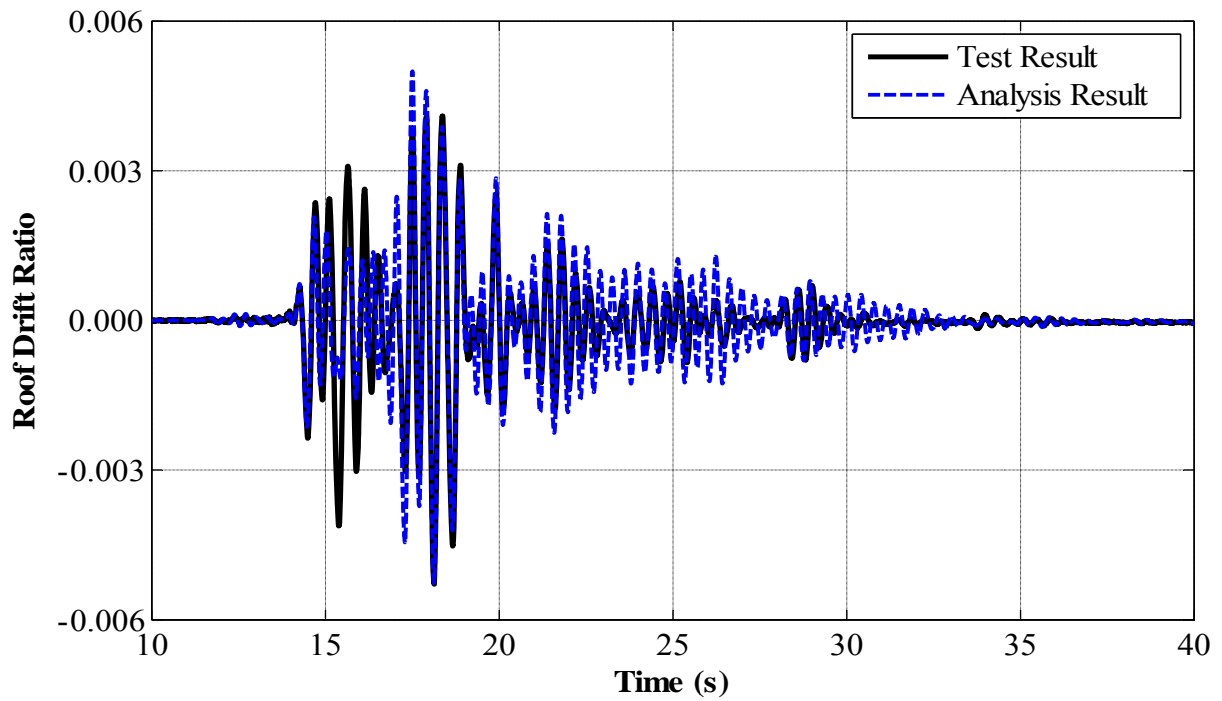

Figure 4.77 - Roof drift ratio-time comparison of results for 50% Kobe motion

174
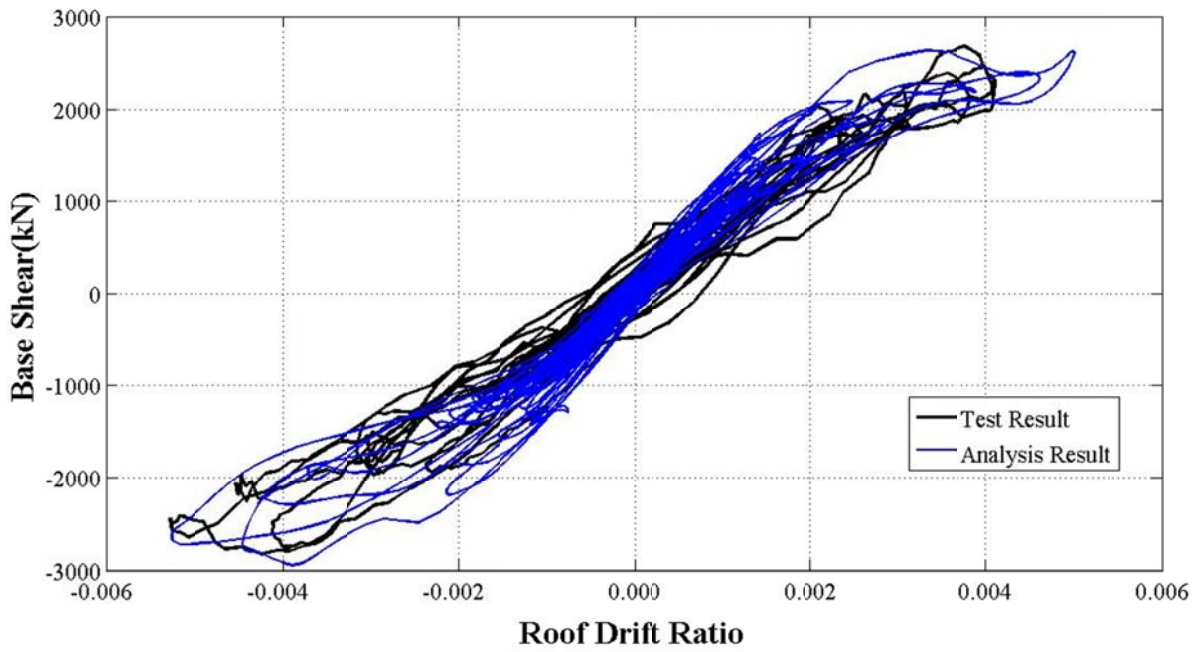
Figure 4.78 - Base shear-roof drift ratio comparison of results for 50% Kobe motion
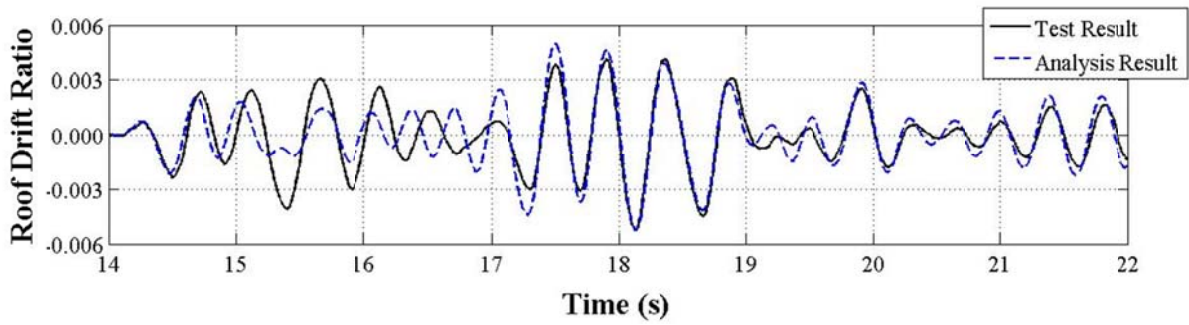
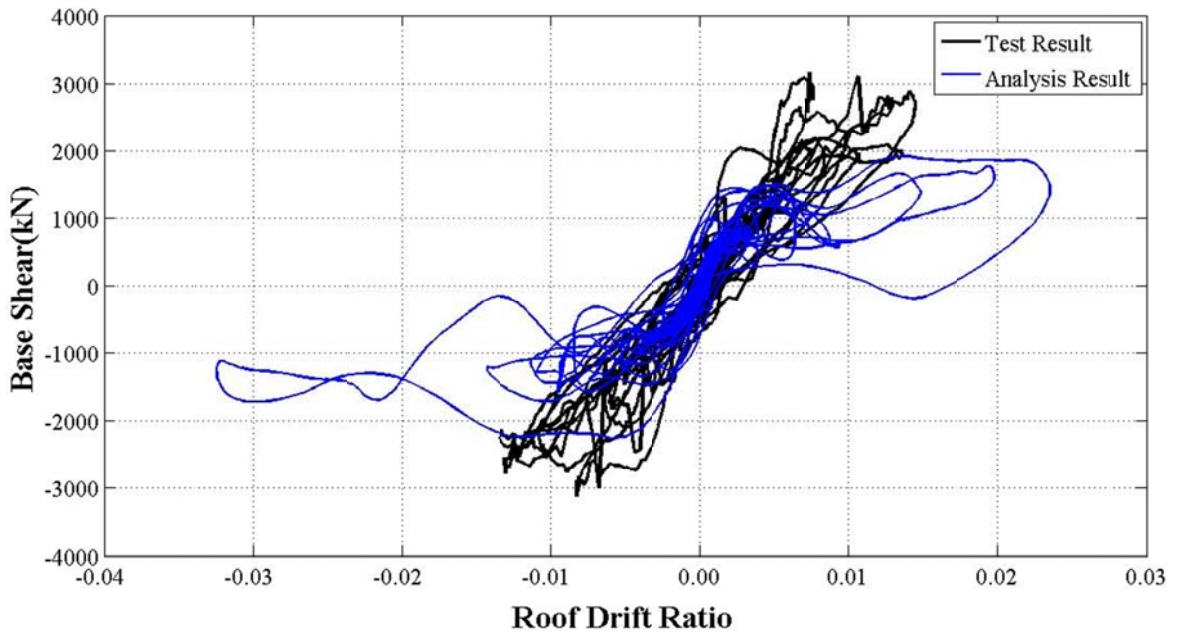**Figure 4.79 - Roof drift ratio-time comparison of results for 50% Kobe motion**
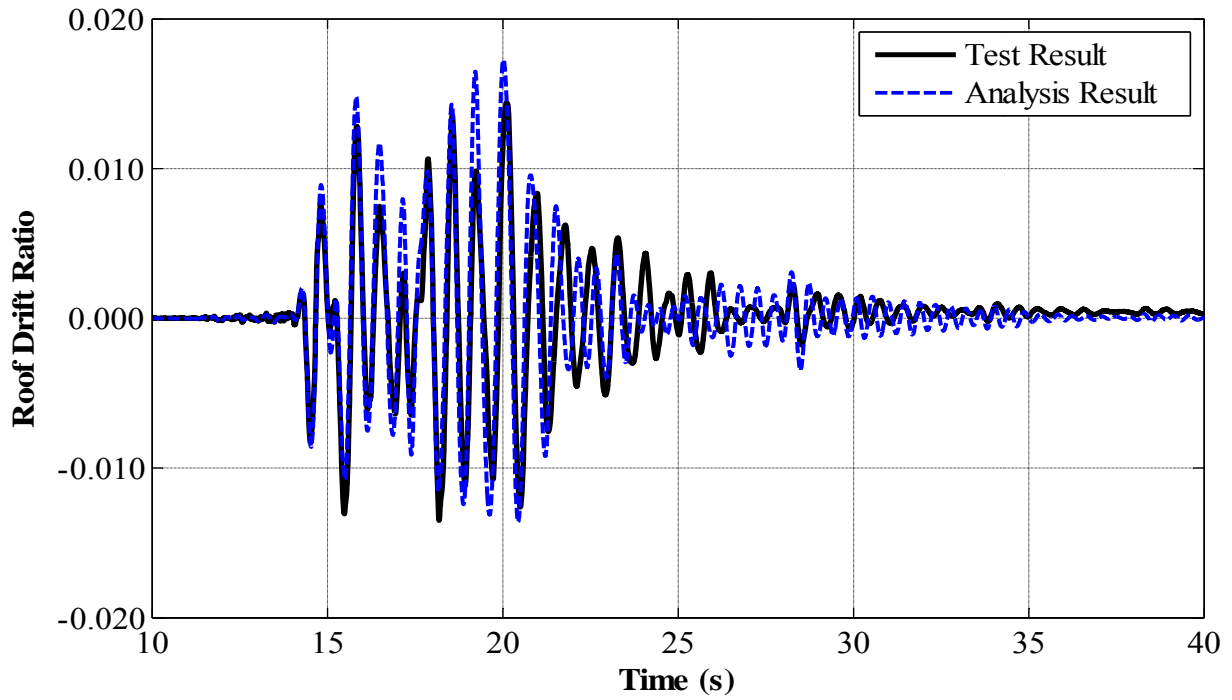
Figure 4.80 - Roof drift ratio-time comparison of results for 100% Kobe motion

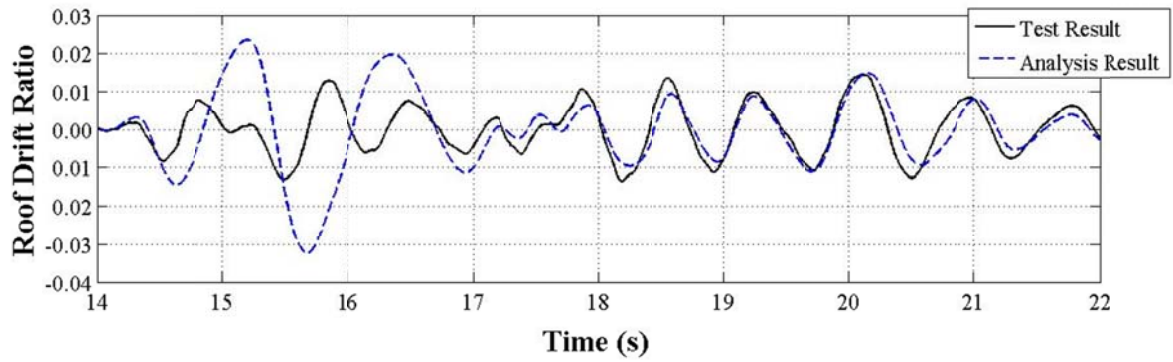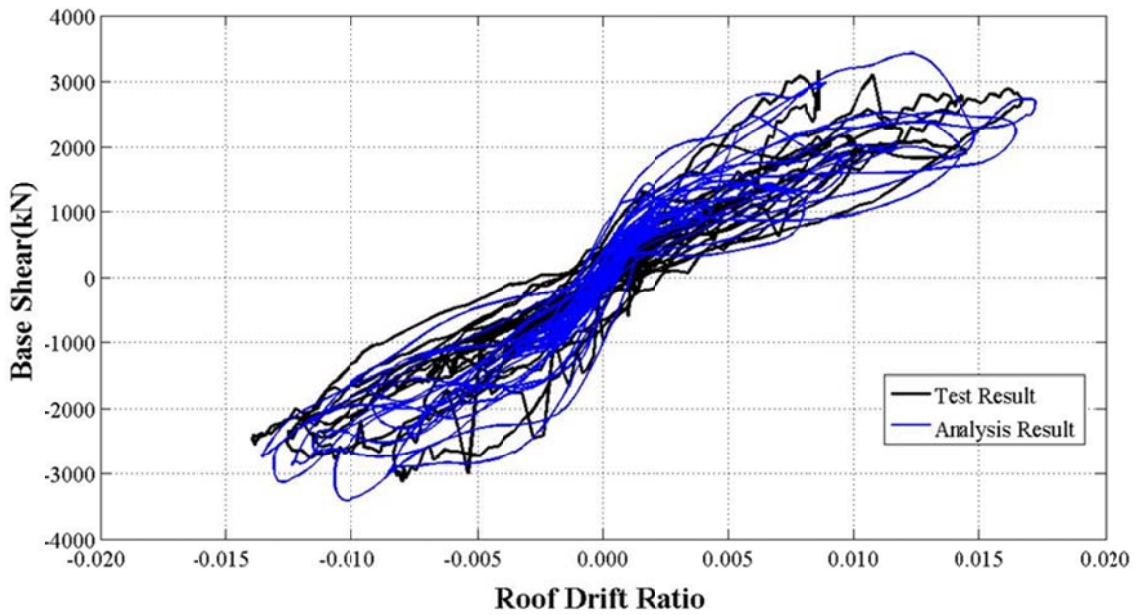**Figure 4.81 - Base shear-roof drift ratio comparison of results for 100% Kobe motion**
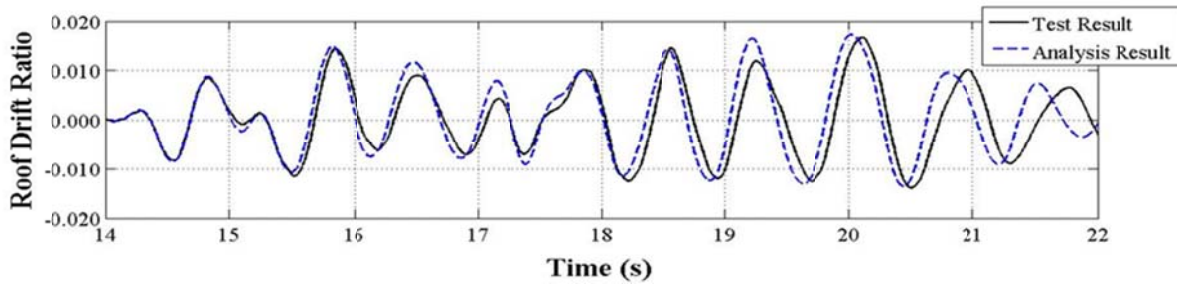
Figure 4.82 - Roof drift ratio-time comparison of results for 100% Kobe motion

Base shear versus roof drift ratio relationships for all motions show the flag-shaped hysteresis typical of unbonded post-tensioned concrete. The analytical model and test results are in very good agreement for important engineering parameters, such as stiffness, maximum base shear, and maximum roof drift. For all excitations, energy dissipated during the earthquake simulation (area inside the hysteresis curve) is estimated with good accuracy. Although estimated maximum roof drift ratios are very close to the test results, phase shifts in roof drift ratio versus time series are significant for some parts of the response.

The base shear versus roof drift ratio and roof drift ratio versus time relationships for the 25% Kobe motion are shown in Figure 4.75 and Figure 4.76, respectively. The numerical model is slightly stiffer than the test specimen under this motion. This is apparent in the roof drift ratio response history estimate for the 25% Kobe motion, as it is shifting out-of-phase after 19 s. Vibration period of the test specimen is increasing after 19 s, but the analytical model does not identify this increase in period. For the roof drift ratio versus time response of the 25% Kobe motion, calculated response damps out more slowly that the test results.

The base shear versus roof drift ratio and roof drift ratio versus time relationships for the 50% Kobe motion are shown in Figure 4.78 and Figure 4.79, respectively. The numerical model has a good estimation for the overall stiffness of the test building. The flag shaped hysteresis curve is similar to the test results. However there are some differences in the energy dissipated during the earthquake (area inside the hysteresis curve). The roof drift ratio versus time response of the 50% Kobe earthquake starts out-of-phase with the test results. However, it becomes in-phase with the test results in about 17s, and follows the test building roof drift ratio versus time response accurately (Figure 4.79). Assumed Rayleigh damping properties are in good agreement with the response of 50% Kobe motion. The apparent damping of the numerical simulation is similar to the test specimen for this excitation.

The base shear versus roof drift ratio and roof drift ratio versus time relationships for the 100% Kobe motion are shown in Figure 4.81and Figure 4.82, respectively. The numerical model has good estimates for important engineering parameters such as maximum base shear and maximum roof drift ratio. Response of the numerical model seems slightly stiffer on the base shear versus roof drift ratio relationship (Figure 4.81). It is also observed at the roof drift ratio

versus time response (Figure 4.82) as the slight phase change around 21s. Assumed damping for the analytical model is in good agreement for the response of 100% Kobe excitations.

The axial load variations of the post tensioning (PT) tendons are monitored using load cells on the roof level during the test. The force variation for the PT tendons versus time comparison for the test results and analysis results are shown in Figure 4.83, Figure 4.84, and Figure 4.85 for 25%, 50%, and 100% Kobe motions, respectively.
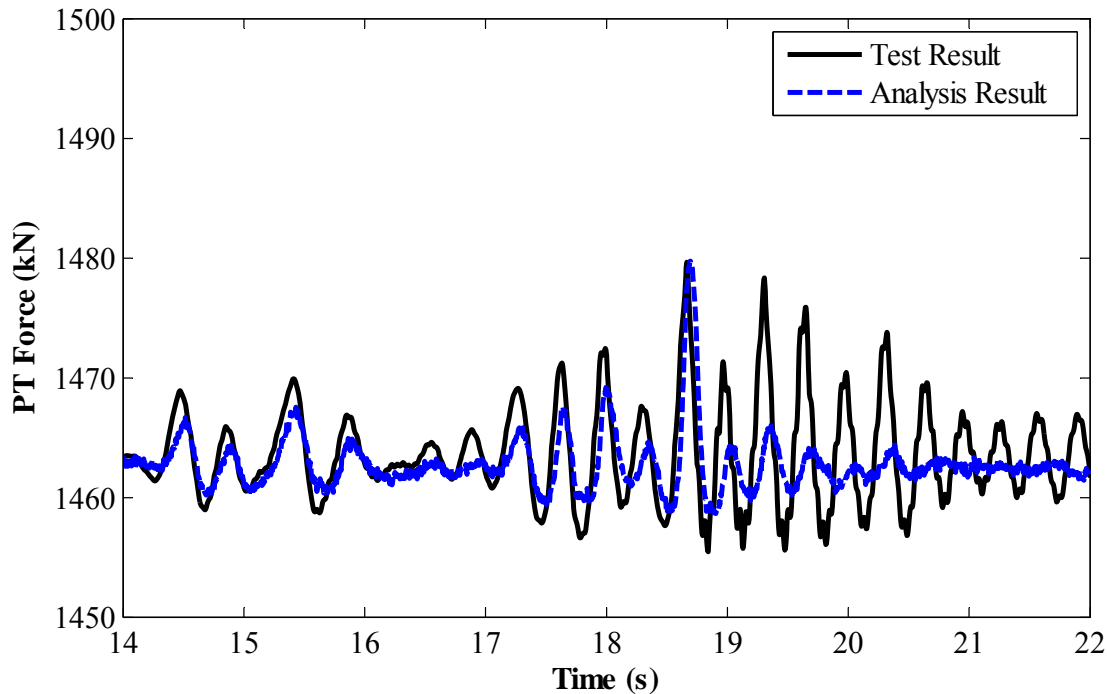
Figure 4.83 - PT force-time comparison of results for 25% Kobe motion

Figure 4.83 shows a good agreement between the calculated and measured PT force variations for 25% Kobe motion. The numerical estimation seems in-phase with the test results until second 19. However, the peak values of these cycles are 10 to 30% lower than the observed values of the test. It is important to mention that the numerical result matches the ultimate peak response very accurately. As expected from the roof drift ratio versus time relationship in Figure 4.76, PT forces are significantly lower than the test results and out-of-phase after 19 seconds.

178
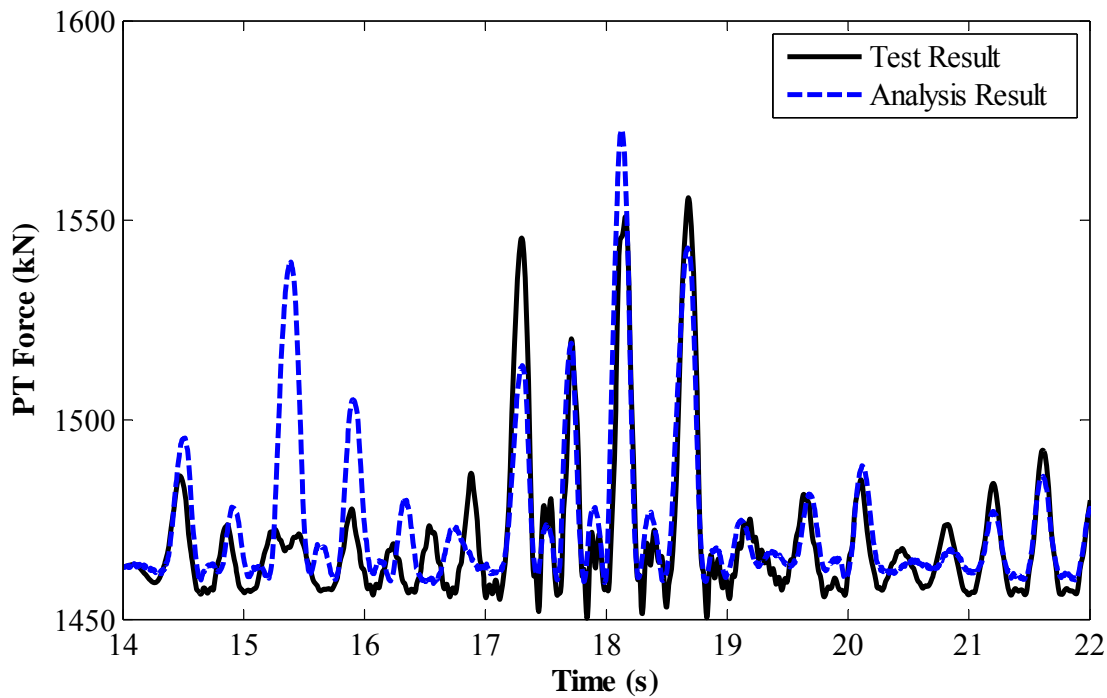
Figure 4.84 - PT force-time comparison of results for 50% Kobe motion

Figure 4.84 shows a good agreement between the calculated and measured PT force variations for 50% Kobe motion. The numerical estimation seems out-of-phase with the test results until second 17. Two peak responses of the numerical model between 15 and 16 seconds largely overestimate the test results. Results of the numerical model become in-phase and have a good match with the test results around 17 seconds. This is very similar to the overall response of the model shown in the Figure 4.79.
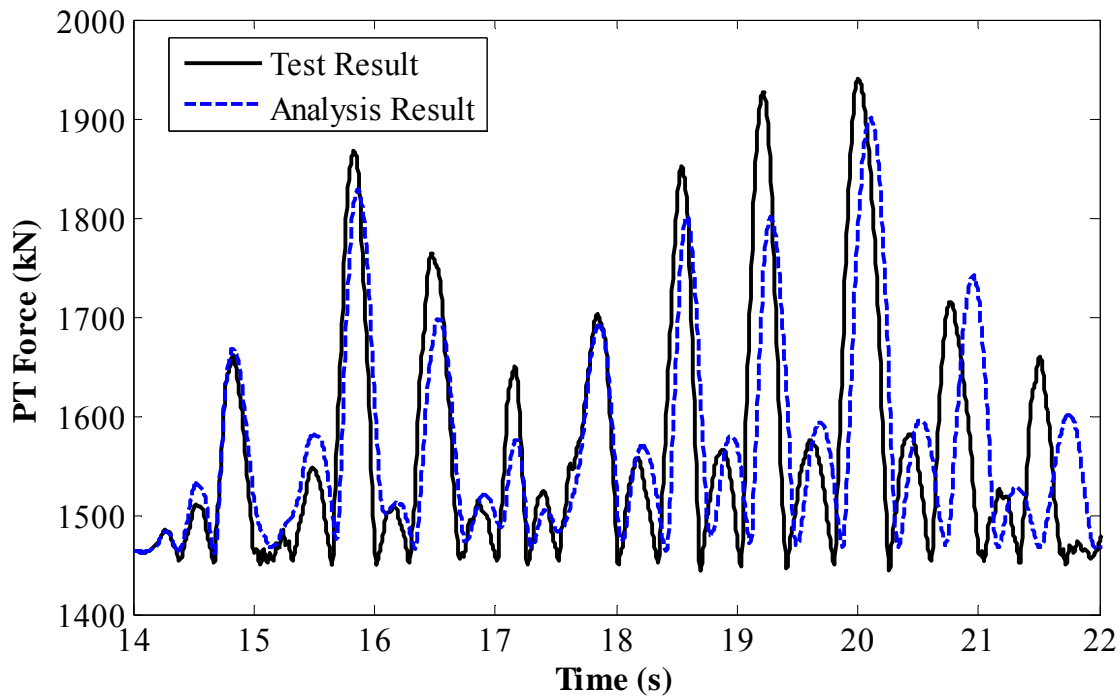
Figure 4.85 - PT force-time comparison of results for 100% Kobe motion

Figure 4.85 shows a very good agreement between the calculated and measured PT force variations for 100% Kobe motion. The numerical model estimates peak responses and their time accurately. The response of the numerical model becomes out-of-phase around 21 seconds. This is very similar to the overall response of the model shown in the Figure 4.82.

The slip between the post-tensioned (PT) wall base and the foundation during the 100% Kobe motion is plotted in Figure 4.86. This shows that the maximum slip at the base of the PT walls during the largest applied ground motion is around 1.5 mm (0.059 inches). This result confirms the modeling assumption of the fixed connection between PT walls and foundation, i.e. ignoring the potential slip surface between the precast wall panel and the foundation.
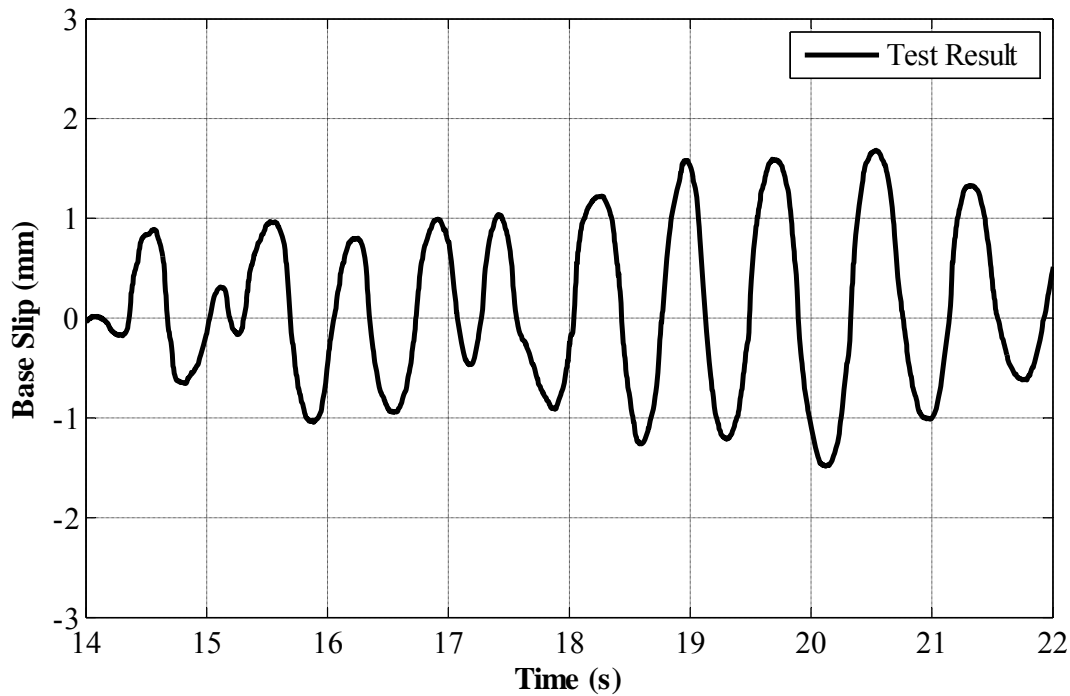
Figure 4.86 - PT wall base slip-time relationship of results for 100% Kobe motion

Figure 4.87 and Figure 4.88 show the deformation variation of the energy dissipation (ED) bars of the PT walls with time for the 25% Kobe earthquake. The test result looks very scattered because of the small magnitude of the displacement. The results of the numerical model match the test results reasonably before 19 seconds.

Figure 4.89 and Figure 4.88 show the deformation variation of energy dissipation (ED) bars of PT walls with time for the 50% Kobe earthquake. The numerical model is not able to simulate the response before 17 seconds. However, after this point test results and analysis results match remarkably well within a 10-20% error range.

Figure 4.91 and Figure 4.92 show the deformation variation of energy dissipation (ED) bars of PT walls with time for the 100% Kobe earthquake. The numerical results follow the test results very closely throughout the whole motion. The numerical model calculates the peak values of deformation of the ED bars approximately 20-30% lower than the observed values from the test specimen.
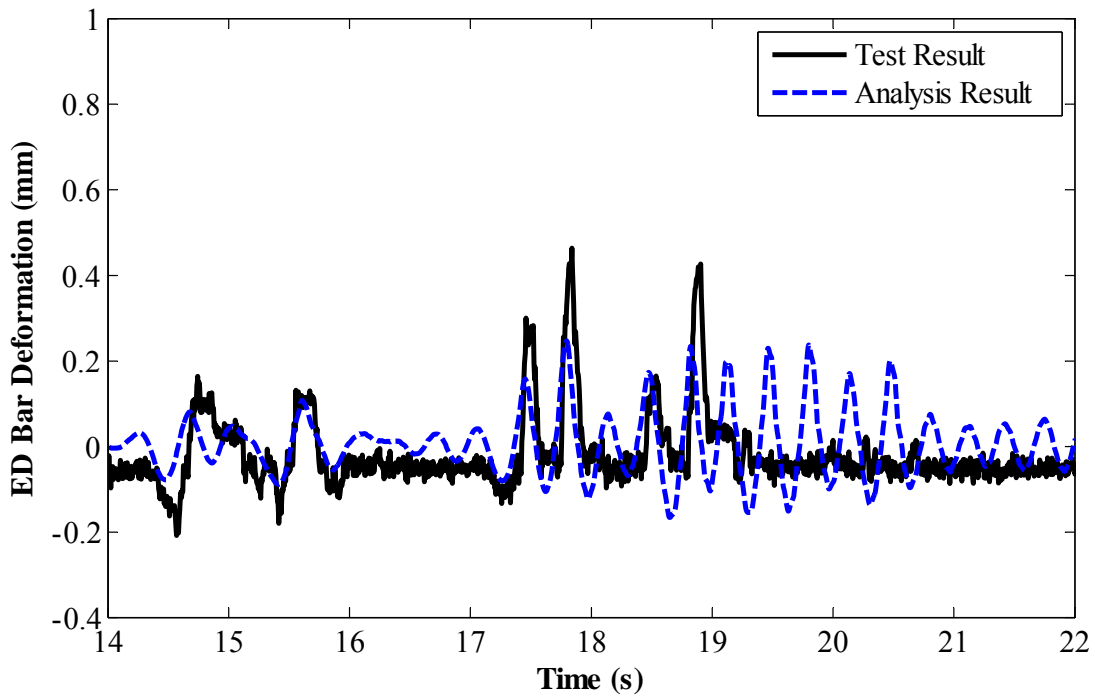
Figure 4.87 - ED bar 1 deformation-time comparison of results for 25% Kobe motion
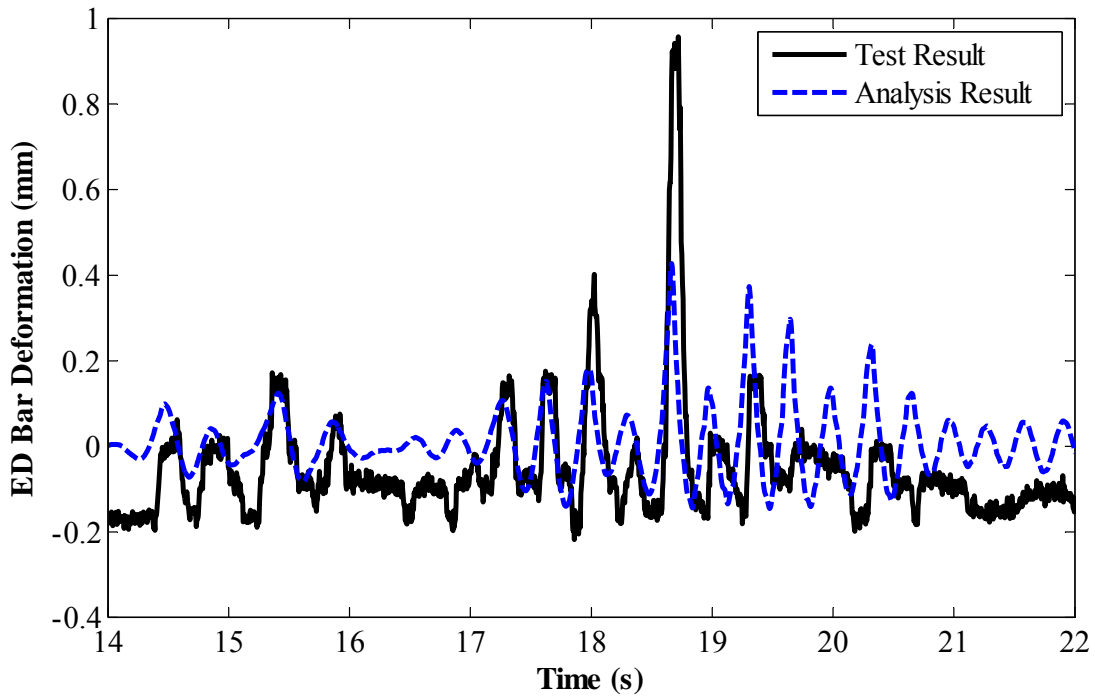
Figure 4.88 - ED bar 2 deformation -time comparison of results for 25% Kobe motion

182
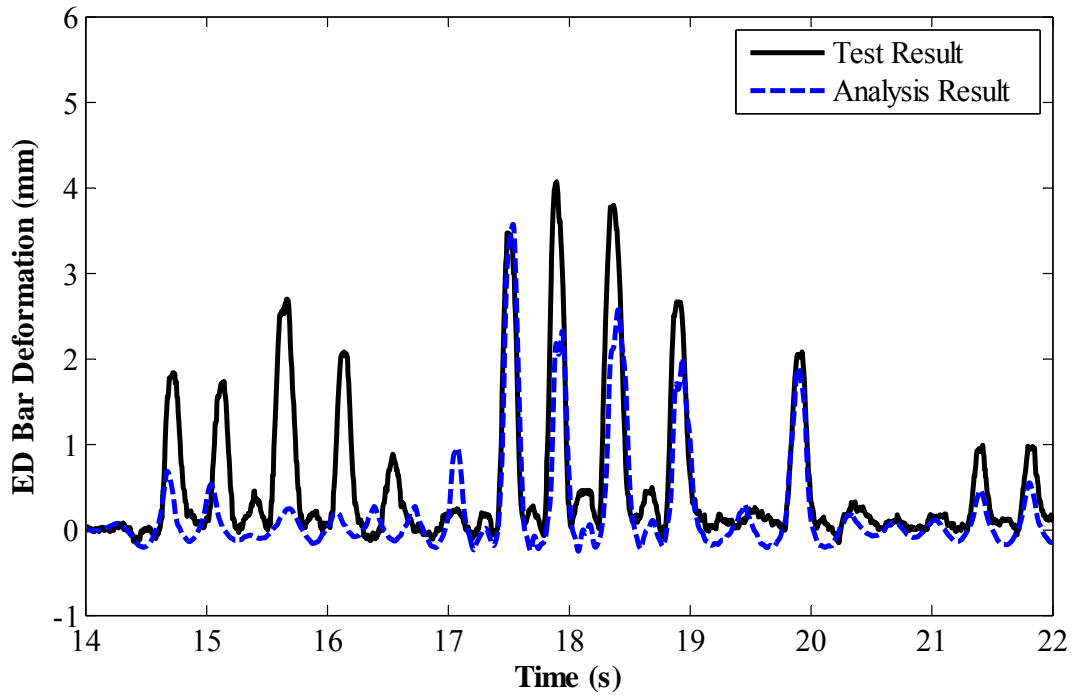
Figure 4.89 - ED bar 1 deformation-time comparison of results for 50% Kobe motion
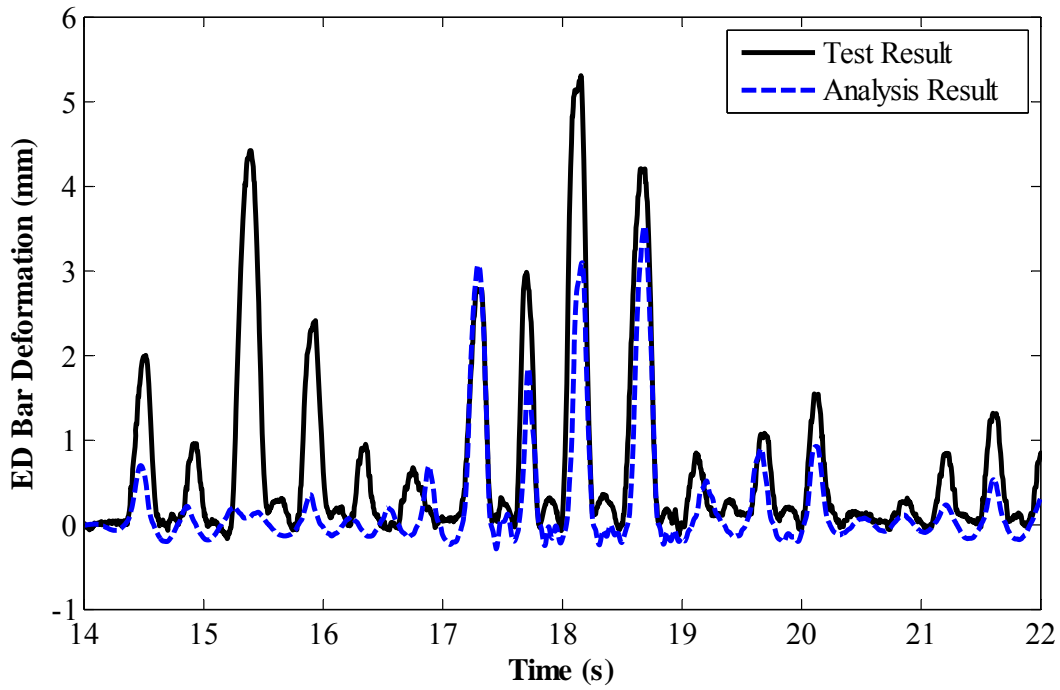
Figure 4.90 - ED bar 2 deformation -time comparison of results for 50% Kobe motion

183
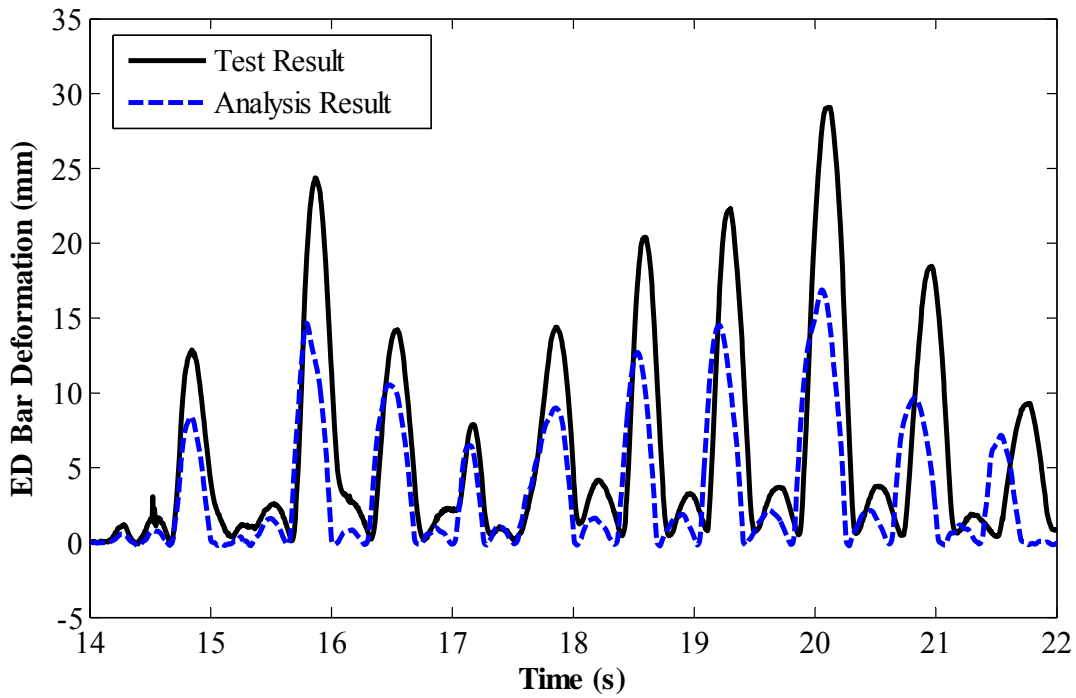
Figure 4.91 - ED bar 1 deformation -time comparison of results for 100% Kobe motion
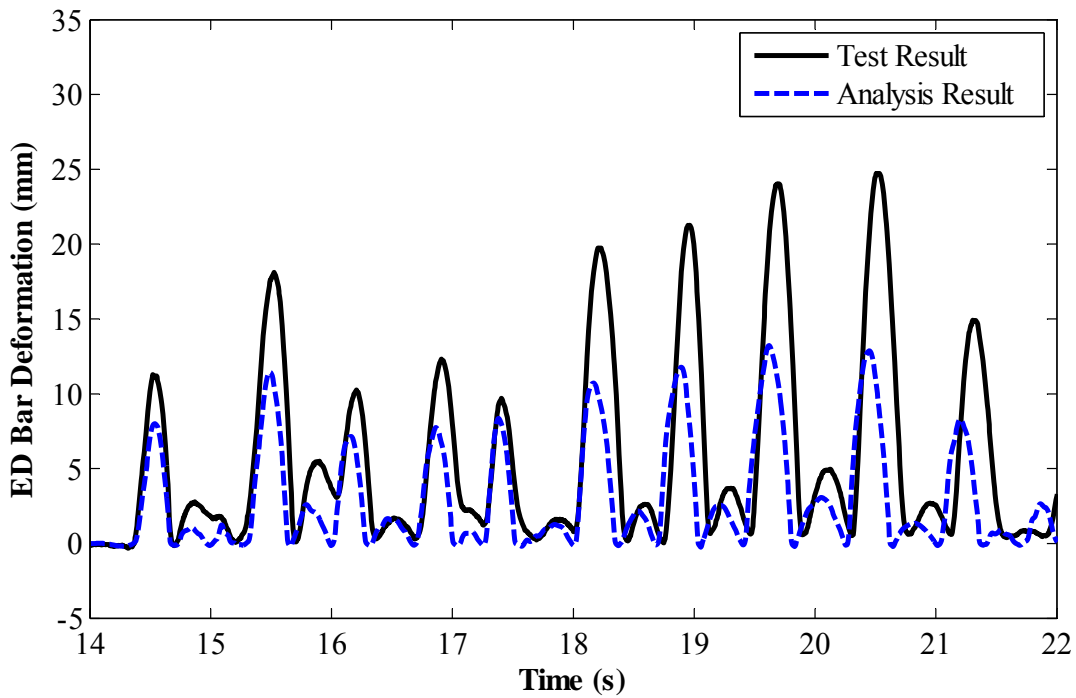
Figure 4.92 - ED bar 2 deformation -time comparison of results for 100% Kobe motion

4.6   Summary, Conclusions

Past earthquakes have shown examples of unsatisfactory performance of buildings using reinforced concrete structural walls as the primary lateral-force-resisting system. This pattern of poor performance pushed researchers to explore alternative design approaches using post-tensioned precast structural walls to better control yielding mechanisms and promote self-centering behavior. In December 2010, the National Research Institute for Earth Science and Disaster Prevention (NIED) in Japan conducted a three-dimensional earthquake simulation test on a full-scale, four-story building using the E-Defense shaking table. The seismic-force-resisting system of the test building comprised two PT frames in one direction and two unbonded PT precast walls in the other direction. The test building was subjected to several earthquake ground motions, ranging from serviceability level to near collapse. The studies, which are reported here, aim to develop practical structural engineering models, to conduct analytical simulations to test the capability of the structural models to replicate behaviors important to structural engineers, and to assess whether available analysis tools are sufficient to model dynamic behavior that results when a full-scale building is subjected to realistic earthquake ground shaking.

The test specimen had a lateral-load-resisting system in the Y-direction was two precast unbonded PT shear walls and one bay unbonded PT center moment frame at the B Axis. Shear walls had a rectangular cross section with a length (l_w) of 2500 mm and a thickness (t_w) of 250 mm with a cross-sectional aspect ratio l_w/t_w of 10. PT walls were 12 m high, and therefore had a slenderness ratio of $H_w/l_w = 4.8$, where H_w is the height of the wall, and l_w is the length of the wall. Wall panels were post-tensioned at the roof level with eccentrically located two bundles of post-tensioning tendons. Eight D22 (22 mm diameter) unbonded mild steel bars (four on each side) were placed with 540 mm eccentricity from the center of the wall cross section. These bars were unbonded through the lower 1.5 m of the first story and connected to the foundation with mechanical couplers. The building was designed using the latest code requirements and design recommendations available both in Japan and the U.S., including the ACI ITG-5.2-09. The test building was subjected to several earthquake ground motions, ranging from serviceability level to near collapse. The input ground motions were scaled JMA-Kobe and JR-Takatori records from the 1995 Hyogoken-Nanbu earthquake. Initially, the 25%, 50%, and 100% scaled versions of JMA-Kobe, the 40% and 60% scaled JR-Takatori motions were applied to the test specimen. The specimen was well instrumented with, accelerometers, displacements transducers, and strain gauges.

The fundamental vibration periods were measured using White Noise excitations prior to the applied ground motions. The initially measured fundamental period of the building was 0.45 seconds in the X-direction and 0.29 seconds in the Y-direction. For the 50% Kobe motion, the maximum story drift ratio was 0.004 for the X-direction and 0.006 for the Y-direction. Under the 100% Kobe motion, the maximum story drift values became 0.039 for the X-direction and 0.017 for the Y-direction. After the 100% Kobe motion, the concrete cover at the boundary regions were spalled at the wall base with a height of one wall thickness. The damage was concentrated in the unbonded energy dissipating bars. The contribution of the wall slip was very small. The damage at the column base was concentrated at a height of 0.5 times the column dimension.

The wall direction (Y-direction) of the building is modeled using the computer program,

Perform 3D, with emphasis on an implementation that would be practical for design-office implementation. This model is subjected to several ground motions to explore the accuracy of the analytical model. Initially, the analytical model of only shear walls was implemented. Structural walls were modeled using four-noded "Shear Wall Elements" (CSI). The axial forces and bending moments on the vertical axis are resisted by fiber cross section. Material stress-strain relationship properties were decided according to the material sample test results. Nonlinear material stress-strain relationships were assigned to the fibers for concrete and reinforcing steel. Shear forces on the element can be resisted by a shear spring. Due to anticipated low shear demands, an elastic shear material was used for walls. PT tendons and energy dissipation (ED) bars are modeled using truss elements with nonlinear material properties. Rayleigh damping is used for nonlinear response history analysis, with parameters set to produce 2 percent damping at periods $0.2T_1$ and T_1, where $T_1 = 0.45$ seconds.

Comparing the test and analytical simulation results, stiffness and base shear were underestimated significantly for all motions. Roof drift ratio time series were also poorly matched for the excitations, with the exception of the 100% Kobe motion after 17 s, for which the response histories matched fairly well. This good estimation could be a result of strength loss caused by heavy damage of the frames, where the response mainly depends on the walls. These results suggest that the contribution of the PT frames in the Y-direction may be significant and should be modeled for successful estimations of response.

Comparison of the wall simulation with test results led to the decision to model the frames in the Y-direction. A modified building model was developed that modeled the frame members on Axes A, B, and C, in addition to the walls. Beams and columns are modeled using nonlinear beam column elements with rigid end zones. Nonlinear fiber sections are assigned through the length of the elements with distributed plasticity. Similar to the shear wall elements, a simplified trilinear curve with a descending portion is used to model concrete and steel materials. Unbonded PT tendons of beams (PG2 & PG3) are modeled with parallel truss elements with nonlinear material properties. Rayleigh damping is used for nonlinear response history analysis, with parameters set to produce 2 percent damping at periods $T_1/8$ and $1.25T_1$, where $T_1 = 0.29$ seconds.

Base shear versus roof drift ratio relationships for all motions show the flag-shaped hysteresis typical of unbonded post-tensioned concrete. Important engineering parameters such as fundamental vibration period, stiffness, hysteresis shape, maximum base shear, and maximum roof drifts are adequately simulated using the numerical model. For all excitations, energy dissipated during the earthquake simulation (area inside the hysteresis curve) is estimated with good accuracy. Although estimated maximum roof drift ratios are very close to the test results, phase shifts in roof drift ratio versus time series are significant for some parts of the response. These discrepancies do not coincide with the peak responses or affect the prediction of the overall behavior of such systems.

For the 25% Kobe motion, the numerical model is slightly stiffer than the test specimen, as it is shifting out-of-phase after 19 s. Vibration period of the test specimen is increasing after 19 s, but the analytical model does not identify this increase in period. For the roof drift ratio versus time relationship, the calculated response damps out more slowly that the test results. For the 50% Kobe motion, the numerical model has a good estimation for the overall stiffness of the test building. The roof drift ratio versus time response of the 50% Kobe earthquake starts out-of-

phase with the test results. However, it becomes in-phase with the test results in about 17s, and follows the test building roof drift ratio versus time response accurately. The apparent damping of the numerical simulation is similar to the test specimen for this excitation. For 100% Kobe motion, the numerical model has good estimates for important engineering parameters such as maximum base shear and maximum roof drift ratio. Response of the numerical model seems slightly stiffer on the base shear versus roof drift ratio relationship. Assumed damping for the analytical model is in good agreement with the response.

The developed numerical model is able to simulate the PT force-time relationship in a very good agreement with the test results for 100% Kobe motion. For the 25% and 50% Kobe motions, there are some discrepancies in the simulation but numerical model was able to estimate the peak response quantities. The Perform 3D model was able to estimate the ED bar deformation-time relationship with a 20 to 30% difference in all motion. This discrepancy is a topic needs to be further studied.

Important engineering parameters such as fundamental vibration period, stiffness, hysteresis shape, maximum base shear, and maximum roof drifts are adequately simulated using the numerical model. There are, however, some discrepancies in the modeling of these responses with time. These discrepancies do not coincide with the peak responses or affect the prediction of the overall behavior of such systems. Moreover, the proposed numerical model is able to simulate the actions in building components such as the PT tendons and the ED bars. These results indicate that, while further improvements may be desirable, the selected modeling approach is capable of producing seismic response estimates of sufficient accuracy to be used for detailed design of unbonded post-tensioned, precast structural wall systems

Chapter 5.   Conclusions

The purpose of this study was to improve our understating of the seismic behavior and limitations of current design practices of reinforced concrete shear walls. The first part of the study assessed the collapse of the Alto Rio building as a result of earthquake shaking. Since Alto Rio building was designed using modern building codes (ACI 318-95), an understanding of the reasons of collapse will improve our understanding of how better to design similar buildings in the United States and around the world. The second part of the study uses data from a three-dimensional earthquake simulation test on a full-scale, four-story, precast post-tensioned concrete shear wall building. The goal was to develop practical structural engineering models, to conduct analytical simulations to test the capability of the structural models to replicate behaviors important to structural engineers, and to assess whether available analysis tools are sufficient to model dynamic behavior that results when a full-scale building is subjected to realistic earthquake ground shaking.

5.1   Collapse Investigation of a Concrete Shear Wall Building

The M_w 8.8 2010 Maule Chile earthquake affected over twelve million people in central south Chile, severely damaging more than 50 multi-story reinforced concrete buildings and causing partial or total collapse of four other such buildings. Among these, the 15-story residential Alto Rio building stands out as the first modern shear wall building to collapse by overturning during an earthquake. The recorded ground motions approximately 1.2 km (0.75 miles) away from Alto Rio show that shaking lasted more than 120 seconds with peak ground accelerations of 0.402g and 0.397g in east-west and north-south directions, respectively. Using the building plans and a post-earthquake reconnaissance report, reasons of collapse are investigated with linear elastic, nonlinear static, and nonlinear dynamic analyses, in Chapter 3.

A linear elastic model of the whole Alto Rio building was prepared using effective (cracked) section properties of the structural elements. The fundamental periods in transverse and longitudinal directions were typical of values for Chilean wall buildings, with values of $N/19$ and $N/21$, respectively, where N = number of stories. Calculated wall axial load ratios ranged from 0.05 to 0.07 $P/f_c'A_g$, where P considers expected loads (1.0D + 0.25L).

A nonlinear static analysis was conducted on an analytical model representing inelastic material properties of walls along axes 8 and 13 in the building transverse direction; this portion was deemed representative of the seismic-force-resisting system of the building. The model was loaded with an inverted triangular lateral force pattern. For loading to the east (collapse) direction, critical lateral strength degradation occurred due to crushing of the wall boundary at the east edge of the east wall along axis 13 at around 0.7% roof drift ratio, followed by similar crushing of the east part of wall along axis 8 around 1.0% roof drift ratio. The crushing zone occurred adjacent to a vertical discontinuity in the wall cross section. Solid wall panels beneath the stack of openings were calculated to undergo cracking and inelastic response, without failure, for loading in this direction. For lateral load toward the west, those same solid wall panels

sustained shear failures, as indicated by initiation of shear strength degradation, at approximately 0.9% roof drift ratio. This was followed by fracture of the longitudinal reinforcement at the east side of the east walls along Axis 13 at 1.6% roof drift ratio. Apart from the isolated shear failure of the solid panel beneath the stack of openings, analyses indicate that shear failure was not an initiator of building failure. In another nonlinear static analysis the effects of lap splices to the response are investigated. For lateral load toward the west, the roof drift capacity of the model decreased dramatically to 0.65%, which is caused by the lap splice failure at the east side of the east walls.

The effect of modeling decisions such as modeling of shear behavior of walls and the softening slope of the concrete material stress-strain relationship are also investigated for understanding of the model sensitivity for these parameters. Nonlinear static analysis of a model with linear elastic shear stress-strain relationship assigned for the whole model was conducted and compared with the previous model with nonlinear shear behavior. There was an apparent difference in the overall stiffness of these two models. It showed that the failure modes except the failure of shear panels are calculated with the same order with the inelastic shear material model. However; there were some discrepancies in drift capacities and strength of the model that can be critical to the dynamic response of such models. It was concluded that the inelastic modeling of shear should be employed by practicing engineers.

Dynamic analysis of a single-degree-of-freedom (SDOF) model was established to represent the effective first translational mode response of the Alto Rio building in the transverse direction. The SDOF model was excited by the ground motions recorded in Concepción, 1.2 km (0.75 miles) away from Alto Rio. Studies using this model indicate that building collapse would occur toward the east, as observed following the earthquake, at around 22 seconds into the ground motion, and that this result was relatively insensitive to the properties of the SDOF model. After a deformation cycle as large as 1.3% roof drift ratio in the west direction, the SDOF model collapses to the east (collapse) direction at around 22 seconds of the excitation. In the cycle to the east at around 20 seconds, concrete crushes under compression for both walls on Axes 13 and 8, respectively. Right after that the loading cycle changes direction and damages the shear panels on both Axes 8 and 13 at around 21 seconds. It is followed by a large cycle to the east direction around 22 seconds, where the structure permanently displaced to the east. This permanent displacement of the model is also an indicator of the collapse to the east direction. The final result of the dynamic SDOF analysis is consistent with the observed damage and collapse of the building.

In another nonlinear static analysis the effects of lap splices to the response are investigated. In light of the results of Hardisty et al. (2014), a Perform 3D model was modified to account for possible failure of the lap splices. Results of Hardisty et al. (2014) suggested that a value of $2\varepsilon_y$ would be a good approximation for the ultimate strain (ε_u) capacity of unconfined lap splices under cyclic loading.

For loading the model to the east, the direction in which collapse occurred, the drift capacity of the model was same as in the previous analysis of model not accounting for lap splice effects. However, there is relatively greater strength degradation after the crushing of the wall along axis 13. For lateral load to the west, unlike the previous results, the first significant event is the failure of shear panel on the Axis 13 at 0.62% roof drift ratio. It is followed by the failure of the longitudinal reinforcement lap splices at the east side of the east walls along Axis 13 at

0.82% roof drift ratio. This shows that the modifications done to account for lap splices affect the tension controlled failure dramatically, decreasing the drift capacity of the building to half of the previous model.

Similar to the previous analysis, a second single-degree-of-freedom (SDOF) model was established to represent the effective first translational mode response of the Alto Rio building in the transverse direction, accounting for the lap splice effects. After a deformation cycle as large as 1.2% roof drift ratio in the west direction, the SDOF model collapses to the east (collapse) direction at around 22 seconds of the excitation. The first significant event of the structure response under dynamic analysis is the damage at the shear panel on the Axis 13 in a cycle to the west around 15 seconds. In the cycle to the east at around 20 seconds, concrete crushes under compression for both walls on Axes 13 and 8y. Right after that the loading cycle changes direction to the west and causes the failure of the lap splices on the east side of the east wall on Axis 13 at around 21 seconds. It is followed by a large cycle to the east direction around 22 seconds, where structure permanently displaced to the east. This permanent displacement of the model is also an indicator of the collapse to the east direction. The results of the dynamic analysis of the modified SDOF system are very close to the analysis of the original model. This demonstrates that although the possible effects of the lap splices can change the nonlinear static analysis results of the Alto Rio building, it neither had a dramatic effect on the dynamic SDOF analysis, nor changed the mode of collapse.

Lateral wall buckling as another possible factor for collapse is also investigated. Buckling seems to be not a significant factor in the collapse of Alto Rio building. Possible effects of different modeling parameters such as; the descending slope of the concrete stress-strain relationship, and modeling decision of elastic or inelastic stress-strain relationship for shear behavior are investigated. These modeling parameters seem to affect the analysis results. However, they do not change the nature or the sequence of failure modes.

The nonlinear static and dynamic SDOF analysis results demonstrate that the Alto Rio building was susceptible to collapse to the east direction. The main factors contributing to the failure include: the configuration of T and L-shaped wall cross sections, vertical discontinuities at the east side of the building, and high shear stresses in the solid wall panels below the stack of openings. The structural drawings and reconnaissance data suggest that the absence of confined boundary elements and the occurrence of lap splices of longitudinal bars without sufficient transverse reinforcement could be other factors that contributed to the collapse. However, the analysis of models modified according to the behavior of lap splices demonstrated that lap splices have a very minor effect on the overall behavior of the building under this specific earthquake motion. The specific analyses reported in this study indicate one plausible failure sequence, that is, initiation of shear damage in the solid wall panel immediately below the stack of openings, crushing and buckling failure of the walls at the discontinuity between the first and second stories on the east side of the building, and subsequent failure of the tension chord on the west side of the building as it collapsed toward the east. Other failure sequences are also plausible, depending on details of the ground motion and structural model, but these were not indicated by the present study. Observed damage after the earthquake (IDIEM, 2010) is consistent with the findings of the analysis results.

5.2 Seismic Performance and Modeling of Post-Tensioned Precast Concrete Shear Walls

A three-dimensional earthquake simulation test on a full-scale, four-story, prestressed concrete building was conducted using the E-Defense shaking table facility. The lateral-load-resisting system in the Y-direction was two precast unbonded PT shear walls and one bay unbonded PT center moment frame at the B Axis. The input ground motions were scaled JMA-Kobe and JR-Takatori records from the 1995 Hyogoken-Nanbu earthquake, applied in a sequence of 25%, 50%, and 100% scaled versions of JMA-Kobe, and then 40% and 60% scaled JR-Takatori motions. The specimen was well instrumented with accelerometers, displacements transducers, and strain gauges.

In Chapter 4, the wall direction (Y-direction) of the building is modeled using the computer program, Perform 3D, with emphasis on an implementation that would be practical for design-office implementation. A comparison of the simulation and test results is done to assess the capability of currently available models to simulate the response of a real PT building under gradually increasing earthquakes. Initially, the analytical model of only shear walls was implemented. Comparing the test and analytical simulation results, stiffness and base shear were underestimated significantly for all motions. Roof drift ratio time series were also poorly matched for the excitations, with the exception of the 100% Kobe motion after 17 s, for which the response histories matched fairly well. This good estimation could be a result of strength loss caused by heavy damage of the frames, where the response mainly depends on the walls.

Comparison of the wall simulation with test results led to the decision to model the frames in the Y-direction. A modified building model was developed that modeled the frame members on Axes A, B, and C, in addition to the walls. Base shear versus roof drift ratio relationships for all motions show the flag-shaped hysteresis typical of unbonded post-tensioned concrete. Important engineering parameters such as fundamental vibration period, stiffness, hysteresis shape, maximum base shear, and maximum roof drifts are adequately simulated using the numerical model. There are, however, some discrepancies in the modeling of these responses with time. These discrepancies do not coincide with the peak responses or affect the estimation of the overall behavior of such systems. Moreover, the proposed numerical model is able to simulate the actions in building components such as the PT tendons and the ED bars. These results indicate that, while further improvements may be desirable, the selected modeling approach is capable of producing seismic response estimates of sufficient accuracy to be used for detailed design of unbonded post-tensioned, precast structural wall systems.

5.3 Recommendations for Future Studies

Although proposed analysis methods are state of the art, future work needs to be done in order to improve both design practice in reinforced concrete walls and post-tensioned precast concrete shear walls. Some of the topics that need to be investigated for the continuation of this study are:

- **Component testing wall building details.** Even though already verified numerical modeling was employed in the analysis of the Alto Rio building, experimental work is required for verification. Component tests of unconfined boundary elements, lap splices, vertical discontinuities, shear panels is missing from the literature and would improve the current knowledge and design practice.
- **Further investigation of the PT force and ED bar deformation estimations.** The analysis and results on the E-Defense test of PT walls are satisfactory for design and assessment of the post-tensioned precast concrete shear walls. However, further investigation of the simulation discrepancies especially at the PT tendon force and ED bar displacement values should be carried out. These parameters are very important for the design of these walls and miscalculation of these values can lead to overly conservative designs.
- **Further investigation of the E-Defense tests.** In Chapter 4, we only studied the 25%, 50%, and 100% Kobe motions. It would be beneficial to investigate the rest of the test motions, namely 40% and 60% Takatori motions. Test specimens were further damaged in these stages and modeling of damaged or near collapse state of PT walls are also crucial for analyses of existing structures. Three-dimensional analyses should also be carried out.
- **Investigation of the design space of PT walls.** The three dimensional full-scale E-Defense tests gave us a chance to verify our modeling techniques against real life conditions. Having verified numerical models provides us the opportunity to explore the design space of PT wall systems. Any change in design parameters such as post-tensioning force, ED bar area, changes in eccentricities, or material properties could be just modified in the current model and their effect on the response of PT walls could be investigated. This could improve and verify the current design practices of PT walls.
- **Verification of current PT wall force-displacement relationships.** The verification of PT wall force-displacement relationships (pushover) against the response of the E-Defense tests could be a great opportunity. The force-displacement relationships in the literature are developed using cyclic pseudo-dynamic experiments. Comparison of them against a three dimensional full-scale test under earthquake motions would give us the opportunity to verify and improve those relationships.

REFERENCES

1. ACI 318-95 (1995), "Building Code Requirements for Structural Concrete (ACI 318-95) and Commentary," American Concrete Institute, Farmington Hills, Michigan.

2. ACI 318-08 (2008). Building Code Requirements for Structural Concrete (ACI 318-08) and Commentary, American Concrete Institute, Farmington Hills, Michigan

3. ACI 318-11 (2011), "Building Code Requirements for Structural Concrete (ACI 318-11) and Commentary," American Concrete Institute, Farmington Hills, Michigan.

4. ACI ITG-5.2-09 (2009). Requirements for Design of a Special Unbonded Post-Tensioned Precast Shear Wall Satisfying ACI ITG-5.1 (ACI ITG-5.2-09) and Commentary, American Concrete Institute, Farmington Hills, Michigan

5. American Society of Civil Engineers (2006), "Seismic Rehabilitation of Existing Buildings", ASCE Standard ASCE/SEI 41-06.

6. American Society of Civil Engineers (2010). "ASCE/SEI 7-10: Minimum Design Loads for Buildings and Other Structures," Reston, VA, 650 pp.

7. Aristizabal-Ochoa, J.D., (1983), "Cracking and Shear Effects of Structural Walls", Journal of Structural Engineering, ASCE, V.109, No. 5, pp. 1267-1275

8. ATC 94 (2013). "Recommendations for Seismic Design of Reinforced Concrete Wall Buildings based on Studies of the 2010 Chile Earthquake," NIST GCR 13-917-25, National Institute of Standards and Technology.

9. Balkaya, C., and Kalkan, E. (2004). "Three-dimensional effects on openings of laterally loaded pierced shear walls." J. Struct. Eng., 10.1061/(ASCE)0733-9445(2004)130:10(1506), 1506–1514.

10. Barbosa, A. R. (2011). "Simplified vector-valued probabilistic seismic hazard analysis and probabilistic seismic demand analysis: Application to the 13-story NEHRP reinforced concrete frame-wall building design example." Ph.D. thesis, Dept. of Structural Engineering, Univ. of California, San Diego.

11. Bentz, E. (2000). "Sectional analysis of reinforced concrete members," Ph.D. dissertation, Dept. of Civil Engineering, University of Toronto, Toronto, ON.

12. Bolong, Z.; Mingshun, W.; and Kunlian, Z., (1980), "A Study of Hysteretic Curve of Reinforced Concrete Members Under Cyclic Loading", Proceedings, 7th World Conference on Earthquake Engineering, V. 6, Istanbul, Turkey, pp. 509-516.

13. Chai, Y.H., and Elayer, D.T., 1999, "Lateral stability of reinforced concrete columns under axial reversed cyclic tension and compression," Structural Journal, Vol. 96, No. 5, pp. 780-789.

14. Chopra, A. K. (2011). "Dynamics of Structures Theory and Applications to Earthquake Engineering Fourth Edition", Prentice Hall, Upper Saddle River, NJ.

15. Coleman, J., and Spacone, E. (2001). "Localization Issues in Force-Based Frame

Elements", Journal of Structural Engineering, American Society of Civil Engineers, 127(11), 1257-1265.

16. Colotti, V. and Vulcano, A., (1987), "Behavior of Reinforced Concrete Structural Walls Subjected to Severe Cyclic Loadings", Proceedings, Italian Association of Reinforced and Prestressed Concrete Conference, Stresa, Italy, pp. 87-102 (in Italian).

17. Computers and Structures, Incorporated (CSI), "ETABS Nonlinear, Extended 3D Analysis of Building Structures, Computers and Structures", Berkeley, CA

18. Computers and Structures, Incorporated (CSI), "Perform 3D, Nonlinear Analysis and Performance Assessment for 3D Structures", Berkeley, CA

19. Constantin, C., Filiatrault, A., Uang, C-M., and Foltz, B. (2001). "A post-tensioned energy-dissipating connection for moment-resisting steel structures". Proc. 1st Conf. on Steel and Composite Structures, 1621-1628.

20. Corley, W.G., Fiorato, A.E., and Oesterle, R.G., 1981, "Structural walls," Structural Journal, Vol. 72, No. 4, pp. 77-132.

21. Dazio, A.; Beyer, K.; and Bachmann, H. (2009). "Quasi-static Cyclic Tests and Plastic Hinge Analysis of RC Structural Walls," Engineering Structures, V. 31, pp. 1556-1571.

22. Der Kiureghian, A., and Y. Nakamura (1993). "CQC modal combination rule for high-frequency modes:. Earthquake Engineering and Structural Dynamics, 22(11), 943-956

23. Earthquake Engineering Research Institute, (2010). "EERI Special Earthquake Report-June 2010: The Mw 8.8 Chile Earthquake of February 27, 2010," Oakland, CA.

24. Elwood, K.J., and Eberhard, M.O. (2009). "Effective Stiffness of Reinforced Concrete Columns" , ACI Structural Journal, V. 106, No. 4, pp. 476-484

25. Elwood, K.J., Matamoros, A.B., Wallace, J.W., Lehman, D.E., Heintz, J.A., Mitchell, A.D., Moore, M.A., Valley, M.T., Lowes, L.N., Comartin, C.D., and Moehle, J.P. (2007). "Update to ASCE/SEI 41 Concrete Provisions". Earthquake Spectra. 23:3,493-523.

26. El-Tawil, S., Kuenzli, C. M., and Hassan, M. (2002). "Pushover of hybrid coupled walls. I: Design and modeling." J. Struct. Eng., 10.1061/(ASCE)0733-9445(2002)128:10(1272), 1272–1281.

27. Englekirk, R.E. (2002). "Design-construction of the Paramount-A 39-story precast prestressed concrete apartment building". PCI Journal. 47:4,56-71.

28. Fajfar, P. and Fischinger, M., 1990, "Mathematical Modeling of RC Structural Walls for Nonlinear Seismic Analysis", Proceedings, European Conference on Structural Dynamics, V. 2, Bochum, Germany, pp. 471-478.

29. Fischinger, M; Vidic, T.; Selih, J.; Fajfar, P.; Zhang, H.Y.; and Damjanic, F.B., (1990), "Validation of a Macroscopic Model for Cyclic Response Prediction of RC Walls", in N.B. Bicanic and H. Mang (eds.), "Computer Aided Analysis and Design of Concrete Structures", V. 2, Pineridge Press, Swansea, pp.l 131-1142.

30. Fischinger, M.; Vidic, T.; and Fajfar, P., (1991), "Evaluation of the Inelastic Response of a R.C. Building with a Structural Wall Designed According to Eurocode 8", Proceedings,

International Conference on Buildings with Load Bearing Concrete Walls in Seismic Zones, Paris, France, pp. 487-498.

31. Fischinger, M.; Vidic, T.; and Fajfar, P., (1992), "Nonlinear Seismic Analysis of Structural Walls Using the Multiple-Vertical-Line-Element Model", in H. Krawinkler and P. Fajfar (eds.), "Nonlinear Seismic Analysis of RC Buildings", Elsevier Science Publishers Ltd., London and New York, pp.191-202.

32. Hardisty, J.N., Villalobos, E., Richter, B.P., Pujol, S. (2014). " The Strength and Toughness of Reinforcement Lap Splices in Unconfined Boundary Elements", ACI Structural Journal (submitted)

33. Hassan, M., and El-Tawil, S. (2003). "Tension flange effective width in reinforced concrete shear walls." ACI Structural Journal, 100(3), 349–356.

34. Holden, T., Restrepo, J.I., and Mander J.B. (2003). "Seismic Performance of Precast Reinforced and Prestressed Concrete Walls", Journal of Structural Engineering 129:3,286-296.

35. Ichioka, Y., Kono S., Nishiyama M., and Watanabe F. (2009). "Hybrid System Using Precast Prestressed Frame with Corrugated Steel Panel Damper", Journal of Advanced Concrete Technology. 7:3,297-306.

36. IDIEM (2010). "Peritaje Estructural Edificio Alto Río, Ciudad de Concepción, Informe Final, Descripción de Caida y Factores Asociados al Colapso, Revisión 1," Informe No 644.424-00, Centro de Investigación, Desarrllo e Innovación de Estructuras y Materiales (IDIEM), University of Chile.

37. Ikenaga, M., Nagae T., Nakashima M., and Suita K. (2007). "Cyclic loading test of self-centering column bases developed for reduction of residual deformations", Architectural Institute of Japan. J. of Struct. Construct. Engrg.,612, 223-230.

38. Jiang, H., Kurama, Y., (2010). "Analytical modeling of medium-rise reinforced concrete shear walls," ACI Structural Journal, vol. 107, no. 4, pp. 400–410.

39. Kabeyasawa, T., 1997, "Design of RC Shear Walls in Hybrid Wall System", Proceedings, The Fourth Joint Technical Coordinating Committee, U.S.-Japan Cooperative Seismic Research on Composite and Hybrid Structures, Monterey.

40. Kabeyasawa, T.; Shiohara, H.; Otani, S.; and Aoyama, H., (1983), "Analysis of the Full-Scale Seven-Story Reinforced Concrete Test Structure", Journal of the Faculty of Engineering, University of Tokyo (B), V. 37; No. 2, pp. 431-478.

41. Kent, D.C., and Park, R. (1971). "Flexural members with confined concrete." J. Struct. Div., ASCE, 97(7), 1964-1990.

42. Keshavarzian, M. and Schnobrich, W.C., (1984), "Computed Nonlinear Response of Reinforced Concrete Wall-Frame Structures", Report No. SRS 515, University of Illinois at Urbana, Champaign.

43. Kotronis, P., and et al. (2009). "The seismic behavior of reinforced concrete structural walls: experiments and modeling." The 1755 Lisbon Earthquake: Revisited, Springer, Netherlands, 363–376.

44. Kurama, Y., Pessiki, S., Sause, R., and Lu, W-L. (1999). "Seismic behavior and design of unbonded post-tensioned precast concrete walls", PCI Journal. 44:3, 72-93.

45. Lehman, D., and Moehle, J. P. (2000). "Seismic Performance of Well-Confined Concrete Bridge Columns" Report No. PEER 1998/01, Pacific Earthquake Engineering Research Center, University of California, Berkeley, 295 pp.

46. Lu, Y., Panagiotou, M., (2014). "Three-Dimensional Cyclic Beam-Truss Model for Nonplanar Reinforced Concrete Walls", Journal of Structural Engineering, ASCE, published online April 13, 2013.

47. Mander, J.B., and Cheng, C-T. (1997). "Seismic resistance of bridge piers based on damage avoidance design", Tech. Rep. No. NCEER-97-0014, National Center for Earthquake Engineering Research, Dept. of Civil and Environmental Engineering, State Univ. of New York, Buffalo, N.Y.

48. Mander, J.B., Priestly, M.J.N., and Park R. (1988). "Theoretical Stress-Strain Model for Confined Concrete", Journal of Structural Engineering, ASCE, V. 114, No. 8, pp. 1804-1826

49. Maruta, M. and Hamada, K. (2010). "Shaking table tests on three story precast prestressed concrete frame", Architectural Institute of Japan. J. of Struct. Construct. Engrg., 75:648,405-413.

50. Massone, L.M., (2006). "RC Wall Shear – Flexure Interaction: Analytical and Experimental Responses," Doctoral Dissertation, University of California, Los Angeles.

51. Mazzoni, S., McKenna, F., and Fenves, G., (2010). "Open System for Earthquake Engineering Simulation User Manual", Berkeley, CA.

52. Menegotto, M. and Pinto, E., (1973), "Method of Analysis for Cyclically Loaded Reinforced Concrete Plane Frames Including Changes in Geometry and Non-Elastic Behavior of Elements Under Combined Normal Force and Bending", Proceedings, IABSE Symposium on Resistance and Ultimate Deformability of Structures Acted on by Well-Defined Repeated Loads, Lisbon, Portugal.

53. Moehle, J. P. (2013). CE 244 Class Reader, University of California, Berkeley, Chapter 6, 45-47.

54. Monti, G., and Nuti, C. (1992), "Nonlinear Cyclic Behavior of Reinforcing Bars Including Buckling," Journal of Structural Engineering, American Society of Civil Engineers, 118(12), 3268-3284.

55. Naeim F., B. Schindler, J.A. Martin, and S. Lynch (1990). "Hidden Zones of High Stress in Seismic Response of Structural Walls," Proceedings, 1990 Structural Engineers Association of California Convention, pp. 402-422.

56. Nagae, T., Tahara, K., Matsumori T., Shiohara, H., Kabeyasawa T., Kono, S., Nishiyama, M., Wallace, J., Ghannoum, W., Moehle, J.P., Sause R., Keller, W., and Tuna, Z. (2011). "Design and Instrumentation of the 2010 E-Defense Four-Story Reinforced Concrete and Post-Tensioned Concrete Buildings", Technical Report 2011/104, Pacific Earthquake Engineering Research Center, University of California, Berkeley

57. NIST GCR 14-917-25 (2014). "Recommendation for Seismic Design of Reinforced Concrete Wall Buildings Based on Studies of the 2010 Maule, Chile Earthquake". *National Institute of Standards and Technology*

58. Niwa, N. et al. (2005). "Seismic response control of precast prestressed concrete frames by dampers at beam's end, Architectural Institute of Japan", Summaries of Technical Papers of Annual Meeting Architectural Institute of Japan. C-2, Structures IV, pp. 749-750.

59. Official Chilean Code NCh 433.of.96. (1996). "Seismic Design of Buildings", Instituto Nacional de Normalizacion, Santiago, Chile.

60. Oesterle, R. G.; Fiorato, A. E.; Johal, L. S.; Carpenter, J. E.; Russel, H. E.; and Corley, W. G. (1976). "Earthquake Resistant Structural Walls - Tests of Isolated Walls," Report to the National Science Foundation, Construction Technology Laboratories, Portland Cement Association, Skokie, IL., 315 pp.

61. Oesterle, R. G.; Aristizabal-Ochoa, J. D.; Fiorato, A. E.; Russel, H. E.; and Corley, W. G. (1979). "Earthquake Resistant Structural Walls - Tests of Isolated Walls - Phase II," Report to the National Science Foundation, Construction Technology Laboratories, Portland Cement Association, Skokie, IL., 325 pp.

62. Orakcal, K., (2004)., "Nonlinear Modeling and Analysis of Slender Reinforced Concrete Walls", Doctoral Dissertation, University of California, Los Angeles.

63. Orakcal, K., and Wallace, J. W. (2006). "Flexural modeling of reinforced concrete walls - Experimental verification." ACI Struct. J., 103(2), 196–206.

64. Palermo, D., and Vecchio, F. J. (2007). "Simulation of cyclically loaded concrete structures based on the finite-element method." J. Struct. Eng., 10.1061/(ASCE)0733-9445(2007)133:5(728), 728–738.

65. Pampanin, S. (2005). "Emerging solutions for high seismic performance of precast/prestressed concrete building", J. Advanced Concr. Tech., 3:2,207-223.

66. Pampanin, S., Amaris, A., and Palermo, A. (2006). "Implementation and testing of advanced solutions for jointed ductile seismic resisting frames", Proceedings, 2nd International Fib Congress, ID8-20, Naples, Italy.

67. Panagiotou, M., Kim, G., Barbosa, A., and Restrepo, J. I. (2009). "Response verification of a reinforced concrete bearing wall building located in an area of high seismic hazard." Rep. prepared for the Portland Cement Association, Skokie, IL.

68. Panagiotou, M., Restrepo, J. I., Schoettler, M., and Kim, G. (2012). "Nonlinear cyclic truss model for reinforced concrete walls." ACI Struct. J., 109(2), 205–214.

69. Paulay, T., and Priestley, M.J.N., 1993, "Stability of ductile structural walls,"Structural Journal, Vol. 90, No. 4, pp. 385-392.

70. Parra, P.F., and Moehle, J.P., (2014), "Lateral buckling in reinforced concrete walls.", *Proceedings of the 10th National Conference in Earthquake Engineering* , Earthquake Engineering Research Institute, Anchorage, AK, 2014

71. PEER/ATC-72-1 (2010), "Modeling and Acceptance Criteria for Seismic Design and

Analysis of Tall Buildings," Applied Technology Council, Redwood City, CA.

72. Perez, F.J., Sause, R., and Pessiki, S. (2007)" "Analytical and Experimental Lateral Load Behavior of Unbonded Posttensioned Precast Concrete Walls," ASCE Journal of Structural Engineering, V. 133: No. 11, pp. 1531-1540.

73. Perez, F.J., Pessiki S. and Sause, R. (2013). "Experimental Lateral Load Response of Unbonded Post-Tensioned Precast Concrete Walls," ACI Structural Journal, V. 110: No. 6, pp. 1045-1056.

74. Petrangeli, M. (1999). "Fiber element for cyclic bending and shear of RC structures II: Verification," Journal of Engineering Mechanics, vol. 125, no. 9, pp. 1002–1009.

75. Pilakoutas, K. and Elnashai, A. (1995). "Cyclic Behavior of Reinforced Concrete Cantilever Walls, Part I: Experimental Results," ACI Structural Journal, V. 92: No. 3, pp. 271-281.

76. Pilakoutas, K. and Elnashai, A. (1995). "Cyclic Behavior of Reinforced Concrete Cantilever Walls, Part II: Discussions and Theoretical Comparisons," ACI Structural Journal, V. 92: No. 4, pp. 425-433.

77. Priestley, M.J.N. (1991). "Overview of the PRESSS research program". PCI Journal. 36:4,50-57.

78. Priestley, M.J.N. (1996). "The PRESSS program current status and proposed plans for phase III", PCI Journal. 41:2,22-40.

79. Priestley, M.J.N. , Sritharan, S., Conley, J.R., and Pampanin, S. (1999). "Preliminary results and conclusions form the PRESSS five-story precast concrete test building", PCI Journal. 44:6,42-67.

80. Priestley, M.J.N., and Tao, J-T. (1993). "Seismic response of precast prestressed concrete frames with partially debonded tendons", PCI Journal. 38:1,58-69.

81. Rahman, A., and Restrepo, J.I. (2000). "Earthquake resistant precast concrete buildings: Seismic performance of cantilever walls pre-stressed using unbonded tendons", Research Rep. No. 2000-5, Dept. of Civil Engineering, Univ. of Canterbury, Christchurch, New Zealand

82. Ramirez, P., and Vivallos, J., (2009). :Microzonificacion Sismica de la Ciudad de Concepción", Chile, in XII Congreso Geologico Chileno, Santiago, Chile.

83. Razvi, S., and Saatcioglu, M. (1999). "Confinement Model for High-Strength Concrete", Journal of Structural Engineering 125:3,281-289.

84. Rejec, K., T. Isaković, and M. Fischinger (2011). "Seismic shear force magnification in RC cantilever structural walls designed according to Eurocode 8," Bulletin of Earthquake Engineering, DOI 10.1007/s10518-011-9294-y, 20 pp.

85. Renadic (2010). "Red de Cobertura Nacional de Acelerografos", Departamento de Ingenieria Civil, Facultad de Ciencias Fisicas y Matematicas, Universidad de Chile

86. Ricles, J.M., Sause, R., Garlock, M.M., and Zhao, C. (2001). "Posttensioned seismic-resistant connections for steel frames", Journal of Structural Engineering 127:2,113-121.

87. Ricles, J.M., Sause, R., Garlock, M.M., and Zhao, C. (2001). "Posttensioned seismic-resistant connections for steel frames", Journal of Structural Engineering 127:2,113-121.

88. Roy, H.E.H, Sozen, M.A. (1965). "Ductility of Concrete in Flexural Mechanics of Reinforced Concrete," SP12, American Concrete Institute/American Society of Civil Engineers, Detroit, pp. 213–235.

89. Saiidi, M., and Sozen, M. A. (1981), "Simple Nonlinear Seismic Analysis of R/C Structures," Journal of Structural Engineering, American Society of Civil Engineers, 107(ST5), 937-952.

90. Skinner, R.I., Robinson, W.H., and McVerry, G.H. (1993). "An introduction to seismic isolation", Wiley, New York.

91. Sittipunt, C., andWood, S. L. (1993). "Finite element analysis of reinforced concrete shear walls." Civil Engineering Studies, Structural Research Series No. 584, Univ. of Illinois, Urbana.

92. Stanton, J., Stone W., and Cheok, G.S. (1997). "A hybrid reinforced precast frame for seismic regions", PCI Journal. 42:2,20-32.

93. Sozen, M.A., P. Monteiro, J.P. Moehle and H.T. Tang (1992). "Effects of Cracking and Age on Stiffness of Reinforced Concrete Walls Resisting In-Plane Shear," Proceedings, Fourth Symposium on Current Issues Related to Nuclear Power Plant Structures, Equipment and Piping, Orlando, Florida, December 9-11, 1992.

94. Sugata, M. and Nakatsuka, T. (2005). "Study for flag shaped hysteresis model of precast prestressed flexural member with unbonded tendons and mild steels", Architectural Institute of Japan. . J. of Struct. Construct. Engrg., 598,133-140.

95. Takayanagi, T. and Schnobrich, W.C., (1976), "Computed Behavior of Reinforced Concrete Coupled Shear Walls", Report No. SRS 434, University of Illinois at Urbana, Champaign.

96. Thomsen, J. H. and Wallace, J. W. (1995). "Displacement-Based Design of RC Structural Walls - An Experimental Investigation of Walls with Rectangular and T-Shaped Cross-Sections". Report No. CU/CEE-95/06, Department of Civil Engineering, Clarkson University, Potsdam, New York, 353 pp.

97. Thomsen, J. H. and Wallace, J. W. (2004). "Displacement-Based Design Procedures for Slender Reinforced Concrete Structural Walls - Experimental Verification," Journal of Structural Engineering, ASCE, V. 130, No. 4, pp. 618-630.

98. Toranzo, L., Carr A.J., and Restrepo, J.I. (2001). "Displacement based design of rocking walls incorporating hysteretic energy dissipators". Proc. 7th Int. Seminar on Seismic, Passive Energy Dissipation and Active Control of Vibration of Structures.

99. U.S. Geological Survey (USGS), (2010). USGS Earthquake Hazards Program: Magnitde 8.8 – Offshore Bio-Bio, Chile, available at earthquake.usgs.gov/earthquakes/eqinthenews/2010/us2010tfan/

100. Vecchio, F.J, Collins, M.P., (1986). "The Modified Compression-Field Theory for Reinforced Concrete Elements Subjected to Shear", ACI Journal, Proceedings V. 83 No.

2, March-April 1986, pp. 219-231.

101. Villalobos, E.J. (2014). "Seismic Response of Structural Walls with Geometric and Reinforcement Discontinuities," Ph.D. dissertation, Dept. of Civil Engineering, Purdue University, West Lafayette, IN.

102. Vulcano, A. and Bertero, V.V., (1986), "Nonlinear Analysis of RC Structural Walls", Proceedings, 8th European Conference on EQ Engineering, V. 3, Lisbon, Portugal, pp 6.5/1-6.5/8.

103. Vulcano, A. and Bertero, V.V., (1987), "Analytical Models for Predicting the Lateral Response of RC Shear Walls: Evaluation of Their Reliability", EERC Report No. UCB/EERC-87/19, Earthquake Engineering Research Center, University of California, Berkeley.

104. Vulcano, A.; Bertero; V.V.; and Colotti, V., (1988), "Analytical Modeling of RC Structural Walls", Proceedings, 9th World Conference on Earthquake Engineering, V. 6, Tokyo-Kyoto, Japan, pp. 41-46.

105. Vulcano, A., (1992), "Macroscopic Modeling for Nonlinear Analysis of RC Structural Walls", in H. Krawinkler and P. Fajfar (eds.), "Nonlinear Seismic Analysis of RC Buildings", Elsevier Science Publishers Ltd., London and New York, pp.181-190.

106. Wallace, J.W., Moehle, J.P., (1989). "The 1985 Chile Earthquake: An Evaluation of Structural Requirements for Bearing Wall Buildings," Report N° UCB/EERC-89-05.

107. Wallace, J.W., Moehle, J.P., (1993). "An Evaluation of Ductility and Detailing Requirements of Bearing Wall Buildings Using Structural Walls," Journal of Structural Engineering, pp. 121(1).